UNIVERSITA’ DEGLI STUDI DI PADOVA

Sede Amministrativa: Università degli Studi di Padova

DIPARTIMENTO DI GEOSCIENZE

SCUOLA DI DOTTORATO IN SCIENZE DELLA TERRA

CICLO XXVI

STRUCTURE AND MECHANICAL PROPERTIES OF SEISMOGENIC FAULT ZONES IN CARBONATES

Direttore della Scuola : *Ch.mo Prof. Massimiliano Zattin*

Supervisore : *Prof. Giulio Di Toro*

Cotutore: *Dr. Steven A. F. Smith*

Dottorando: *Michele Fondriest*

2014

UNIVERSITÀ
DEGLI STUDI
DI PADOVA

Sede Amministrativa: Università degli Studi di Padova

Dipartimento di Geoscienze

SCUOLA DI DOTTORATO DI RICERCA IN: Scienze della Terra
CICLO XXVI

STRUCTURE AND MECHANICAL PROPERTIES OF SEISMOGENIC FAULT ZONES IN CARBONATES

Direttore della Scuola : Ch.mo Prof. Massimiliano Zattin
Supervisore : Prof. Giulio Di Toro
Cotutore : Dr. Steven A. F. Smith

Dottorando: Michele Fondriest

Riassunto

In molte regioni sismiche dell'area Mediterranea, tra cui l'Italia e la Grecia, gran parte dei terremoti, anche distruttivi, enucleano e propagano in sequenze di rocce carbonatiche della crosta superiore (terremoto dell'Aquila, 2009, M_w 6.1). Questo è vero soprattutto per le sequenze di *foreshock* e *aftershock*. Le indagini sismologiche, geofisiche e geodetiche forniscono dei parametri fondamentali per la caratterizzazione delle sorgenti sismiche (momento sismico, caduta di sforzo statico, energia elastica irradiata) ma non hanno risoluzione spaziale sufficiente per descrivere in maniera dettagliata la geometria delle sorgenti sismiche e i processi chimico-fisici attivi nelle zone di faglia durante un terremoto. Questi aspetti limitano fortemente la nostra conoscenza della fisica dei terremoti.

In questa tesi la struttura interna e le proprietà meccaniche di zone di faglia sismogenetiche in rocce carbonatiche sono state studiate utilizzando un approccio multidisciplinare e complementare rispetto a quello classico basato su dati sismologici principalmente ricavati dall'inversione delle onde sismiche. I metodi utilizzati sono: (i) il rilevamento strutturale di dettaglio di zone di faglia esumate in carbonati con tecniche di terreno e di telerilevamento (ad es. utilizzo di un drone per ottenere immagini ad alta risoluzione di grandi affioramenti), (ii) la realizzazione di prove meccaniche su roccia (e polveri di roccia) in condizioni di deformazione rilevanti per il ciclo sismico (utilizzo di apparati di tipo rotary, pressa uniassiale e Split Hopkinson Pressure Bar), (iii) lo studio mineralogico-microstrutturale (microscopia ottica e a scansione elettronica, microsonda elettronica, diffrazione a raggi X su polveri, catodoluminescenza, microtomografia a raggi X, interferometria in luce bianca, analisi di immagine) di rocce di faglia naturali e sperimentali per vincolare i processi chimico-fisici attivi in carbonati durante un terremoto.

Sono state selezionate due zone di faglia in dolomie: la zona di faglia del Passo della Borcola (BPFZ) e la zona di faglia di Foiana (FFZ). Entrambe le zone di faglia sono esumate da profondità < 3 km e affiorano nel settore delle Alpi Meridionali (Italia). L'architettura interna delle due zone di faglia è fortemente controllata dalla riattivazione di strutture ereditate come sistemi di giunti a scala regionale e superfici di strato.

La BPFZ è una faglia secondaria trascorrente appartenente al sistema della Linea Schio-Vicenza. La presenza all'interno della BPFZ di zone di scivolamento estremamente localizzate e spesso organizzate in livelli cataclastici ed ultracataclastici con bordi irregolari (a lobi e cuspidi), iniettati lungo fratture estensionali e caratterizzati da una forte selezione granulometrica ha suggerito l'attivazione di fenomeni di fluidizzazione durante la propagazione di rotture sismiche in un ambiente ricco in fluidi.

La FFZ è una faglia transpressiva sinistra a scala regionale che presenta sistematiche variazioni nella propria struttura interna (e.g. spessore della zona di faglia, orientazione e cinematica delle faglie minori) lungo la direzione e l'immersione della faglia. La zona di faglia esposta è caratterizzata dalla presenza di dolomie frantumate senza evidenze significative di deformazione per taglio (dolomie frantumate *in-situ*)

associate a faglie con piccoli rigetti (< 0.5 m) e superfici a specchio con clasti troncati. L'assenza di vene o fratture sigillate indica che la fagliazione è avvenuta in un ambiente povero in fluidi.

L'origine delle faglie con superfici a specchio e delle dolomie frantumate *in-situ* della FFZ è stata investigata attraverso esperimenti eseguiti (1) con un apparato di tipo *rotary* imponendo basse ed alte velocità (0.0001-1 m/s) di scivolamento su polveri di dolomia e (2) con un pressa uniassiale e una Split Hopkinson Pressure Bar imponendo basse ed alte velocità di deformazione (quasi-statiche 10^{-3} s^{-1}, dinamiche > 50 s^{-1}) su cilindri di dolomia. Applicando le condizioni di sforzo normale e rigetto stimate per le faglie della FFZ, superfici a specchio simili a quelle naturali in termini di rugosità delle superfici e di microstrutture (presenza di clasti troncati lungo le superfici di faglia), sono state prodotte negli esperimenti di tipo rotary solo a velocità di scivolamento cosismiche ($v \geq 0.1$ m/s). Inoltre dolomie frantumate *in-situ* con microstrutture simili a quelle descritte lungo la FFZ (frammenti di roccia con dimensioni fino a qualche millimetro allungati nella direzione di applicazione del carico e zone di microfratturazione incipiente) sono state prodotte negli esperimenti con la Split Hopkinson Pressure Bar solo a ratei di deformazione > 200 s^{-1} : tali ratei di deformazione sono in genere associati alle perturbazioni di sforzo dovute al passaggio di una rottura sismica. Pertanto l'associazione di dolomie frantumate *in-situ* tagliate da faglie discrete con superfici a specchio è stata interpretata come il risultato della propagazione di rotture sismiche nelle porzioni superficiali della FFZ.

Infine, a livello qualitativo, la complessità strutturale delle due zone di faglia studiate in termini di geometria del *network* di faglie e fratture, distribuzione spaziale delle rocce di faglia, orientazione e cinematica delle faglie, è confrontabile sia con la distribuzione del danneggiamento di faglia predetta da simulazioni di rotture sismiche, sia con la struttura di sorgenti sismogenetiche attuali in carbonati desunta da osservazioni sismologiche.

Abstract

In many seismically active areas (e.g. Italy, Greece) earthquakes, sometimes destructive, nucleate within (aftershocks surely do) and propagate through carbonates in the upper crust (e.g. L'Aquila earthquake, 2009, M_w 6.1). Seismology, geophysics and geodesy furnish key parameters related to the earthquake source (e.g. seismic moment, static stress drop, radiated energy) but lack sufficient resolution to constrain detailed three-dimensional fault zone geometry and coseismic on- and off-fault deformation processes at scales relevant to earthquake physics.

In this thesis it is proposed to study the internal structure and mechanics of fault zones hosted in carbonate rocks using a multidisciplinary approach, complementary to the seismological-based one. This includes detailed structural survey to quantify the architecture of exhumed fault zones in carbonates both by field and remote sensed methods (e.g. use of a drone to get high-resolution aerial images), rock deformation experiments under conditions relevant to the seismic cycle (e.g. use of rotary shear apparatus, uniaxial press, Split Hopkinson Pressure Bar), microstructural-mineralogical characterization (optical and scanning electron microscopy, electron microprobe analyses, X-ray powder diffraction, cathodoluminescence, X-ray microtomography, white light interferometry, image analysis) of natural and experimental fault rocks to infer the physico-chemical processes occurring during earthquakes.

Two fault zones cutting dolostones exhumed from < 3 km depth in the Italian Southern Alps were described: the Borcola Pass Fault Zone (BPFZ) and the Foiana Fault Zone (FFZ). In both cases the internal structure of the two fault zones was strongly influenced by the reactivation of preexisting anisotropies such as regional-scale joint sets and bedding surfaces.

The BPFZ is a secondary strike-slip branch of the regional Schio-Vicenza Line that developed in a fluid-rich upper crustal environment. The microstructural characteristics of the principal and secondary slip zones of the BPFZ, including detailed analysis of the clast size distribution of injected cataclasites, suggested coseismic fluidization processes during faulting, most likely related to the propagation of ancient seismic ruptures in to the shallow crust.

The FFZ is a major sinistral transpressive fault zone that developed in a fluid-poor upper crustal setting. Systematic along-strike and down-dip changes in the structure of the FFZ were recognized, allowing a comparison to be made between field observations and the predictions of three-dimensional earthquake rupture simulations. A noteworthy characteristic of the FFZ is the presence of thick belts (hundreds of meters) of in-situ shattered dolostones cut by discrete mirror-like fault surfaces.

The origin of mirror-like fault surfaces and in-situ shattered dolostones in the FFZ was investigated using, respectively, low- to high-velocity (0.0001-1 m/s) rotary shear friction experiments on dolostone gouges and low- to high-strain rate (quasi-static 10^{-3} s^{-1}, dynamic > 50 s^{-1}) uniaxial compression tests on dolostone rock cylinders. At applied normal stresses and displacements consistent with those estimated for the FFZ, experimental mirror-like fault surfaces comparable to the natural examples (e.g. clast truncation

along fault surfaces, similar surface roughness) were formed in rotary-shear experiments only at seismic slip rates ($v \geq 0.1$ m/s). I suggest therefore that small-displacement mirror-like fault surfaces developed in dolostone gouge layers represent markers of seismic slip. In-situ shattered dolostones similar to those found within the FFZ (i.e. rock fragments up to a few millimeters in size elongated in the stress wave loading direction, incipient zones of microfracturing down to the micrometer scale) were formed during uniaxial compression tests only above strain rates of ~ 200 s^{-1}. The association of in-situ shattered dolostones cut by discrete mirror-like fault surfaces is interpreted to record the propagation of multiple earthquake ruptures within the shallow crustal portions of the FFZ.

Lastly, the structural complexity of the studied fault zones in terms of three-dimensional geometry of the fault-fracture network, fault rock spatial distribution, fault orientation and kinematics, compares favorably to the predicted damage distribution in three-dimensional earthquake rupture simulations, as well as the structure of active seismic sources hosted in carbonate rocks as illuminated by seismological techniques.

Table of contents

Chapter 1. Introduction

1. Earthquake occurrences in carbonate rocks

Many seismically active regions on Earth, including the Mediterranean area, the Himalayan-Tethyan mountain chain and the Canadian Rockies, contain thick sequences (up to 4-10 km) of sedimentary carbonates (mainly limestones and dolostones) in the brittle upper crust. In the central Mediterranean area, Italy, the Balkans and the Aegean region are affected by moderate to large shallow crustal earthquakes and seismic sequences (i.e. hypocenters of the main shocks at 7-15 km of depth) associated with thrust, normal and strike-slip faults. Tectonic settings include the frontal parts of fold- and thrust belts and back-arc extensional basins. The active faults represent the source of modern and historical destructive earthquakes up to $M_w \sim 7$ (e.g. Irpinia-Basilicata (Italy), 1980, M_w 6.9; Western Macedonia (Greece), 1995, M_S 6.6; Barka and Reilinger, 1997; McKenzie, 1978, Westaway and Jackson, 1984; Stiros, 1995). Although the mainshocks of some of these earthquakes are likely to have initiated within the crystalline basement, rupture propagation in to the shallow crust occurred within overlying carbonate rocks. This is especially true for foreshock and aftershock sequences, which are typically hosted entirely (i.e. both rupture initiation and propagation) within carbonate rocks (Fig.1-3). **Fault zones hosted in carbonates represent significant seismogenic sources and their investigation in terms of fault zone structure and fault-related deformation processes is fundamental to improve our knowledge of earthquake mechanics.** In this thesis the structure and mechanical properties of seismogenic fault zones in carbonates are investigated by combining (i) field description of exhumed fault zones in carbonates (principally dolostones), (ii) rock deformation experiments, and (iii) mineralogical-microstructural characterization of natural fault rocks and experimental products.

1.1 Seismological and geophysical characteristics of earthquake sequences in carbonates

In this section I briefly summarize a series of seismological and geophysical observations concerning recent moderate to large magnitude seismic events hosted in carbonate rocks and characterized by different kinematics: the 2009 L'Aquila seismic sequence (normal fault system, Central Apennines, Italy), the 2012 Emilia sequence (thrust fault system, Po Plain, Italy), and the 1998 and 2004 Bovec-Krn sequences (strike-slip fault system, Slovenian Alps, Slovenia). Regardless of the different kinematics, these three seismic sequences display common features including the geometrical complexity of the activated fault network, the long lasting spatio-temporal evolution of seismic events and the heterogeneity in elastic properties measured within the seismogenic fault zones.

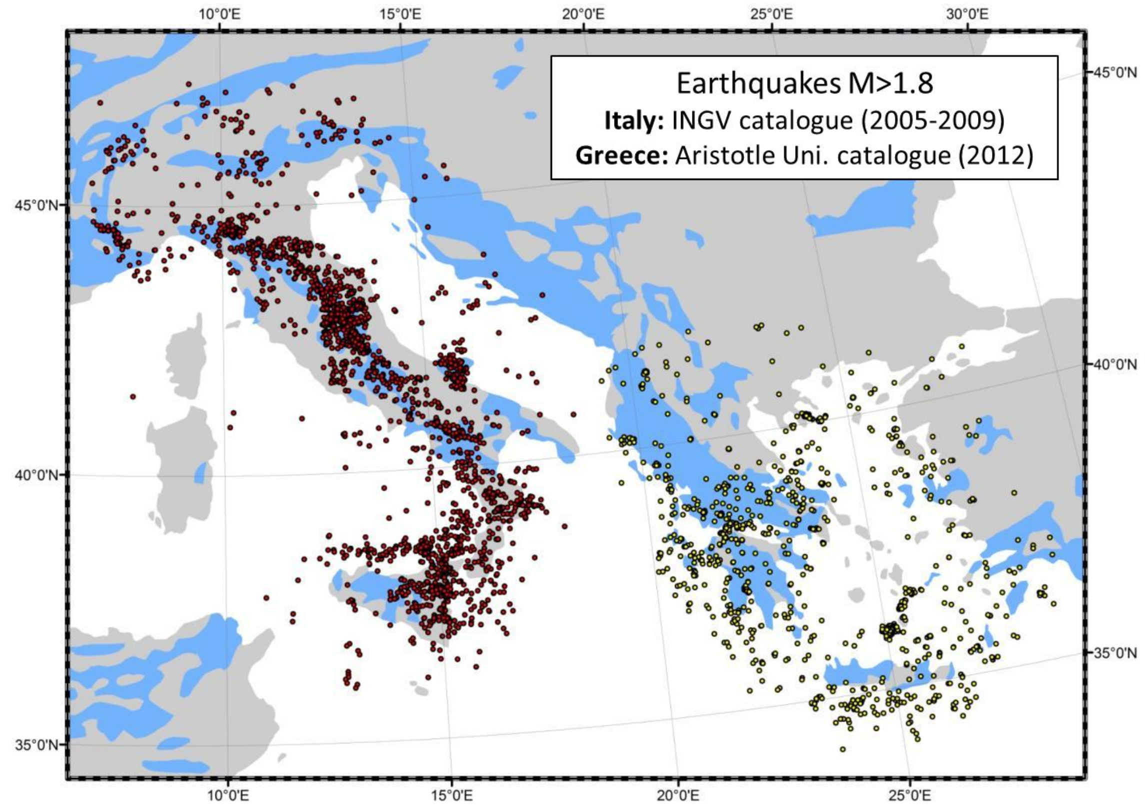

Fig.1 Map showing the spatial distribution of carbonate rocks (blue areas) on the surface in the central Mediterranean area (from Dürr et al., 2005). Epicenters of earthquakes with M > 1.8: INGV catalogue (period 2005-2008) are red spots, Aristotle University catalogue (year 2012) are yellow spots.

L'Aquila seismic sequence, April 2009

On 6 April 2009, after a foreshock sequence lasting around 4 months and culminating with a M_w 4 foreshock on March 30, the Paganica Fault near the town of L'Aquila ruptured to produce a M_w 6.1 main shock followed by thousands of aftershocks, including major aftershocks of M_w 5.6 and M_w 5.4 on 7 April and 9 April, respectively (Chiarabba et al., 2009). The mainshock was located at ~ 8.6 km depth and produced almost pure dip-slip normal faulting (Chiarabba et al., 2009; Chiaraluce, 2012). The spatio-temporal distribution of the foreshocks was complex: the foreshocks were clustered along the mainshock fault plane until the 30th March event, which activated a minor antithetic off-fault segment, and then jumped back to mainshock fault plane a few hours before the M_w 6.1 rupture. These observations, combined with variations in the V_P/V_S ratio in the mainshock region, suggested the involvement of fluids in the evolution of the foreshock sequence (Lucente et al., 2010). The spatio-temporal distribution of aftershocks indicated that at first the main rupture propagated unilaterally to the southeast. After that, seismicity migrated toward the northwest, where three $M_W \geq 5.0$ events activated the Campotosto Fault. A process of fluid discharge has been used to model the observed seismicity migration (Di Luccio et al., 2010; Chiaraluce et al., 2011a; Malagnini et al., 2012). Based on high-resolution relocations of both foreshocks and aftershocks the structure of the fault system activated during the April 2009 seismic sequence was reconstructed with a spatial resolution down to c. 0.1 km (Valoroso et al., 2013). The fault system consisted of a 50 km long en-echelon system of normal faults containing two major faults: the high-angle L'Aquila Fault (corresponding to the Paganica Fault on the surface) and the listric Campotosto Fault (likely corresponding to the Monti della Laga Fault on the surface) (Chiaraluce, 2012). The geometrical complexity of the fault system was represented by the presence of multiple antithetic and synthetic fault segments tens of meters long in both the hanging wall and footwall, along with bends and cross fault intersections along the main fault and fault splays (Valoroso et al. 2013). Moreover, the spatial distribution of aftershocks defined a "seismogenic damage zone" with a width ranging between 0.3 km and 1.5 km (Valoroso et al., 2013). The crustal structure in the area of the L'Aquila earthquake sequence is characterized by Jurassic–Cretaceous carbonate sequences with a thickness of up to 8–10 km due to imbrication and crustal thickening during fold-and thrust belt development (Ghisetti and Vezzani, 1999; Patacca et al., 2008). Although the main rupture of the L'Aquila seismic sequence may have nucleated within the crystalline basement, it propagated through the carbonate sequence, whereas almost all of the aftershocks both nucleated and propagated within the carbonates (Chiarabba et al., 2009, 2010) (Fig.2).

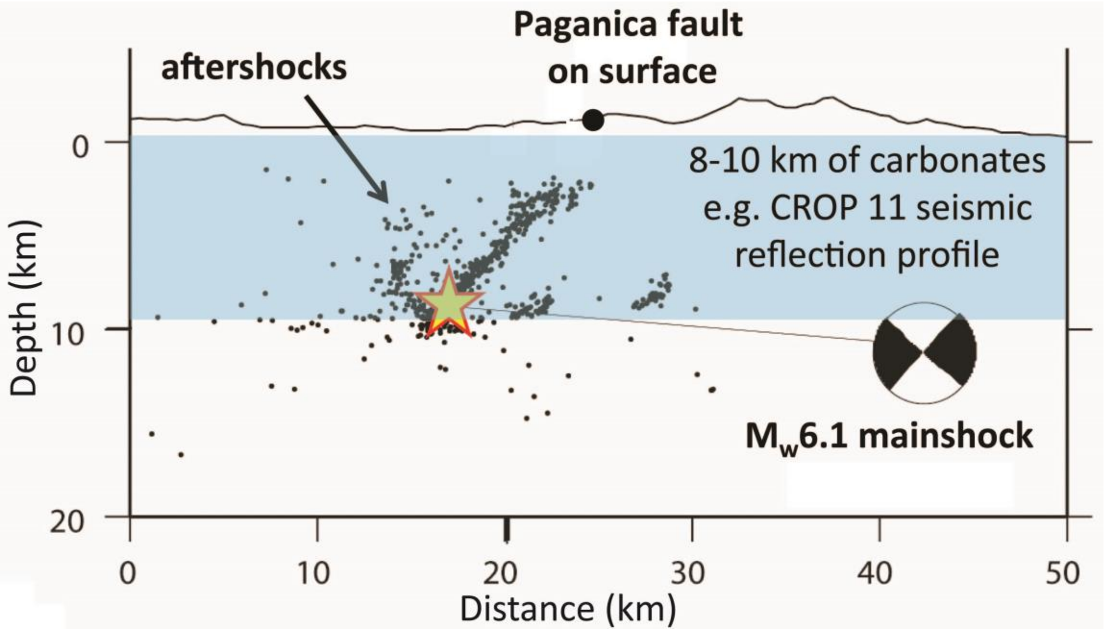

Fig.2 (previous page) Cross section of the L'Aquila area showing the distribution in depth of the mainshock and aftershocks of the April 2009 seismic sequence. The aftershocks illuminate the Paganica Fault, where the main rupture of the 9th of April nucleated, and other subparallel faults. Since the thickness of the carbonate sequence in the area is ca. 8-10 km, most of the aftershocks are located within carbonate rocks. (modified from Chiaraluce et al., 2011).

Emilia seismic sequence, May-June 2012

The May-June 2012 Emilia seismic sequence was characterized by two destructive earthquakes, M_L 5.9 on 20th May and M_L 5.8 on 29th May, followed by hundreds of aftershocks affecting the central sector of the Po Plain (La Vecchia et al., 2012; Ventura and Di Giovanbattista, 2013). The two mainshocks ruptured two buried, sub-parallel thrusts of the Northern Apennines associated with growing anticlines: the Ferrara thrust and the Mirandola thrust. The aftershocks following the 20th May event were distributed along an E-W axis in correspondence to the Ferrara anticline. Most of the earthquakes were located on the frontal ramp of the Ferrara thrust and were concentrated at depths < 10 km. The aftershocks migrated eastward with time. The aftershocks of the 29th May event were mainly located on the frontal ramp of the Mirandola thrust at depths of 5-10 km and migrated westward with time. The main event on the 20th May propagated eastward while that of 29th May poropagated westward. Therefore the spatial distribution of the aftershocks was controlled by the frontal and lateral ramps of the main thrusts. The seismicity of the Emilia sequence, including the main shocks and a majority of the aftershocks, developed within the Mesozoic-Tertiary carbonates and the overlying Miocene to Holocene units (Ventura and Di Giovanbattista, 2013) (Fig.3). Calculations of thrust activation at shallow depths (mainshock hypocentral depths are 5-7 km) indicate the presence of suprahydrostatic pore pressures, which seemed to play a significant role in earthquake nucleation during this sequence (Ventura and Di Giovanbattista, 2013).

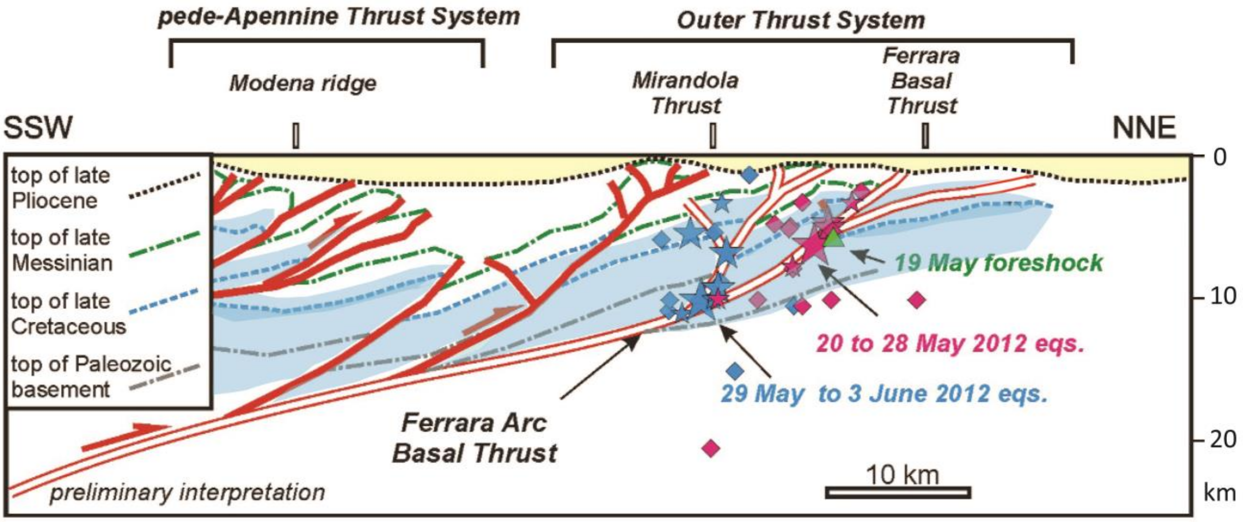

Fig.3 Cross section of the Po plain area where May-June 2012 Emilia seismic sequence occurred. Seismicity involved the buried frontal thrusts of the Apennines. Pede-Apennine thrusts are represented with thick red lines whereas outer thrusts are represented with double thin red lines. The 19 May foreshock and the 20-28 May events are located aroung the Ferrara thrust, while the 29 May to 3 June events are located around the Mirandola thrust. Chronological boundaries of the sedimentary sequence are traced. Holocene deposits are in yellow. Carbonate rocks are in blue. The majority of the earthquake hypocenters are located within carbonate rocks. (modified from La Vecchia et al., 2012).

Bovec-Krn seismic sequences, April 1998 and July 2004

The Bovec-Krn seismic sequences of April 1998 and July 2004 activated the right-lateral strike-slip Bovec-Krn Fault (northwestern Slovenia) with two main shocks of M_D 5.6 and 5.1 respectively. The mainshock in April 1998 nucleated at a depth of c. 6.9 km on the sub-vertical Bovec-Krn Fault and was followed by hundreds of aftershocks with M_D up to 4.6. The spatial distribution of aftershocks was consistent with the activation of several sub-vertical surfaces broadly parallel to the strike of the mainshock fault (Bressan et al., 2009). The mainshock in July 2004 nucleated at a depth of c. 6.0 km on the Bovec-Krn Fault and was followed by aftershocks with M_D up to 3.6. In this case, the spatial distribution of aftershocks was characterized by a diffuse pattern consistent with the activation of many minor fault planes possessing a wide range of orientations (Bressan et al., 2009). By combining tomographic analyses of the fault zone and the upper-crustal sedimentary sequence with high-quality earthquake relocations it was suggested that the two mainshocks and a majority of the aftershocks nucleated within an high-rigidity body of platform limestones and dolomitic limestones between 2 and 10 km depth. Moreover, the most energetic aftershocks nucleated in correspondence to significant variations of elastic properties within the fault zone (both V_P and V_P/V_S), which might correspond to lithological changes or variations in fracture density (Bressan et al., 2009). Aftershock focal mechanisms showed fault plane solutions (strike-slip but also many normal and reverse events) and fault plane orientations different to those of the two main shocks.

Combined, these observations suggest that seismic sequences hosted in sedimentary carbonate rocks are characterized by a complexity in the temporal and spatial distribution of the aftershocks. Part of this complexity might be controlled by the heterogeneity of the host rocks in terms of mechanical properties (e.g. facies changes) and the presence of preexisting anisotropies that could be reactivated (e.g. bedding surfaces, joints). Moreover, the occurrence of fluids of various origins (e.g. mantle, meteoric) has been suggested to play a significant role in the nucleation and propagation of mainshocks, foreshocks and aftershock ruptures in carbonate rocks. Recent high-resolution imaging of active seismogenic fault zones in carbonates highlighted a degree of geometrical complexity resembling that observed in the field by structural geologists (Valoroso et al., 2013). This highlights the need for detailed field descriptions of the structure of exhumed fault zones in carbonates to help constrain the results of increasingly high-resolution geophysical studies. Additionally, detailed microstructural analysis of both natural and experimental fault rocks will help to understand the physico-chemical processes (e.g. role of fluids in earthquake nucleation and propagation) active during the seismic cycle that occur on length-scales too fine to be inferred using “classical” seismological and geophysical investigations.

2. Structure of exhumed fault zones in carbonates

Schematically, the internal structure of fault zones often consists of a well-defined fault core surrounded by a damage zone that passes in to relatively undeformed host rocks affected by background deformation (Chester et al., 1993; Antonellini and Aydin, 1994; Caine et al., 1996; Childs et al., 2009). The fault core (up to few meters thick) is the zone in which most displacement is accommodated and it may contain one or more thin (sub-centimeter) slip zones that bound tabular or lens-shaped volumes of fault rocks (Sibson, 2003; Faulkner et al., 2003; De Paola et al., 2008; Wibberley et al., 2008). The slip zones themselves often contain smooth to light-reflective (i.e. mirror-like) slip surfaces lined by grooves and slickenlines (e.g. Power and Tullis, 1989; Siman-Tov et al., 2013). The damage zone is a wide zone of fracturing and subsidiary faulting up to hundreds of meters thick in which the host rock fabric is not entirely obliterated, although fracturing typically becomes more intense toward the fault core (Cowie and Scholz, 1992; Billi et al., 2003; Mitchell and Faulkner, 2009).

Several studies in recent years have documented that faulting in carbonates is strongly controlled by preexisting anisotropies within the host rock such as bedding surfaces, veins, pressure solution seams and joints (e.g. Mollema and Antonellini, 1999; Billi et al., 2003; Graham et al., 2003; Agosta and Aydin, 2006; Kurz et al., 2008, Hausegger et al., 2010; Molli et al., 2010). Fault zone growth in carbonates involves the progressive shearing and interaction of these inherited structures, ultimately leading to the development of new slip zones and slip surfaces.

As an example, Agosta and Aydin (2006) described the structure of a large-displacement, basin-bounding normal fault zone (Venere Fault, Central Apennines, Italy) within platform carbonates. Normal faults in this example initiated by shearing of pressure-solution seams inherited from a previous contractional deformation phase. Synkinematic formation and subsequent shearing of new pressure-solution seams and joints/veins led to the development of elongate pods of fragmented carbonates. With ongoing deformation and exhumation two sets of conjugate normal faults developed within the fault zone through the fragmented carbonates. Mollema and Antonellini (1999) described the nucleation of a conjugate system of strike-slip faults a few kilometers in length within dolostones of the Sella Group (Southern Alps, Italy), starting from a preexisting en-echelon joint set oriented parallel to the regional maximum compressive stress direction. Aydin et al. (2010) reported the formation of a complex system of fractures and faults on the eastern limb of the Majella anticline (Central Apennines, Italy). In this case, normal and strike-slip faults developed by shearing of both bedding surfaces and pressure solution seams.

Carbonate sedimentary rocks (i.e. mainly limestones and dolostones) are characterized by highly variable physical properties, depending both on the depositional facies and diagenetic history (e.g. Tiab and Donaldson, 1996; Lucia, 1999). Carbonates are more sensitive to diagenetic processes than siliciclastic rocks (e.g. Anselmetti and Eberli, 1993; Fournier and Borgomano, 2009). For example, carbonate porosity and permeability can change dramatically with time and burial depth (Eberli et al., 2003). Moreover, other frequently occurring processes such as dolomitization (the process of calcium to magnesium substitution) can lead to a rearrange and general decrease in porosity (i.e. reduction of intergrain porosity due to rombohedral packing of dolomite crystals) and a change of rock mechanical properties (e.g. increase of the Young modulus; Lucia, 2007; Matonti et al., 2012). Many of these processes are significantly enhanced within fault zones, especially those affected by a prolonged and polyphase deformation history (De Paula, 2011; Matonti et al., 2012). As a result, the structure of fault zones hosted in sedimentary carbonate rocks can be highly heterogeneous in terms of both rock fabric, mineral composition, and physical (e.g. porosity) and mechanical (e.g. rock strength, elastic wave velocity) properties of the fault rocks from the macro- down to the micro-scale. This complexity can strongly affect the permeability structure of the fault zones as well as their mechanical behavior both during long-lasting quasi-static deformation and dynamic earthquake ruptures (Wibberley et al., 2008).

Recent descriptions of fault zones cutting carbonate sequences characterized by lithlogical (i.e. pure vs. marly limestones) and fabric (i.e. massive vs. bedded) heterogeneities highlighted the development of different fault rock assemblages in the different protoliths. In particular, localized deformation features such as sub-centimeter thick ultracataclastic slip zones occured within massive pure limestones, whereas thicker zones of more distributed deformation characterized by pressure-solution mechanisms developed in bedded marly-rich protoliths (Bullock et al., 2013; Gratier et al., 2013; Tesei et al., 2013). Matonti et al. (2012) described significant changes in the structure of the Castellas Fault (southeastern France) including variations of fault core thickness and damage zone fracture pattern, in relation to fabric changes (i.e. depositional facies, degree of cementation) within compositionally homogeneous limestones.

The relative abundance of fluids during faulting strongly affects the structure of fault zones and fault rock assemblages. In general, an abundance of fluids during faulting is suggested by well cemented pods and layers of breccias, cataclasites and ultracataclasites surrounded by damage zones containing veins and subsidiary faults with evidence for pressure-solution deformation processes (e.g., Hausegger et al., 2010; Brosch and Kurz, 2008). A relative paucity of fluids during faulting can be inferred from damage zones characterized by highly fragmented and incohesive carbonates with no veins (e.g., Salvini et al., 1999; Billi et. al, 2003).

3. Coseismic on- and off-fault deformation processes in carbonate rocks

Earthquakes occur along faults as the result of a sudden release of elastic strain energy stored in the wall rocks during prolonged (from years to millennia) quasi-static deformation driven by the far-field stress loading (Gilbert, 1909; Reid, 1910). Rupture nucleation, propagation and arrest are controlled by the complex interplay between the far-field stress resolved on the fault and the strength of the fault, both of which evolve in space and time. The main controlling factors are: fault geometry, mechanical and chemical effects of fluids, long-term variations of fault rock mechanical properties, long-term or sudden changes of the stress field (Sibson, 1973; Rice, 1992; Stein, 1999; Scholz, 2002; Miller et al., 2004; Gomberg et al., 2005; Handy et al., 2007).

The propagation of earthquake ruptures along faults occurs because rock strength (and friction) decreases with increasing slip and slip rate (Rice, 2006). A series of theoretical calculations and experimental studies demonstrated that at the tip of a propagating dynamic rupture (i.e. rupture speed comparable to the Rayleigh wave velocity of the host material; Freund, 1990) extreme transient stress perturbations and strain rates can lead to permanent inelastic deformation of the wall rocks (e.g. Grady and Kipp, 1987; Reches and Dewers, 2005; Doan and Gary, 2009; Ma and Andrews, 2010). Reches and Dewers (2005) estimated the attainment of dynamic tensile stresses up to 5 GPa and volumetric strain rates of 10^5 s^{-1} at distances of a few millimeters from the rupture tip (no off-fault inelastic yielding is considered), which would produce fine-grained fault gouges by “localized” rock pulverization. Experiments on the dynamic loading of rocks (Grady and Kipp, 1987; Doan and Gary, 2009) and simulations of earthquake ruptures (Ben-Zion and Andrews, 1998; Andrews, 2005; Ma and Andrews, 2010) suggest that wall rocks can be fractured up to distances of hundreds of meters from the fault due to the transient stresses and strain rates related to the passage of both the rupture tip and high-frequency (up to 10-100 Hz) compressive and shear seismic waves. Peculiar fault rocks that are widely considered to be formed by coseismic off-fault damage are so-called pulverized rocks (Dor et al., 2006a). These fault rocks are fragmented down to the micrometer scale without apparent shear deformation. To date, pulverized rocks have mainly been reported within crystalline (plutonic or metamorphic) host rocks, where they form thick belts up to hundreds of meters wide along major strike-slip faults (Wilson et al., 2005; Dor et al., 2006a). The only example of pulverized rocks reported in carbonates was described by Agosta and Aydin (2006) from the damage zone of the Venere Fault (Central Apennines, Italy). The so-called pulverized rocks in this example consist of limestones reduced to fragments varying from a few centimeters to a few millimeters in size, significantly larger than the fragments reported in pulverized crystalline rocks (typically sub-millimeter). The occurrence of thick belts of fragmented limestones and dolostones lacking significant shear deformation was also reported along other large fault zones such as the Mattinata Fault (southern Italy, Salvini et al., 1999; Billi and Storti, 2004) and the Dent Fault (northwestern England; Tarasewicz et al., 2005). Detailed field and experimental studies are needed to constrain the origin of these pulverized fault rocks and their possible relation to coseismic damage.

During an earthquake, immediately after the passage of the rupture tip propagating at about 3 km/s, coseismic slip is accommodated along the fault surface at an average sliding velocity of ~ 1 m/s (estimates derived from seismic inversion data, e.g., Heaton, 1990). Though the ratio of the average coseismic displacement D over the entire ruptured fault length L is in the range of 10^{-4}-10^{-5} for most earthquakes (e.g. Sibson, 1989), the amount of slip along strike can be extremely heterogeneous (see for instance the slip distribution of the L'Aquila 2009 Mw 6.1 and the Tohoku Mw 9.0 earthquakes: Cirella et al., 2009; Ide et al., 2011: Ito et al., 2011; Kyriakopoulos et al., 2013). Slip distribution is often not related to hypocenter location; instead, it seems to be related to fault surface roughness and pre-rupture stress distribution (which are related), pore fluid distribution, wall rock stiffness and frictional properties of the fault zone rocks: these factors control the rupture propagation mode (i.e. crack-like vs. pulse-like) and, as a consequence, the final seismic slip distribution (e.g., Fang and Dunham, 2013; Scholz, 2002). Most theoretical, field and experimental studies suggest that during seismic slip a large percentage of the total mechanical work is converted in to heat, which is restricted to a relatively narrow band within and adjacent to a thin (often < 1mm thick) slip zone along the fault (Sibson, 2003; Chester et al., 2005; Rice, 2006; Pittarello et al., 2008). Within the slip zones of carbonate-bearing faults, the transient temperature rise due to frictional heating may lead to a series of physical and chemical transformations such as flash heating and weakening at asperity contacts, expansion or vaporization of pore fluids, decarbonation of CO_3-bearing minerals (calcite, dolomite, siderite, etc.), production of nanoparticles and plastic recrystallization and sintering (Han et al., 2007a,b; Sulem and Famin, 2009; De Paola et al., 2011; Goldsby and Tullis, 2011; Niemeijer et al., 2012; Tisato et al., 2012; Smith et al., 2013). All of these processes accompany a dramatic reduction in frictional strength observed in high-velocity rotary shear experiments on both solid rocks and gouges, although in detail the mechanisms resulting in the strength reduction are still debated (e.g. Di Toro et al., 2011; Han et al., 2010, 2011; De Paola et al., 2011; Tisato et al., 2012). Expansion or vaporization of pore fluids may increase fluid pressures to supra-lithostatic values, leading to a reduction in effective normal stress across the fault (Hubbert and Rubey, 1959; Sibson, 1973; Lachenbruch, 1980; Rice, 2006). Other weakening effects may occur in the slip zones due to the production of layers of nanoparticles, both by extreme comminution and decomposition reactions (e.g. <1 μm particles of lime starting from calcite), which may deform at high-velocity by crystal plasticity (deformation mechanisms: diffusion creep and superplasticity; De Paola et al., 2013).

Some of these short-lived (up to a few seconds) coseismic processes can potentially leave a signature in the geological record, allowing the recognition of ancient seismicity in exhumed fault zones. For example, localized shear heating in impure limestones and dolostones may activate decarbonation reactions leading to the formation of nanoparticles of periclase (MgO), magnetite (Fe_3O_4) and magnesioferrite ($MgFe_2O_4$), which have better preservation potential with respect to lime. Recently, Collettini et al. (2013) reported the occurrence of ultracataclastic layers a few hundreds of micrometers thick containing evidence of mineral decomposition along the Spoleto thrust that cuts through pure and marly limestones. The presence of skeletal crystals of calcite coupled with vesicles and an amorphous silicate matrix derived from the clay fraction in the marly limestones was interpreted to result from a high-temperature pulse associated to the propagation of an earthquake rupture. Smith et al. (2013) reported the occurrence of dynamic recrystallization in proximity to the principal slip surface of calcite gouges deformed at seismic slip velocities (~ 1 m/s) in rotary shear experiments. The dynamically recrystallized layers (crystal size 1-10 µm) were < 300 µm thick and showed strong shape- and crystallographic-preferred orientations. A similar microstructure was recognized in nature along the Garam thrust (South Korea) that was exhumed from < 5 km depth and cuts through limestones and dolostones. In the Garam thrust, a < 2 cm thick layer of dynamically recrystallized calcite lining the principal slip surface of the thrust and showing shape- and crystallographic-preferred orientations comparable to the experimental samples was interpreted to result from shear strain localization and frictional heating during seismic slip. The occurrence of cataclastic to ultracataclastic layers up to a few centimeters thick containing injection-type microstructures has also been reported within the slip zones of fault zones in carbonates (e.g. Tre Monti Fault, Borcola Pass Fault, Spoleto Thrust; Smith et al., 2011; Fondriest et al., 2012; Tesei et al., 2013). These rocks are typically interpreted as fluidized fault rocks formed due to a sudden release or increase of fluid pressure related to the propagation of earthquake ruptures (Smith at al., 2011; Fondriest et al., 2012). The achievement of high fluid pressure gradients within the fluidized fault rocks is often inferred by the presence of hydrofracture veins (micrometers to centimeters thick) both interlayered with and departing from fluidized rock layers (Smith et al., 2011; Boullier et al., 2009; Rowe et al., 2012b). The origin of mirror-like fault surfaces, a typical feature of many exposed faults cutting calcite- and dolomite-built rocks exhumed from shallow depths, is matter of debate (e.g., Chen et al., 2013; Fondriest et al., 2013; Siman-Tov et al., 2013; Verberne et al., 2013) and will be discussed in this thesis. Surely, further microstructural (TEM, micro-Raman, SEM-catholuminescence, isotopic, etc.) and experimental studies (i.e. sub-seismic to seismic slip rates experiments performed on gouges in the presence of fluids) are required to determine the origin of these fault zone rocks and the related structural features.

4. Earthquakes mechanics in carbonates: a multidisciplinary approach

Earthquakes are traditionally studied using geophysical (e.g. seismic wave inversion) or remote-sensed methods (e.g. GPS, InSAR). These methods allow the retrieval of key parameters related to the earthquake source (e.g. seismic moment, static stress drop, radiated energy) (Kanamori and Brodsky, 2004) but typically lack sufficient resolution to constrain on- and off-fault processes (fracture energy, fault friction) at scales relevant for earthquake mechanics (Di Toro et al., 2012).

Direct information on active seismogenic sources is retrieved from fault-drilling projects that allow the integration of in situ geophysical measurements (strain rate, pore pressure, etc.) with sampling of fault rocks (e.g. Alpine fault drilling project, Sutherland et al., 2012; Chelungpu fault drilling project, Boullier et al., 2009; San Andreas Fault Observatory at Depth, Zoback et al., 2011; Wenchuan fault drilling project, Li et al., 2012; J-FAST fault drilling project, Brodsky et al., 2013). Nevertheless, the investigated rock volumes in drilling projects are too small to allow a three-dimensional characterization of the fault zone internal structure.

Although increasingly high-resolution seismological techniques (e.g. high-precision hypocenters relocation, tomography based on different seismic observables; e.g. Di Stefano et al., 2011, Valoroso et al., 2013) and numerical simulations of seismic ruptures (e.g. Ma and Andrews, 2010) are furnishing invaluable constraints on the geometry and mechanical structure of seismogenic fault zones, the study of exhumed fault zones, based on field structural mapping and fault rock characterization, remains the best tool to describe in detail the architecture of seismogenic faults.

Rock deformation experiments performed under earthquake-like conditions (slip rates of m/s, slip up to several meters, stresses of tens of MPa and rupture speeds of km/s) provide direct information about the physical and chemical processes occurring in fault zones during the seismic cycle. Major advantages of these experiments are (i) the production of artificial seismic fault rocks that can be directly compared to natural ones, potentially leading to the identification of markers of earthquake ruptures in the field and (ii) the determination of several earthquake source parameters that are out of the range of seismological investigation (e.g., friction).

This thesis deals with the investigation of earthquake mechanics in carbonate host rocks, more specifically dolostones, by means of a multidisciplinary approach, including:

1) field description of fault zones in dolostones that were exhumed from seismogenic depths
2) rock mechanics experiments: (i) low- to high-velocity rotary shear friction experiments; (ii) split Hopkinson Pressure Bar tests; (iii) low-strain rate uniaxial compression tests
3) mineralogical and microstructural characterization of natural and experimental fault materials.

The principal aims of this study are (i) to characterize in detail the internal structure of ancient seismogenic fault zones in dolostones, (ii) to recognize mineralogical and microstructural indicators of ancient seismicity (i.e.,fault zone rocks produced during seismic slip and rupture propagation), and (iii) to estimate useful earthquake source parameters (e.g., coseismic fault strength, fracture energy) by integrating (i) and (ii).

To achieve these goals, two shallowly-exhumed (<3 km) fault zones cutting dolostones in the Italian Southern Alps were studied: the Borcola Pass Fault Zone (BPFZ) and the Foiana Fault Zone (FFZ) (Chapter 2). The BPFZ is a secondary strike-slip fault with complex internal structure characterized by tens of sub-vertical fault strands reactivating regional joint sets. Peculiar microstructures within the localized slip zones suggest the occurrence of coseismic fluidization during the propagation of earthquake ruptures. The FFZ is a major sinistral transpressive fault zone characterized by significant along-strike and down-dip variations in fault zone thickness, damage intensity and fault kinematics. The occurrence of in-situ shattered dolostones in belts up to hundreds of meters wide cut by discrete faults with mirror-like slip surfaces is interpreted to record the propagation of multiple seismic ruptures in the shallow crust. In Chapter 3 the origin of faults with mirror-like slip surfaces is investigated by combining field observations of natural faults in the FFZ with low- to high-velocity rotary shear friction experiments on dolostone gouges. Mirror-like slip surfaces comparable to the natural ones in terms of both surface roughness and microstructures are formed only at seismic slip rates ($v \geq 0.1$ m/s) at the normal stresses and displacements estimated for the FFZ. Therefore, small displacement (< 0.5 m) mirror-like faults in dolostone gouges are proposed as markers of seismic faulting. In Chapter 4 the origin of the in-situ shattered dolostones is investigated by combining low- to high-strain rate uniaxial compression tests on dolostone rock cylinders of the Mendola Formation (i.e. host rock of the FFZ). Preliminary results indicate that in-situ shattered dolostones comparable to those described along the FFZ (i.e. few millimeters in size rock fragments elongated in the stress wave loading direction and incipient zones of microfracturing down to the micrometer scale) are formed only above strain rates of ~ 200 s^{-1}, which can be attained in the wall rocks of a propagating earthquake rupture.

Chapter 2. Structure of exhumed seismogenic fault zones in dolostones

1. Introduction

Fault zones cutting limestones and dolostones represent significant seismogenic sources in several areas worldwide, including Italy (e.g. Friuli (Italian Fore-Alps) earthquake, 1976, $M_w = 6.4$; Colfiorito (Northern Apennines), 1997, $M_w = 6.0$; Bovec-Krn (Slovenian Alps), 1998, $M_D = 5.6$; L'Aquila (Central Apennines), 2009, $M_w = 6.1$; Emilia (Po Plain), 2012, Mw = 6.0; Jackson, 1994; Amato et al., 1998; Chiaraluce et al., 2005; Galli et al., 2008; Bressan et al., 2009; Chiarabba et al., 2009; INGV report, 2012).

The seismogenic behavior of faults strongly depends on fault zone internal structure and fault rock constitutive properties (Scholz, 2002). In the last few years increasingly high-resolution seismological techniques (e.g. high-precision hypocenters relocation, tomography based on different seismic observables) have yielded new constraints on the geometry and velocity structure of active seismogenic fault zones down to length scales of < 100 m (Chiaraluce et al., 2011; Di Stefano et al., 2011, Valoroso et al., 2013, Nemser and Cowan, 2011; Thurber, 2013). Further information on the coseismic off-fault damage distribution can be retrieved from 3D numerical simulations of seismic ruptures (e.g. Ma and Andrews, 2010). Nevertheless the study of exhumed fault zones remains one of the best ways to characterize both the geometry of faults (e.g. fault surface roughness) and the spatial distribution and physical (i.e. mechanical and transport) properties of fault rocks at scales relevant to seismic rupture dynamics.

Most theoretical, field, microstructural and experimental rock deformation studies suggest that during seismic slip a large percentage of the total mechanical work is converted in to heat, which in some cases is restricted to a relatively narrow layer (the so-called "principal slip zone", often < 1 mm thick) adjacent to through-going fault surfaces (Sibson, 2003; Chester et al., 2005; Rice, 2006;). Such intense but short-lived frictional heat pulses generated during earthquakes can trigger a variety of mechanical and chemical effects in the surrounding rocks (e.g. frictional melting, mineral decomposition and plasticity) that can potentially leave a signature in the geological record (see section 3 of Chapter 1; Rice, 2006; Han et al., 2007a,b; Smith et al., 2013). It follows that detailed microstructural and mineralogical characterization of natural and experimentally-produced fault rocks is of paramount importance in gaining direct information about the physical and chemical processes occurring on faults during the seismic cycle and controlling earthquake source physics (i.e. coseismic shear stress, earthquake energy budgets, dynamic fault weakening mechanisms and slip rate variability; Kanamori and Brodsky, 2004).

In this chapter I describe and compare the macro- to micro-scale internal structure of two fault zones located in the Italian Southern Alps, hosted in dolomitic rocks and exhumed from shallow depths (i.e. < 3 km). The fault zones are: (i) the Borcola Pass Fault Zone (BPFZ) (described in section 2 of this chapter), a secondary fault zone that developed in a fluid-rich environment and (ii) the Foiana Fault Zone (FFZ) (described in section 3 of this chapter), a crustal-scale fault zone that developed in a relatively fluid-poor environment. By integrating detailed field and microstructural characterization of the fault rock assemblages with dedicated rock deformation experiments (Chapters 3 and 4) the two fault zones are inferred to have hosted seismic activity in the past and are considered to be exhumed equivalents of the active seismic sources responsible for a large part of the shallow crustal seismicity in carbonates of the Mediterranean area.

The Borcola Pass Fault Zone (BPFZ) is a few kilometers in length and is a strike-slip branch of the regional-scale Schio-Vicenza Line. The BPFZ cuts through both sedimentary dolostones and dolomitic marbles. The fault network that developed along the BPFZ was strongly controlled by a regional-scale array of preexisting anisotropies (joints) in the host rocks. The presence of cohesive, well cemented fault rocks indicates an abundance of fluids during faulting. Detailed microstructural and mineralogical characterization of the principal and secondary slip zones suggested the activation of fluidization processes likely related to the propagation of ancient seismic ruptures in the shallow crust under fluid-rich conditions.

The Foiana Fault Zone (FFZ) is a major (~ 30 km long) sinistral transpressive fault zone cutting sedimentary dolostones. The FFZ consists of intensely fragmented dolostones lacking evidence of significant shear strain (i.e. in situ shattered dolostones; see section 3 of this chapter) that are locally cut by networks of discrete faults with highly reflective “mirror-like” slip surfaces. In general, the absence of veins and sealed fractures suggests a paucity of fluids during faulting. Detailed field and aerial structural mapping conducted along several well exposed sections of the fault zone allowed the recognition of significant changes in the structure of the FFZ over ~ 6 km in strike length. In particular, significant variations in fault zone thickness, fault orientations and fault kinematics were observed, together with a strong influence of preexisting anisotropies. On the basis of experimental and microstructural observations (discussed in Chapters 3 and 4) it is suggested that the association of shattered dolostones with “mirror-like” slip surfaces records the occurrence of ancient earthquake ruptures propagating at shallow depth along the FFZ. This allows the structure of the FFZ deduced from field observations to be compared with predictions of three-dimensional earthquake rupture simulations and with the structure of active seismic sources retrieved by seismological techniques.

2. Borcola Pass Fault Zone: a secondary fault zone in a fluid-rich environment

Abstract

The structure of an exhumed strike-slip fault zone hosted in dolostones, the Borcola Pass Fault Zone (BPFZ, Italian Southern Alps), was studied by means of field and microstructural analysis. Ambient conditions of faulting were ca. 1.6-1.7 km and 50°C. The BPFZ consists of a > 80 m wide damage zone cut by three systems of sub-vertical secondary faults striking approximately N-S, E-W and NW-SE. N-S and E-W striking faults reactivated pre-existing Jurassic-Paleogene joints with spacing between 0.2-0.5 m, whereas NW-SE striking faults were newly formed during post-Paleogene activity associated with movements along the nearby Schio-Vicenza Line. The core of the BPFZ consists of dolostone fault rock lenses bound by slip zones up to 10 cm thick. Both the principal and secondary slip zones consist of cement-supported dolomitic cataclasites and dolomite-filled veins. Some slip zones contain a sub-centimetre thick "vein-like" cataclastic layer (Layer-A) located immediately beneath the slip surface that truncates another cataclasite below (Layer-B). Detailed microstructural and clast size distribution analysis suggests that Layer-A experienced fluidization (cuspate-lobate boundaries, injection structures, strong grain sorting: $D < 1$ for clast diameters smaller than 300 μm) possibly related to fast fault slip following seismic ruptures. In light of these observations a conceptual model is proposed for the formation of Layer-A, and the structure of the BPFZ is compared to that of an active seismogenic fault cutting carbonates.

This study was performed in collaboration with Steven Smith, Giulio Di Toro, Dario Zampieri and Silvia Mittempergher. A modified version of this chapter was published as the following paper: Michele Fondriest, Steven A.F. Smith, Giulio Di Toro, Dario Zampieri and Silvia Mittempergher (2012) Fault Zone Structure and Seismic Slip Localization in Dolostones, an example from the Southern Alps, Italy, Journal of Structural Geology, v.45, p.52-67.

2.1 Geological and seismotectonic setting of the study area

The eastern Southern Alps of Italy are a SSE-vergent fold and thrust belt delimited to the west by the NNE-SSW-trending Giudicarie Belt and the relatively undeformed foreland block of the Lessini Mountains, and to the east by the NW-SE-trending Idria and Ravne Lines. The structure of the chain consists of an imbricate fan of SSE-vergent thrust-sheets involving Variscan crystalline basement and Permo-Mesozoic sedimentary cover dominated by limestones and dolostones (Doglioni, 1990; Schönborn, 1999; Transalp Working Group, 2002) (Fig 1).

The regional geometry of the thrust sheets is controlled to a large extent by NNW-SSE to NNE-SSW-trending Early Permian to Triassic and Jurassic normal faults. These pre-existing normal faults experienced extensional or oblique-extensional reactivation during the Mesozoic and Paleogene until their last dominant strike-slip movement or inversion during the Neoalpine (Miocene) orogenic phase (Zampieri et al., 2007). Post-Miocene linkage between the frontal thrust sheets and the Giudicarie Belt was provided by major strike-slip faults, including the regional-scale NW-SE-trending Schio-Vicenza Line (Massironi et al., 2006) (Fig.1). The Schio-Vicenza Line is at least 100 km long and runs from the Venetian plain south of Padova to the Adige Valley near Trento (Fig 1; De Pretto, 1920; Semenza, 1974; Bigi et al., 1990; Dal Piaz and Martin., 1998; Castellarin et al., 2006). In particular, the Schio-Vicenza Line passes through the Borcola Pass where the main fault does not outcrop but a well-developed array of approximately N-S striking secondary fault zones can be recognized. One of these, termed the Borcola Pass Fault Zone (BPFZ), is described in detail in this study (Fig.2).

The BPFZ outcrops within three quarries close to the highest point of the Borcola Pass (1207 m a.s.l.) (Fig.2). Host rocks exposed in the quarries are dolomitized peritidal limestones of the Dolomia Principale (DP) Formation, an Upper Triassic lithostratigraphic unit with a local thickness of about 800 m (Sedea and Di Lallo, 1984; Zampieri and Massironi, 2007). Intrusion of basaltic sills and dykes of Paleogene age (Zampieri, 1995) resulted in local contact metamorphism and the formation of lenses of brucite- and lizardite-bearing dolomitic marble (De Vecchi, 1966; De Vecchi and De Zanche, 1974*)*.

Significant clustering of earthquakes related to activity along the Schio–Vicenza system occurs in the Lessini Mountains and in the Mount Pasubio area, close to the BPFZ (Galadini and Galli, 1999). This area is characterized by long-term, small magnitude seismicity (Boschi et al., 1995; Viganò et al., 2008) and experienced several registered earthquakes with M > 4 in the last forty years (M_W = 4.6 and M_W = 4.8, 1968; M_W = 4.9, 1989; three $4 < M_W < 5$ earthquakes, 1981-2002). The hypocenters of these earthquakes localized within the crystalline basement between 7 and 10 km depth. Focal mechanism solutions are consistent with sinistral transpression along N-S striking faults and dextral transcurrence along NW-SE striking faults (Sleijko et al., 1989; Castello et al., 2004; Zampieri and Massironi, 2007; Viganò et al., 2008) (Fig.1). More generally, moderate to large earthquakes, including thrust (e.g. Belluno, 1873, estimated M_w = 6.3; Friuli, 1976, M_w = 6.4) and strike-slip earthquakes (Bovec-Krn, 1998, M_D = 5.6 and 2004, M_D = 5.1) are widespread in the eastern Southern Alps. The hypocenters of such earthquakes localize within, and ruptures propagate through, both the crystalline basement and the sedimentary cover that includes the thick Dolomia Principale Formation (up to 1.5 km thick; Anselmi et al., 2011; Chiarabba et al., 2005;

Galadini et al., 2005; Burrato et al., 2008; Bressan et al., 2009). In particular, it is thought that the main shocks of the Bovec-Krn seismic sequences (M_D = 5.6, hypocentral depth = 6.9 km; M_D = 5.1, hypocentral depth = 6.0 km; Bressan et al., 2009) nucleated within carbonate rocks along a NW-SE trending right-lateral strike-slip fault zone (Bovec-Krn Fault). Aftershock sequences were located between 2 and 10 km depth and activated secondary fault branches with different orientations. The fault systems studied here, the main Schio-Vicenza Line and the secondary BPFZ, thus represent exhumed equivalents of the Bovec-Krn Fault and its associated secondary fault branches respectively (see section 2.6.4).

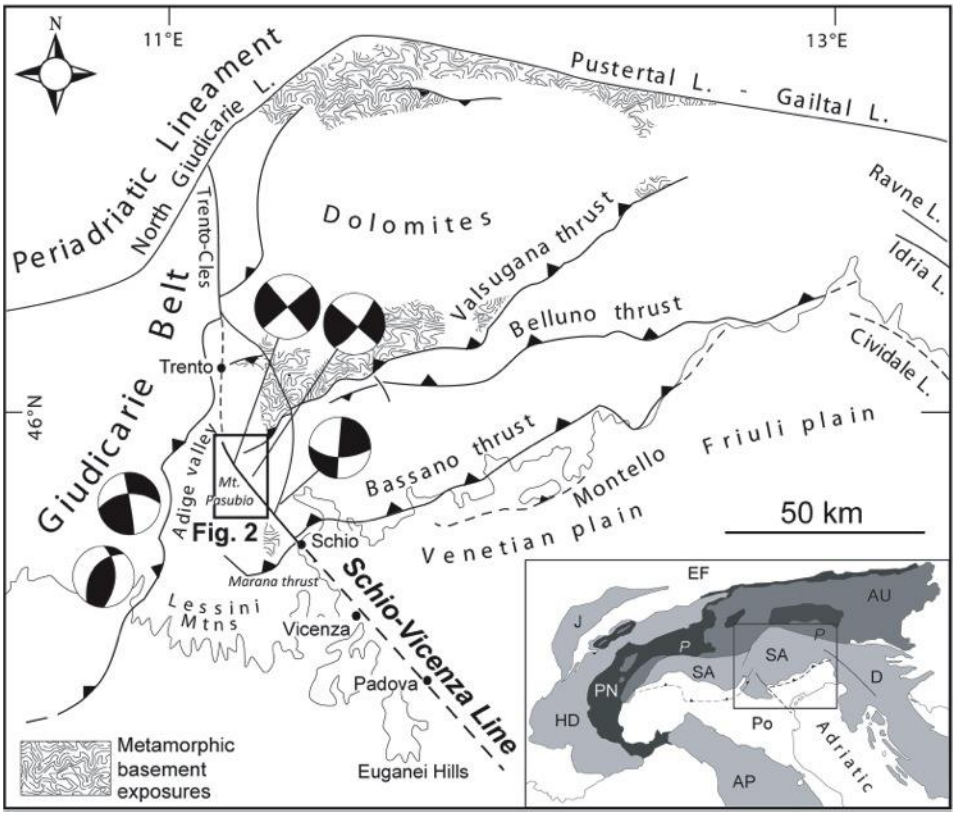

Fig.1 Simplified structural map of the central-eastern Southern Alps showing the main faults, their kinematics (from Miocene onwards) and the exposures of Variscan metamorphic basement (modified from Zampieri et al., 2007). The Schio-Vicenza Line is highlighted and the black box represents the area investigated by remote sensing (section 3, Fig.2). The inset in the lower right shows the location in the Italian peninsula (legend: Southern Alps (SA); Dinarides (D); Austroalpine (AU); Penninic (PN); Helvetic-Dauphinois (HD); Jura (J); European Foreland (EF); Po Plain (PO); Apennines (AP); Periadriatic Lineament (P))**.** Reported focal mechanisms summarize seismological data (M_D > 4.5) taken from Slejko et al. (1989), Galadini and Galli (1999) and Viganò et al. (2008) describing the present seismicity of the Giudicarie Belt and of the Schio-Vicenza system.

2.2 Remote sensing structural analysis

Remote sensing analysis using orthorectified photo mosaics, Google Earth images and digital surface models was used to characterize the regional scale pattern of tectonic lineaments associated with the Schio-Vicenza Line, focusing on the Borcola Pass area (analyzed zone: 6-7 km wide, ca. 10 km long) (Fig.2).

The Schio-Vicenza Line displays a segmented geometry. From Posina to the Borcola Pass, the Schio-Vicenza Line is easily recognizable and shows good continuity, whereas from the Borcola Pass northwards only isolated fault segments could be identified (Fig.2).

Surrounding the trace of the Schio-Vicenza Line is a regionally-significant network of lineaments that reach a maximum density within the Upper Posina Valley (Fig.2). The lineaments are typically characterized by high dip angles (i.e. their surface traces are independent of topography), and three main sets were identified: 1) N-S-trending lineaments (such as the BPFZ described in this section); 2) E-W-trending lineaments and 3) NW-SE-trending lineaments (Fig.2). The NW-SE-trending lineaments are broadly parallel to the Schio-Vicenza Line. The trace of the BPFZ itself is recognizable in aerial photos for a length of approximately 600 m, which represents a lower limit for the actual fault length (probably on the order of a few kilometers) (Fig.2).

2.3 Field description of the fault zone

The BPFZ is exposed in the Upper Terragnolo Valley within an abandoned quarry (1146 m a.s.l. and about 1000 m north of the Borcola Pass) which offers three dimensional exposures of the fault zone structure. The quarry contains several sub-parallel, N-S striking faults as well as arrays of secondary faults and veins described below. The most well exposed N-S trending fault in the quarry is here defined as the Borcola Pass Fault (Fig.2, 3). Although determination of displacement across the Borcola Pass Fault was not possible due to a lack of well defined structural markers it is considered the principal fault within the quarry because: 1) it is the only fault associated with a well-defined topographic lineament visible both in aerial photographs and in the quarry exposures (Fig.2); 2) it is the only fault with a complex geometry that includes meter-scale fault rock lenses and meter-scale fault surface roughness (Fig.4) (Sagy et al., 2007).

Structural characterization and systematic sample collection (N=27) were conducted along quarry walls excavated broadly perpendicular and broadly parallel to the Borcola Pass Fault. Three structural profiles were carried out along the quarry walls: the first (profile A) running along the surface of the roughly N-S striking Borcola Pass Fault, and the second and third (profiles B and C) broadly perpendicular to fault strike (Fig.3).

The ca. N-S striking Borcola Pass Fault runs through the middle of the quarry, and on its eastern side has a ca. 4 m wide gully with no exposure. Profiles B and C were carried out on either side of the gully, and together represent an 81 m long transect across the damage zone of the Borcola Pass Fault (Fig.3, 5). Almost all of the observed secondary faults were characterized by striated surfaces but typically lacked clear shear sense indicators. Shear sense in some cases was established by using asymmetric Riedel shears and fracture patterns found at the outcrop scale, and also from associated microfractures with millimeter-scale displacements found in polished hand samples and thin sections.

2.3.1 The Borcola Pass Fault

The Borcola Pass Fault cuts two different host rocks in the quarry, crystalline dolostones of the Dolomia Principale (DP) formation in the upper 10 m of the quarry, and, in the lower 10 m of the quarry, dolomitic marbles generated by contact metamorphism of the DP during intrusion of Paleogene basaltic sills and dykes (Fig.4). The surface of the Borcola Pass Fault (Strike: N5E-N20E; Dip Azimuth: N275E-N290E; Dip Angle: 80-85) outcrops over a length of ca.30 m and a height of ca. 20 m and is characterized by an undulating geometry both parallel and perpendicular to the mean orientation of fault striae (Fig.4). The boundary between dolomitic marbles and dolostones is marked by an unusually large step in the fault surface (ca. more than 2 m of relief) that we interpret as due to the change in lithology. Fault striae indicate near pure strike-slip movement, although striae are observed to curve slightly in correspondence to fault surface bumps. Macroscopic and microscopic analysis of secondary fracture patterns suggests a sinistral shear sense for the Borcola Pass Fault (see sections 2.6.2).

The fault surface is surrounded by a centimeter- to meter- thick fault core which itself is surrounded by a tens of meter wide damage zone cut by secondary fault strands. Both of these components are described separately in the following sections here below.

2.3.2 Core of the Borcola Pass Fault

Significant changes in both fault core thickness and fault geometry were noted passing from the dolomitic marbles to the dolostones. Within the dolomitic marbles the fault core consists of a thin (<1-2 cm) cataclastic layer cut by the principal fault (Fig.6a). Instead, within the dolostone (DP) the fault core consists of meter-scale fault rock lenses elongated along strike and surrounded by different strands of the principal fault (Fig.4). The fault rock lenses are typically composed of dolomitic breccias and protocataclasites whereas the slip zones of the principal fault consist of layers up to 10 cm thick of well cemented cataclasite containing subrounded clasts of dolostone up to several centimeters in size.

(i) Microfractures adjacent to the Borcola Pass Fault within dolomitic marble

Dolomitic marbles adjacent to the Borcola Pass Fault are cut by two sets of sub-vertical hybrid fractures filled by different generations of dolomite cement: 1) an older NE-SW oriented set consisting of veins <100 µm thick are consistently cross-cut by; 2) a NW-SE oriented set consisting of 100 µm-1 mm thick hybrid fractures characterized by steps and rhomb-shaped pull-apart structures (Fig.6a, b). At the contact between the dolomitic marble and the dolomite veins the protolith is characterized by a brownish halo rich in opaque minerals (mainly oxides) likely related to fluid-rock interactions. Both fracture sets (ca. NE-SW and ca.NW-SE) are cut by the slip zone of the Borcola Pass Fault (Fig.6b).

2.3.3 Damage zone

The width of the damage zone of the Borcola Pass Fault exceeds the total length of profiles B and C (81 m, see Fig. 3 and 5). Field observations at distances of several hundreds of meters from the quarry suggest that the damage zone exposed in the quarry is characterized by a higher fracture density than host rocks outside the fault zone. The damage zone contains secondary faults and a well-developed network of joints, dolomite veins and shear fractures. Veins up to several centimeters thick are often found lining secondary fault surfaces (described in the following sub-sections below). Although we have not quantified changes in fracture density in the damage zone, fracture density generally increases approaching the Borcola Pass Fault, and inherited structural anisotropies such as joints are increasingly sheared. Secondary fractures in the damage zone are organized into three distinct systems with different strikes: 1) N-S oriented system (i.e. parallel to Borcola Pass Fault); 2) E-W oriented system; 3) NW-SE oriented system (i.e. parallel to the Schio-Vicenza Line) (Fig.3, 5).

(i) N-S oriented secondary fractures

The N-S oriented system of secondary fractures (Strike: N20W-N21E; Dip Azimuth: N240E-N291E; Dip Angle: 72-90) (red cyclographic traces in Fig.3) is the most continuous and penetrative fracture system within the damage zone. It is represented by a systematic set of joints and reactivated joints spaced 5-20 cm apart, frequently exploited by the intrusion of basaltic dykes (Fig.7a). Within dolomitic marbles the joints are often sealed by millimeter- to centimeter thick dolomite veins possessing a brownish colour. Close to the Borcola Pass Fault, N-S oriented secondary fault strands are characterized by polished and well striated fault surfaces. Fault striae indicate almost pure strike-slip movements. Some N-S oriented secondary faults cutting dolostones are associated with centimeter-thick layers of well cemented cataclasites (section 2.4.2, Fig.8b).

(ii) E-W oriented secondary fractures

The E-W oriented system of secondary fractures (Strike: N70E-N122E; Dip Azimuth: N340E-N28E, N175E-N190E; Dip Angle: 72-90) (grey cyclographic traces in Fig.3) is represented by a systematic set of laterally continuous joints spaced 15-60 cm apart, as well as reactivated joints displaying a wide range of slickenline orientations. Many E-W-trending joints cutting dolomitic marbles are intruded by Paleogene basaltic dykes or surrounded by brown alteration haloes centimeters to tens of centimeters thick. Such alteration haloes, consisting of dolomite/ankerite + Mg-calcite + microcrystalline lizardite (determined by optical microscope, field-emission scanning electron microscopy and X-ray powder diffraction) were most likely generated by interaction of the dolomitic marbles with magmatic fluids derived from the basaltic intrusions. The alteration bands are cut by late veins of Mg-calcite up to several centimeters thick.

(iii) NW-SE oriented secondary fractures

The NW-SE oriented secondary fractures (Strike: N125E-N162E Dip Azimuth: N215E-N252E, N61E-N70E; Dip Angle: 60-90) (blue cyclographic traces in Fig.3) are represented by faults (Fig.8a) that are more widely and irregularly spaced (spacing between 1-18 m), nevertheless spacing systematically decreases towards the Borcola Pass Fault, particularly on the east side (Fig.5). These faults strike broadly parallel to the Schio-Vicenza Line and are younger than N-S and E-W secondary fractures since they cut Paleogene sills and dykes (Fig.7b). All NW-SE oriented faults show well polished fault surfaces with strike-slip to oblique-slip slickenlines. Often two or three generations of overprinting fault striae are visible suggesting rotation of fault-bounded blocks in the damage zone. Within dolostones the NW-SE oriented secondary faults are associated with centimeter-thick, well-cemented cataclasites containing dark grey clasts of dolostone surrounded by a light grey matrix (Fig.8c). Toward the slip surfaces, texturally distinct layers of ultracataclasite a few millimeters thick were recognized together with the presence of a peculiar, well cemented “vein-like” cataclastic layer that is the subject of a detailed analysis in section 2.4.2.

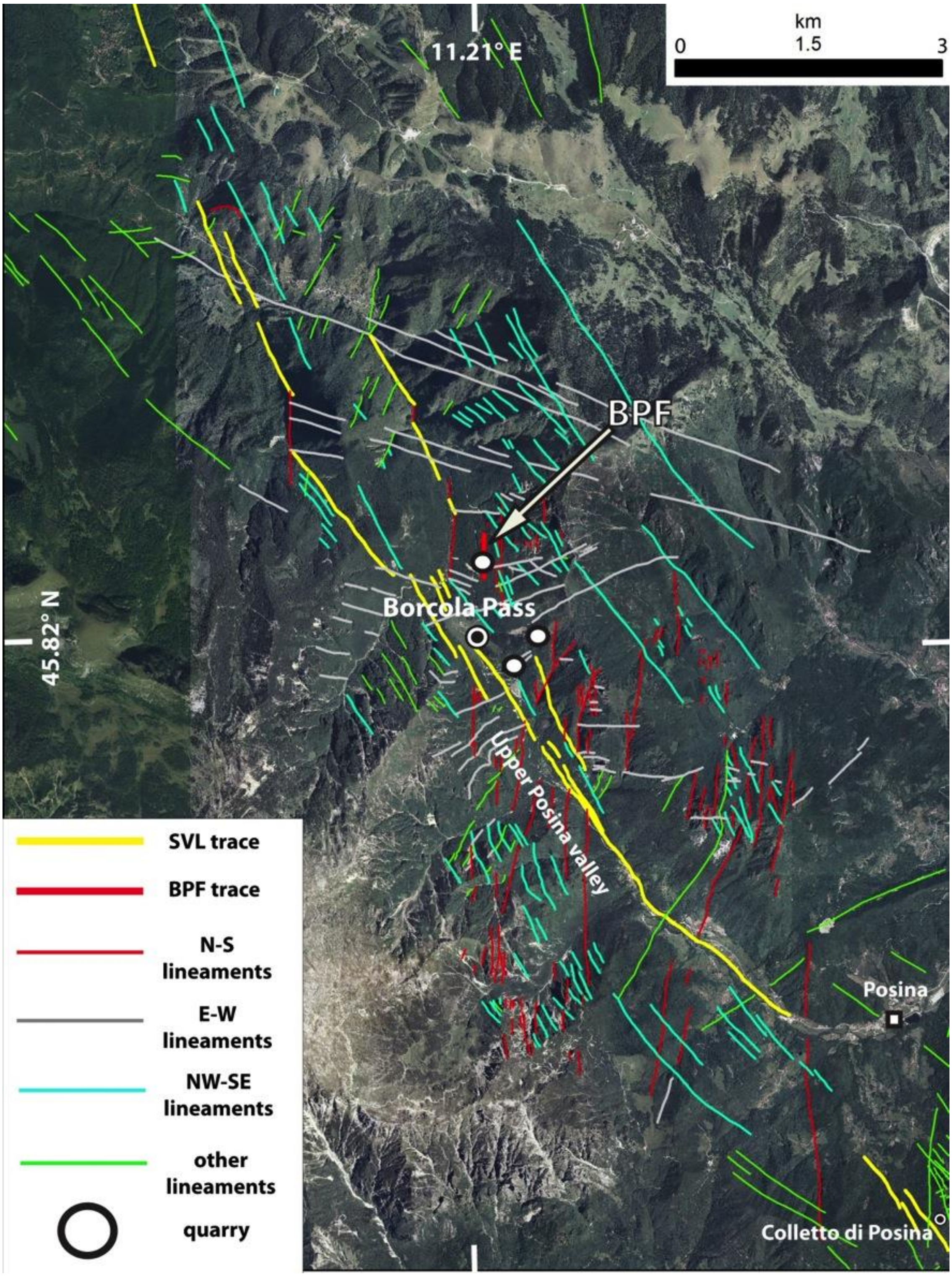

Fig.2 Pattern of tectonic lineaments in the Borcola Pass area. Lineament recognition is based on structural interpretation of orthorectified aerial photomosaics, Google Earth images and digital surface models. The trace of the Schio-Vicenza Line (SVL) is represented by thick yellow lines. The trace of the N-S trending Borcola Pass Fault (BPF, see white arrow) is represented by a thick red line, and passes through one of the quarries studied in detail. Secondary lineaments associated with the Schio-Vicenza Line are represented by thin red, grey and blue lines that correspond to different orientations. Lineaments with other orientations or potentially related to other principal faults ("other lineaments") are represented by thin green lines.

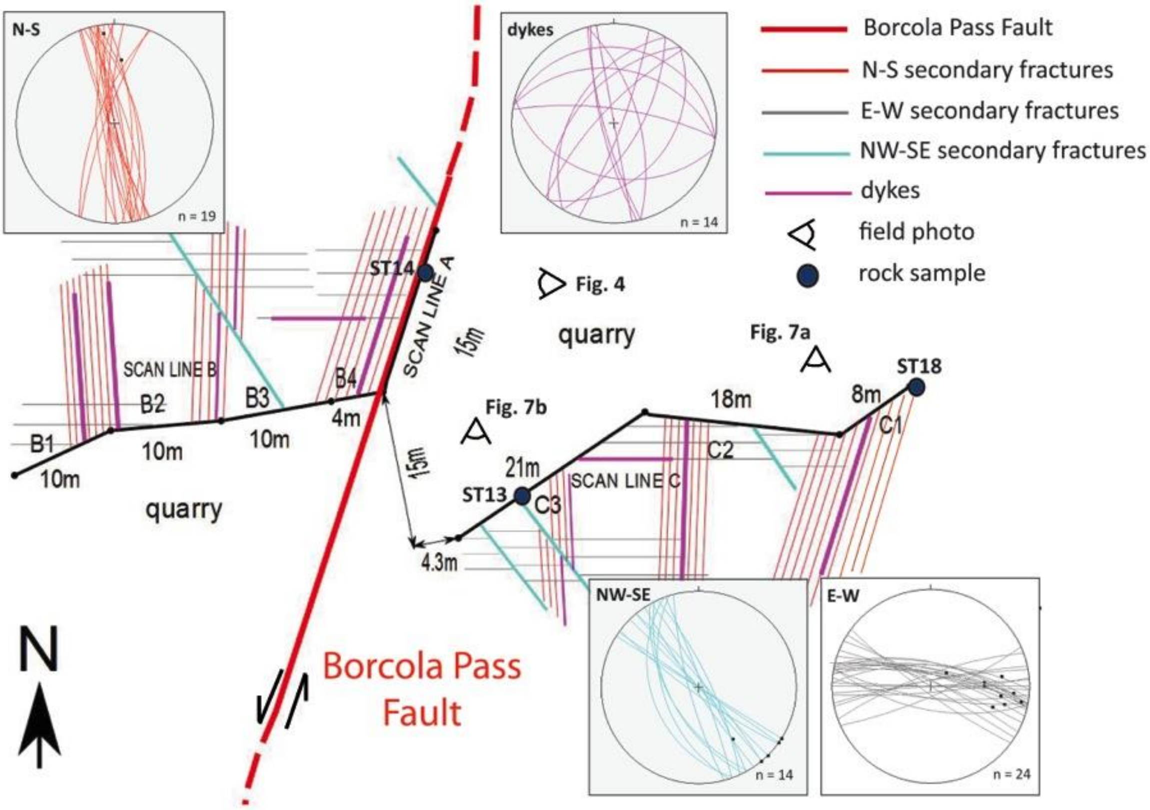

Fig.3 Plan view of the studied BPFZ exposure in the quarry. The spacing of the secondary fracture systems is exaggerated but correctly scaled from one set to another. The right-lateral throw along the NW-SE secondary faults is only qualitative as fault displacements could not be measured in the field, see section 2.3. No information about the displacement along the Borcola Pass Fault was available. The plots represent the attitudes of the secondary fractures/faults and basaltic dykes. Black dots in the plots represent fault slickenlines. Traces of structural profiles (A, B1-B4, C1-C3), sample locations (ST13, ST14, ST18) and points of view for Figures. 4, 7a, and 7b are also reported.

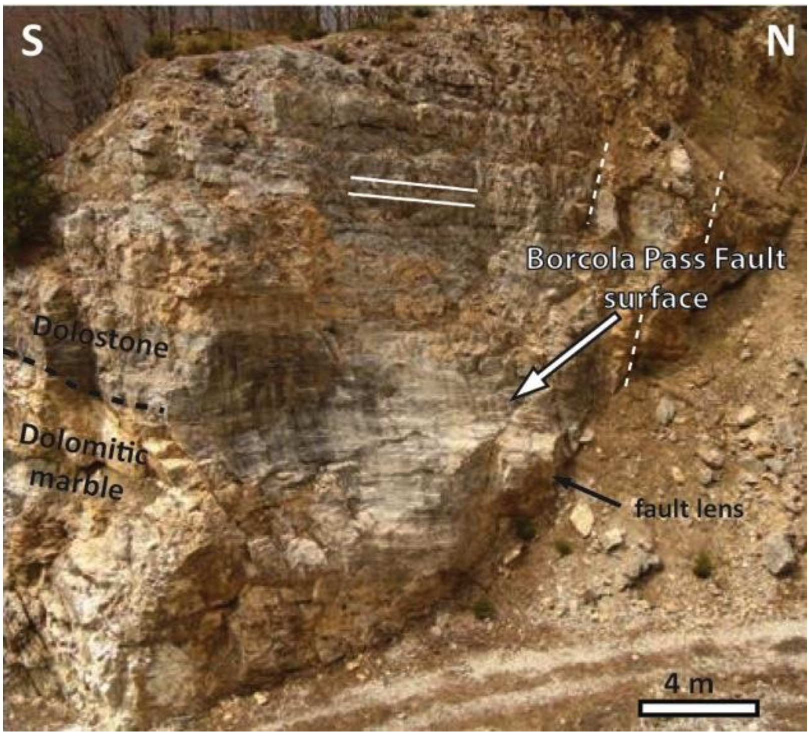

Fig.4 The exposure of Borcola Pass Fault surface on the quarry wall. Note the strike-slip grooves on the fault surface that is characterized by meter-scale undulations both parallel and perpendicular to the grooves. In the upper part of the quarry wall sub-horizontal bedding of the Dolomia Principale (white lines in the figure) and sub-vertical E-W oriented secondary fractures (white dashed lines in the figure) cutting the outcrop are recognizable. The protolith transition (dolostone/dolomitic marble) is marked by the black dashed line. Meter-scale fault rock lenses are present along the fault surface (see section 2.3.1).

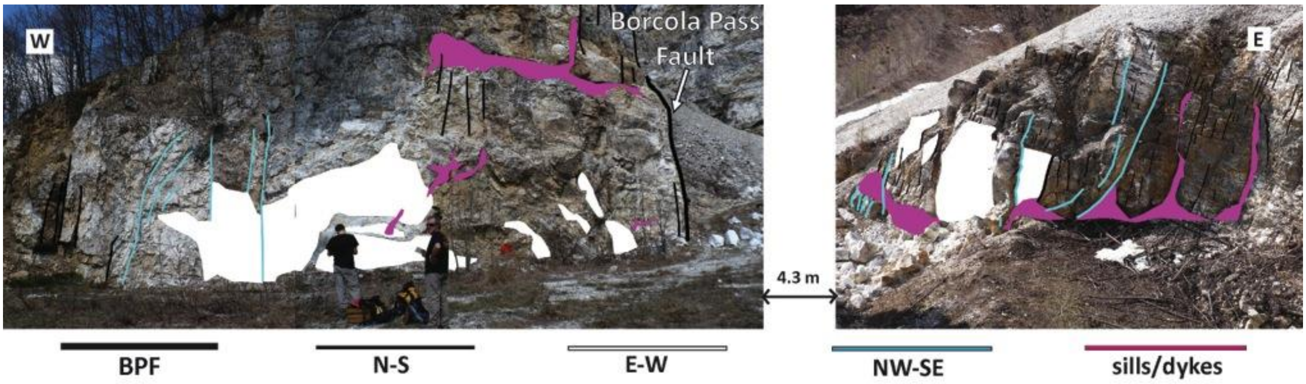

Fig.5 E-W section (scan lines B+C) of the BPFZ (damage zone and fault core). The photograph on the right (scan line C) has been flipped to aid visualization of the continuous transect (see Fig.4). Borcola Pass Fault, secondary fractures/faults and basaltic sills/dykes are reported. E-W secondary fractures/faults are represented as white surfaces because they are parallel to the section. Note that basaltic dykes never intrude NW-SE secondary faults.

2.4 Microstructures of the slip zones

Microstructural observations of slip zones were carried out on polished thin sections cut perpendicular to the fault slip surfaces and both parallel and perpendicular to fault lineations using optical microscopy (OM, Department of Geosciences, Padova), field-emission scanning electron microscopy (FE-SEM, INGV, Rome) and optical cathodoluminescence microscopy (OM-CL, Joseph Fourier university, Grenoble). Mineral composition of the slip zones was determined by semi-quantitative X-ray powder diffraction analysis (XRPD, Department of Geosciences, Padova). I refer to both the *slip surface* and the underlying *slip zone* when describing samples (e.g. Smith et al., 2011). The *slip surface* corresponds to the fault surface itself, sometimes containing slickenlines and surface grooves that indicate the direction of slip. The *slip zone*, up to several centimeters thick, immediately underlies the slip surface and contains variably developed fault rock materials that are described following the classification scheme of Sibson (1977). Collectively, the slip surface and slip zone are thought to accommodate the bulk of fault displacement during the seismic cycle and mostly during individual earthquakes (e.g. Sibson, 2003).

Access to quarry exposures was limited in places due to the steep topography. Because of this, we collected samples from the slip zone of the main Borcola Pass Fault only within dolomitic marbles in the lower 10 m of the quarry. Instead, slip zones of secondary faults in the damage zone were sampled only within dolostones: in dolomitic marbles the secondary faults were typically sharp and lacked well-developed fault rock materials. Below, we first describe the slip zone of the Borcola Pass Fault where it cuts dolomitic marbles. We then describe the slip zones of secondary faults where they cross-cut dolostones.

2.4.1 Slip zone of the Borcola Pass Fault

The slip zone of the Borcola Pass Fault typically consists of a < 1-2 cm thick protocataclastic to cataclastic layer cross-cut by the slip surface itself (Borcola Pass Fault surface; Fig 6). Protocataclasites contain highly fractured clasts of dolomitic marble, altered dolomitic marble and dolomite veins with little or no fine-grained intergranular matrix (Fig 6b). Towards the slip surface the protocataclastic fabric passes to a cataclastic fabric containing sub-millimeter clasts of dolomite surrounded by a finer-grained matrix (Fig.6b).

The slip zone contains sub-vertical shear fractures in some cases oriented ~15°-20° to the slip surface. The shear fractures have millimeter-scale displacements and a left-lateral shear sense, consistent with an origin as synthetic Riedel shears (R) (Fig.6a,b). Other minor R shears hundreds of microns to a few millimeters in length are observed to cut the host rock and the lower boundary of the slip zone. All the shear fractures are defined by higher porosity domains (Fig.6c).

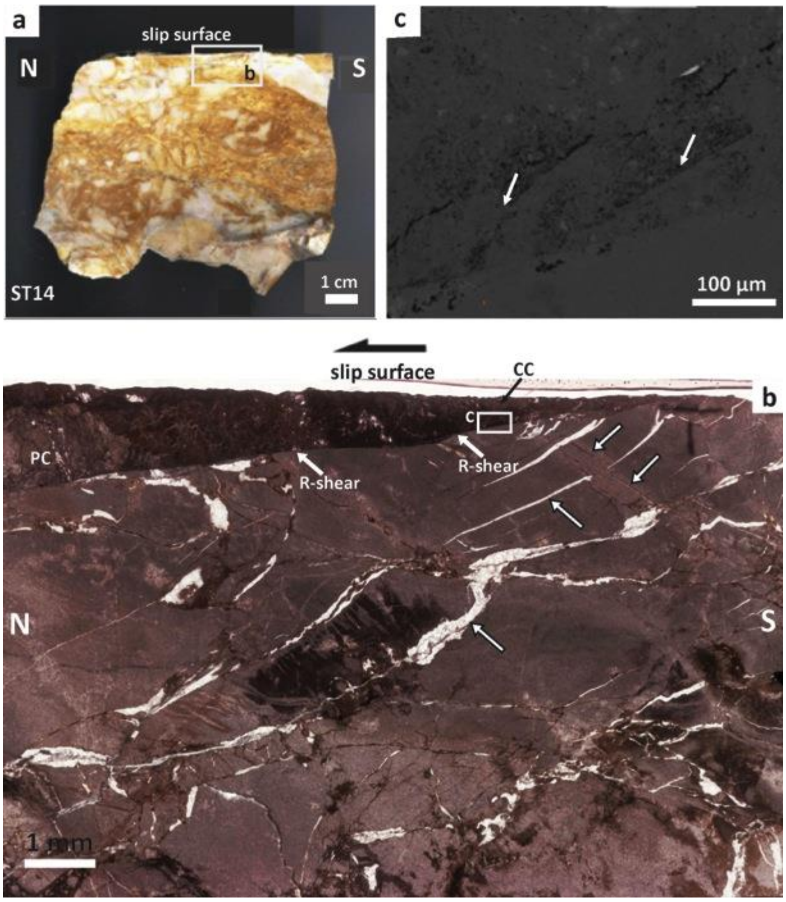

Fig.6 Slip zone of the Borcola Pass Fault within dolomitic marble (sample ST14). (a) Scan of the polished sample cut parallel to slickenlines and perpendicular to the slip surface (see Fig.4 for sample location); "slip surface" is the Borcola Pass Fault surface itself. (b) Scan of the thin section (see (a) for thin section location). The slip zone is made of a few millimeters thick wedge-shaped cataclastic layer truncated at the top by the slip surface and at the bottom by a R-shear consistent with left-lateral sense of shear on the fault. The slip zone assemblage evolves from protocataclasite (PC) to cataclasite (CC) approaching the slip surface. The two sets of hybrid fractures cutting the host rock and striking ca. NW-SE and ca. NE-SW respectively, are marked by white arrows with black borders. The NW-SE striking set cuts dextrally (micrometric separation) the ca.NE-SW striking set. (c) Detail of the lower slip zone boundary (FESEM-BSE image) (see (b) for image location): the few hundreds micrometers long R-shears (white arrows in the image) are consistent with left-lateral shear of the fault.

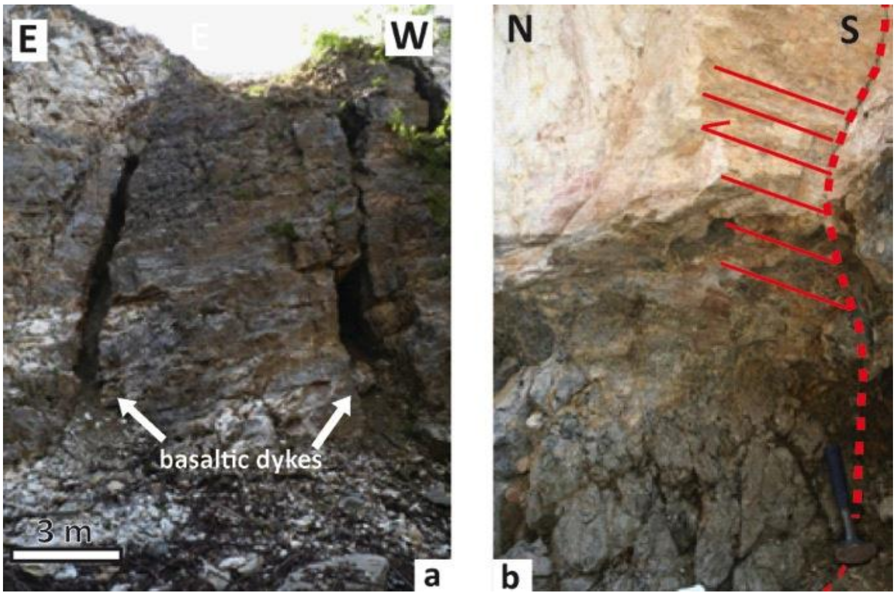

Fig.7 Cross-cutting relationships between basaltic sills/dykes and joints and secondary faults. (a) Paleogene sub-vertical basaltic dykes intruded along N-S oriented joints cutting the sub-horizontal bedding (ca. 1 m average thickness) within the dolostone. (b) A NW-SE secondary fault cutting a Paleogene basaltic sill. Note the striated fault surface cutting the basalt. The arrow indicates the movement of the missing block (right lateral strike-slip fault).

2.4.2 Slip zones of secondary faults from the damage zone

The slip zones of secondary faults are typically 5-8 cm thick and consist of dolomite cement-supported cataclasites with <2% Mg-rich calcite (XRPD analysis) occurring as a late vein infill (Figs 5, 8, 9). Clasts are typically subangular and composed of (1) micritic or microsparry dolomite with interstitial opaque minerals (mainly oxides), and (2) polymict clasts (reworked cataclasite, veins or older slip zones that record more than one deformation event). Large elongated clasts (up to 1-2 cm long) show evidence of intragranular extension fracturing (Billi et al., 2010), often along stromatolitic laminations (Fig.9a). The clasts are surrounded by small angular fragments up to 10 µm in size generated by chipping processes (Billi, 2010). The cement between the clasts consists of zoned, polygonal dolomite crystals >10 µm in size. FESEM and elemental EDS (Energy Dispersive Spectrometry) analysis show that dolomite crystal zoning is due to cyclic compositional variations (i.e., Ca-rich, bright in color, Mg-rich, dark in color) (inset in Fig.9a). The slip zones are generally characterized by clast size reduction toward the slip surfaces, coupled with crystal size reduction within the surrounding cement. In some cases the cement is cross-cut by shear bands lined by dolomite crystals a few µm in size (Fig.10b).

The most striking microstructure of the secondary slip zones is a sub-centimeter to centimeter thick "vein-like" cataclastic layer immediately beneath the slip surface (defined here as Layer-A: Figs 8c, 9a). Layer-A only occurs within some of the secondary slip zones where it sharply cross-cuts the underlying cataclastic layers described above (defined here as Layer-B) (Fig. 8c, Fig.9a, Fig.10a,b).

(i) The vein-like cataclastic layer (Layer-A)

Layer-A consists of a whiteish cement-rich layer with a maximum thickness of 1.5 cm containing isolated clasts of dolostone (micritic or microsparry dolomite clasts or polymict clasts) with diameter < 2.5 mm (Fig.8c, 9a, 10a, b). Layer A is truncated at the top by the exposed slip surface (i.e. the fault surface, slip surface 1) and bound at the bottom by another slip surface that separates Layer-A from Layer-B (slip surface 2). The exposed slip surface is a polished surface that truncates individual dolomite clasts, whereas slip surface 2 truncates clasts within Layer-B (Fig.9a,10a) and is lined by dolomite crystals a few µm in size.

In some cases the exposed slip surface (slip surface 1) is not in direct contact with Layer-A but is separated from Layer-A by a 2-5 mm thick texturally distinct ultracataclasite (Fig.10a,b). This ultracataclasite contains multiple sub-layers with variable thickness (hundreds of µm to a few millimeters) and undulatory boundaries both parallel and perpendicular to the slip direction (Fig 10a,b).

In three dimensions Layer-A displays a complex geometry (Fig 10a,b). In sections parallel to the slip direction Layer-A has a continuous and relatively planar lower boundary and an upper boundary characterized by a cuspate-lobate form, with the cusps pointing downwards in to Layer-A (Fig 10a). Instead, in sections perpendicular to the slip direction Layer-A pinches out laterally (Fig.10b).

Clasts within Layer-A are suspended within a zoned dolomite cement consisting of polygonal (rombohedral) crystals with an average size of 30-40 µm (Fig.9a, Fig.10a,b). OM-CL images show a fine-grained (few µm in size) crystalline matrix at the contacts of dolomite crystals and within open fractures (Fig.10d). Furthermore, many dolomite clasts are surrounded by a fringe of chemically distinct material a few µm thick (brown in OM and light orange in OM-CL, Fig.10d), most likely related to interaction of the clasts with a surrounding chemically reactive fluid. Around the clasts the cement is often cross-cut by black, fine-grained laminations that depart from the clasts like flow lines (Fig.10a,b).

Several veins (V1 and V2 in Fig.9a) depart from Layer-A in to Layer-B and cut across slip surface 2. The veins are bordered by µm-thick bands of black crystalline gouge similar to that found along slip surface 2. It seems likely that these veins originated as Riedel shear fractures and were subsequently filled by dolomite cement (R and R’ for a right-lateral sense of movement in Fig.9a).

From FESEM observations the vein fill consists of different generations of dolomite and late precipitation of Mg-calcite. OM-CL images indicate the presence of fragmented clasts of dolostone and dolomite crystals derived from Layer-A (Fig.10c).

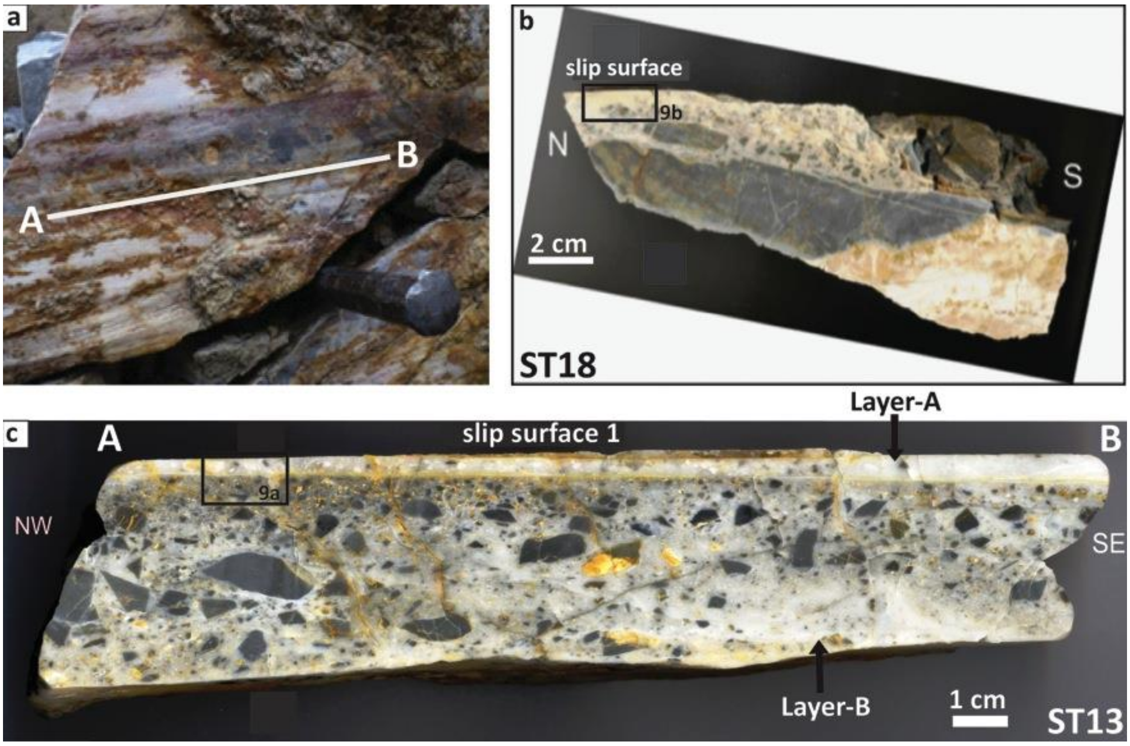

Fig.8 Secondary faults and slip zones within dolostone. (a) Surface of a NW-SE oriented secondary fault cutting dolostone: debris is cemented on the striated surface (b) Polished sample (ST18, see Fig.4 for sample location) cut parallel to slickenlines and perpendicular to the slip surface of a N-S striking secondary fault. (c) Polished sample (ST13, see Fig.4 for sample location) cut parallel to slickenlines and perpendicular to the slip surface of a NW-SE striking secondary fault. The slip zone contains a < 1 cm thick whitish in colour cataclastic layer (Layer-A) truncated by the slip surface (slip surface 1) and truncating a grey in colour cataclasite at the bottom (Layer-B).

2.5 Clast size distributions of the slip zones within dolostone

Two dimensional clast size distributions (CSDs) of two samples taken from secondary slip zones (ST13 and ST18) (Fig.8b,c) were determined by analysis of high resolution scans of polished hand samples and thin sections. Sample ST13 comes from a NW-SE trending secondary fault and contains the "vein-like" cataclastic layer (Layer-A) described above. For this sample, CSD was determined for Layer-A and Layer-B separately with the aim of quantifying microstructural differences. Sample ST18 comes from a north-south trending secondary fault containing a cataclastic fabric. The studied slip zones were composed of dolostone clasts within a dolomitic cement (see section 2.4.2), rendering automatic recognition of clasts problematic. For this reason, clasts were identified and traced manually (Fig.11). We used Image J software (http://rsbweb.nih.gov/ij/) for measurement of clast dimensions. Since clasts have an angular to subrounded shape, clast size was expressed as the diameter d of a circle with the same area A of the clast ($d=2(A/\pi)^{0.5}$; Marone and Sholz, 1989). Size frequency data were measured at different magnifications, starting from scanned images of hand samples, polished thin sections and from photomicrograph (optical microscope) mosaics of selected areas at 4X and 10X magnification. SEM images were not used due to the lack of contrast between matrix and clasts. An area of 25 square pixels (corresponding to d≈100 µm for scanned images of hand samples, d≈30 µm for scanned images of thin sections, d≈8 µm and d≈5 µm for photomicrographs at 4X and 10X magnification respectively) was chosen as the lower cutoff grain size for CSD analysis, because particles smaller than this value were not well defined in the processed images. Resulting CSDs (Fig.11) were obtained by combining size frequency data over the whole particle dimension range (5 -10^4 µm in diameter) using a similar procedure to that described by Monzawa and Otsuki (2003). The cumulative number of clasts (N) larger than a given diameter d was plotted in log(N)-log(d) diagrams with N the number of clast larger than d. CSD curves following a linear trend in the investigated dimensional range were described by a power law relationship $N \sim d^{-D}$ ($\log(N) \sim -D\log(d)$), where D is the fractal dimension (Turcotte, 1986). The “strength” of the power law relationship in the selected fractal range is shown by the value of R^2 (correlation coefficient), which is between 0.955 and 0.993 for the best-fit line in the log-log distributions in all the studied cases. Though such a small dimensional range (three orders of magnitude) cannot be used to determine if the clast distribution is statistically self-similar, we used D in this case to quantify relative differences between the studied slip zones and discuss possible mechanisms to account for the distributions.

The CSDs of sample ST13 Layer-B (blue curve in Fig.11) and ST18 (green curve in Fig.11) cover a clast size range of 5 - 10^4 µm and 30 - 10^4 µm respectively. In both cases the lower limits of the CSD are artificial and correspond to the lower cutoff diameter we chose for the analysis, whereas the upper limits of the CSD are real. It follows that the shallower segments of the CSD curves, toward smaller clast diameters, are strongly influenced by under-sampling effects, whereas the steeper segments, toward larger clast diameters, are determined by the size of the analyzed images. Ignoring these effects at the data tails, the CSDs of sample ST13 Layer-B and ST18 are well described by a power-law relationship with fractal dimensions D of 1.564 and 1.485 respectively.

In contrast the CSD of the vein-like cataclastic layer in sample ST13 Layer-A (red curve in Fig.11), covers a clast size range of 10 - 2.5×10^3 µm, and both lower and upper limits of the CSD are real. The steeper segment of the size-frequency curve toward larger clast diameters is determined by the thickness of Layer-A. The rest of the curve is described by two segments with different slopes: 1) a steeper slope from 300 - 10^3 µm with a fractal dimension D of 1.558; 2) a shallower slope from 10 - 300 µm - with a fractal dimension D < 1 (Fig.11). This indicates that Layer-A consists almost entirely of clasts larger than 300 µm in diameter with the finer fraction notably absent. This type of distribution suggests a grain sorting mechanism operating during the development of Layer A that preferentially removes smaller clasts, discussed below.

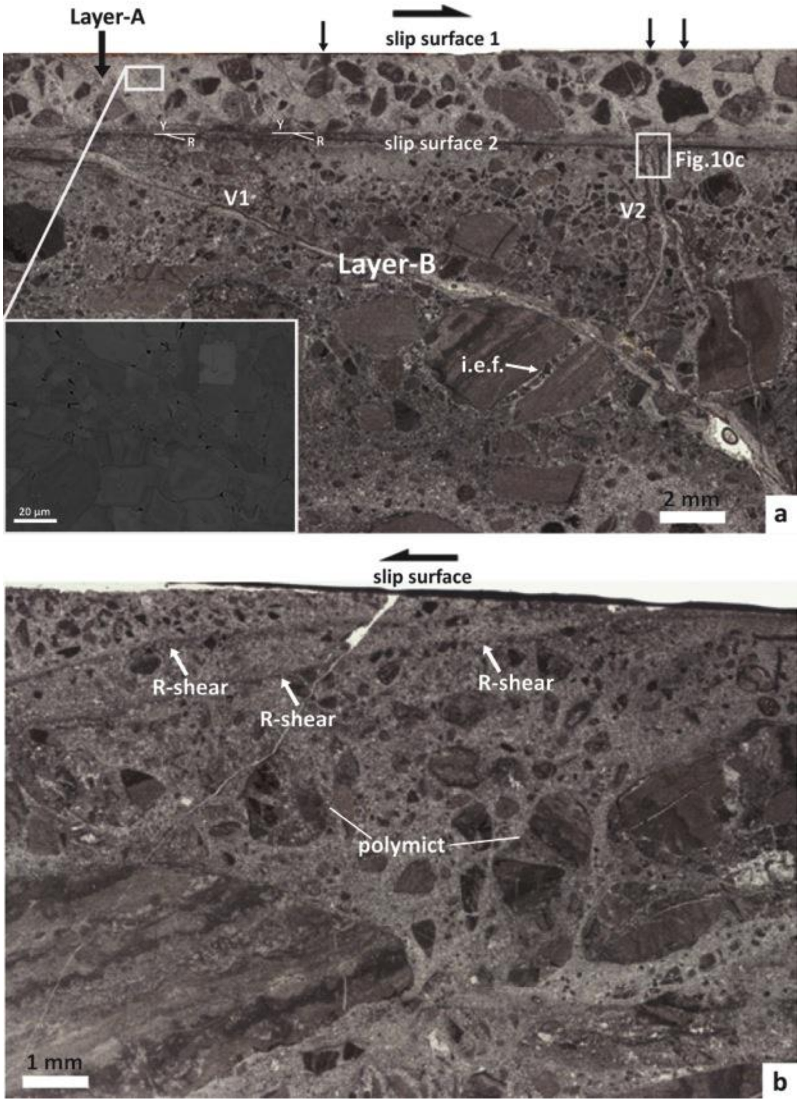

Fig.9 Microstructures of the slip zones within dolostone. (a) Scan of the thin section ST13 thin (see Fig.8c for location). Layer-A is truncated at the top by the exposed slip surface (truncated clasts of dolostones are marked by the black arrows) and bounded at the bottom by a knife-sharp slip surface (slip surface 2). Slip surface 2 is embedded within a 50 µm thick slip zone characterized by the presence of R and Y micro-shears consistent with right-lateral sense of shear along the fault. Clasts within Layer-A are suspended within a vein-like dolomitic cement containing polygonal crystals (average size of 30-40 µm) with compositional zoning (Ca-rich, bright in color, Mg-rich, dark in color in the inset FESEM-BSE image at the lower left corner of the figure). Two veins depart from Layer-A in to Layer-B (V1 and V2). Layer-B consists of a cataclasite with monomineralic and polymict clasts (label polymict in the figure) affected by intragranular extension fracturing (label i.e.f.) and chipping processes. The matrix consists of a dolomitic cement with a minimum crystal size around 10 µm. (b) Scan of thin section ST18 (see Fig.8b for location). Microstructures are similar to Layer-B. Clast size reduction toward the exposed slip surface coupled with the presence of R-shears is evident. R-shears are consistent with left-lateral sense of shear along the fault.

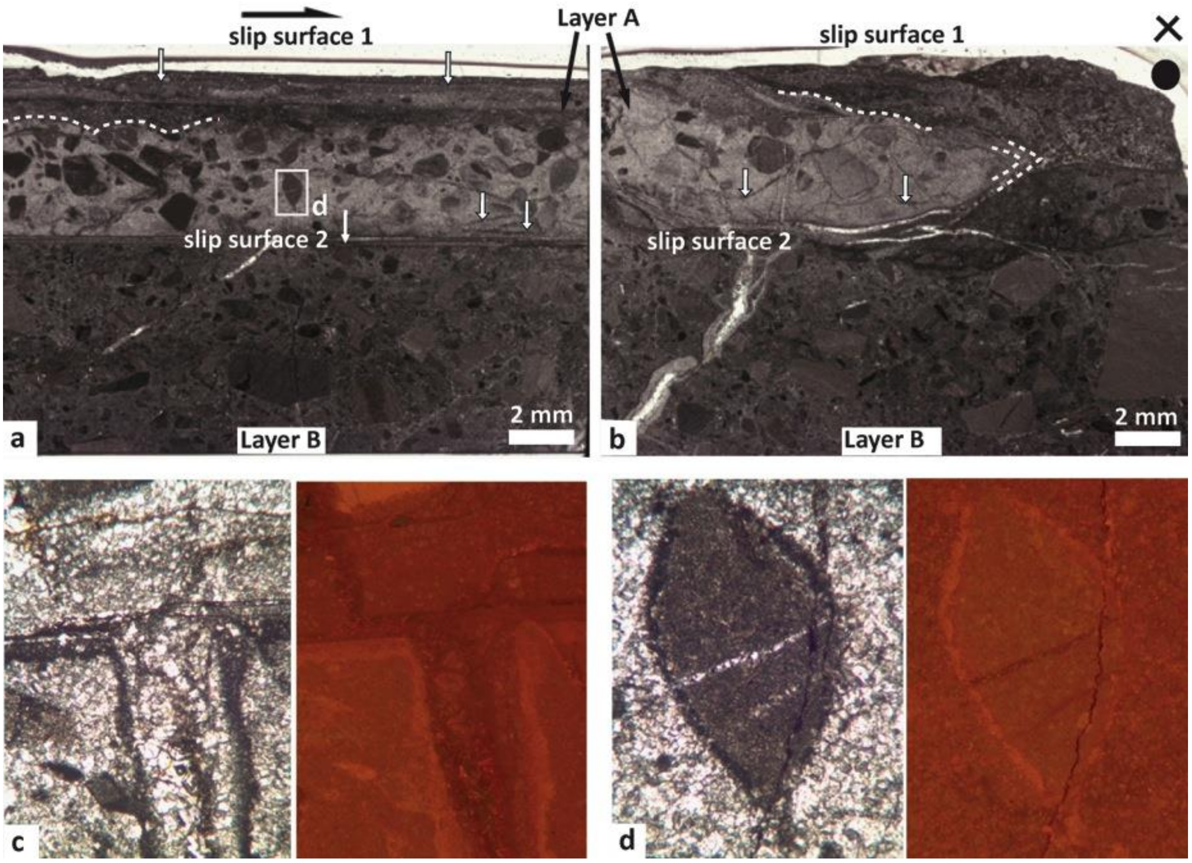

Fig.10 The vein-like cataclastic Layer-A. (a) Scan of thin section cut perpendicular to the fault surface and parallel to fault striae from sample ST13; (b) Scan of thin section cut perpendicular to the fault surface and perpendicular to fault striae from sample ST13. In the section parallel to the slip direction Layer-A has an upper boundary with a cuspate-lobate geometry toward the texturally distinct slip layer above (the white arrows mark the ultracataclastic sub-layers). In sections perpendicular to the slip direction both Layer-A and the ultracataclastic sub-layers show upper undulatory boundaries; moreover Layer-A pinches out laterally (see dashed white lines). Slip surface 2 truncates clasts within Layer-B (see white arrow). Black flow lines cross-cut Layer-A cement around the clasts (see white arrows). (c) OM-CL image showing a detail of a vein departing from Layer A (see Fig.9a for location). Dolostone clasts and dolomite crystals sourced from Layer A are found in the vein. The vein infill is made by different generations of dolomite crystals and minor Mg-calcite. (d) OM-CL image showing the characteristics of clasts in Layer-A (see Fig.10a for the location). A layer light orange in colour rims the clast. A fine-grained (few micrometers in size and dark orange in colour) crystalline matrix seals the space between the cement crystals and the fracture that cuts the clast.

2.6 Discussion

2.6.1 Structure of the Borcola Pass Fault Zone

Several studies in recent years have documented that faulting in carbonates is strongly controlled by preexisting anisotropies within the host rock such as bedding surfaces, veins, pressure solution seams and joints (e.g. Mollema and Antonellini, 1999; Billi et al., 2003; Graham et al., 2003; Agosta and Aydin, 2006; Kurz et al., 2008, Hausegger et al., 2010; Molli et al., 2010). Fault zone growth involves the progressive shearing and interaction of these inherited structures, ultimately leading to the development of new slip zones and slip surfaces.

Within the >80 m wide BPFZ field observations suggest that N-S- and E-W-trending secondary faults reactivated pre-existing Jurassic-Paleogene joints and normal faults. The N-S- and E-W- trending faults were commonly intruded by Paleogene basaltic dykes. The strike of the Borcola Pass Fault itself is approximately N-S, and thus we suggest that it represents an inherited Jurassic-Paleogene structure reactivated during post-Paleogene movements along the Schio-Vicenza Line. On the other hand, NW-SE-trending secondary faults that broadly parallel the Schio-Vicenza Line cross-cut Paleogene basaltic intrusions and represent faults that were newly formed during movements along the Schio-Vicenza Line.

In addition to the presence of pre-existing anisotropies, the structure of the BPFZ is strongly influenced by host rock lithology. The BPFZ cuts two dolomitic protoliths, dolostone and dolomitic marble. Significant changes in both slip zone thickness and deformation intensity were noted passing from the dolostone to the dolomitic marble. Indeed the principal as well as secondary slip zones in dolostone consist of cataclastic and ultracataclastic slip zones up to 10 cm thick, whereas in dolomitic marble the slip zones are protocataclastic to cataclastic and < 1-2 cm thick. We suggest that such differences in slip zone thickness result from the likely higher shear strength and increased stiffness of the dolomitic marble. Further characterization of the mechanical properties of the two different host rocks is required to better constrain this interpretation.

2.6.2. Fault kinematics

Field and microstructural observations (see sections 2.3 and 2.4) suggest that the youngest movements along the Borcola Pass Fault were characterized by left-lateral strike-slip kinematics. Furthermore, Riedel microfractures within the slip zones of secondary faults predominantly indicate a left-lateral sense of shear for N-S oriented secondary faults and a right-lateral sense of shear for NW-SE oriented secondary faults. These kinematics are consistent with the presence of a post-Paleogene NW-SE to NNW-SSE oriented σ_1 in the studied area, leading to right-lateral transcurrence along the northern tract (north of Schio) of the Schio-Vicenza Line. The kinematics recorded in the BPFZ compare favorably with focal mechanism solutions from active seismic sources in the study area (i.e. N-S and NW-SE oriented faults; see section 2.1).

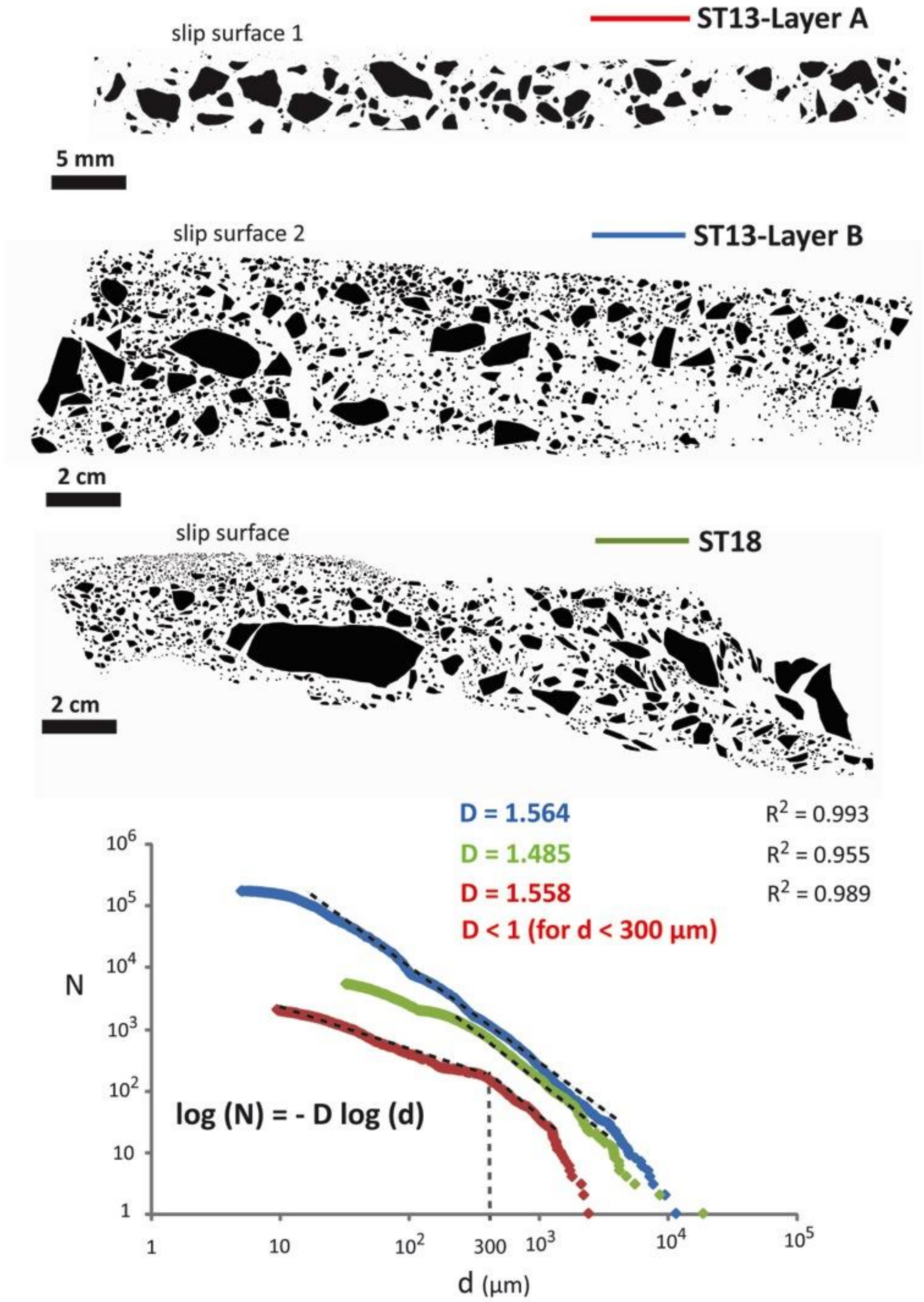

Fig.11 Clasts size distributions (CSDs) of the slip zones within dolostone. The tracings show examples of the figures (clasts were drawn by hand) from samples ST13-Layer-A, ST13-Layer-B and ST18 used for image analysis. The CSD graph shows the number of clasts, *N*, larger than a particular diameter, *d*. Curves for ST13-Layer-B and ST18 are well described by a power-law distribution with comparable fractal dimensions *D*, whereas the CSD curve of ST13-Layer-A is characterized by two segments with different slope. For clast diameters <300 µm ST13-Layer-A has a fractal dimension *D* < 1, indicating an almost total lack of small clasts. See section 2.5 for discussion.

2.6.3 Deformation mechanisms within the slip zones

The slip zones studied here are estimated to be exhumed from a depth of ca. 1.6-1.7 km, corresponding to the thickness of the pre-Miocene sedimentary overburden in the area (Sedea and

Di Lallo, 1984). Assuming a typical crustal geothermal gradient of 30°C/km the ambient temperature at the time of faulting was ca. 50°C.

The slip zones cutting dolostones typically consist of cement-supported cataclasites together with abundant dolomite veins, suggesting fluid flow along the faults. Clasts are sub-angular and fragmented by bulk extensional fracturing and comminution. Toward the slip surfaces grain size reduction leads to the formation of ultracataclasites that are cut by Riedel shears. The most characteristic microstructure of the secondary slip zones is the vein-like cataclastic Layer-A, sometimes separated from the slip surface by a 2-5 mm thick texturally distinct ultracataclasite containing multiple sub-layers. Image analysis demonstrates that Layer-A largely lacks clasts < 300 µm in size, resulting in D < 1 for clast diameters < 300µm. Whereas the "constrained comminution" model of Sammis et al. (1987) can account for the clast size distributions in cataclastic layers adjacent to Layer A (e.g. Layer B that has D ~ 1.6), other deformation processes that result in an absence of small clasts are required to explain the unusual textural characteristics of Layer-A.

Clast size segregation is reported in literature for both natural and experimental fault gouges as an indicator of coseismic fluidization (e.g. Boullier et al., 2009; Ujiie et al., 2011). It has been explained as resulting from the "Brazil nut effect" (BNE) (Williams, 1976), that causes a concentration of larger clasts in the upper part of the fluidized layer, due to the strong difference in dispersive pressure between large and small grains within a granular-fluid shear flow. Considering that the studied faults and veins within the BPFZ are subvertical, we might explain the strong grain sorting within Layer-A (i.e. absence of clasts with d < 300 µm) by the BNE, assuming that the finer particles are concentrated toward the bottom of Layer-A that is not outcropping. Another possibility to explain the absence of small particles in Layer-A is hydrodynamic selection of fine particles within a fluidized gouge.

Several microstructural observations suggest that Layer-A and the ultracataclastic sub-layers adjacent to secondary slip surfaces experienced fluidization:

1. Layer-A displays intrusive relationships with Layer-B (Fig.10b)
2. The upper boundary of Layer-A has a cuspate-lobate geometry, with the cusps directed downwards towards Layer-A. Together with the observation that the ultracataclastic sub-layers display significant thickness variations both parallel and perpendicular to the fault slip direction, this suggests that both Layer-A and the ultracataclastic sub-layers were

characterized by viscous behavior, with a lower viscosity for the ultracataclastic sub-layers (Brodsky et al., 2009) (Fig.10a, b)

3. Layer-A contains clasts that are entirely surrounded by dolomite cement. Although this may partly be an effect of two-dimensional sections, it is rare to find touching clasts in Layer-A either in sections parallel or perpendicular to fault slip, and thus they appear to be isolated from one another (Fig.9a,10a, b).
4. Several veins depart from Layer-A in to Layer-B exploiting previous structures such as Riedel shears. The veins are thicker at the boundary with Layer-A and terminate downwards in to Layer B, suggesting that they are related to build-ups of fluid pressure within Layer-A. Additionally, OM-CL images indicate that fragmented clasts of dolostone and dolomite crystals were transported from Layer-A in to the veins, and that the veins were subsequently filled by dolomite and later Mg-calcite cements (Fig.10c).

Several examples of “fluidized” fault rocks associated with protrusions or injections of one fault rock material into another have been described in different tectonic settings from the field (Rowe et al., 2005; Ujiie et al., 2007; Brodsky et al., 2009; Meneghini et al., 2010; Smith et al., 2008) to the microscopic scale (Otsuki et al., 2003; Smith et al., 2011). The fluidized fault rocks are frequently interpreted as forming due to a sudden release or increase of fluid pressure that allows rock particles to be passively transported by the fluid phase (Monzawa and Otsuki; 2003). The achievement of high fluid pressure gradients within fluidized fault rocks is widely documented by field and microstructural observations of hydrofracture veins (micrometers to centimeters thick) both interlayered with and departing from fluidized rock layers (Smith et al., 2008; Boullier et al., 2009; Smith et al., 2011). The fluid phases are variable in terms of chemical composition (e.g. H_2O rich, CO_2 rich solutions), pressure and temperature conditions (i.e. physical state: liquid, gaseous, supercritical), and origin (i.e. meteoric infiltration, upward crustal or mantle fluid flow, local pore fluids) (Boullier et al., 2004; Smith et al., 2008).

We suggest two different hypotheses to account for fluidization of both Layer-A and the ultracataclastic sub-layers within the BPFZ: 1) focussed fluid flow within the slip zones following earthquake rupture (e.g. fault-valve mechanism of Sibson 1990a), 2) thermal pressurization of pore fluids within the slip zone due to rupture propagation and coseismic shear heating (e.g. Rice, 2006).

Following the first hypothesis slip zones within the BPFZ would have acted as relatively impermeable seals transiently broken by earthquake ruptures (Sibson, 1990). Observations indicate that the dolomitic cataclasites in the BPFZ are well cemented and massive (section 2.4.2), especially close to slip surfaces. This suggests that sealing of the slip zones by mineral precipitation played an important role. Precipitation of mineral cements and veins during the interseismic period would strongly reduce slip zone permeability and favour the build-up of fluid pressure within the more permeable damage zone. The occurrence of a seismic rupture along the cemented slip zones would break the permeability barrier and allow fluids to flow through a network of coseismic fractures. If the fluids released in to the newly formed fracture network were at elevated pressures then fluidization of thin gouge layers may have occurred.

The second hypothesis invokes thermal pressurization within the slip zones during seismic slip. Thermal pressurization describes an abrupt increase of fluid pressure induced by frictional heating resulting in expansion of pore fluids (Sibson, 1973; Rice, 2006; Noda et al., 2009). The coseismic heat pulse may also lead to decarbonation of carbonate-bearing minerals (e.g. calcite and dolomite: Sulem and Famin, 2009; De Paola et al., 2011). In this case we suggest that fluidization of both Layer-A and the ultracataclastic sub-layers could be related to thermal pressurization triggered by expansion of pore fluids (most likely CO_2-rich acqueous fluids) associated with fast (seismic) slip.

The two hypotheses for triggering fluidization in the studied slip zones imply different origins for the fluid phases (i.e. from local or external sources) and different mechanisms of achieving fluid overpressures. Discerning between the two mechanisms is not possible using only microstructural and mineralogical data from the slip zones, and useful constraints will arise from geochemical analysis of the vein and cement phases (e.g. stable isotope analyses of carbon and oxygen). Nevertheless, some considerations can be made concerning fluidization and crystallization processes within Layer-A, and below we describe our favored conceptual model accounting for the development of Layer-A.

(i) Conceptual model for the development of Layer-A

The matrix of Layer-A consists of a dolomitic cement with an average crystal size of 30-40 μm. The dolomite crystals display the typical characteristics of a vein-filling cement (i.e. polygonal crystals, compositional crystal zoning). Similar cement has been described in carbonate veins related to coseismic fluid flow in slip zones of the Nojima fault (Boullier et al., 2004). We interpret the dolomitic cement to be precipitated from a supersaturated fluid phase, likely consisting of an aqueous solution of HCO_3^-, Ca^{2+}, Mg^{2+} etc. and dissolved CO_2.

In the BPFZ strain was localized in thin cataclastic layers flanking the slip surfaces. In the case of rocks with similar properties to dolostone (i.e. shear wave velocity of about 4 km/s, Gueguen and

Palciauskas, 1994) a Mode II rupture propagating at 98% of the Rayleigh speed (an important asymptotic limit in the subsonic regime corresponding to 0.92 the shear wave velocity, e.g., Burridge et al., 1979) will result in tensile stresses of up to 3 GPa and volumetric strain rates exceeding 10^5 s^{-1} in the few millimeters around the rupture tip (Fig. 6 in Reches and Dewers, 2005). Due to intense stress and temperature pulses (up to 500°C for 0.5 m of displacement at seismic slip rates at these depths of 1.5-2 km) at the rupture tip fault rocks fracture and pulverize (e.g. Reches and Dewers, 2005) and pore fluids expand (Rice, 2006) at a much higher rate than solid rock. Under these extreme deformation conditions both CO_2 (with critical temperature and pressure of T_C = 30.25 °C and P_C = 7.3 MPa respectively) and H_2O (T_C = 373.95 °C, P_C =22.06 MPa) are likely to achieve the supercritical state (Kaszuba et al., 2006). Pulverization and fluid expansion will result in the formation of a pressurized hot slurry that hydrofractures and injects the wall rocks driven by the large pressure gradients achieved in the slip zone (because of the opening of new fractures). Such a process may account for fluidization within Layer-A and the adjacent ultracataclasite layers. Fluid injection results in expansion and cooling of the supercritical solution and rapid nucleation of dolomite crystals a few micrometers in size, as observed in the matrix between the cement crystals and within fractured clasts (Fig.10d). This is similar to a process termed Rapid to Slow Expansion of Supercritical Solutions (RESS and SESS) commonly used in industry (e.g. in the field of pharmaceuticals) to obtain small particles (few micrometers) with a controlled size distribution from different solutes (Arai et al., 2002; Yeo and Kiran, 2005). Because the density and viscosity of supercritical H_2O and CO_2 are not high enough to suspend dolostone clasts (since supercritical fluid transport properties lie between those of liquids and gases; Arai et al., 2002; Liebscher, 2010; Heidaryan et al., 2011) we propose a similar rapid crystallization mechanism to explain the observation that clasts within Layer-A are found “floating” within the surrounding cement. After initial nucleation of small dolomite crystals leading to suspension of entrained clasts, crystal growth becomes important resulting in the final polygonal, zoned dolomite cement that dominates Layer-A.

2.6.4 Comparison of the BPFZ with the structure of an active seismogenic fault (Bovec-Krn Fault)

In the last few years increasingly detailed seismological analyses of foreshock-mainshock-aftershock sequences have begun to elucidate the structure of active seismogenic fault zones cutting carbonate sequences (e.g. Bressan et al., 2009; Chiaraluce et al., 2011). For example, Bressan et al. (2009) analyzed the aftershocks of the 12 April 1998 M_D = 5.6 and the 12 July 2004 M_D = 5.1 Bovec-Krn earthquakes along the NW-SE-trending dextral strike-slip Bovec-Krn fault (northwestern

Slovenia). By combining tomographic analyses of the fault zone and the upper-crustal sedimentary sequence with high-quality earthquake relocations they showed that the two main shocks and a majority of the aftershocks nucleated within platform limestones and dolomitic limestones between 2 and 10 km depth. They also showed that aftershocks were more or less symmetrically distributed with respect to the trace of the Bovec-Krn fault within a maximum distance of ca. 2 km from the fault trace. Variations in seismic wave velocities suggested that the fault zone contained branching and minor splay faults (Bressan et al., 2009). In particular, the aftershock distribution of the 1998 earthquake (700 aftershocks with M_D between 1.5.and 4.6) was consistent with the activation of several sub-vertical surfaces broadly parallel to the NW-SE strike of the main fault. Instead, the 2004 aftershock sequence (300 aftershocks with M_D between 1.1 and 3.6) was characterized by a more diffuse pattern consistent with the activation of many minor fault planes in a wide range of orientations (Bressan et al., 2009). In both cases, many of the aftershock focal mechanisms showed fault plane solutions (strike-slip but also many normal and reverse events) and fault plane orientations different to those of the two main shocks.

Qualitatively, the seismological observations of Bressan et al. (2009) compare favorably to the observations reported here for the BPFZ, even although the BPFZ was exhumed from shallower depths (<2 km). The BPFZ represents a secondary fault zone with respect to the major NW-SE trending Schio-Vicenza Line. The BPFZ consists of sub-vertical fault strands with observed lengths ranging from a few meters (secondary faults) to a few kilometers (Borcola Pass Fault). The faults are found in a range of different orientations. Empirical length-magnitude scaling relationships (e.g. Wells and Coppersmith, 1994) suggest that the Borcola Pass Fault may have hosted earthquake ruptures of $M_w \approx 4 - 4.5$ (considering a maximum rupture length of 2 km), whereas secondary faults within the BPFZ may have hosted ruptures of $M_w < 2.5$ (considering a maximum rupture length of 20 m). We suggest that the BPFZ records past aftershock activity related to moderate-large earthquakes ($M_w \approx 5 - 6$) along the nearby Schio-Vicenza Line, in a similar manner to the aftershock sequences following ruptures along the Bovec-Krn fault.

Further field observations concerning the structure of exhumed fault zones will be important to compare to increasingly high-resolution seismological data. In particular, microstructural observations of thin slip zones are essential to understand physico-chemical processes active during fault slip, because such observations are outside the resolution of seismological data (Di Toro et al., 2012).

2.7 Conclusions

The BPFZ is a sinistral strike-slip branch of the Schio-Vicenza Line outcropping in the western Venetian Fore-Alps and cutting two distinct dolomitic protoliths: sedimentary dolostone and dolomitic marble. The fault zone, exhumed from ca. 1.6-1.7 km depth and ca. 50°C, displays a complex structure consisting of a highly heterogeneous fault core and a surrounding damage zone exceeding 80 m in width. The fault core changes thickness where it cuts different host rocks. The damage zone is cross-cut by networks of sub-vertical joints and secondary faults (N-S, E-W and NW-SE oriented) that reactivate pre-existing anisotropies (joints and veins) or represent newly formed structures.

Slip zones cutting dolostone typically consist of cataclasites up to 10 cm thick associated with widespread dolomite veins, attesting to the circulation of fluids within the fault zone. Some of the slip zones contain an unusual vein-like cataclastic layer (Layer-A) up to 1.5 cm thick, often separated from the exposed slip surface by a 2-5 mm thick texturally distinct ultracataclasite containing multiple sub-layers. Fluidization of both Layer-A and the ultracataclastic sub-layers is suggested by geometrical features (cuspate-lobate boundaries, pinch-out terminations), strong grain sorting found in Layer-A (CSD indicates absence of clasts with $d < 300$ µm), and the presence of veins departing from Layer-A and terminating in Layer-B. We correlate fluidization with rapid slip associated with seismic ruptures propagating to shallow depths along the BPFZ. Similar grain size distributions to those found in Layer A may represent a microstructural indicator of fluidization and seismic slip in dolostones.

A comparison of the BPFZ with an active seismogenic strike-slip fault zone cutting carbonates (the Bovec-Krn Fault in Slovenia) highlights the common structural complexity of the two faults, characterized by the presence of several branches and sub-parallel strands that in the case of the Bovec-Krn Fault were activated during the same seismic sequence. Field studies of fault zone structure will help to interpret the results of increasingly high-resolution geophysical studies. In particular, detailed microstructural analysis of slip zones is required to understand physico-chemical processes during the earthquake cycle at a resolution currently unavailable from geophysical data.

3. Foiana Fault Zone: a major fault zone in a fluid-poor environment

Abstract

The Foiana Fault Zone (FFZ) is a major (~ 30 km long) sinistral transpressive fault zone exhumed from depths of 1-2.5 km in the Italian Southern Alps. The fault zone crosscuts Permo-Triassic igneous and sedimentary rocks, the latter including thick sequences of dolostone. At the current exposure level, the FFZ exhibits an increase in cumulative vertical throw in the range of 0.3-1.8 km moving from south to north along fault strike. The fault zone consists of variably fractured and fragmented dolostones locally cut by networks of small-displacement (<0.5 m) faults containing discrete, highly-reflective (so-called "mirror-like") slip surfaces. The mirror-like slip surfaces are typically embedded within fine-grained gouge layers (maximum clast size of few millimeters) up to few centimeters thick. Preservation of bedding planes in the fragmented dolostones indicates a lack of significant shear strain. Instead, the fragmented dolostones were affected by in-situ shattering from the centimeter down to the micrometer scale. In general the absence of veins and sealed fractures within the fault zone suggests a paucity of fluids during faulting. Detailed field and aerial structural mapping conducted along several well-exposed sections of the fault zone allowed the recognition of significant changes in the structure of the FFZ along strike. In particular, large variations in fault zone thickness (from 100 m in the north to more than 300 m in the south) and changes in mean fault orientation and fault kinematics (from dominant oblique- and strike-slip in the north to dip-slip reverse in the south) were observed, together with the reactivation of preexisting anisotropies (i.e. bedding). Overall, the structure of the FFZ, when considered together with the variable exhumation level along strike, compares favorably to the predicted damage distribution in three-dimensional earthquake rupture simulations on strike-slip faults, as well as the structure of active seismic sources hosted in carbonate rocks as illuminated by seismological techniques.

This study was performed in collaboration with Stefano Aretusini, Steven Smith and Giulio Di Toro. I performed all the work described in this chapter. I was assisted (but not continuously) in the field by Stefano Aretusini, Steven Smith and Giulio Di Toro. Some of the field data were reported in the master thesis thesis of Stefano Aretusini (Aretusini, 2013). The material presented here was discussed with Steven Smith, Stefano Aretusini and Giulio Di Toro.

3.1 Tectonic setting of the study area

The eastern Southern Alps of Italy are a SSW-vergent fold and thrust belt extending for ~ 200 km from the Periadriatic Lineament to the upper Venetian Plain, where the active frontal thrusts are buried under Quaternary alluvial deposits (Fig.1). The Periadriatic (or Insubric) Lineament is the most important tectonic boundary in the European Alps since it separates the Alpine collisional wedge to the north (a stack of Europe-vergent nappes dominated by Cretaceous to Oligocene alpine metamorphism and ductile deformation) from the backthrust belt of the Southern Alps dominated by brittle tectonics involving the Variscan crystalline basement and the overlying volcanic and sedimentary cover (Permian to Paleogene in age) (Castellarin et al., 1992, 2006). The Periadriatic Lineament consists of several segments with differing kinematics and geodynamic histories that, in the eastern sector of the chain, are the E-W striking Tonale and Pusteria Lines, and the NNE-SSW striking North Giudicarie Line (Fig.1).

The North Giudicarie Line is usually interpreted as a left-lateral transpressive fault of middle-late Miocene age (Laubscher, 1971, 1988, 1996; Ratschbacher et al., 1991). In its southern sector (Fig.1), the North Giudicarie Line consists of a large-scale reverse fault that places medium to high-grade basement rocks of the Austroalpine domain in the hanging wall on Mesozoic sedimentary cover rocks of the Southern Alps in the footwall (Santini and Martin, 1988; Werling, 1992; Prosser, 1998, 2000). In this area the strike-slip deformation component is largely partitioned in to the footwall of the North Giudicarie Line, within the Southern Alps domain, along N-S to NNE-SSW oriented regional scale faults such as the Trento-Cles Line and the Foiana Fault Zone (Foiana Line auctores: Dal Piaz, 1942; Van Hilten, 1960; Cadrobbi 1965; Prosser 1998, 2000). The Foiana Fault Zone is particularly well exposed in several areas along strike and is the focus of this study (Fig.1).

3.2 The Foiana Fault Zone (FFZ)

3.2.1 Geology and regional-scale geometry of the FFZ

The Foiana Fault Zone (FFZ) is a sinistral transpressive fault zone that strikes sub-parallel to the North Giudicarie Line at a distance of c. 4-5 km to the east (i.e. within the Southern Alps domain). The FFZ is exposed for ~ 30 km from the western Val di Non area to the Adige valley near the village of Lana (northern Italy) (Fig.1). If, as some authors suggest (Van Hilten, 1960; Cadrobbi, 1965), the FFZ is linked to the north with the North Giudicarie Line and to the south with the Trento-Cles Line, a maximum fault zone length of ~ 45 km can be estimated. The average strike of the FFZ is NNE-SSW with dip angles in the range 45°-80° west, increasing from south to north along fault strike.

In detail, three main segments of the FFZ can be distinguished based on changes in average fault zone strike and dominant host rock lithologies: 1) in its northern sector (length ~ 11 km, north of the Palade Pass, Fig.2) the FFZ strikes NNE-SSW, dips c. 80° to the west and puts in contact Variscan basement and Permian intrusions to the west against Permian to lower Triassic cover rocks (mainly vulcanites, volcanic sandstones and marly limestones) to the east (Bosellini et al., 2007). The northern sector is arranged in to two en echelon left-stepping segments with a lateral separation of ~ 600 m; 2) in the central sector (length ~ 10 km; from Salobbi to Palade Pass) the FFZ strikes N-S, dips 50°-70° to the west and places Permian vulcanites in the hanging wall on to middle to upper Triassic dolostones in the footwall; 3) in the southern sector (exposed length ~ 4 km; from Cloz to Salobbi) the FFZ strikes NE-SW and dips 45°-60° to the northwest. This highlights a prominent fault bend between the central and southern sectors. In the southern sector, the fault zone close to Salobbi cuts through middle to upper Triassic dolostones. Further to the south the fault zone is interpreted to lie in the core of a southeast-verging fault-propagation anticline leading to local overturning of the Triassic-Paleogene cover sequence (Fig.2; Bosellini et al., 2007).

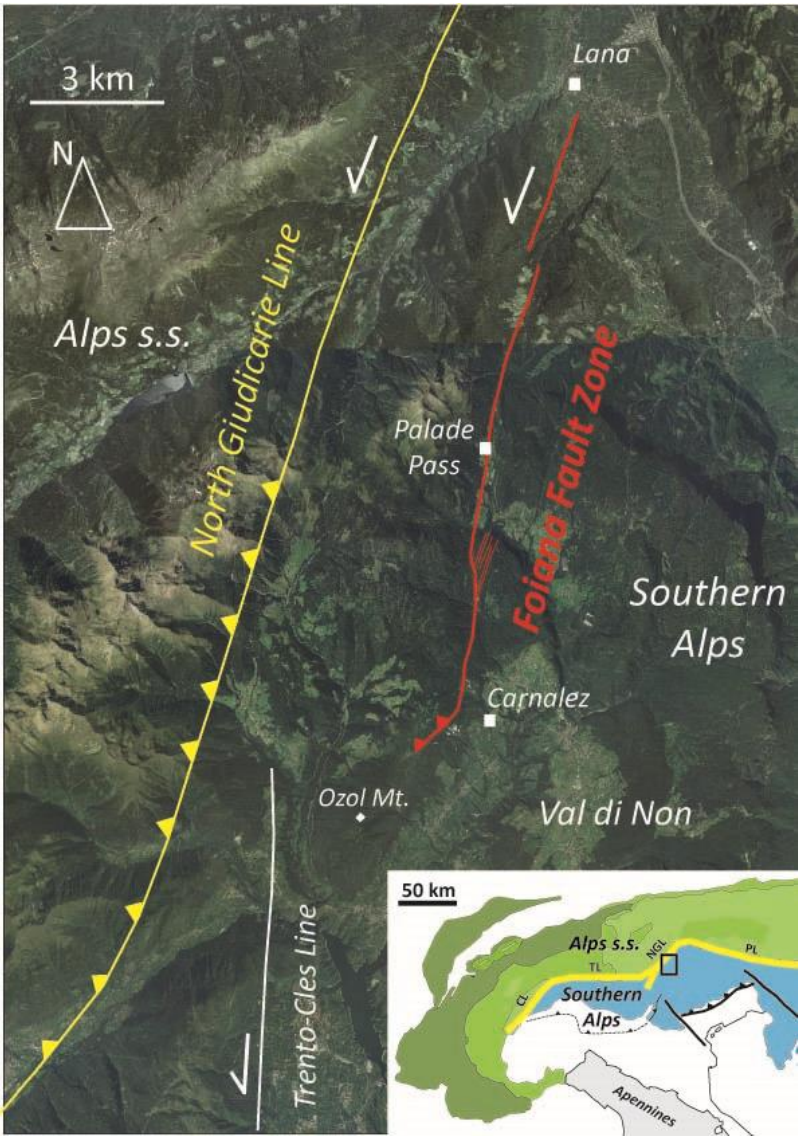

Fig.1 Simplified structural map of the study area around the Foiana Fault Zone (FFZ). The area is located in the inner sector of the eastern Southern Alps (Val di Non area, northern Italy). The main fault in the area is the NNE-SSW-trending sinistral transpressive North Giudicarie Line (yellow line in the figure) which is part of the Periadriatic Lineament (see the inset in the right corner of the figure) and separates the north-vergent Alpine chain to the west (Alps s.s.) from the Southern Alps domain to the east. Other regional-scale faults within the Southern Alps domain are the N-S-trending sinistral strike-slip Trento-Cles Line (white line in the figure) and the NNE-SSW-trending sinistral transpressive Foiana Fault Zone (red line in the figure). The Foiana Fault Zone is ~ 30 km long and runs from the Val di Non area south of the village of Carnalez to the village of Lana in the north. The inset in the lower right corner of the figure defines the location of the study area (small black rectangle). The thick yellow line represents the Periadriatic Lineament and its different segments: Pusteria Line (PL), North Giudicarie Line (NGL), Tonale Line (TL) and Canavese Line (CL). The north-vergent Alpine units are in green and the Southern Alps are in blue. The frontal thrusts and the strike-slip faults delimiting the eastern Southern Alps are represented with thick black lines.

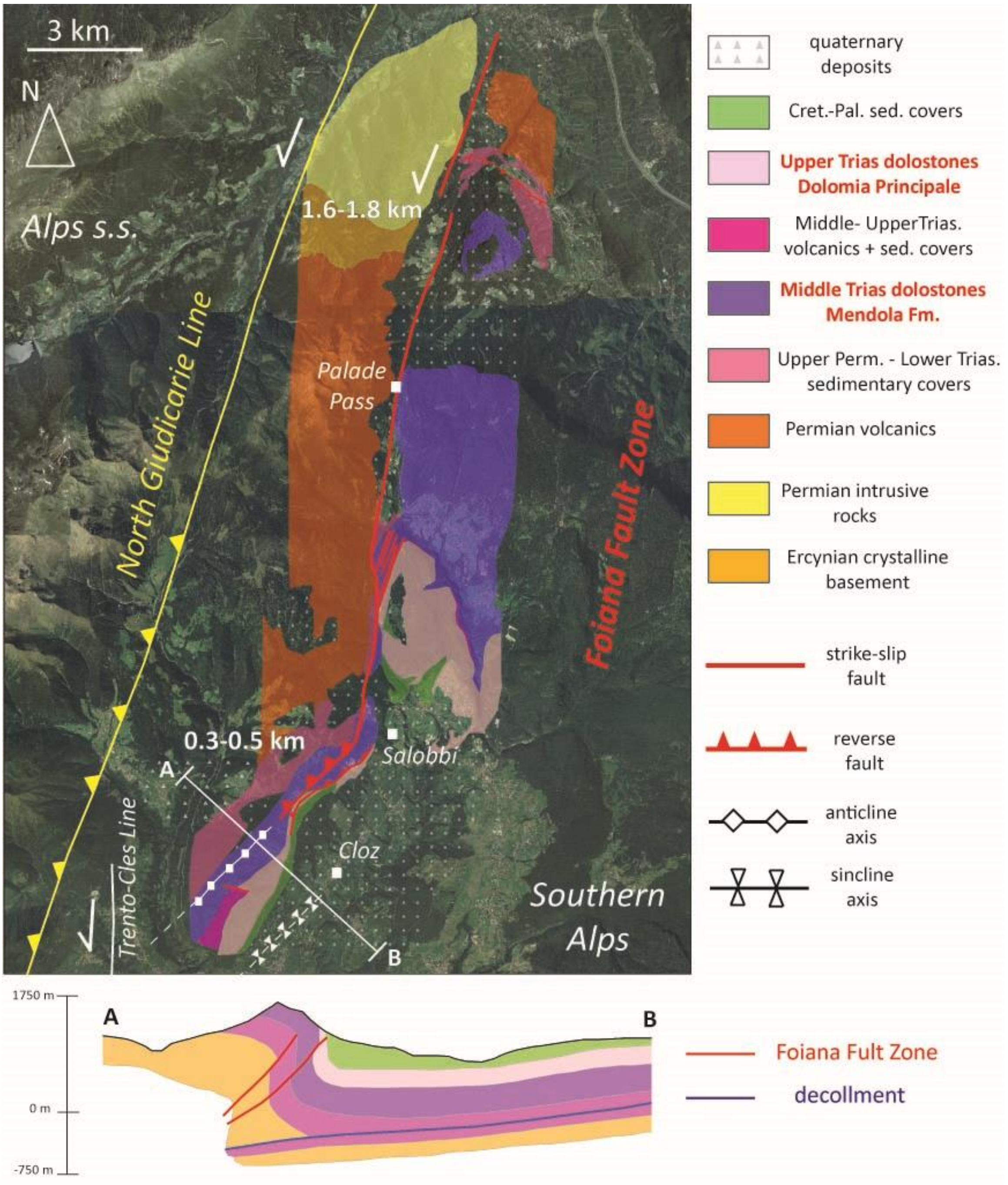

Fig.2 Regional-scale geometry and geology of the Foiana Fault Zone (FFZ). The geology is derived from recently published geological maps of the area (Tavola Fondo, Avanzini et al., 2001; Foglio Appiano, Bosellini et al., 2007) and is shown only within a ~ 6 km wide band adjacent to the FFZ. Three main segments of the FFZ can be identified based on changes in average fault zone strike and geology of the host rocks (see section 3.2.1. of main text for details). The cumulative vertical throw reduces along the strike from 1.6-1.8 km in the northern sector to 0.3-0.5 km in the southern sector where a restraining fault bend occurs. The restraining bend represents the southern termination of the FFZ, associated with a southeast-verging fault-propagation anticline (see the geological section A-B and the main text for further explanations). The inferred decollment shown on the cross section is from Tavola Fondo, Avanzini et al., 2002.

3.2.2 Kinematics and cumulative displacements along the FFZ

Regional-scale geological studies at the beginning of the twentieth century variably interpreted the Foiana Fault Zone as a thrust fault (Schwinner, 1915; Spitz, 1919; Dietzel, 1960) rather than a left-lateral strike-slip fault (Trevisan, 1939; De Sitter, 1956). More recent field-based structural investigations (Van Hilten, 1960; Cadrobbi, 1965; Prosser, 1998; Bosellini, 2007) all consider the Foiana Fault Zone as a sinistral transpressive fault whose kinematic is strongly related to that of the North Giudicarie Line. In particular, kinematic data collected by Prosser (2000) suggest that NNE-SSW to N-S oriented fault strands, characterizing the central and northern sectors of the FFZ, accommodated left-lateral transpressive to pure strike-slip movements in the footwall of the North Giudicarie Line. NE-SW oriented fault strands such as the southern sector of the FFZ accommodated nearly pure dip-slip reverse movements and were active as restraining fault bends. This kinematic framework is consistent with an overall SSE directed shortening direction, well recorded in the fault rock fabric of the North Giudicarie Line (Prosser, 1998) and associated with the main thrusting episode in the Southern Alps (i.e. the “Valsugana phase”, Castellarin et al., 1992) of middle-late Miocene age (about 13 Ma [Serravallian], by apatite fission track data; Zattin et al., 1997).

Cumulative displacements along the Foiana Fault Zone can only be roughly estimated from published geological maps (e.g. Foglio Appiano, Bosellini et al., 2007) and restored geological sections (Prosser, 1998). Estimated cumulative strike slip component along the FFZ is 4-5.5 km in the northern sector and 1.5-2 km in the central sector, progressively reducing to zero at the buried tip of the fault zone in the southern sector. In a similar manner, the cumulative vertical throw reduces along strike from 1.6-1.8 km in the central and northern sectors to 0.3-0.5 km in the southern sector. In the south, compressive deformation is interpreted to be transferred to a regional-scale decollement hosted within evaporitic rocks of early-middle Triassic age, resulting in a total shortening of ~ 5.5 km (Prosser, 1998) (Fig.2).

Based on these observations, the NE-SW striking southern sector of the FFZ represents the southern termination of the fault zone. Moreover, as will be discussed in section 3.8, the southern sector of the FFZ potentially represents a fault zone section exhumed from shallower depths in comparison to the central and northern sectors.

3.3 Studied outcrops

The northern sector of the Foiana Fault Zone (north of the Palade Pass) is largely hidden under Quaternary glacial deposits (Fig.2). Deformation related to the fault is observed only within lower Triassic cover rocks (marly limestones and siltstones of the Werfen Formation) in the footwall where they are folded and cut by small thrusts dipping to the south (Fig.2).

The central and southern sectors of the Foiana Fault Zone (south of the Palade Pass) contain several excellent exposures where the fault zone cuts through middle to upper Triassic dolostones (i.e. Mendola Formation and Dolomia Principale). Since fault rocks in these areas consist of heavily fragmented dolostones that are easily eroded, the fault zone typically outcrops within gullies or areas of badlands (Figs.2,3, 4).

The internal structure (i.e., geometry, thickness, fault kinematics, fault rock types and distributions) of the FFZ was described at three outcrops (outcrops A-C) where the fault cuts through dolomitic host rocks. The studied outcrops are distributed along a strike length of c. 6 km and are, from south to north (Fig.3):

1) Outcrop A, located to the west of the village of Carnalez, is within the NE-SW striking southern sector of the fault zone. Here the FFZ is exposed within several gullies over an area of ~ 0.5 km^2 on the eastern flank of the Ozol Mountain. The fault zone was described in detail within a selected area of ~ 0.06 km^2.
2) Outcrop B is located to the west of the village of Salobbi, within the N-S striking central fault zone sector. Here, the fault zone outcrops within an area of badlands topography ~ 0.05 km^2. The northern part of this outcrop is particularly well exposed along vertical walls artificially excavated for the construction of a road.

Outcrop C is located south of the Dòs de la Cièura, again within the N-S striking central sector. Here the fault zone is exposed in a ~ 40 m long section perpendicular to fault strike and over ~ 150 m parallel to fault strike.

3.4 Host rocks

In the studied outcrops, the FFZ is hosted within sedimentary dolostones belonging to two distinct lithostratigraphic units (Fig.3b): (i) the Mendola Formation and (ii) the Dolomia Principale (Tavola Fondo, Avanzini et al., 2001; Foglio Appiano, Bosellini et al., 2007).

The Mendola Formation (age: mid Triassic; thickness: 200-350 m) consists of light-grey dolostones displaying peritidal cycles up to 0.6-1 m thick with stromatolitic laminations and planar trails of fenestrae (Fig.4). Locally the presence of both pods of reddish marly dolostones and horizons of dark-grey marly dolostones up to tens of centimeters thick is reported (Bosellini et al., 2007).

The Dolomia Principale (age: late Triassic; thickness: 230-250 m) consists of light-grey massive dolostones with fenestrae and stromatolitic laminations organized in benches up to few meters thick.

The upper portion of the two units is characterized by brownish to reddish clay-rich interlayers up to a few centimeters thick and isolated paleokarst and paleosoil deposits with similar mineralogy (dolomite, kaolinite, anatase; from XRD analyses).

At the regional scale, and outside the FFZ, the Mendola Formation and the Dolomia Principale are locally separated by an unconformity surface or by middle to upper Triassic litostratigraphic units (i.e. Basaltic Vulcanites and Travenanzes Formation; see Bosellini et al., 2007 for further information) (Fig.3). Within the FFZ the contact between the Mendola Formation and the Dolomia Principale is everywhere represented by faults (Fig.3).

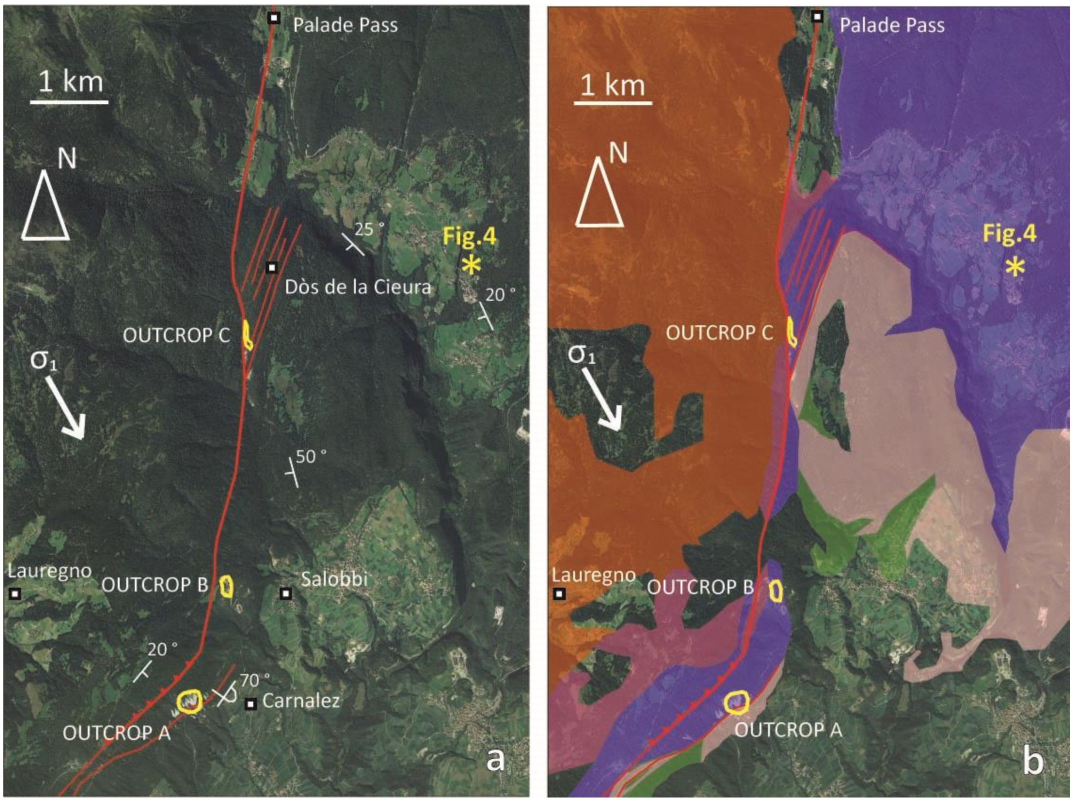

Fig.3 (previous page) Aerial view of the central and southern sectors of the FFZ, south of the Palade Pass. The studied outcrops (A, B and C) are outlined in yellow. All three outcrops are located within the footwall of the main trace (the eastern block) of the FFZ. The white arrow (σ_1) represents the middle-late Miocene (Serravallian) maximum compressive stress axis associated with the main thrusting episode of the Southern Alps and responsible for faulting along the FFZ. (a) White symbols and numbers represent the orientation of bedding at the regional scale around the FFZ. Around the northern and southern sector of the FFZ the bedding is generally dipping WSW with dip angles of 20°-50°. In the southern sector of the FFZ the bedding is affected by the presence of an anticline and is overturned in the footwall block. (b) The studied outcrops of the FFZ cut through sedimentary dolostones belonging to the Mendola Formation and the Dolomia Principale. The colors in the geological map refer to the legend in Fig.2. In this figure quaternary deposits are represented as empty areas.

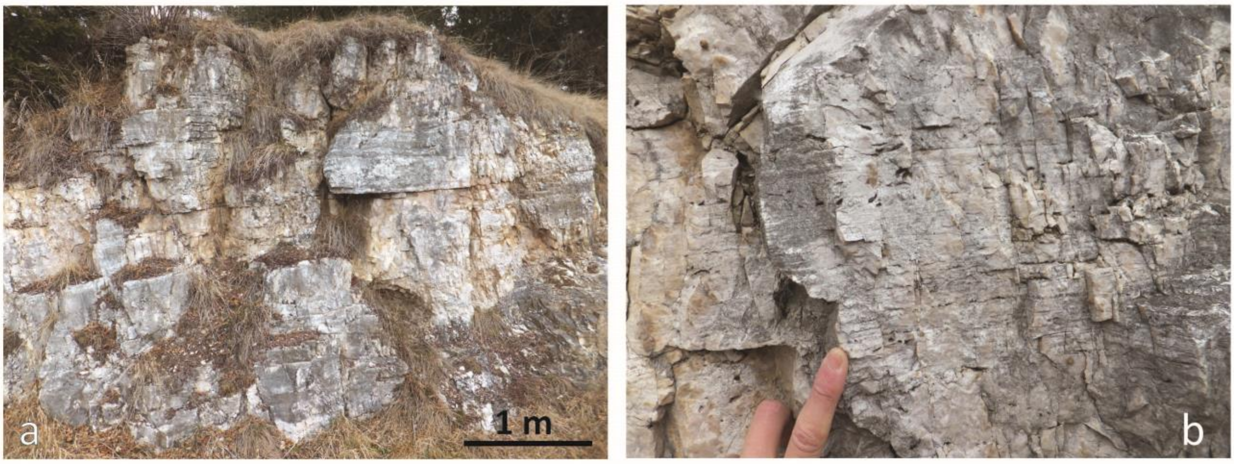

Fig.4 Host rock of the FFZ. (a) Sedimentary dolostones of the Mendola Formation cropping out ~ 3 km to the east of the FFZ (the location of the outcrop is reported in Fig.3). The dolostones are largely undeformed (not affected by joints or faults) and only the bedding surfaces are recognizable. (b) Detail of a typical facies of the Mendola Formation with stromatolitic laminations and planar trails of fenestrae.

3.5 Structural features of the FFZ

In this section I describe the main structural elements (e.g preexisting anisotropies, fragmented dolostones, faults) recognizable at the mesoscale within the Foiana Fault Zone.

3.5.1 Preexisting anisotropies

The undeformed dolomitic host rocks (i.e., Mendola Formation and Dolomia Principale; Fig.4) are rarely exposed in proximity to outcrops of the FFZ. Observations 2-3 km to the east of the FFZ show that the host rocks do not contain joints, veins or pressure solution seams related to previous regional scale deformation phases (Fig.4a). Furthermore, mapping of structural lineaments in the area around the FFZ (Aretusini, 2013) shows a pattern of lineaments consistent with sinistral transpressive activity along the FFZ. Therefore, the only preexisting anisotropies present within the dolomitic host rocks prior to faulting were bedding surfaces (including interbedding of dolomitic layers with more marly horizons).

3.5.2 Fractured and fragmented dolostones

The studied sections of the FFZ (outcrops A-C) cut through dolostones mainly belonging to the Mendola Formation. Only in the lower portion of outcrop A dolostones of the Dolomia Principale occur over ~ 60 m perpendicular to the strike of the FFZ. Other small outcrops (1-3 m in length) of the Dolomia Principale were found within the FFZ just to the east of the Dòs de la Cièura (outcrop C) (Fig.3). The distinction between the two litostratigraphic units within the FFZ was possible only by consulting published geological maps (Foglio Appiano, Bosellini et al., 2007), since the two dolostones are very similar in terms of both sedimentary facies (see section 3.4) and fracture damage characteristics.

In the studied outcrops (A-C) the Foiana Fault Zone typically consists of large volumes (up to hundreds of meters in thickness; see section 3.6 for details) of intensely fractured and fragmented dolostones cropping out within badlands areas or along partially eroded cliffs (Fig.5a). Fragmented dolostones are defined here as those affected by pervasive extensional fracturing resulting in the formation of rock fragments from a few centimeters down to a few millimeters in size (Fig.5). It is observed that larger fragments are typically delimited by three to five fracture sets and often show a prismatic shape. Most of the fractures are open, while sealed fractures and veins were only sporadically observed (Fig.5). The sets of fractures affecting the fragmented dolostones within the FFZ are not present outside of the fault zone (compare Fig.4b and Fig.5c).

The smaller (milimetric scale) rock fragments are angular and result from a dense network of extensional fractures (average fracture spacing < 1 cm). These highly fragmented dolostones are strongly affected by water and frost weathering that often produces a loose and thick (up to several centimeters) cover of regolith over the outcrops. This made the surveying (e.g., Fig. 9), sampling and study of the in-situ microstructures of these fault rocks particularly difficult.

One of the most remarkable characteristics of the fragmented dolostones within the FFZ is the absence of significant shear strain. This is documented by the preservation of primary sedimentary features in the host rocks, such as bedding surfaces, marly dolostone horizons and stromatolitic laminations, even in the most highly fragmented areas (Fig.5b).

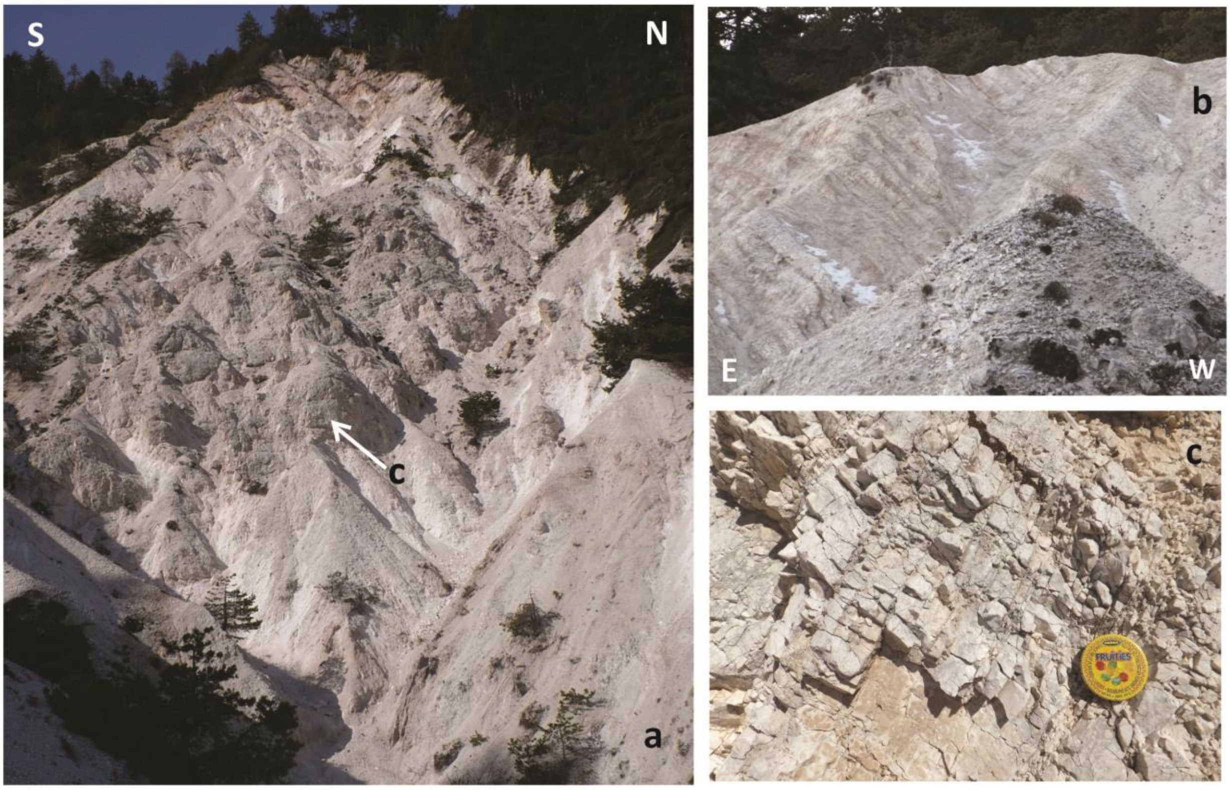

Fig.5 Exposures of fragmented dolostones within the FFZ at Outcrop A. (a) The fragmented dolostones are mainly exposed in heavily eroded gullies and areas of badland topography. A few of the more continuous faults can be seen cutting the fragmented dolostones (white arrows) (b) Intercalations of dark brown marly dolostone up to c. 20 cm thick can be seen lying parallel to bedding. The bedding is preserved even in highly fragmented areas, suggesting a lack of shear strain. (c) Detail of the fragmented dolostones affected by extensional fractures delimiting prismatic rock fragments ranging from a few centimers to a few millimeters in size. The object for scale is approximately 2 cm in diameter.

3.5.3 Discrete faults and fine-grained fault rock layers

The fragmented dolostones within the FFZ are locally cut by networks of discrete faults containing fine-grained fault rock layers up to a few centimeters thick (usually < 5 cm; Fig.6). Macroscopically, the fine-grained layers are whiter in color and more cohesive compared to the surrounding fragmented dolostones (Fig.6b,c). The fine-grained layers show a maximum clast size of a few millimeters and are frequently cut by discrete faults that can be divided in to two types: (i) polished fault surfaces that, under natural light, have a specular "mirror-like" finish (Fig.6; Chapter3; Fondriest et. al 2013), and (ii) minor faults with rough, poorly polished, surfaces cutting marly horizons and containing an enrichment of clay minerals.

(i) Mirror-like faults

A majority of the faults cutting through fragmented dolostones within the FFZ are characterized by polished, mirror-like surfaces. Many of these faults are lined by brownish flames of iron oxides and hydroxides (hematite and goethite; XRPD analyses, see chapter 3) that define elongate fault striae (Fig.6b). The mirror-like reflectance of these faults suggests that they are very smooth at length scales approaching the wavelength of visible light. In particular, according to the Rayleigh roughness criterion, a surface reflects specularly light if the root mean square (RMS) of surface roughness is smaller than 100 nm at wavelength $\lambda = 550$ nm (an average value for visible light) (Beckmann and Spizzichino, 1963; Siman-Tov et al., 2013). Nevertheless at length scales larger than 1 mm, the mirror-like faults of the FFZ often show: (i) slip surfaces (slickensides) with fault striae and surface grooves with amplitudes of up to a few millimeters, and (ii) curviplanar fault traces (i.e. intersection between fault and outcrop surface) (Fig.6a,c).

Considering that the traces of the mirror-like faults typically show lateral continuity in the range 1-20 m, and that measured displacements along the mirror-like faults are 0.04-0.5 m (see section 3.6 for details), I suggest that the mirror-like faults within the FFZ are relatively small structures with estimated total lengths of the order of a few hundred meters or less.

Fig.6 Fault networks cutting fragmented dolostones of the FFZ. (a) Two sub-parallel minor faults with sharp slip surfaces cutting through fragmented dolostones. (b) Detail of a “mirror-like” slip surface containing brownish flames of iron oxide and hydroxides (hematite and goethite from XRPD analyses) elongated along fault striae. (c) Two mirror-like faults cutting through fragmented dolostones. The faults contain up to a few centimeters of fine-grained whitish fault rock.

(ii) Minor faults cutting marly dolostones

Minor faults cutting the marly facies of the Mendola Formation are found within the FFZ. These are: (a) faults intersecting paleosoil or paleokarst deposits, and (b) faults with clay concentrations on the surface.

(a) In the first case the faults are associated with up to a few-centimeters of clay-rich gouge that is yellowish to reddish in color (XRPD mineralogy of the gouge: dolomite, kaolinite, anatase ± hematite). The clay-rich gouge is smeared along the fault surfaces and in some cases also along secondary fault branches. The gouge layer is typically surrounded by fragmented dolostones (Fig.7a).

(b) The second case is represented by small fault surfaces with lateral continuity of up to several tens of centimeters, lined by thin (less than 1 mm) reddish layers enriched in clays. I tentatively interpret them as fault surfaces affected by weathering or exploited as pressure-solution seams (Fig.7b).

Fig.7 Examples of minor faults cutting marly dolostones. (a) Fault cutting a paleosole deposit. The fault is associated with a reddish to yellow clay-rich gouge layer (XRPD mineralogy of the gouge: dolomite, kaolinite, anatase ± hematite). Some of the gouge is also smeared along secondary fractures. (b) Surface enriched in iron oxides-hydroxides and clays within fragmented dolostones. The surface, which seems to be affected by dissolution processes, cut through a fine-grained fault rock layer.

3.6 Structural map of the FFZ

In this section I describe how the internal structure of the Foiana Fault Zone changes along strike from south to north. To address this question I performed detailed structural mapping of the FFZ at three oucrops (A-C, see section 3.3) distributed along fault strike (Fig.3). Structural features including total fault zone thickness, spatial distribution and relative abundance of fault rocks, and fault orientations and dominant kinematics were measured within the FFZ and compared from one outcrop to the other.

3.6.1 Methodology

Mapping of the FFZ was performed along scan lines oriented parallel and perpendicular to the average strike of the FFZ. Scan lines were used in places where the fault zone crops out along small natural rock walls or artificial road cuts (e.g., outcrops B and C). The typical structural dataset collected along a scan line included: orientations of bedding, joints, faults; data of spacing and fault kinematics if available; systematic sampling of fault rocks. In the case of outcrop A, which contains large exposures of the FFZ within badlands and eroded gullies, the fault zone was described in detail within a selected area of ~ 0.06 km^2. Mapping of the fault zone in this area was performed using a high-resolution (1 pixel ~ 16 cm^2) geo-referenced photomosaic as a basemap, obtained by surveying the outcrop with an unmanned aerial vehicle (UAV[1]). Structural measurements were taken at stations evenly distributed across the outcrop and located using a handheld GPS (accuracy typically +/- 2 m). Information such as the GPS position of the structural stations, exposures of the various fault rocks and traces of faults were transferred and digitized (using ArcGIS software) on to the aerial photomosaic of the outcrop.

(1) The aerial survey with the unmanned aerial vehicle (UAV) was performed by the Chartagena Srl on 23th October 2011. A camera CANON EOS 550D was mounted on the UAV. 330 photographs were taken at altitudes in the range 1220-1320 m. 13 GPS control points were used to orthorectify the photographs and the construction of the photomosaic.

3.6.2 *Adopted fault rock classification scheme*

Deformed dolostones within the FFZ were distinguished in the field using a scheme based on fracture spacing and the average size of rock fragments (Fig.8):

1) Fractured dolostones, affected by two or three sets of joints. Based on the average spacing of the joint sets two subdivisions were recognized (Fig.8):
    - Moderately fractured dolostones: average joint spacing (s) larger than 1 m
    - Intensely fractured dolostones: average joint spacing (s) between 0.1 m and 1 m
2) Fragmented dolostones, affected by three to five joint sets having the effect of isolating individual prismatic rock fragments. Based on the average size of the rock fragments two subdivisions were recognized (Fig.8):
    - Poorly fragmented dolostones, with average rock fragment sizes (d) larger than 3 cm. The maximum rock fragment size is <10 cm.

- Highly fragmented dolostones, with average rock fragment sizes (d) between 0.1 cm and 3 cm. This type of fault rock often outcrops within small erosive gullies and is crosscut by the discrete faults described in section 3.5.3.

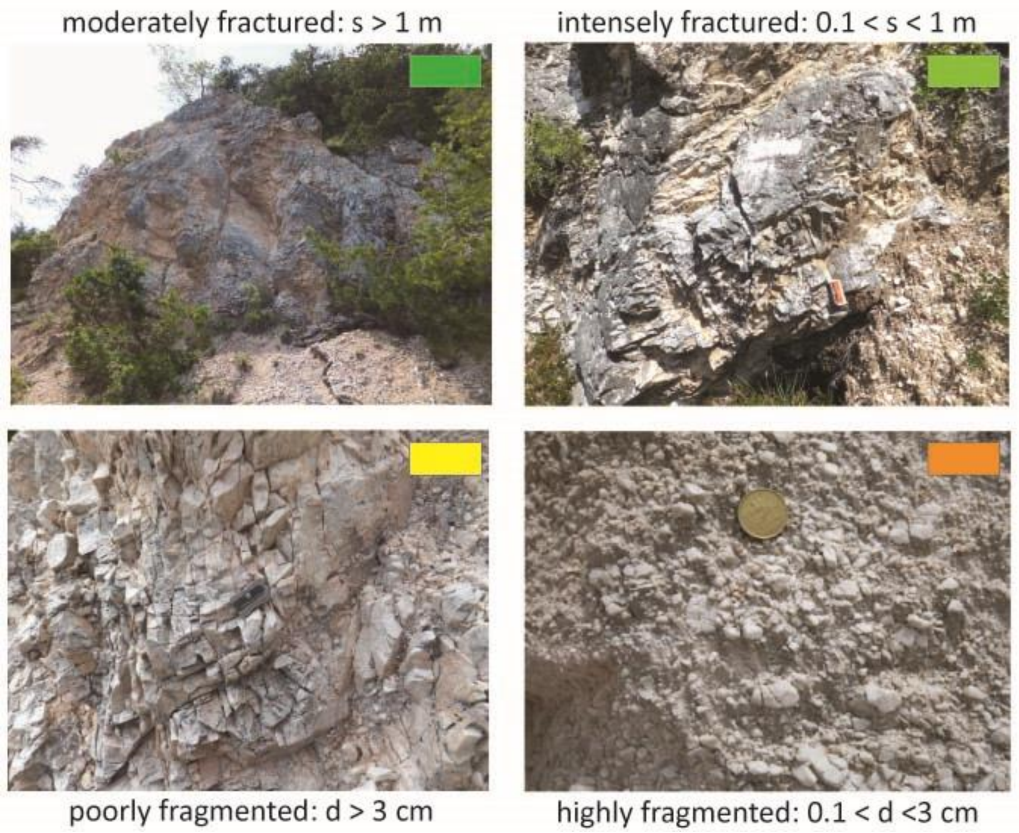

Fig.8 Fault rock classification scheme adopted to map the FFZ. Moderately fractured dolostone: dark green. Intensely fractured dolostone: light green. Poorly fragmented dolostone: yellow. Highly fragmented dolostone: orange.

3.6.3 Determination of the fault "rank"

The master fault of the FFZ is never outcropping. Thus the faults measured in the field are all meso-scale structures characterized by a lateral continuity of few meters. In the following text (sections 3.6.4-3.6.6) a different "rank" is attributed to the measured fault sets, which are distinguished between "main" and "secondary" faults. The main fault set is the most persistent in the field and it is parallel even to the average strike of the FFZ or to structural lineaments recognizable at the kilometer scale in aerial images and geological maps. In the rose diagrams showing the distribution of the fault strikes (see Figs. 9, 11, 12) the main fault set is the set with the highest frequency, whereas the secondary fault sets are those with relative lower frequency.

3.6.4 Outcrop A

Outcrop A is located to the west of the village of Carnalez in the NE-SW striking southern sector of the FFZ. With respect to the main trace of the FFZ identified on aerial photographs and published geological maps, outcrop A is in the footwall block and is representative of deformation occurring within a restraining bend close to the southern tip of the fault zone (Fig.3).

Fig.9 shows a structural map and two cross sections of outcrop A. The mapped area is ~ 0.06 km^2 and covers two main areas of badlands. Elevations range from ~ 1250 m in the NW of the mapped area to ~ 1100 m in the SE. Fault rocks are typically well exposed along ridges isolated by the effect of water runoff. ENE to NE trending valleys and incisions, easily recognizable on the aerial image, developed parallel to the main set of faults (marked as red lines in Figs.9a).

The main fault set strikes ENE-WSW to NE-SW (from N45° to N75°) with dip angles in the range 40°-80° NNW to NW (Fig.9e,f). The dominant fault kinematics, based on the measurement of fault surface lineations and grooves (Fig.9g) and the observation of offset structural markers (e.g. marly horizons), are dip-slip reverse with a slight left-lateral component (Fig.9g). The orientation of this fault set is similar to that of the preserved sedimentary bedding which is vertical to locally overturned in this area due to presence of the anticline (Figs.9h,10). Many of the faults within this outcrop exploited the bedding as a preexisting anisotropy.

The exposed fault zone at outcrop A is more than 300 m thick (Fig.10b) and is dominated by poorly and highly fragmented dolostones (i.e., yellow and orange areas in Figs.9a). Isolated layers and pods of both moderately and intensely fractured dolostones up to a few meters thick (i.e., dark and light green areas in Figs.9a) occur in the NW and SE of the outcrop . Two cross sections (A,B in Fig.9b,c) running almost perpendicular to the mean strike of the main fault set show the presence of 10-40 m thick bands of highly-fragmented dolostones alternating with up to 10 m thick bands and lenses of poorly-fragmented dolostones. The boundaries between highly-fragmented and poorly-fragmented dolostones are mainly discrete faults, suggesting a fault zone structure characterized by alternating sub-parallel fault rock bands with different intensities of fragmentation. Measurements of fault rock thickness along the two cross sections (A,B; Fig.9d) indicate that the FFZ at outcrop A mainly consists of highly-fragmented dolostones.

The orientation of the fracture sets was measured within fractured and poorly-fragmented dolostones. Three to five sets of joints were recognized (Fig.9i). The three most frequent joint sets are (i) NNE-SSW striking subvertical joints, (ii) ENE-WSW to NE-SW striking subvertical joints, and (iii) ENE-WSW to NE-SW striking joints broadly parallel to the main fault set (i.e., dip angles 40°-80°).

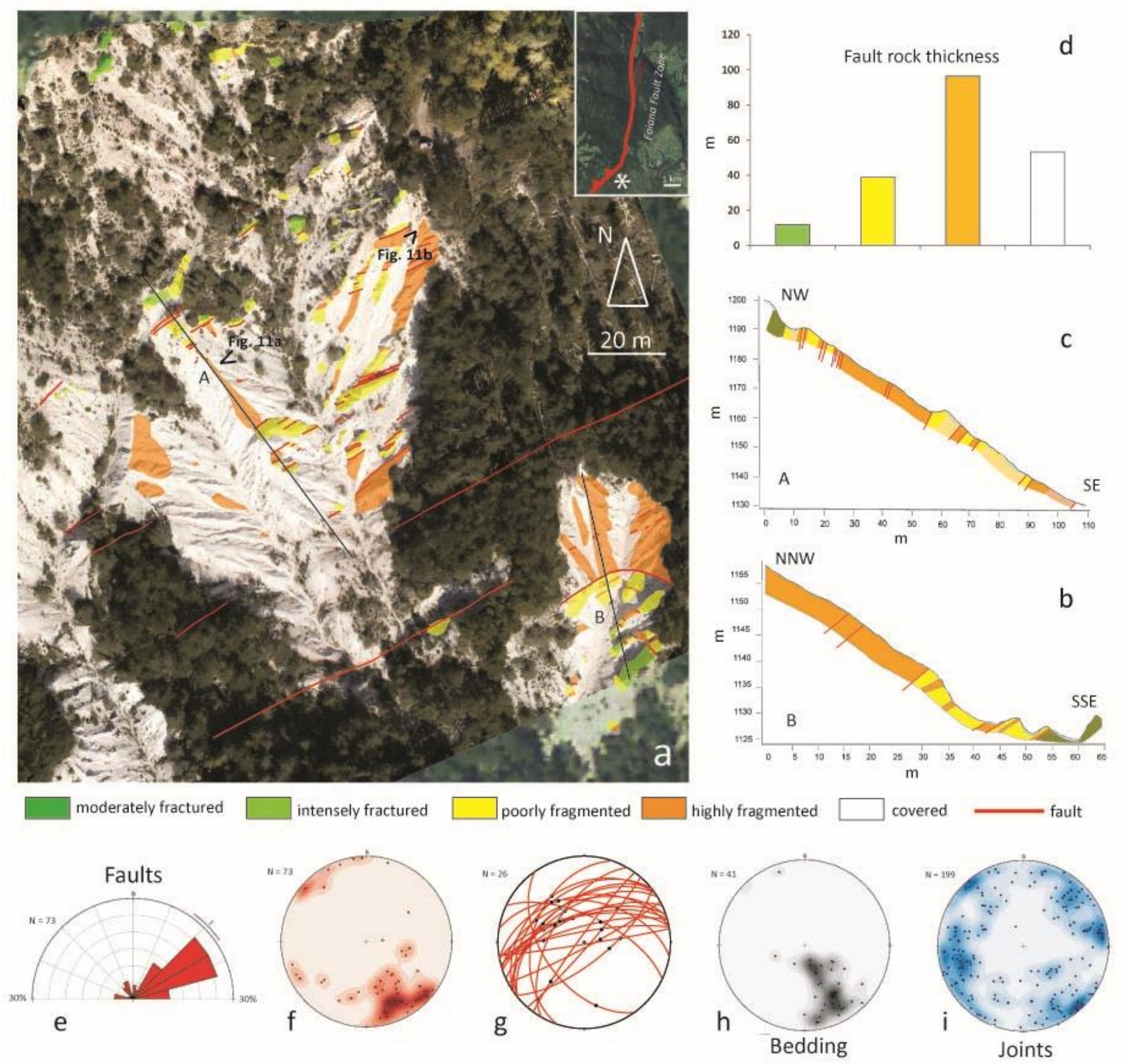

Fig.9 Fault rock distribution based on structural mapping at outcrop A. (a) Structural map of outcrop A within an area of 0.06 km^2 (the location of the outcrop along the FFZ is shown in the inset). The aerial image used as a basemap is a high-resolution (1 pixel ~ 16 cm^2) geo-referenced photomosaic obtained by surveying the outcrop with an unmanned aerial vehicle (UAV). Main fault traces are represented as red lines. The areas that are not colored on the map are covered in surface regolith. Black lines labeled as A and B are the traces of the two cross sections shown in parts b and c. Locations where photographs of Fig.13a,b were taken are indicated. (b,c) Cross sections oriented almost perpendicular to the mean FFZ strike. The fault zone consists of sub-parallel bands of both poorly and highly fragmented dolostones delimited by faults. Note that in the cross sections the distribution of poorly and highly fragmented dolostones has been inferred in areas covered by regolith. (d) Histogram of fault rock thickness measured along sections A and B. The FFZ at outcrop A consists mainly of highly fragmented dolostones. (e) Rose diagram of the strike of faults. The main (i.e., more frequent) strike of the faults is ENE-WSW with a scattering of ~ 30° (from N45° to N75°). (f) Stereoplot of poles of faults. Dip angles are in the range 40°-85° NW. (g) Stereoplot of sub-population of faults (great circles) for which fault lineations (black dots) could be measured. Fault lineations indicate mainly dip-slip movements, with the sense of slip determined as reverse from offset structural markers. (h) Stereoplot of poles to bedding. The orientation of the bedding is sub-parallel to the faults. (i) Stereoplot of poles to fractures. Several fracture sets are recognized, and described in section 3.6.3. (All stereographic projections in the figure are equal area, lower hemisphere).

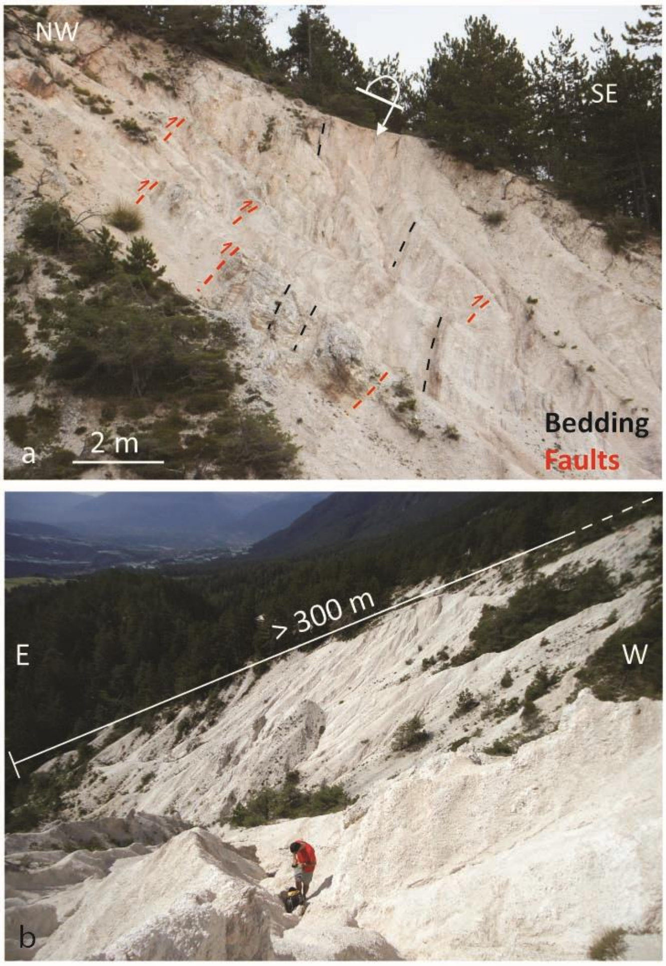

Fig.10 (a) Photograph of the eastern flank of outcrop A. The bedding (outlined by black dashed lines in the figure), recognizable due to the presence of grey layers of marly dolostones, is subvertical to overturned in this area. Many of the faults (outlined by red dashed lines in the figure) exploit the bedding surfaces. (b) Photograph of the eastern part of outcrop A. The exposed fault zone contains >300 m of fractured and fragmented dolostones.

3.6.5 Outcrop B

Outcrop B is located in the N-S striking central sector of the FFZ, c. 2 km to the north of the bend between the central and southern sectors (Fig.3). The fault zone crops out within ~ N-S oriented roadcuts ~ 120 m in length. The orientation of the roadcuts, approximately parallel to the mean strike of the FFZ in this area, was not suited to map the spatial arrangement of fault rocks within the fault zone. However, the presence of recently cut vertical rock walls up to 6 m high with almost no debris accumulation offered clear exposures of the fault networks within the FFZ (Fig.11a). The fault zone here consists of poorly to highly fragmented dolostones. Although the total thickness of the FFZ in this area could not be measured, the distribution of badlands topography and the orientation of the main fault sets at this outcrop (see below) suggest a total thickness of <200 m.

Measured faults show quite dispersed attitudes (Fig.11a,d-f) but a main (more frequent) conjugate set with faults striking ENE-WSW and dipping moderately to steeply (dip angles 40°-85°) NW or SE is recognized (11d). The dominant kinematics of this fault set is dip-slip with reverse throws in the range of 0.04-0.5 m determined from offset structural markers (bedding surfaces and horizons of marly dolostone, e.g. Fig.11c,f). Less frequent (secondary) fault sets strike ~ E-W and ~ N-S (in this case the low frequency is likely due to orientation of the studied section). Bedding in this area dips moderately to the west with dip angles of 40°-50° (Fig.11g). The dominant set of faults does not exploit the preexisting bedding as observed for outcrop A. No clear cross-cutting relationships were observed between the main and secondary fault sets. Many of the faults at this outcrop, belonging both to the main fault set and to the secondary sets, are characterized by mirror-like slip surfaces (Fig 11b).

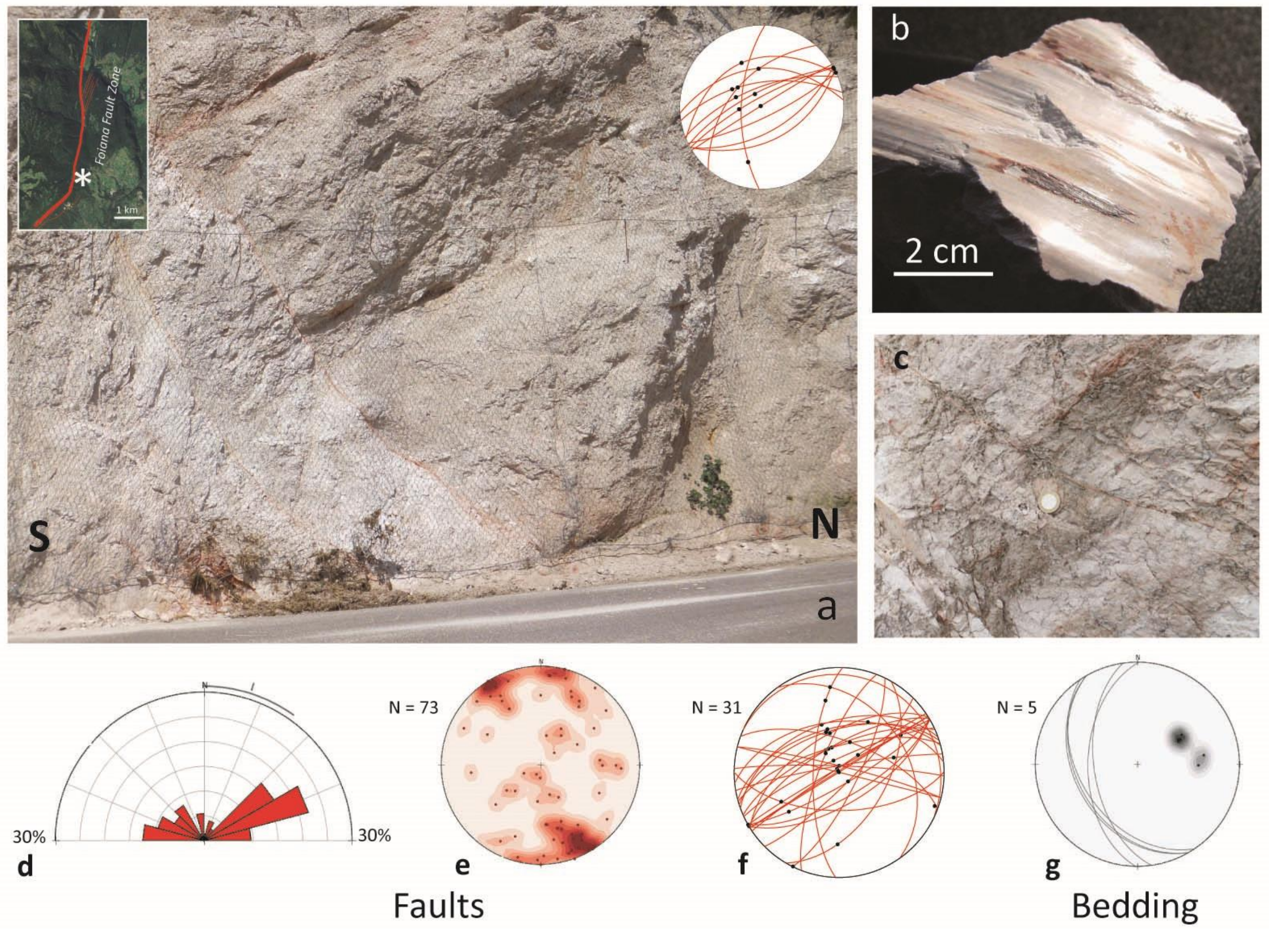

Fig.11 Characteristics of the FFZ at Outcrop B. (a) A typical exposure of the FFZ within outcrop B along the road cut. The fault zone consists of fragmented dolostones cut by dense networks of faults. Many of the faults are characterized by light-reflective mirror-like slip surfaces. Stereoplot in the upper right corner shows orientation of mirror-like slip surfaces (great circles) and surface lineations (black dots) at this roadcut. Slip surfaces have predominantly ENE-WSW strikes, dip-angles of 40°–85° NW or SE, and reverse dip-slip kinematics. Inset in the upper left corner shows the location of outcrop B along the FFZ. (b) Photograph of a mirror-like slip surface under natural light. (c) Mirror-like fault cutting a marly dolostone horizon with a reverse separation of c. 5 cm. (d) Rose diagram of the strike of faults. most of the faults strike ENE-WSW (from N60° to N75°) The fault show scattered orinetations. (e) Stereoplot of poles to faults. The faults are quite variable in dip in the range 40°-85°. (f) Stereoplot of sub-population of faults (great circles) for which fault lineations (black dots) could be measured. (g) Stereoplot of poles to bedding. The bedding at this outcrop is not exploited by the main set of faults. (All stereographic projections in the figure are equal area, lower emisphere).

3.6.6 Oucrop C

Outcrop C is located at Dòs de la Cièura, a 2 km long ridge characterized by the presence of regularly spaced, sub-parallel NNE-SSW trending lineaments, interpreted as strands of the FFZ (see Fig.3). The main trace of the FFZ does not outcrop in the area, since it runs along a valley filled by alluvial deposits. The FFZ in this area dips regionally to the west at an angle of ~ 70° (see Appiano geological map) and puts in contact Permian volcanics in the hangingwall against Triassic dolostones of the Mendola Formation in the footwall (Fig.3). Cumulative vertical throw in this sector of the FFZ is 1.6-1.8 km (vertical separation calculated from Appiano geological map, Bosellini et al., 2007). The studied outcrops comprise different sections of the FFZ footwall block over ~ 40 m distance perpendicular to the mean fault strike and ~ 150 m distance parallel to the mean fault strike.

Fig.13a shows a structural map of the FFZ constructed along a cross section perpendicular to the regional fault strike. In this area, the main set of faults (red in Fig.12a) strikes NNE-SSW with dips ranging from subvertical to steeply (dip angles > 75°) east dipping. This main fault set is quite clustered in orientation (strikes vary within a range of 15°) and locally has a regular fault spacing of 2-3 m (e.g. see scan line 4 in Fig.12a). The main fault set is broadly parallel to the series of lineaments (lateral continuity up to few kilometers) recognized from remote sensing on the Dòs de la Cièura ridge. A further two secondary (less frequent) fault sets are recognized, one ~ E-W striking sub-vertical and another ~ WNW-ESE striking and dipping 50°-60° to the SW (Fig.12). Some of the secondary faults have polished and mirror-like slip surfaces. Fault striae of the secondary fault sets indicate oblique- to pure strike slip kinematics (Fig.12d).

Approaching the main trace of the FFZ bedding in the dolostones is progressively rotated towards parallelism with the FFZ (i.e., rotation in dip from N 205° to N 290° and in dip angles from 50° to 80°, see Fig.13). Bedding surfaces are often reactivated by N-S striking faults with sinistral transpressive kinematics and characterized by polished to mirror-like slip surfaces (Fig.13). The few kinematic data available for the NNE-SSW striking main set of faults suggest sinistral oblique- to strike-slip kinematics.

In sections perpendicular to the regional strike of the FFZ the exposed fault zone is > 40 m thick and consists mainly of poorly fragmented dolostones (yellow areas in Fig.12a,f). These are cut by sub-vertical, NNE-SSW striking faults associated with bands of highly fragmented dolostones (orange areas in Fig.12a) up to tens of centimeters thick.. Since the main trace of the FFZ and the exposed cross section are separated by ~ 50 m of no exposure, the thickness of the FFZ is estimated to be around 100 m in this area (see aerial photograph in Fig. 13a).

Fractures were measured within poorly-fragmented dolostones. Three to five sets of fractures were recognized (Fig.12e). The three most frequent joint sets are (i) NNE-SSW striking subvertical joints (parallel to the main fault set), (ii) E-W striking subvertical joints, and (iii) WNW-ESE striking joints dipping steeply to the south (dip angles 50°-60°).

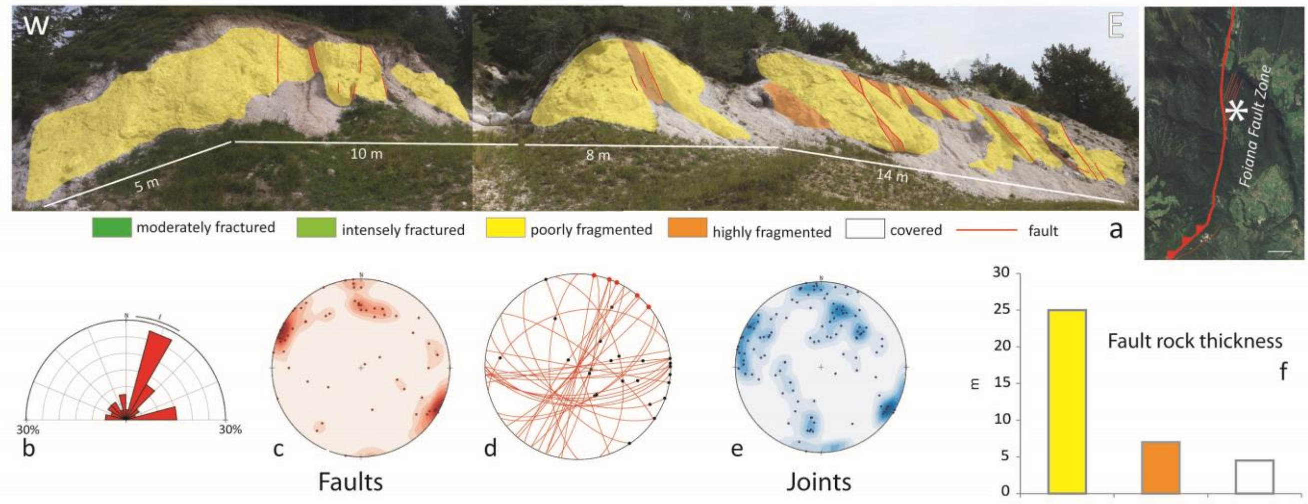

Fig.12 Structural map and faulting within the FFZ at outcrop C. (a) Structural map of outcrop C in a section almost perpendicular to mean FFZ strike (the location of the outcrop along the FFZ is shown in the aerial image on the right). Outcropping fault rocks are represented with the same colors defined in Fig.8, fault traces are represented as red lines, and areas without color are covered by regolith. (b) Rose diagram of the strike of the faults. The strike of the faults are clustered in two directions: NNW-SSW and ~E-W. The NNW-SSE direction is related to the main set of faults, while the ~E-W direction is related to a set of secondary faults. (c) Stereoplot of poles to faults. The faults show only high dip angles > 75°. (d) Stereoplot of a sub-population of faults (great circles) for which fault lineations (dots) could be measured. Faults of the main set (NNW-SSE oriented) are undersampled because they usually crop out within erosive gullies where the fault surfaces are not preserved. Black dots are measured fault lineations, red dots show inferred left-lateral strike-slip kinematics along the NNW-SSE oriented fault set but a small dip-slip component is not excluded. (e) Stereoplot of poles to fractures. See the main text for description of the data. (f) Histogram of fault rock thickness measured along the scan lines in Fig.12a. The FFZ at outcrop C mainly consists of poorly fragmented dolostones. (All stereographic projections in the figure are equal area, lower emisphere).

3.6.7 Summary

In all of the studied outcrops, the FFZ is dominated by fractured or fragmented dolostones. Preexisting structures such as bedding surfaces are frequently reactivated by faults, many of which are characterized by polished, mirror-like slip surfaces. However, there are notable differences in the internal structure of the FFZ moving along fault strike from south (outcrop A) to north (outcrop C). The main differences as summarized in Table 1 are as follows:

1) The total thickness of the FFZ decreases from south to north. This is consistent with regional geological maps (Bosellini et al., 2007) that mark the poorly-exposed area between outcrops A and B as a "cataclastic zone" up to several hundred meters wide.

2) The proportion of highly fragmented dolostones with respect to poorly fragmented dolostones decreases moving from south to north.
3) The attitudes of the faults (i.e. strike and dip angles) are scattered in outcrop A, largely scattered in outcrop B, and clustered in outcrop C where a clear separation between main and secondary fault sets occurs. A general decrease in the scattering of the fault attitudes (in particular of the main fault set) is recognizable moving from south (outcrop A and B) to north.
4) Faults in the south are dominantly dip-slip reverse faults whereas in the north strike-slip to oblique-slip faults become more common.

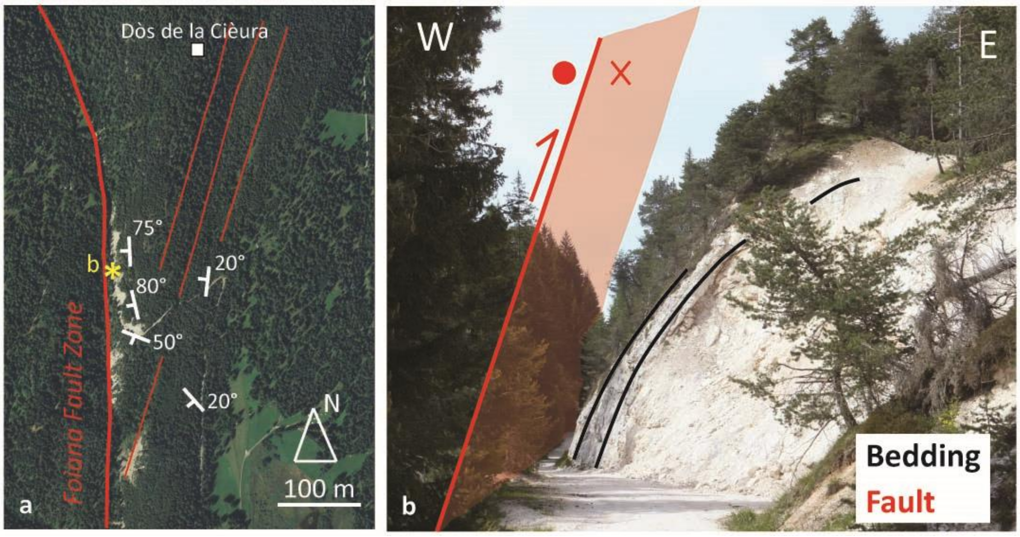

Fig.13 Rotation of bedding towards the main trace of the FFZ at outcrop c. (a) Aerial view of the Dòs de la Cièura area (outcrop C). The thick red line represents the main trace of the FFZ. The thin red lines represent the stack of NNE-SSW-trending lineaments affecting the Dòs de la Cièura ridge. White symbols and numbers refer to the orientation of bedding which is rotated approaching the FFZ. (b) Detail of the bedding dragged along the main trace of the FFZ in the footwall block. The location where the photograph is taken is reported in Fig.13a.

FFZ	Outcrop A	Outcrop B	Outcrop C
Fault zone thickness	> 300 m	> 200 m	> 100 m
Fault rock proportion	highly fragmented >> poorly fragmented		low fragmented >> poorly fragmented
Average FFZ strike	NE-SW	N-S	N-S
Strike of the main fault set	ENE-WSW to NE-SW	ENE-WSW to NE-SW, scattered	NNE-SSW
Dominat fault kinematics	dip-slip reverse	dip-slip reverse	left-lateral oblique- to strike-slip
Bedding reactivation	Yes, by the main fault set	Yes, by a secondary fault set	Yes, by the main fault set
Mirror-like faults	Yes	Yes	Yes

Table 1

3.7 Microstructure of the fine-grained layers adjacent to mirror-like faults

The Foiana Fault Zone mainly consists of fragmented dolostones affected by pervasive fracturing, cut by discrete faults with polished to mirror-like (i.e. light reflective) slip surfaces. Mirror-like faults are typically associated with fine-grained layers up to a few-centimeters thick that are whiter and more cohesive in nature with respect to the surrounding fragmented dolostones (section 3.5.1).

Oriented samples (n=70) of polished and mirror-like faults and associated fine-grained layers were systematically collected during mapping of the FFZ. Since a majority of the faults cut through highly friable rocks (i.e., poorly to highly fragmented dolostones, see Figs.9,11,12) the samples were initially preserved with medium-viscosity epoxy resin directly in the field. From these, some samples (N=42) were further consolidated with low-viscosity epoxy resin at the Department of Geosciences in Padova and cut to produce polished thin sections oriented perpendicular to the fault surfaces and parallel to fault surface lineations. Microstructural investigation of the fine-grained rock layers was performed using optical microscopy (OM, Department of Geosciences, Padova) and scanning electron microscopy using both a thermionic emitter (SEM, Department of Geosciences, Padova) and field emitter (FE-SEM, INGV, Rome). Several thin sections were observed under optical microscopy cathodoluminescence (OM-CL, Department of Geosciences, Padova) to reveal further details of the microstructure of the dolostones and infrequent veins. The mineralogical composition of the dolostones was determined by semi-quantitative X-ray powder diffraction (XRPD, Department of Geosciences, Padova).

Fragmented dolostones below the fine-grained layers are affected by an extensional fracture pattern with no preferential orientation. Only in some cases Riedel-type fractures accommodating small shear displacements (up to few millimeters) are observed (Fig.14).

The fine-grained layers cut by polished and mirror-like slip surfaces are typically a few millimeters to a few centimeters (usually < 5 cm) thick and sometimes have wedge-like or irregular shapes (Figs.6, 14,15). These fault rocks (XRPD mineralogy: 100% dolomite) have a maximum clast size of a few millimeters, significantly smaller than the maximum dimension of the rock fragments in the surrounding fragmented dolostones (i.e., up to few centimeters). The clasts within the fine-grained layers are typically sub-angular and are surrounded, at the optical microscope scale, by dark brown to black matrix materials, containing dolostone clasts <10 μm in size (Figs. 14,15). The most striking characteristic of the fine-grained layers is the absence of significant shear strain even at distances of only a few tens to hundreds of micrometers from the mirror-like fault surfaces.

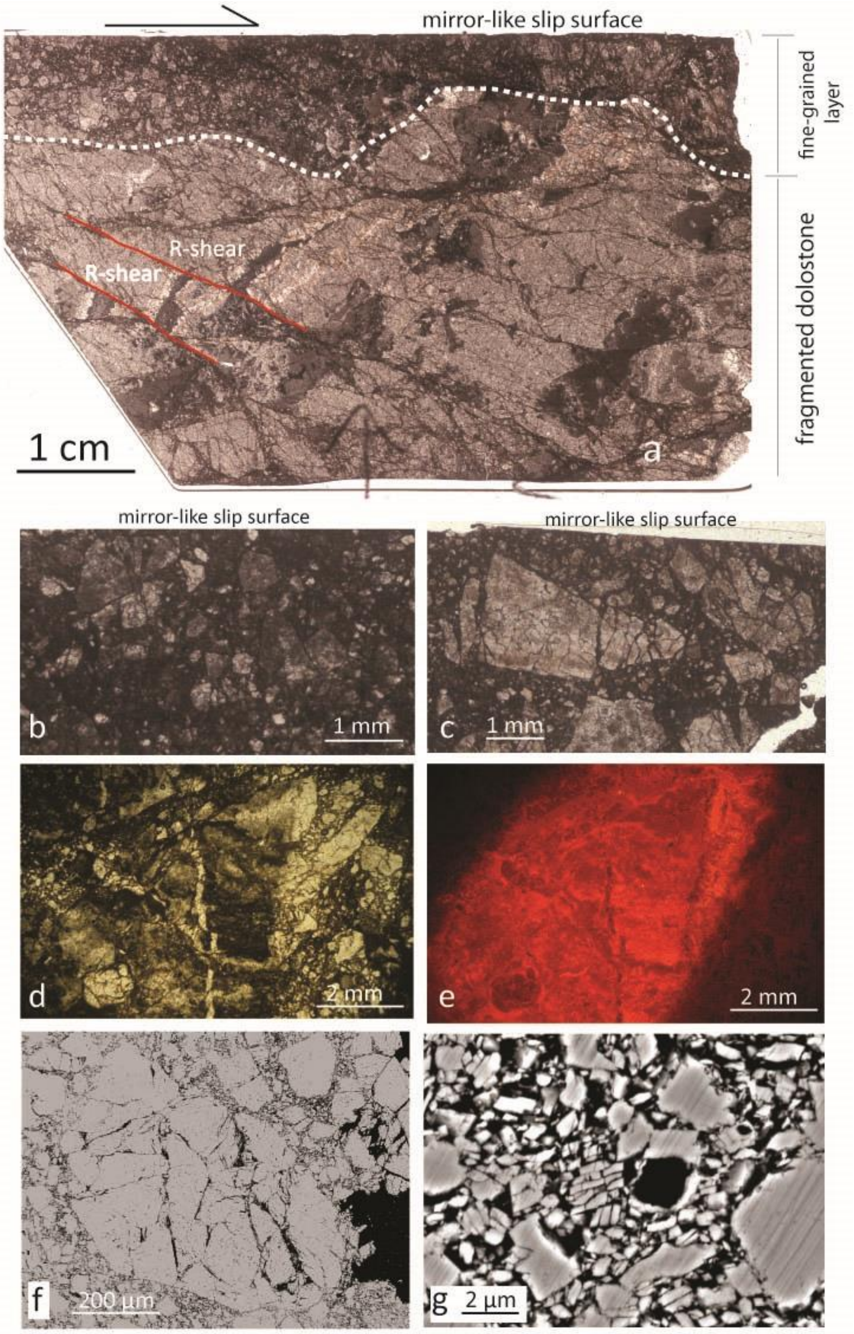

Fig.14 Microstructures of the fine-grained rock layers adjacent to mirror-like faults. (a) High-resolution thin section scan (plane polarized light) of the fault rock material adjacent to a mirror-like slip surface. Just below the mirror-like slip surface an up to 2 cm thick fine-grained rock layer (delimited at the base by the white dashed line) is recognizable. The layer consists of dolostone clasts up to few millimeters in size within a fine-grained matrix. The fault rock below is a fragmented dolostone dominated by extensional fracturing. Some Riedel-shear fractures with small (few millimeters) displacements are also recognizable. Images from (b) to (g) show characteristic microstructures within the fine-grained layer. (b-c) Optical microscope (OM) images (plane polarized light). The fault rock is dominated by extensional fracturing also in proximity to the mirror-like slip surfaces. This is demonstrated by the presence of exploded clasts, often affected by radial fractures. (d-e) OM and OM-CL images (plane polarized light). OM image shows a fragment of algae affected by intense extensional fracturing. OM-CL image shows a series of dark and light rims within the algae which are in continuity and not affected by shear strain. (f) Exploded clast a few hundred micrometers in size. (g) Pervasive extensional fracturing within the matrix down to sub-micrometer scale.

According to the classification scheme of Sibson (1977), the fine-grained fault rock layers can be defined as cataclastites or ultracataclasites. However, many of the fine-grained layers contain a a number of peculiar microstructures :

1) "exploded clasts" affected by radial fracture patterns. In these types of clast, each individual fragment lies adjacent to its counterpart indicating no significant shearing (see OM and OM-CL images) (Fig.14b-f).
2) pervasive and variably oriented extensional fracturing and splitting of clasts down to the micrometer scale (Fig.14g).
3) the presence of elongate chains of split clasts (possibly resulting from the development of force chains in the fine-grained gouge layers) oriented at 60°-80° to the fault surfaces (Fig.15c).
4) relatively large (>100 µm) dolostone clasts that are sharply truncated by the mirror-like slip surfaces (e.g. Fig.15b). This suggests extreme shear strain localization along the slip surfaces.

The matrix of the fine-grained layers contains sub-micrometer sized bridges of dolomite cement along grain boundaries and in pore spaces (Fig.15d). In some cases, moving toward the mirror-like fault surfaces, a general decrease of porosity is observed (e.g. matrix in Fig.15b), with the development of fabrics suggesting compaction processes (e.g., rounded clasts that seem to derive by matrix compaction, indentation structures). Similar microstructures are frequently reported in both natural and experimentally deformed porous granular rocks (Tondi et al., 2006; Cilona et al., 2012).

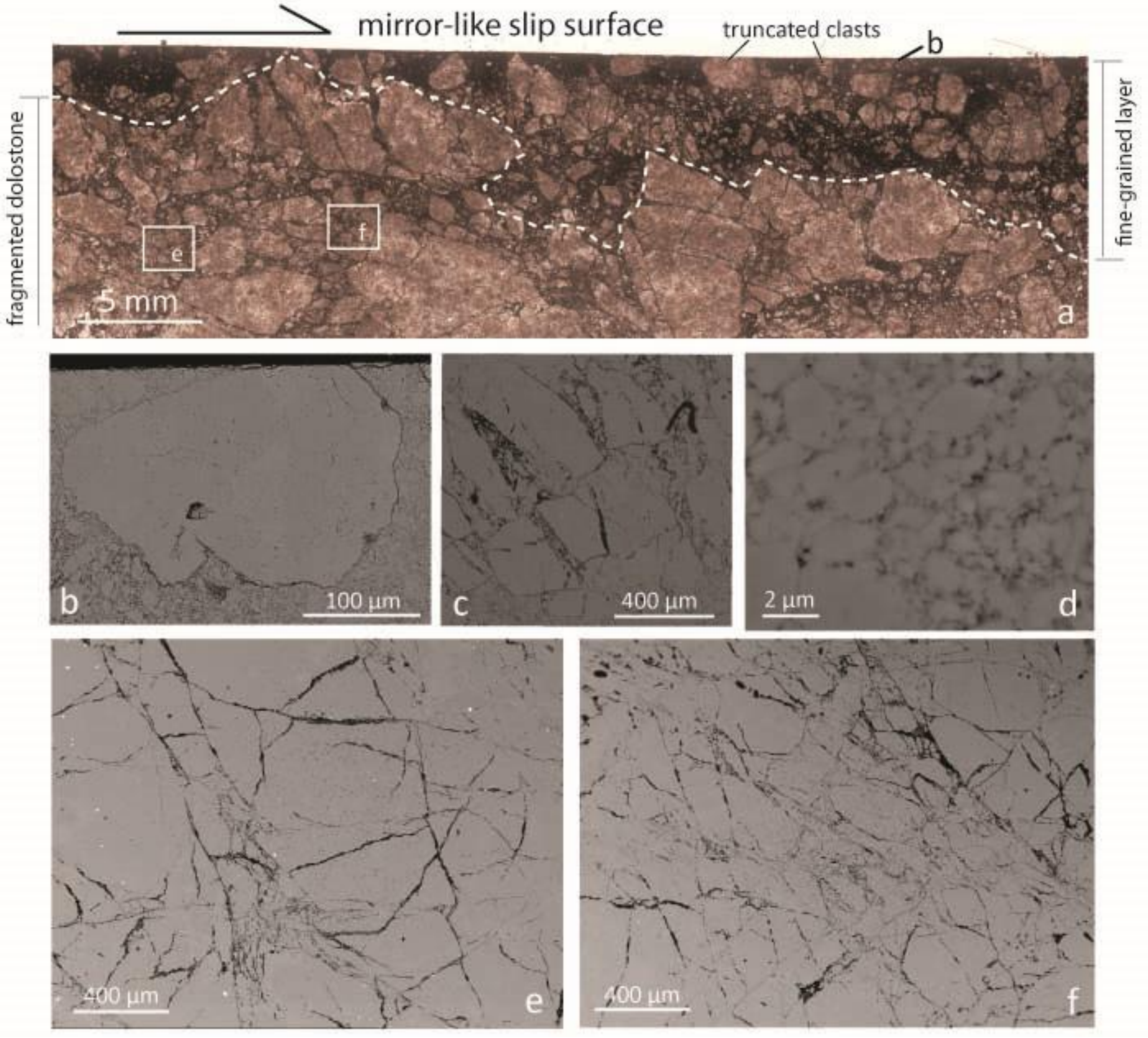

Fig.15 Microstructure and fracture patters adjacent to mirror-like faults. (a) High-resolution thin section scan of the fault rock material adjacent to a mirror-like slip surface. A fine-grained rock layer cut by the mirror-like slip surface and fragmented dolostones below are recognizable. Images from (b) to (d) show characteristic microstructures within the fine-grained layer. Images (e) and (f) describe the fracture pattern of the fragmented dolostones. (b) Dolostone clast sharply truncated by the mirror-like slip surface. Other truncated clasts are indicated in Fig.15a. (c) Chains of splitclasts lying at a high angle to the slip surface (the slip surface is parallel to the upper border of the image). (d) Detail of the matrix next to the mirror-like slip surface. The clasts are rounded and indented suggesting compaction processes. The pores within the clasts are partially filled by sub-micrometer grains of dolomite. (e-f) Fragmented dolostones are affected by an extensional fracture pattern with no preferential orientation

3.8 Discussion

3.8.1 In situ-shattered dolostones within the FFZ

The occurrence of large exposures of fragmented dolostones along the FFZ was initially reported in regional-scale studies of the 1960s (e.g. Van Hilten, 1960; Cadrobbi, 1967). Van Hilten (1960) interpreted the intense fragmentation of the dolostones at the southern termination of the FFZ as the result of a large gravitational collapse (i.e. rockslide) originating on the slopes of the Ozol Mountain to the west. He termed the fragmented dolostones within this rockslide "megabreccias" (italian: "*megabrecce*"). Cadrobbi (1967) mapped several bodies of fragmented dolostones along the FFZ and interpreted them as fault rocks. He named such fault rocks "cataclastic dolostones" (italian: *dolomie cataclastiche*) and pointed out that primary sedimentary features in the dolostones, such as bedding surfaces, were surprisingly well preserved in the fault rocks despite the fragmentation.

In this study, field and microstructural observations within the FFZ showed that the main fault rocks are fractured and fragmented dolostones (accounting for almost the entire volume of the exposed FFZ; Figs.9,11) associated with fine-grained fault gouge layers that are cut by polished and mirror-like slip surfaces. Fragmentation resulted from pervasive fracturing, producing individual rock fragments ranging in size from a few millimeters to a few centimeters. Fractures within the fragmented dolostones are everywhere dominated by one set lying sub-parallel to the main set of faults, and one set almost perpendicular to the main set of faults. This fracture pattern was documented in both the southern and central sectors of the FFZ, which have different orientations (Figs.9, 12), suggesting that the fracturing process was fault-related. This interpretation is supported by the occurrence of relatively intact rocks in the folded dolestones at distances of several hundreds of meters east and west of the fault zone (e.g. Figure 4). A second observation in support of this interpretation is that at outcrop A, characterized by the overturning of the dolostone bedding due to presence of a prominent anticline fold (cross section in Fig. 2), the fracture pattern within the fragmented dolostones is not controlled by buckling. Given the box-type anticline fold with NW-SE shortening direction, buckling and overturning of the Mendola Fm. strata would result in the formation of ENE-WSW striking sub-horizontal joints, but this fracture set is fairly absent in the area (Fig. 9f).

One of the most important characteristics of the fault zone is the lack of significant shear strain within the fragmented dolostones and fine-grained gouge layers, suggested by:

1) the preservation of primary sedimentary features at the macroscale (e.g. intercalations of marly dolostones parallel to the bedding and stromatolitic laminations) even in the most intensely fragmented areas of the fault zone;
2) the nature of fracturing at the microscale (exploded clasts with radial fractures; chains of split clasts), which produced densily fractured clasts that nevertheless retain their original shapes and contain individual pieces that fit together like a jigsaw puzzle.

The lack of significant shear strain at both the macro- and micro-scale is frequently observed in so-called “pulverized fault zone rocks”, widely interpreted as the product of earthquake ruptures propagation along large faults (Dor et al., 2006; Doan and Gary, 2009; Yuan et al., 2011). Pulverized fault rocks are unique in comparison to other fault rocks since they (i) appear to have been shattered in-situ, (ii) have a very fine grain size (i.e. ≤ 1 mm on average) due to intense fracturing, and (iii) do not display evidence of significant shear strain. To date, pulverized rocks have been found along major (i.e., hundreds to thousands kilometers long) strike-slip faults mainly within crystalline (i.e., igneous or metamorphic) host rocks (e.g., Brune et al, 2001; Wilson et al., 2005; Dor et al., 2006, 2009; Mitchell et al., 2011). Pulverized rocks typically preserve the primary features of the local host rocks (e.g. grain boundaries in crystalline rocks) but are easily reduced to a powder upon removal, even with a finger, from the outcrops. In addition, in the most well studied example of pulverized rocks along the Mojave section of the San Andreas fault, the distribution of damage with respect to the main fault trace was found to be strongly asymmetric (Dor et al., 2006a,b). To my knowledge, the only report of pulverized rocks within carbonate host rocks is from Agosta et al. (2006) along the Venere Fault (Central Apennines, Italy). The so-called pulverized rocks in this example were found within a c. 1 m thick band adjacent to the fault core, and consist of finely comminuted (maximum rock fragment size ~ 1 cm) limestones with well-preserved sedimentary layering. The pulverized limestones along the Venere Fault show a larger average grain size with respect to the pulverized rocks found in crystalline host rocks.

Several authors have suggested that pulverized fault zone rocks are of seismic origin based on both theoretical and experimental arguments (Ben-Zion and Shi, 2005 ; Doan et al., 2009; Mitchell et al., 2011; Yuan et al., 2011). Brune (2001) suggested that sliding on a non-planar fault during earthquakes at seismogenic depths generates intense variations in normal stress sufficient to fracture the local wall rocks. According to this model, successive earthquake ruptures result in repeated fracturing of the rock mass without significant shear. Ben-Zion and Shi (2005) simulated extensive off-fault plastic yielding (equivalent to fracturing) by modeling the propagation of dynamic ruptures along faults separating media with different elastic properties (i.e. bi-material interfaces). The ruptures propagating along such interfaces (i.e., "wrinkle-like pulses") were associated with strong extensional loading within the medium characterized by the higher shear wave velocity (i.e., the stiffer medium). Based on their models, the repeated occurrence of ruptures propagating from depth and with the same directivity is expected to produce strongly asymmetric rock damage approaching the ground surface.

From an experimental point of view, Doan and Gary (2009) and Yuan et al. (2011) used Split Hopkinson Pressure Bar tests to investigate high strain rate deformation in granites. They demonstrated that granite pulverization occurred at very high strain rates (>150 s^{-1}) even at small finite strains. Similar experiments performed on Carrara marble produced pulverized rocks with coarser fragment sizes (Doan and Billi, 2011). Such extremely high strain rates leading to rock pulverization may be associated with strong stress perturbations transiently produced within the host rocks by the passage of earthquake ruptures along a fault.

Rock pulverization is expected to occur up to a maximum depth of c. 3-4 km, where confining pressures are sufficiently low that they can be dynamically exceeded by off-fault stress perturbations induced by rupture propagation and the intense radiated seismic field. The restriction of pulverized rocks to relatively shallow depths is confirmed by both field studies of natural pulverized rocks (Dor et al., 2009) and experimental observations (Yuan et al., 2011).

The exposed FFZ is estimated to be exhumed from a depth of ~ 1-2.5 km, considering the thickness of the pre-Miocene sedimentary overburden in the area and the increasing cumulative vertical throw along fault strike moving from south to north (Bosellini et al., 2007). Based on this and the evidence for in-situ shattering of the dolostones, I interpret both the fragmented dolostones and the fine-grained layers within the FFZ, both of which lack evidence for having accommodated significant shear strains, as fault rocks produced during the propagation of ancient earthquake ruptures. In particular, the fine-grained layers associated with mirror-like faults show microstructural characteristics comparable to those of pulverized rocks described in crystalline protoliths. The fragmented dolostones, which show larger average rock fragment sizes (i.e. ~ 1 cm on average) with respect to pulverized rocks (i.e. ≤ 1 mm on average), can be tentatively interpreted as the product of seismic damage (i.e. seismic fracturing) at larger distances (i.e. up to tens of meters) from the fault cores.

The fine-grained layers associated with mirror-like faults are more cohesive with respect to the surrounding fragmented dolostones and to other pulverized fault rocks described in literature.

This is mainly due to the presence of sub-micrometer bridges of dolomite cement connecting the dolostone clasts and the matrix (see Fig. 15d). The occurrence of the cement bridges, which frequently do not completely fill the intergranular porosity, within the fine-grained layers coupled with the scarcity of veins and sealed-fractures within the fragmented dolostones around, implies the presence of small amounts of fluids along the faults. Regardless of their origin, which might be extremely various, these fluids were likely responsible for healing processes during post-seismic or inter-seismic periods. In the same way the compaction features and the porosity reduction occurring in proximity to the fault surfaces and sometimes overprinting the dominant in-situ shattered fault rock fabric (Fig.15d), suggest the activation of low strain rate deformation processes likely during post-seismic or inter-seismic periods.

3.8.2 Mirror-like slip surfaces and seismic faulting within the FFZ

Mirror-like slip surfaces are one of the most remarkable structural features within the FFZ. These faults were easily recognized in the field because they specularly reflect the sunlight. According to the Rayleigh roughness criterion a surface will reflect natural sunlight (average wavelength = 550 nm) if the mean amplitude of the surface roughness is < 100 nm at a length scale L = 550 nm (Beckmann and Spizzichino, 1963; Siman-Tov et al.,2013). This implies that the mirror-like slip surfaces of the FFZ are extremely smooth at the microscale. Mirror-like slip surfaces are widespread within the FFZ, especially in its southern sector (outcrop B). In this sector, they are well exposed and can be seen to displace marly horizons with small (0.04 – 0.5 m) reverse offsets.

A dedicated experimental study was performed to understand the origin of the mirror-like slip surfaces. This study is described in chapter 3 of this thesis (published as Fondriest et al., 2013) and I provide here only a brief summary of the main results.

Low- to high-velocity rotary shear experiments were performed on dolostone gouges at deformation conditions approaching those estimated for the mirror-like slip surfaces within the FFZ: normal stresses up to 26 MPa, displacements in the range 0.02 - 3.5 m and slip velocities ranging from sub-seismic to seismic in the interval 0.0001 - 1.13 m/s. Mechanical data coupled with surface roughness measurements (using White Light interferometry) and microstructural observations of the experimentally-deformed gouges indicate that mirror-like slip surfaces (obeying the Rayleigh roughness criterion) (i) form only at seismic slip velocities (> 0.1 m/s) at the applied normal stresses, (ii) are related to strong dynamic weakening (i.e. drop of both shear stress and friction coefficient), (iii) are associated with extreme strain localization within the gouge layers (most shear strain accommodated along the slip surfaces and within an adjacent slip zone up to 20 μm thick). At these experimental conditions the frictional power density (shear stress × slip velocity at any moment during the experiments) dissipated in the gouge layers was comparable to that estimated for natural earthquakes (1-10 MW/m^2; Sibson, 1980).

Mirror-like slip surfaces within the FFZ have surface roughness and microstructural characteristics that compare favorably to the experimental mirror-like slip surfaces (see chapter 3 for detail). In particular, both natural and experimentally deformed gouges show evidence of extreme shear strain localization along the mirror-like slip surfaces and an absence of significant shear strain within the adjacent gouge layers. Additionally, both natural and experimental mirror-like slip surfaces are associated with truncation of relatively large dolostone clasts embedded within the surrounding gouge layers, a peculiar microstructure produced only at seismic slip velocities (in the experiments) and indicative of extreme shear strain localization. Collectively, the experimental data and microstructural observations indicate that small-displacement mirror-like slip surfaces in dolostone gouges of the FFZ were most likely produced by extreme frictional power dissipation during seismic slip and therefore represent markers of seismic faulting. Future work could usefully assess whether this conclusion is applicable to other lithologies and for larger displacement faults. For example, mirror-like slip surfaces have previously been observed to form in high-velocity experiments performed on calcite and siderite gouges (Han et al., 2007; Smith et al., 2013), and have also been described in the field within relatively large-displacement (>10s meters) fault zones in limestone (Siman-Tov et al., 2013). Recently, well-polished fault surfaces were produced in calcite gouges sheared at sub-seismic slip rates (Verberne et al., 2013). Though a quantitative determination of the roughness of these "sub-seismic" fault surfaces is still lacking (to be mirror-like, surfaces should satisfy the Rayleigh criterion, see section 3.5.3) the main microstructural difference between seismic and sub-seismic fault surfaces is the lack, in the latter, of truncated clasts (Verberne, personal communicaton to Giulio Di Toro).

3.8.3 Structural complexity of the FFZ

Detailed structural mapping of the FFZ highlighted significant changes in the along-strike structure of the fault zone. In particular, moving from south (outcrop A) to north (outcrop C), (i) the average fault zone thickness decreases from > 300 m to ~ 100 m, (ii) deformation becomes increasingly localized on to discrete faults (i.e., the proportion of highly fragmented dolostones with respect to poorly-fragmented ones is significantly reduced), (iii) the scattering of fault attitudes is generally decreasing, and (iv) the kinematics of faulting switches from dominant dip-slip reverse to involving an important left-lateral oblique- to strike-slip component (see Table 1). These observations suggest that the FFZ becomes wider and more structurally "complex" approaching the southern fault termination.

Bedding surfaces within the dolostones are frequently exploited by small-displacement mirror-like faults. The exploitation of preexisting anisotropies such as bedding surfaces, veins, pressure solution seams and joints is a common situation in carbonate sedimentary sequences (e.g., Graham et al., 2003; Agosta et al., 2006; Hausegger et al., 2010). At the southern termination of the FFZ individual faults exploit overturned bedding surfaces on the eastern limb of a fault propagation anticline across the full thickness of the exposed fault zone (~ 300 m, Figs.9a,10b). Instead, towards the north, at the Dòs de la Ciéura, individual faults exploit bedding surfaces that are progressively rotated in to parallelism with the master fault, but over an across-strike distance of only a few meters (Fig.13b).

In the following two sections I discuss models that may account for the changes in along-strike fault zone structure in the FFZ. The first is related to the regional change in fault orientation observed to take place between the southern and central fault zone sectors, and the second follows predictions of damage patterns in dynamic rupture simulations on strike slip faults.

(i) Effect of static stress field and regional scale fault geometry

The orientation of the FFZ changes at the regional scale, which may have a strong influence on fault zone structure and kinematics. With respect to the NNW-SSE-striking principal compressive stress axis (σ_1) during faulting (Fig.3; Valsugana deformation phase; Castellarin et al.,1992), the southern sector of the FFZ (outcrop A) strikes at high angles and represents a restraining bend. This is consistent with the southern sector being dominated by dip-slip reverse kinematics. Instead, towards the north, at the Dòs de la Cièura (outcrop C) the FFZ strikes N-S to NNW-SSE, at lower angles to the principal compressive stress axis. Here, the fault zone has an important oblique- to strike-slip component (Fig.3). Such regional-scale changes in the orientation of the FFZ with respect to the principal compressive stress axis can also account for the along strike variations of fault zone thickness, which is wider at the southern restraining bend where almost pure compression is accommodated. The thickening of the fault zone in correspondence with a fault tip is a frequent observation within other fault zones and is also predicted by several models of fault zone growth (e.g., Kim et al., 2004, for a review). Moreover the occurrence of a maximum in the scattering of fault attitudes at outcrop B, which is located next to the change of strike of the FFZ from ~ NE-SW to ~ N-S, can be explained as the result of stress concentration at a geometrical asperity of the FFZ.

(ii) Off-fault dynamic effects of earthquake ruptures

As previously discussed, the association of fragmented dolostones and mirror-like fault surfaces is interpreted to record the propagation of ancient seismic ruptures along the FFZ. Below, I compare the structure of the FFZ (i.e., an exhumed seismogenic fault zone in dolostones) to (i) the results of earthquake rupture simulations along strike-slip faults, and (ii) the structure of active seismogenic sources hosted in carbonate rocks as retrieved by modern seismological techniques.

Ma and Andrews (2010) performed three-dimensional finite element simulations of dynamic ruptures along a strike-slip fault within an homogeneous elastic medium. The medium (i.e. host rocks) was allowed to deform inelastically following a Drucker-Prager yield criterion (i.e., shear fracturing in 3D) due to stress perturbations associated with the passage of the rupture tip and seismic wave fronts. This model predicts (i) an off-fault damage distribution with a "flower-like" shape, consisting of a relatively broad damage zone near the surface that rapidly narrows with depth (increasing confining pressure), and (ii) the formation of secondary structures with scattered orientations and kinematics (reverse to normal) nearer to the surface, giving way to sub-parallel structures with dominant strike-slip kinematics at depth (Fig.16).

Two lines of evidence suggest that the exhumation depth represented by outcrops of the FFZ increases from c. 1 km in the south (outcrop A) to c. 2.5 km in the north (outcrop C): 1) The cumulative vertical throw across the FFZ (balanced reconstructions from published geological maps; Avanzini et al., 2001; Bosellini et al., 2007) is 0.3-0.5 km at outcrop A, near the southern fault tip, progressively increasing northward to 1.6-1.8 km at outcrop C; 2) the thickness of the pre-Miocene sedimentary overburden in the area is c. 1 km (Bosellini et al., 2007). Considering the northward increase in exhumation depth together with changes in fault zone thickness and dominant kinematics (Table 1), the structure of the FFZ is qualitatively comparable to the theoretical results of Ma and Andrews (2010).

In the last few years increasingly high-resolution seismological techniques (e.g., high-precision hypocenters relocation, seismic tomography) have yielded new constraints on the geometry of active seismogenic fault zones at depth (Bressan et al., 2009; Chiaraluce et al.,2011; Di Stefano et al., 2011; Valoroso et al., 2013). For example, Valoroso et al. (2013) investigated the anatomy of the normal fault system cutting carbonate host rocks (limestones and dolostones) that hosted the 2009 L'Aquila foreshock - mainshock ($M_w = 6.1$) - aftershock sequence. Their study was based on the high-precision double-difference (± 10 m formal error) relocation of ~ 64000 earthquakes (both foreshocks and aftershocks) spanning a timeframe of more than one year. This substantial dataset possesses a magnitude of completeness of 0.7 (more than 1 unit lower than other state-of-the-art earthquake catalogues), allowing fine details of the fault zone structure to be reconstructed at a resolution (meters to tens of meters) comparable to that used by field geologists studying exhumed fault zones. One of the main results arising from the work of Valoroso et al. (2013) was the definition of a “seismological damage zone” (SDZ), defined for each fault strand as the total width enclosing 95% of the relocated aftershocks. The SDZ in their study showed marked variations along fault strike, ranging from ~ 0.3 km width in relatively planar areas of the fault zone (e.g. the area where the mainshock nucleated) to ~ 1.5 km width toward the southern tip of the fault zone, where rupture directivity was reported. Moreover, toward the fault tips, increasing fault zone complexity was also reported, including (i) multiple antithetic and synthetic fault segments tens of meters long in both the hangingwall and the footwall, (ii) fault bends and jogs at different scales, (iii) intersections between principal faults and secondary fault splays, and (iv) they also reported more complexity in fault kinematics based on nodal plane solutions. The fault system activated during the L’Aquila seismic sequence is not comparable in terms of dominant kinematics (i.e normal dip-slip) to the exhumed FFZ (i.e. left-lateral transpressive on average). Nevertheless, the study of Valoroso et al. (2013) offers an important insight in to the geometrical complexity of fault zones in carbonate host rocks, and many of the general characteristics of the L’Aquila seismic sequence (increasing damage zone width towards fault tip; increasing complexity of fault plane solutions at fault tips) compare favorably to the structural features recognized within the exhumed FFZ.

The FFZ consists of large volumes of fragmented dolostones cut by mirror-like faults (see chapter 3), the latter being traceable in the field for strike lengths of no more than c. 20 m. The FFZ is exposed for ~ 30 km along strike and thus may have hosted earthquake ruptures up to $M_w = 6.5$ (based on empirical length-magnitude scaling relationships; e.g. Wells and Coppersmith, 1994). Assuming total lengths of <300 m for individual mirror-like faults suggests that they may have hosted earthquake ruptures up to $M_w = 2$, associated with average coseismic slips of a few centimeters at most (Wells and Coppersmith, 1994). One can thus speculate that the exposed FFZ might record the cumulative history of many large seismic ruptures and their associated foreshock and aftershock sequences.

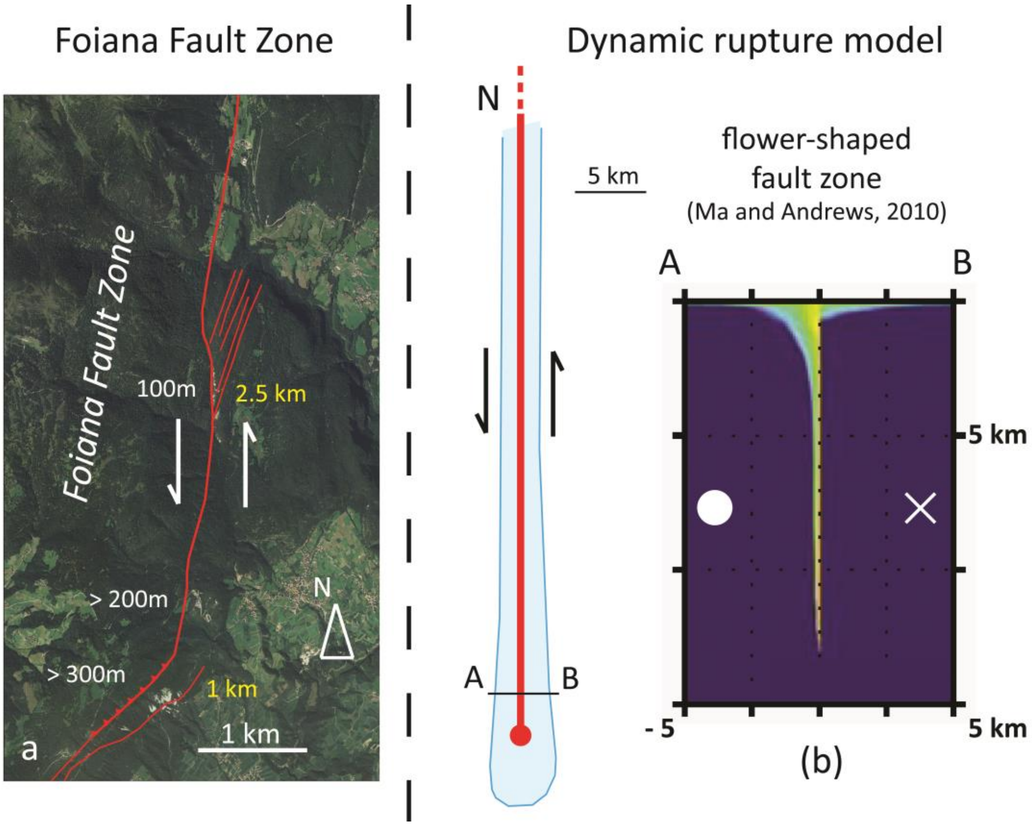

Fig.16 Comparison of the internal structure of the FFZ with the results of dynamic rupture simulations (Ma and Andrews 2010). (a) Aerial view of the FFZ. The FFZ is a left-lateral transpressive fault striking on average NNE-SSW. White and yellow numbers indicate, respectively, the thickness (from field mapping) and the estimated exhumation depth (from geological maps and cross section reconstructions) of the different segments of the FFZ. Assuming that deeper portions of the FFZ are exposed further to the north, the structure of the FFZ compares favourably with the predicted damage patterns in dynamic rupture simulations along strike slip faults (parts b and c). (b) Coseismic damage zone (blue area) produced around a left-lateral strike-slip fault (thick red line) by an earthquake rupture propagating from north to south (adapted from Ma & Andrews 2010). A-B is a vertical section across the coseismic damage zone in a direction perpendicular to fault strike. The damage zone is predicted to have a flower-like shape with a broad damage zone near the surface that rapidly narrows at depth.

3.9 Conclusions

The Foiana Fault Zone (FFZ) is a ~ 30 km long NNE-SSW-trending sinistral transpressive fault zone exhumed from depths of 1-2.5 km that cuts Triassic dolostones in the Italian Southern Alps. Cumulative vertical throw increases from 0.3-0.5 km in the south, where a NE-SW-striking restraining fault bend occurs, to 1.6-1.8 km in the north.

The FFZ consists largely of fragmented dolostones that did not accommodate significant shear strains. The absence of veins and sealed fractures within the fault zone suggests a paucity of fluids during faulting. Networks of small-displacement (<0.5 m) faults locally cut the fragmented dolostones, often reactivating bedding surfaces. The faults contain fine-grained gouge layers up to a few centimeters thick associated with discrete and through-going mirror-like slip surfaces. Microstructural observations of the fine-grained layers indicate: (i) a lack of significant shear strain, even at a few micrometers distance from the mirror-like fault surfaces, (ii) pervasive fracturing, (iii) exploded clasts with radial fracture patterns, and (iv) chains of split clasts oriented at high angles (60-80°) to the fault surfaces. Similar macro- and micro-structural features have been reported in pulverized fault zone rocks, widely interpreted as a shallow-level (<3-4 km) product of earthquake ruptures propagating along large faults. We interpret the fragmented dolostones and fine-grained rock layers in the FFZ to record the passage of ancient earthquake ruptures. This conclusion is supported by the results of rotary shear experiments performed on dolostone gouges, which demonstrated that small-displacement mirror-like faults similar to those recognized within the FFZ form only at deformation conditions approaching the seismic range (see chapter 3 of this thesis).

Moving from south to north along fault strike, (i) the thickness of the FFZ decreases from more than 300 m to ~ 100 m, (ii) the variability in the attitudes of faults (including mirror-like examples) decreases (i.e. fault attitudes are more dispersed to the south with respect to the north), and (iii) fault kinematics change from dominant dip-slip reverse to include a significant left-lateral oblique- to strike-slip component. These changes in fault zone structure may reflect a number of factors, including 1) regional-scale variations in fault strike (i.e. the presence of a restraining bend in the southern sector), 2) co-seismic fracturing that is predicted in 3D seismic rupture simulations to occupy a wider zone at shallow crustal levels, or 3) increasing fracture damage accumulated during seismic sequences in the area around the southern fault tip.

4. Fluid-rich vs. fluid-poor conditions during seismic faulting

In this chapter I described the structure of two fault zones hosted in dolomitic rocks and exhumed from shallow depth (i.e. < 3 km).

The Borcola Pass Fault Zone (BPFZ) is a minor (few kilometers long) left-lateral strike slip fault zone cutting sedimentary dolostones and dolomitic marbles. The fault zone is > 80 m thick and consists of sub-vertical fault strands exploiting regional-scale sets of joints related to a previous extensional deformation phase. The rock volumes delimited by the fault strands are affected by discrete joints and shear fractures which are locally sealed by dolomite cement. The fault strands are typically associated to up to few centimeters thick cohesive cataclastic to ultracataclastic layers supported by a vein-like dolomite cement with zoned polygonal crystals. Sinkinematic dolomite veins were also observed next to the fault surfaces. Finally the presence of fluidized cataclastic layers supported by dolomite cement suggest the occurrence of seismic ruptures propagating along the BPFZ in a shallow crustal fluid-rich environment. The occurrence of ancient seismic ruptures is also suggested by the presence of faults with polished to mirror-like slip surfaces.

The Foiana Fault Zone (FFZ) is ~ 30 km long sinistral transpressive fault zone cutting sedimentary dolostones. The southern sector of the fault zone consists of a restraining bend where almost pure compression is accommodated. The fault zone is up to more than 300 m thick and consists of fragmented dolostones reduced in rock fragments from few centimeters down to few millimeters in size. The fragmented dolostones are affected by joints and open fractures with no evidence of mineral sealing. The faults reactivate the bedding, which is overturned due to the presence of a prominent anticline fold in the southern sector of the FFZ, and is dragged along the master fault of the FFZ in the northern sector. The common presence of faults with mirror-like slip surfaces cutting through fragmented dolostones lacking evidence of significant shear strain is interpreted to record the occurrence of ancient seismic ruptures propagating along the FFZ. The presence of intergranular submicrometer bridges of dolomite cement only within the fine-grained rock layers in proximity to the mirror-like slip surfaces and the absence of veins and sealed fractures in the fragmented dolostones around suggest paucity of fluids during faulting within the FFZ.

The relative abundance of fluids within the BPFZ with respect to the scarcity of fluids within the FFZ, inferred from the study of the fault rock assemblages, can be tentatively explained in terms of fault mechanics. Indeed the BPFZ is characterized by a pure strike-slip kinematics while the FFZ is characterized by an overall transpressive kinematics which becomes a pure compression within the southern restraining fault bend. This implies that faulting within the FFZ was active under an higher mean stress (i.e. $[\sigma_1 + \sigma_2 + \sigma_3]/3$, where σ_1, σ_2, σ_3 respectively are maximum, intermediate and minimum principal stresses), which likely prevented the incoming of fluids within the fault zone. The relative low level of the mean stress within the BPFZ is also suggested by the presence of sinkinematic veins and hybrid fractures next to the fault surfaces. Moreover the regional scale joint set exploited by the faults might have acted as fluid conduits during faulting.

The mean stress level can also account for the difference in damage intensity between the two fault zones, which cut similar host rocks. Indeed the relative low in mean stress BPFZ is characterized by slightly deformed rock volumes between the main fault strands, while the higher in mean stress FFZ consists of hundreds of meters thick intensely fragmented dolostones.

Chapter 3. Mirror-like fault surfaces in dolostones

Abstract

Earthquakes occur along faults in response to plate tectonic movements, but paradoxically are not widely recognized in the geological record, severely limiting our knowledge of earthquake physics and hampering accurate assessments of seismic hazard. Light-reflective ("mirror-like") fault surfaces are widely observed geological features, especially in carbonate-bearing rocks of the shallow crust. Here I report on the occurrence of mirror-like fault surfaces cutting dolostone gouges in the Italian Alps. Using friction experiments, I demonstrate that the mirror-like surfaces develop only at seismic slip rates (~1 m/s) and for applied normal stresses and sliding displacements consistent with those estimated on the natural faults. Under these experimental conditions, the frictional power density dissipated in the samples is comparable to that estimated for natural earthquakes (1–10 MW/m^2). These results indicate that small-displacement mirror-like surfaces in dolostone gouges are a signature of seismic faulting, and can be used to estimate power dissipation during ancient earthquake ruptures.

This study was performed in collaboration with Steven Smith, Thibault Candela, Stefan Nielsen, Karen Mair and Giulio Di Toro. A modified version of this chapter was published as the following paper and data repository item: Michele Fondriest, Steven A.F. Smith, Thibault Candela, Stefan B. Nielsen, Karen Mair & Giulio Di Toro (2013) Mirror-like faults and power dissipation during earthquakes, Geology, v.41, p.1175-1178, doi: 10.1130/G34641.1, Data Repository Item 2013329.

1. Introduction

Seismological and geophysical methods allow the retrieval of key parameters related to the earthquake source (e.g., seismic moment, static stress drop) (Kanamori and Brodsky, 2004) but typically lack sufficient resolution to constrain the physico-chemical processes and the dynamic stress on fault surfaces during seismic slip (Beeler, 2006; Di Toro et al., 2012). At present, pseudotachylytes (i.e., solidified friction-induced melts) are the only widely accepted indicator of ancient seismicity along fault zones (Sibson, 1975; Cowan, 1999). Pseudotachylytes are primarily hosted within crystalline (metamorphic or plutonic) protoliths and do not form in many other rock types within the shallow crust, including carbonates (Sibson and Toy, 2006). The absence of other robust indicators of seismic faulting is a major limitation in our understanding of earthquake physics.

Theoretical and experimental studies indicate that faults are weakened during earthquakes irrespective of fault rock composition (Di Toro et al., 2011; Goldsby and Tullis, 2011). Due to the large mechanical work rate dissipated on fault surfaces during seismic slip several mechano-chemical processes (e.g., flash heating, frictional melting, decomposition reactions) can be activated resulting in a reduction of dynamic frictional strength (Di Toro et al., 2011). In the case of carbonate-bearing fault rocks coseismic decarbonation can produce thin (10–100 µm) layers of nanometric particles in which deformation localizes (De Paola et al., 2011; Han et al., 2007a). Although certain decomposition products are stable over wide pressure-temperature (*P*-*T*) ranges (e.g., magnetite in the case of siderite decarbonation), it is unlikely that they will be preserved in a recognizable form over geological time scales (Han et al., 2007b). In this study, I report field and experimental evidence that mirror-like fault surfaces in dolostone gouges, for total sliding displacements up to ~1 m, form only at seismic deformation conditions.

2. Natural mirror-like fault surfaces of the Foiana Fault Zone

The Foiana Fault Zone (FFZ) is a NNE-SSW–striking, sinistral transpressive fault zone in the Italian Southern Alps (Fig.1a). The fault zone is 100–300 m thick and exposed for ~30 km along strike within outcrops exhumed from 1–2.5 km depth (geological map of Bosellini et al., 2007). The southern termination of the Foiana Fault Zone is characterized by heavily fractured Triassic dolostones exposed in badlands topography over an area of ~0.2 × 0.3 km^2 (Fig.1a). Many of the outcrops contain faults with fine-grained gouge layers (grain sizes 0.001–2 mm; Fig.1b) up to a few centimeters thick (usually < 5 cm). The fine-grained layers are cut by discrete mirror-like slip surfaces (Figs.1c,d) that truncate large dolostone clasts (Fig.1e). Surface roughness analysis by white light interferometry (WLI, see section 3.4) reveals the extremely smooth nature of the mirror-like surfaces, with a mean roughness amplitude of ~2 µm at the scale of WLI measurements (Fig.1d). Mirror-like slip surfaces consist of 100% dolomite (i.e. no decarbonation products such as periclase or Mg-calcite were detected by XRPD analyses, section 3.5). In some cases, brownish “flames” of iron oxides and hydroxides (hematite and goethite from XRPD analyses) are smeared along fault lineations. The mirror-like slip surfaces have observed lengths in the field of 1–20 m, dominant ENE-WSW strikes with dip angles of 30°–85°, and dip-slip reverse kinematics (Fig.1b). Measured displacements of 0.04–0.5 m across the mirror-like surfaces are constrained by offset of structural markers (mainly marly horizons within the dolostones; Fig.1b).

For mirror-like faults of the FFZ, normal stress at the time of faulting was estimated with the following assumptions: 1) no large-scale tilting during exhumation of the faults; 2) Andersonian stress field in a compressional regime (i.e. vertical stress σ_v corresponds to minimum principal stress σ_3); 3) hydrostatic pore pressure (λ=0.4); 4) static friction coefficient of 0.6; 5) no cohesion on the faults. Given these simplifications a range of normal stresses (30-50 MPa) was determined at 1.2 km depth by solving the condition for frictional sliding on reverse faults (Sibson, 1974) with dip angles in the range 30°-70°. The depth of faulting was determined as 1.2 km, considering the thickness of the pre-Miocene sedimentary overburden in the area and the cumulative vertical throw in the southern sector of the FFZ (0.3-0.5 km) estimated from recent geological maps (Tavola Fondo, Avanzini et al., 2002; Foglio Appiano, Bosellini et al., 2007).

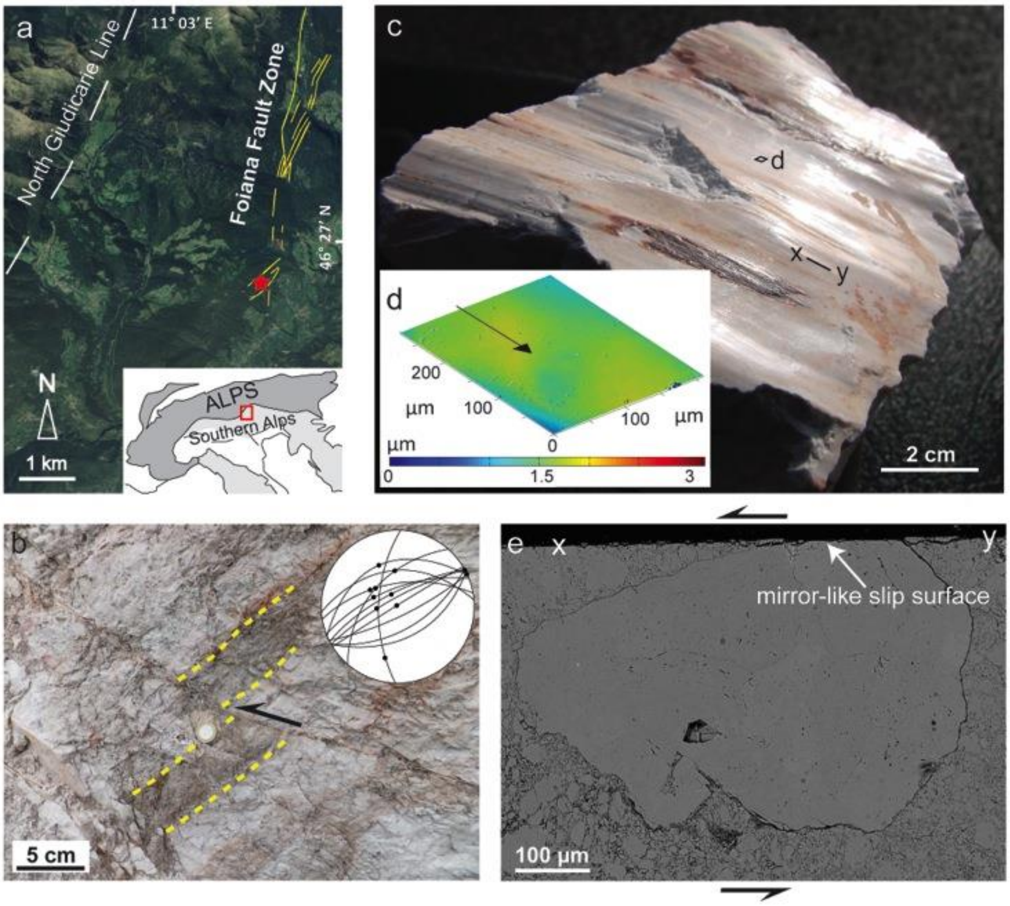

Fig.1 Natural mirror-like slip surfaces from the Foiana Fault Zone (FFZ). (a) The FFZ is located in northern Italy (see inset in lower right corner) and runs sub-parallel to the North Giudicarie Line, a segment of the Periadriatic lineament. The southern FFZ displays a NE-SW-striking restraining bend associated with wide zones of pulverized dolostones (red star). (b) Natural mirror-like fault cutting a marly-dolostone horizon with a reverse separation of 0.05 m. The stereoplot (equal-area, lower hemisphere) shows the orientation of mirror-like slip surfaces (great circles) and surface lineations (black dots). The slip surfaces have predominantly ENE-WSW strikes, dip-angles in the range 30°-85° and reverse dip-slip movements. (c) Photograph of a mirror-like slip surface under natural light. (d) Digital elevation model of mirror-like slip surface derived from WLI over an area of 200×300 μm^2 (see square in section Fig. 1c). Mean roughness amplitude is ~2 µm. Arrow shows slip direction. (e) SEM image (backscattered mode) of dolomite gouge and large clast cut by mirror-like slip surface along profile x-y (parallel to surface undulations; see Fig. 1c). Deformation is strongly localized in a compact and ultra-fine grained layer adjacent to the slip surface.

3. Experimental and Analytical Methods

To understand the origin of the mirror-like slip surfaces along the FFZ, low- to high-velocity experiments were performed using the **S**low to **Hi**gh **V**elocity rotary-shear friction **A**pparatus (SHIVA) at the Istituto Nazionale di Geofisica e Vulcanologia (INGV) in Rome (Di Toro et al., 2010) at conditions approaching those estimated for the Foiana Fault Zone. Tests were conducted on 3-mm-thick layers of dolostone gouge (100% dolomite, grain size <250 µm) collected from the fault zone outcrops and mounted in a purpose-built gouge sample holder (Smith et al., 2013). Normal stress on the gouge layers was held constant at up to 26 MPa during the tests, approaching the normal stresses estimated for the mirror-like slip surfaces of the FFZ (30-50 MPa; section 2). Slip rates were 0.0001–1.0 m/s and both acceleration and deceleration were 6 m/s^2. Total sliding displacements were in the range of 0.02–1 m (Table 1).

After the experiments, the slip zones were retrieved from the gouge sample holder (see section 3.2). The roughness of the discrete slip surfaces that formed during the experiments was measured with WLI (section 3.3), and the mineralogy of the fine-grained slip zones was determined with X-ray powder diffraction (section 3.4). Deformed gouges were impregnated with epoxy, and petrographic sections perpendicular to the gouge layers and approximately parallel to the slip direction were prepared for geochemical (electron microprobe analyzer) and microstructural (field emission scanning electron microscope) analyses (see sections 3.4, 3.5).

3.1 Rotary shear friction experiments in position-control mode with SHIVA

Measured displacements across the mirror-like slip surfaces of the FFZ are relatively small (in the range 0.04 - 0.5 m) and well constrained due to the presence of markers (i.e. 5 -15 cm thick horizons of marly dolostone) that are cross-cut by the slip surfaces. Friction experiments on dolostone gouges were performed with SHIVA in "position-control mode", allowing total displacements to be precisely controlled in the range estimated for the natural slip surfaces. Control of the total displacement meant that for several small-displacement experiments (e.g. s526 with a displacement of 0.07 m) the target slip velocity was not reached before deceleration commenced. Before each experiment 5 g of dolomite gouge was homogeneously distributed in the gouge holder between the two confinement rings (for details of the gouge holder and calibration tests see Smith et al., 2013) and loaded up to 1.6 MPa using an air press. The gouge holder was then assembled and installed in SHIVA.

Each experiment consisted of three steps: 1) loading of the sample (gouge layer) to the target normal stress; 2) deformation of the sample under the conditions summarized in Table 1; 3) unloading and recovery of the deformed sample for further analytical work.

3.2 Recovery of experimental samples and measurements of mirror-like area percentages

After each experiment the sample holder was placed on the worktop with the stationary side to the top. The stationary side of the gouge holder was then carefully raised up and removed to reveal the deformed gouge layer. The deformed gouge was compact (especially after experiments at velocities >0.1 m/s) and typically parted along a main slip surface that developed close (<200 μm) to the boundary between the gouge layer and the base disc in the stationary side of the gouge holder. This allowed relatively easy recovery of the entire gouge layer and main slip surface from the rotary side of the gouge holder (transferral of slip surface fragments from the stationary side were quite rare).

Photographs of the experimental slip surfaces were taken using a high-resolution digital camera under the light of a table lamp to highlight the parts of the slip surfaces with a mirror-like finish. The mirror-like parts of the slip surfaces were traced on the high-resolution digital images and the areal percentage of the total slip surface with a mirror-like finish was calculated for each experiment using Image J software (http://rsbweb.nih.gov/ij/).

3.3 Measurements of slip surface roughness by White Light Interferometry (WLI)

The roughness of both natural and experimental slip surfaces was measured by WLI (Zygo NewView) with the aim of quantifying and comparing the surface roughness characteristics at different slip velocities. Digital Elevation Models (DEM) acquired with this instrument allowed the estimation of slip surface roughness with vertical resolution of ~ 0.1 nm for length scales of 0.2 – 250 μm. One way to fully characterize micro-roughness at all scales accessible to WLI is to compute the root mean square correlations of thousands of individual, parallel profiles extracted from the DEMs. The root mean square correlation method (Candela et al., 2009) was used to compute the root mean square amplitude roughness (RMS) for length scale L in the direction parallel to slip. Each individual profile extracted from the slip surfaces was divided into windows of width δx. The window size was varied between the sampling distance to the size of the profile, and for a given δx, the standard deviation of the height difference was calculated and then averaged over all the possible bands of fixed width δx spanning the profile. The results obtained for each individual profile were then averaged to obtain a mean estimate of the RMS of the surfaces for every length scale L (i.e. window sizes).

3.4 XRPD analyses performed on gouge layers

The mineralogy of both the undeformed dolostone starting material and the deformed gouges was determined by X-ray powder diffraction analyses (XRPD) in the Department of Geosciences at the University of Padova. For each deformed gouge two separate XRPD analyses were performed: one analysis was performed on bulk gouge collected after the experiment, and a second analysis was performed on gouge scraped from the slip surfaces using a sharp razor blade. The scraped material was estimated to be derived from a layer no thicker than ~50 μm adjacent to the slip surface. The mineralogy of some natural mirror-like slip surfaces was determined in the same way.

XRPD data were obtained by step scanning using an automated diffractometer system (Philips X’Change) with incident- and diffracted-beam soller slit (0.04 rad.). The instrument was equipped with a curved graphite diffracted-beam monochromator and a gas proportional detector. Divergence and antiscatter slits of 1/2° were used so that the irradiated area could be confined to the sample at angles >10 °2θ. A receiving slit of 0.2 mm was used. A long fine focus Cu X-ray tube was operated at 40 kV and 30 mA. Diffraction pattern was obtained using a step interval of 0.02 °2θ with a counting time of 15 s. The scan was performed over the range 3–70 °2θ. The program High Score Plus (PANalytical) was used for phase identification and Rietveld refinement (Rietveld, 1967).

3.5 EMP-WDS chemical analysis

A chemical map, covering an area of 1374 μm^2 next to the slip surface of experiment s433 (experimental conditions: $v = 1.13$ m/s, $\sigma_n = 17.3$ MPa, $d = 0.25$ m) was obtained using an Electron Microprobe (JEOL JXA-8200 EMP at INGV in Rome) equipped with a Wavelength Dispersion

Spectrometer (WDS). The chemical map was carried out by scanning the sample (polished carbon-coated thin section) with an electron beam moving on a matrix of 512 x 512 pixel^2 with a point spacing of 0.0724 µm. For each point analysis the concentration in weight of the elements Ca, Mg and O was measured.

3.6 Estimates of temperature increase within experimental slip zones

Assuming that, once formed in the experiments, all slip was accommodated along the main slip surface, the 1D heat diffusion equation of Carslaw and Jaeger (1959) (solved numerically as equation A1 in Nielsen et al., 2008) was used to calculate the maximum bulk temperature increase along the slip surface. The equation takes the form:

$$T(t) = \frac{1}{\rho\, Cp\, \sqrt{k\pi}} \int_0^t \frac{1}{2}\, \frac{\tau(t')v(t')}{\sqrt{t-t'}}\, dt \qquad [°\mathrm{C}]$$

where T is temperature, t is time, ρ is the rock density, C_p is the thermal capacity, k is the thermal diffusivity, v is the slip velocity and τ is the shear stress. The following values for dolomite (at T = 300 K) were used : ρ = 2900 kg/m^3, C_p = 858 J/kgK, k = 1.9 10^{-6} m^2/s.

The calculation was done for two experiments run at velocity of ~ 1 m/s, normal stress of 17.3 MPa and increasing sliding displacement: ~ 0.1 m for experiment s432, ~ 1 m for experiment s435 (see section 5).

# Exp.T	Grain size (µm)	Normal stress (MPa)	Max. slip vel. (m/s)	Acceleration/ Deceleration (m/s^2)	Total displacement (m)	Sampling frequency (Hz)
s428	<250	13	1.13	6	0.512	25000
s429	<250	13	0.113	6	0.504	2500
s430	<250	17.3	1.13	6	0.504	25000
s431	<250	17.3	1.13	6	0.406	25000
s432	<250	17.3	1.13	6	0.098	25000
s433	<250	17.3	1.13	6	0.249	25000
s434	<250	17.3	1.13	6	0.019	25000
s435	<250	17.3	1.13	6	1.019	25000
s436	<250	17.3	0.113	6	0.105	2500
s437	<250	17.3	0.00113	6	0.219	250
s438	<250	17.3	0.00113	6	0.748	250
s524	<250	17.3	1.13	6	3.548	25000
s525	<250	17.3	0.113	6	0.859	250
s526	<250	26	1.13	6	0.068	25000
s527	<250	17.3	0.000113	6	0.111	250
s648	<250	17.3	0.00113	6	0.37	250

Table 1 Summary of experimental conditions for sixteen experiments performed on dolomite gouge.

4. Results

4.1 Mechanical data and microstructures

At seismic slip rates of 1 m/s and normal stresses of 17.3 MPa, experiments on the dolostone gouge revealed an abrupt reduction of the friction coefficient (μ) from a peak value of 0.7 to a value of 0.4 after ~0.1 m of slip, and 0.25 after ~0.9 m of slip (Fig.2a). The instantaneous frictional power density [$\Phi(t) = \tau(t) V(t)$, where τ is shear stress and V is slip rate] dissipated in the gouge layers reached values of ~ 4–8 MW/m^2 during the constant-velocity part of the experiments (Fig.2a). This was associated with progressive development of a light-reflective, mirror-like slip surface within the gouge layers (Figs.2b-e). Experiments terminated at progressively larger displacements showed an increase in the area of the slip surface with a mirror-like finish (Fig.2a; Fig.3). One experiment performed at a higher normal stress of 26 MPa (s526; see the Table 1), where Φ reached values of >10 MW/m^2, exhibited a well-developed mirror-like slip surface (~40% of the surface area) after only 0.07 m of slip (Fig.4). At the scale of the WLI measurements, the mean roughness amplitude of the experimental mirror-like slip surfaces was ~4 µm (Fig.2c), similar to the mirror-like slip surfaces of the FFZ faults (Fig.1d).

The experimental mirror-like slip surfaces were embedded in a compact, fine-grained layer <20 µm thick, in which deformation was localized (Fig.2e). The layer consisted of partially welded dolostone clasts 0.1–10 µm in size, and larger clasts truncated by the mirror-like slip surfaces (Figs.2d,e), as was observed along faults of the FFZ (Fig.1e).

At intermediate slip rates of 0.1 m/s and normal stresses of 17.3 MPa, only moderate reductions in μ were observed. Instantaneous power density reached ~1 MW/m^2 and the mirror-like slip surfaces were developed after 0.5–0.8 m of slip (Fig.3). At sub-seismic slip rates of 0.0001–0.001 m/s and 17.3 MPa normal stress, the value of μ remained constant at ~0.7 during the experiments, instantaneous power density was 0.008–0.04 MW/m^2 (Fig.5a), and no mirror-like slip surfaces developed after 1 m of slip (Figs.5b-e). WLI analysis showed that slip surfaces formed at sub-seismic velocities had mean roughness amplitude of ~30 µm at the scale of WLI measurements (Fig.5c).

Dolostone gouges deformed at sub-seismic slip velocities were characterized by the presence of an up to 1 mm thick fine-grained layer approaching the slip surface. The deformation within the fine-grained layer was diffusely accommodated by comminution (clast size down to few micrometers or less) and formation of Riedel shears (Figs.5d,e).

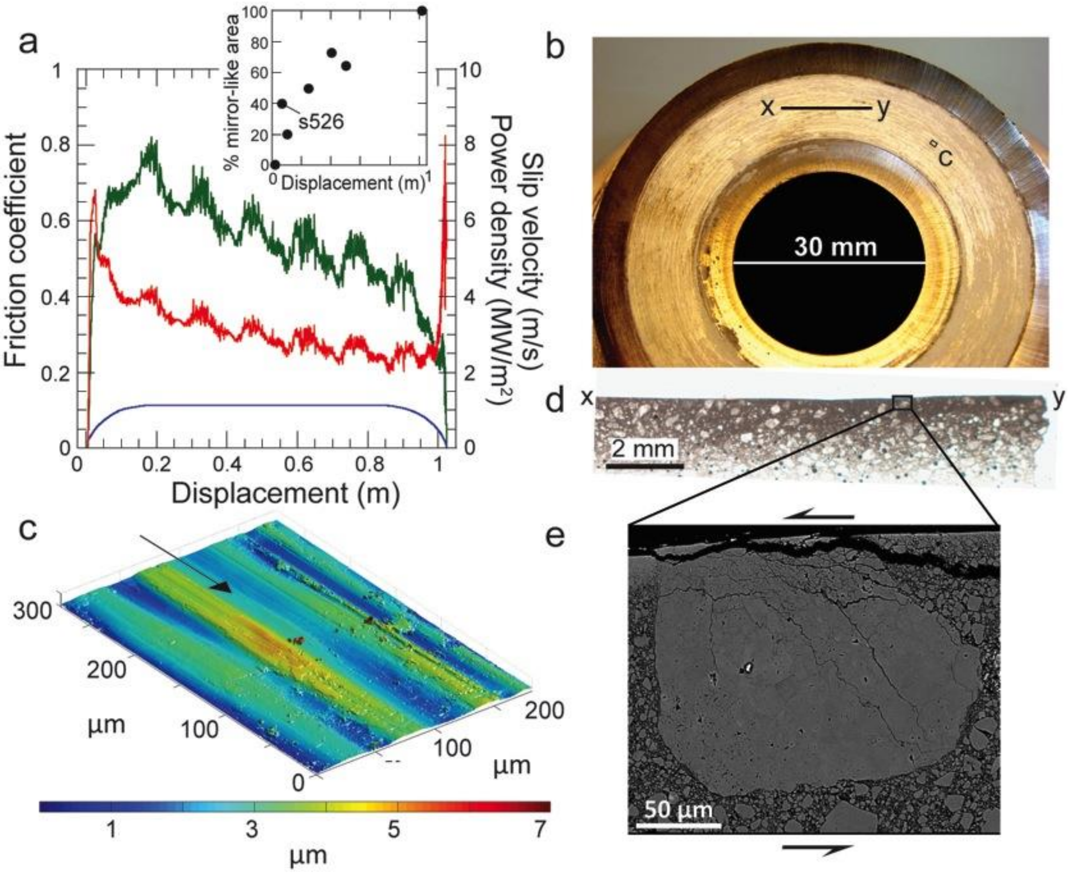

Fig. 2 (next page) Experimental data and mirror-like slip surfaces produced at normal stresses of 17.3 MPa and maximum slip velocities of 1 m/s. (a) Friction coefficient (red curve), slip velocity (blue curve) and frictional power density (green curve) versus displacement for experiment s435 (1 m displacement). The friction coefficient drops from a peak value of 0.68 to ~0.4 after ~0.1 m of slip. Frictional power density is in the range 4–8 MW/m^2 at the target slip velocity. Black circles along the friction curve schematically represent the total displacements of five other experiments (note that the values of the friction coefficient at these data points are not those measured in the experiments) run at identical conditions of normal stress and maximum slip velocity, and one experiment (s526) run at a higher normal stress of 26 MPa (Data Repository). The inset graph plots the percentage of slip surface area with a mirror-like appearance versus displacement. (b) Photograph of mirror-like slip surface produced in experiment s431 (0.4 m slip). In this experiment 73% of the slip surface had a mirror-like appearance. (c) WLI digital elevation model of mirror-like slip surface from experiment s431 over an area of 200×300 μm^2 (see square in Fig.2b). Mean roughness amplitude was ~4 μm. Arrow shows the slip direction. (D) Thin section photomicrograph of dolomite gouge along profile x-y (see Fig. 2b). (E) SEM image (backscattered mode) of large dolomite clast truncated by mirror-like slip surface. The slip surface is surrounded by a compact and ultra-fine grained layer <20 μm thick.

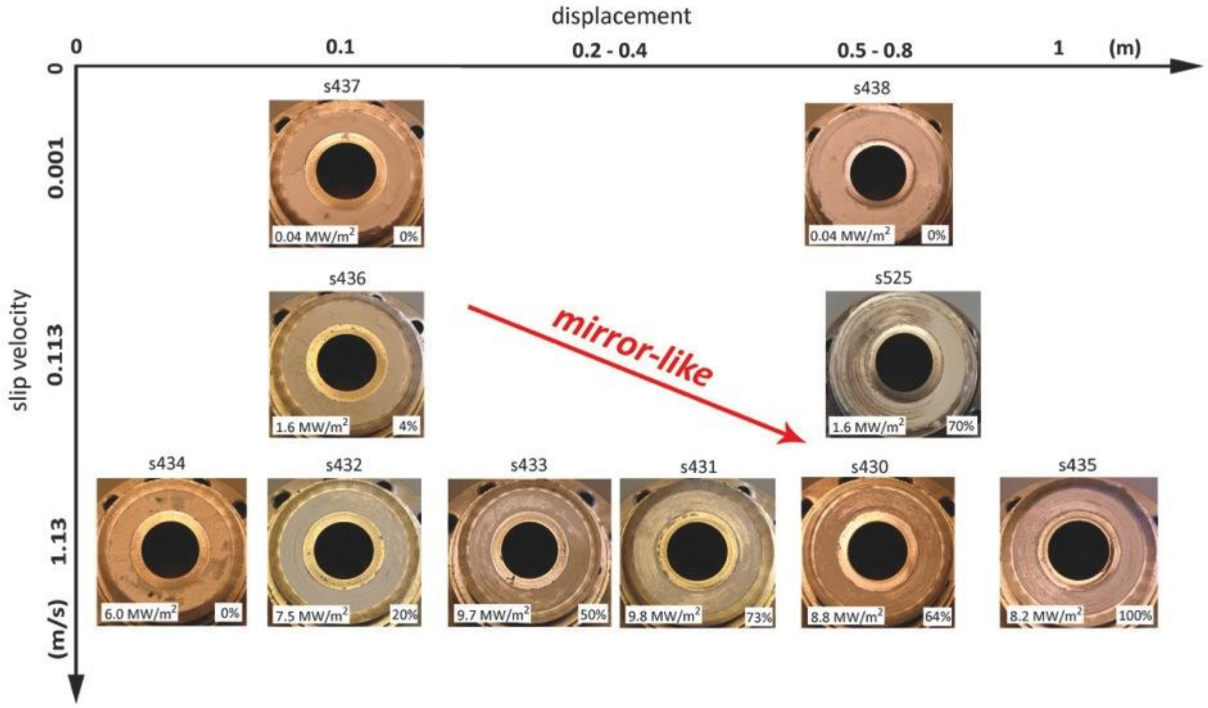

Fig.3 Experimental slip surfaces produced at 17.3 MPa normal stress in the slip velocity range 0.001-1 m/s. For each experiment values of the maximum frictional power density (in MW/m^2) and the percentage of slip surface with a mirror-like appearance are indicated. Mirror-like slip surfaces start to form after 0.5-0.8 m at a slip velocity of 0.1 m/s, but well-developed mirror-like slip surfaces are formed at a maximum slip velocity of 1 m/s for displacements ≥ 0.25 m.

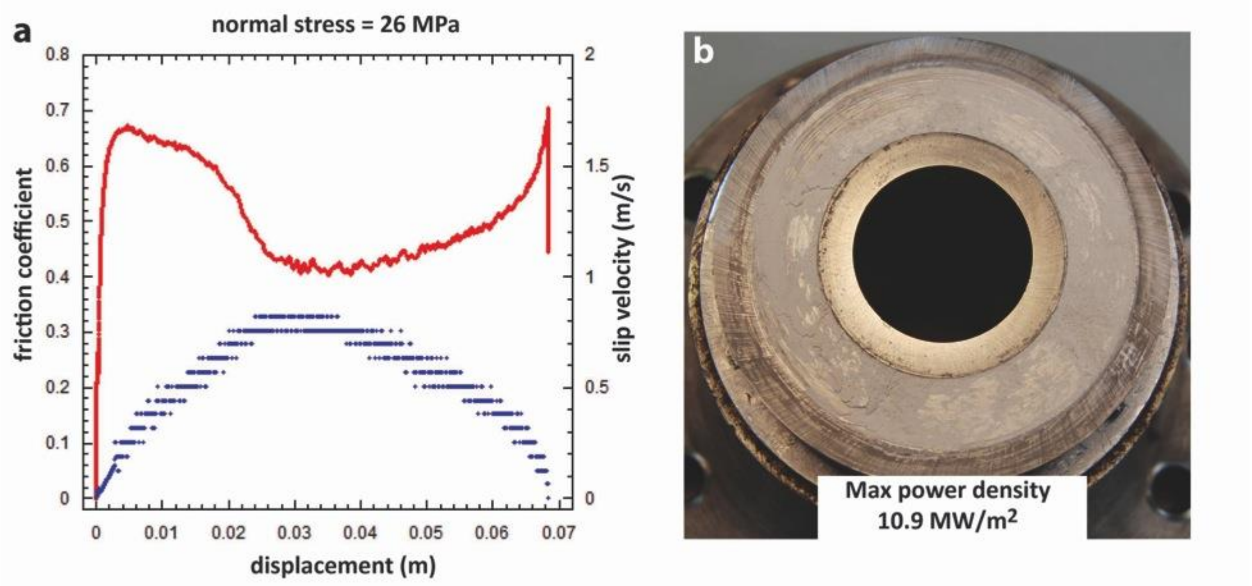

Fig.4 Experiment s526 at 26 MPa normal stress designed to reproduce the estimated deformation conditions during the formation of the mirror-like fault surface shown in Fig.1B. (a) Friction coefficient (red curve) and slip velocity (blue curve) versus displacement. Note that the total displacement was 0.07 m. The friction coefficient drops from a peak value of ~ 0.67 to a minimum value of ~ 0.44 obtained after 0.035 m of displacement. (b) Mirror-like slip surface, covering ~ 40 % of the slip surface area, produced during experiment s526. Maximum frictional power density dissipated in the sample was 10.9 MW/m^2.

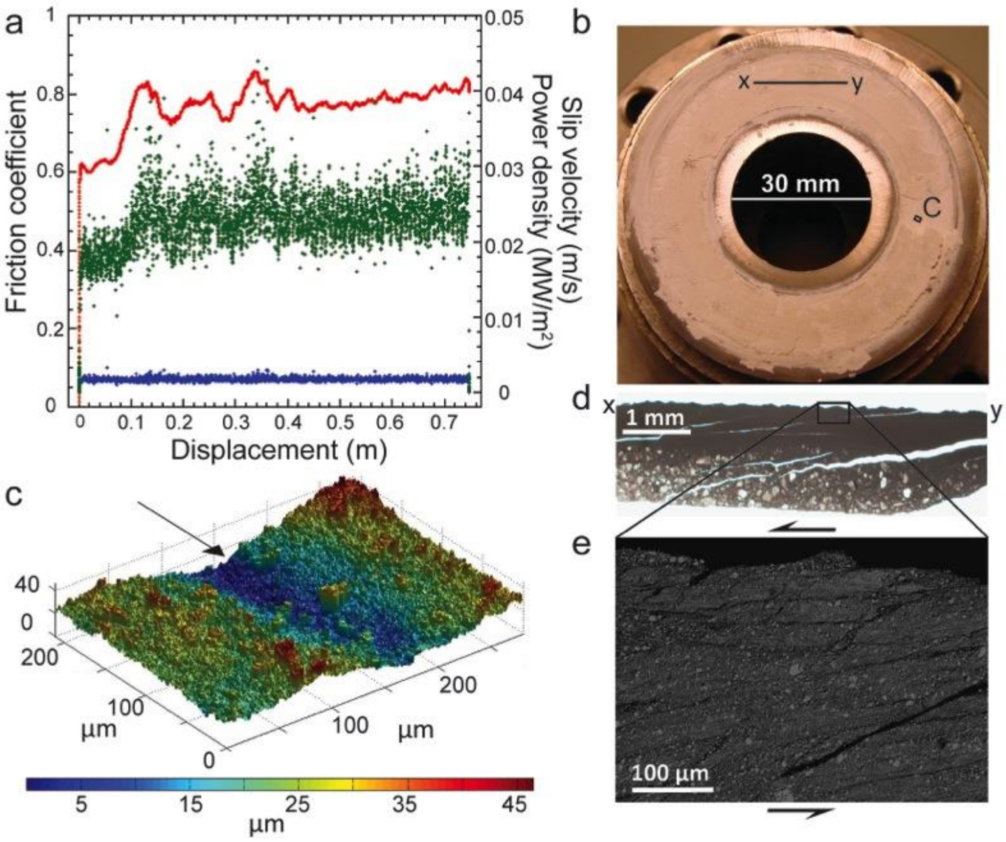

Figure 5. (previous page) Experimental data and slip surfaces produced at maximum slip velocities of 0.001 m/s. (a) Friction coefficient (red curve), slip velocity (blue curve) and frictional power density (green curve) versus displacement for experiment s438. The friction coefficient remained at ~0.7 during the experiment and frictional power density was in the range 0.02–0.03 MW/m^2. (b) Photograph of slip surface produced in experiment s438. The slip surfaces formed at this velocity do not have a mirror-like finish. (c) WLI digital elevation model of slip surface from experiment s438 over an area of 200×300 µm^2 (see square in Fig. 5B). Arrow shows the slip direction. (d) Photomicrograph of thin section of dolomite gouge along profile x-y (see Fig. 5B). (e) SEM image (backscattered mode) of sample s438: deformation was diffusely accommodated by comminution and formation of Riedel shears.

4.2 Mineralogy of the deformed gouge layers

XRPD analyses show that the starting gouge material was composed of 100% dolomite. Dolomite gouges deformed at intermediate to seismic slip velocities (≥ 0.1 m/s) contained up to 12.5 wt% Mg-calcite and up to 4.0 wt% periclase (Fig.6), both of which are typical products of dolomite decarbonation. Mg-calcite and periclase were detected only in the gouges scraped from the mirror-like slip surfaces and not in the samples of bulk gouge. Gouges deformed at sub-seismic slip velocities ≤ 0.001 m/s contain only dolomite both in the bulk gouge and in the gouge scraped from the slip surfaces (Table 2).

Detailed observations of experimental slip zones by Scanning Electron Microscopy (SEM) allowed the recognition of small (< 100 µm in length) elongate patches of nanoparticles lining some of the mirror-like slip surfaces formed at slip rates of 1 m/s. These patches were characterized by a lighter grey color in BSE-SEM images compared with the rest of dolomite gouge, suggesting a different chemical composition. An EMPA-WDS chemical map of the area around one of these patches (experiment s433: v = 1.13 m/s, σ_n = 17.3 MPa, d = 0.25 m) was performed (Fig.7). The chemical analysis indicates that the patch of nanoparticles (light grey material in Fig.7) is relatively enriched in Ca (25.4 wt%) and Mg (13.2 wt%) and depleted in O (43.8 wt%) with respect to the surrounding dolomite gouge (grey in Fig. S5; Ca = 19.0 wt%, Mg = 11.5 wt%, O = 51.5 wt%). The average chemical composition of the patch suggests that it is mainly composed of Mg-calcite and periclase, consistent with the results of XRPD analysis indicating that both of these materials are present along the experimental mirror-like surfaces.

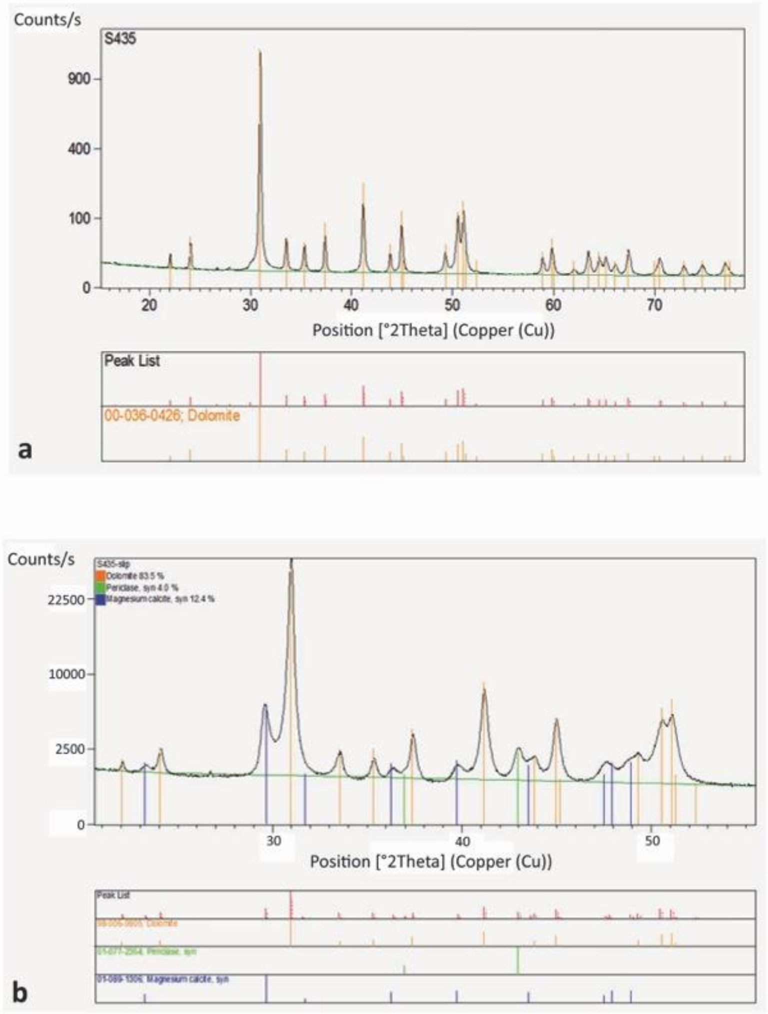

Fig.6 X-ray diffractograms for experimental sample s435 (experimental conditions: slip vel. = 1.13 m/s, normal stress = 17.3 MPa, displacement = 1 m). (a) Diffractogram of sample s435 bulk gouge. The gouge consists of 100 wt% dolomite. (b) Diffractogram of sample s435 for gouge immediately adjacent to mirror-like surface, collected by scraping along the mirror-like slip surface. The gouge consists of dolomite (83.5 wt%), Mg-calcite (12.4 wt%) and periclase (4.0 wt%).

# Exp.	Slip velocity (m/s)	Normal stress (MPa)	Displacement (m)	Mineralogy (%)
s430	1.13	17.3	0.504	Dol (93.8), Mg-cal (6.1), Per (0.1)
s433	1.13	17.3	0.249	Dol (94.6), Mg-cal (4.6), Per (0.8)
s435	1.13	17.3	1.019	Dol (83.5), Mg-cal (12.4), Per (4.0)
s438	0.00113	17.3	0.748	Dol (100)
s525	0.113	17.3	0.859	Dol (98.8), Mg-cal (1.0), Per (0.2)

Table 2 Summary of XRPD quantitative (Rietveld method) analyses performed on dolomite gouges recovered after five experiments. The mineralogy in the last column refers only to gouges collected by scraping material from the experimental slip surfaces (not samples of bulk gouge). The program High Score Plus (PANalytical) was used for phase identificati

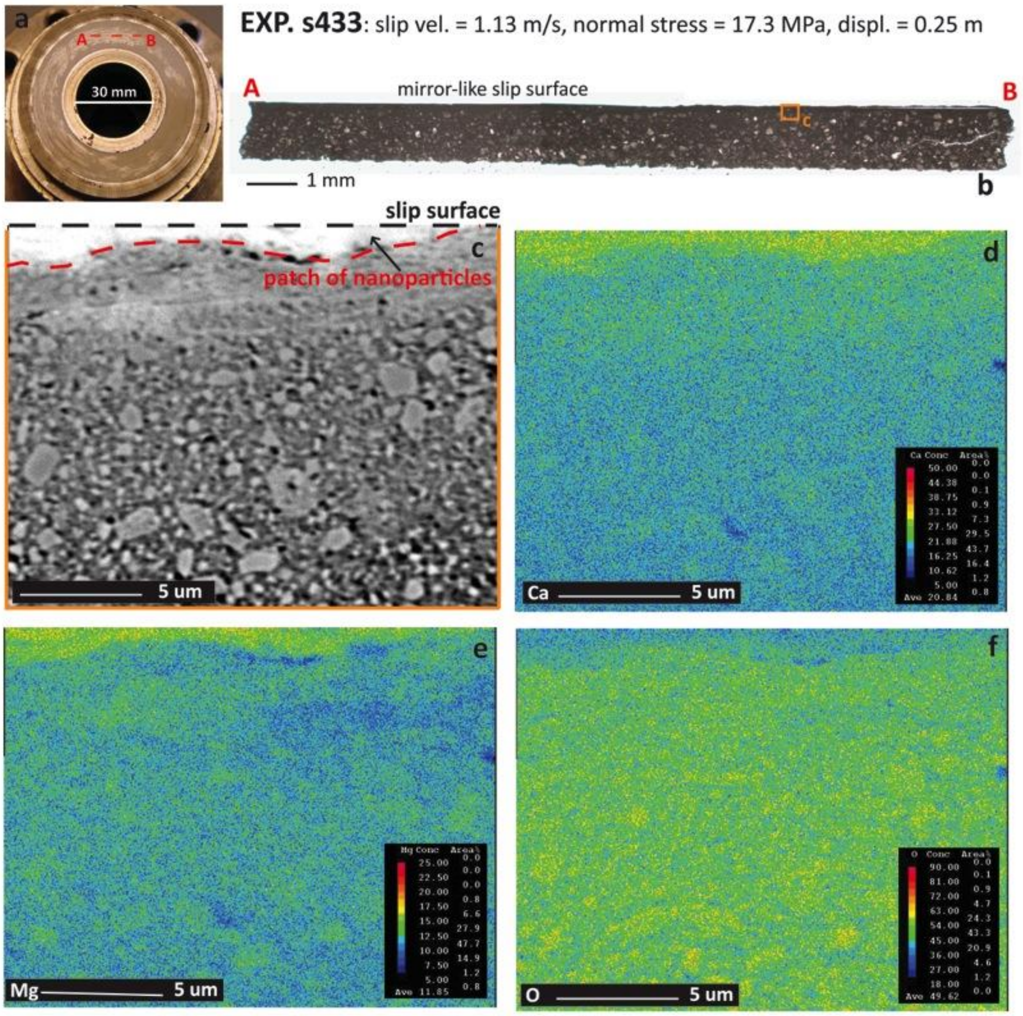

Fig.7 EMP-WDS chemical map for experimental sample s433. (a) Mirror-like slip surface recovered after experiment s433. (b) Thin section scan of sample s433 cut along profile A-B (see Fig.7a). (c) BSE-SEM image of the area covered by the EMP-WDS chemical map (see inset in Fig.7b for map location within the sample). The patch of nanoparticles is light grey in colour to white and is immediately below the mirror-like slip surface (see the black arrow). (d-f) Chemical maps of the concentration of Ca, Mg and O. The patch of nanoparticles is clearly distinguishable in all three maps: it is relatively enriched in Ca and Mg and depleted in O with respect to the surrounding dolomite gouge.

4.3 Slip surface roughness and power dissipation

The root mean square (RMS) roughness (Candela et al., 2009) was computed at all scales accessible to WLI (0.2–250 µm) for slip surfaces from high-, intermediate- and low-velocity experiments. The analysis showed that for the same displacement and normal stress, the slip surfaces became smoother with increasing slip velocity (i.e., RMS curves are at a lower vertical position in Fig.8a inset). The roughness of the slip surfaces developed at 1 m/s was closest to the natural mirror-like surfaces from the Foiana Fault Zone (Fig.8a). According to the Rayleigh roughness criterion, a surface will reflect specularly natural light (wavelength 550 nm) if the RMS roughness is <100 nm at a length scale L = 550 nm (Beckmann and Spizzichino, 1963; Siman-Tov et al., 2013). Indeed, both the natural and experimental slip surfaces with a mirror-like appearance reported here (the latter associated with Φ = 4–10 MW/m^2) meet this criterion (Fig.8a). In contrast, experimental slip surfaces formed at sub-seismic slip velocities and lacking a mirror-like finish have RMS roughness >100 nm at L = 550 nm (Fig.8a).

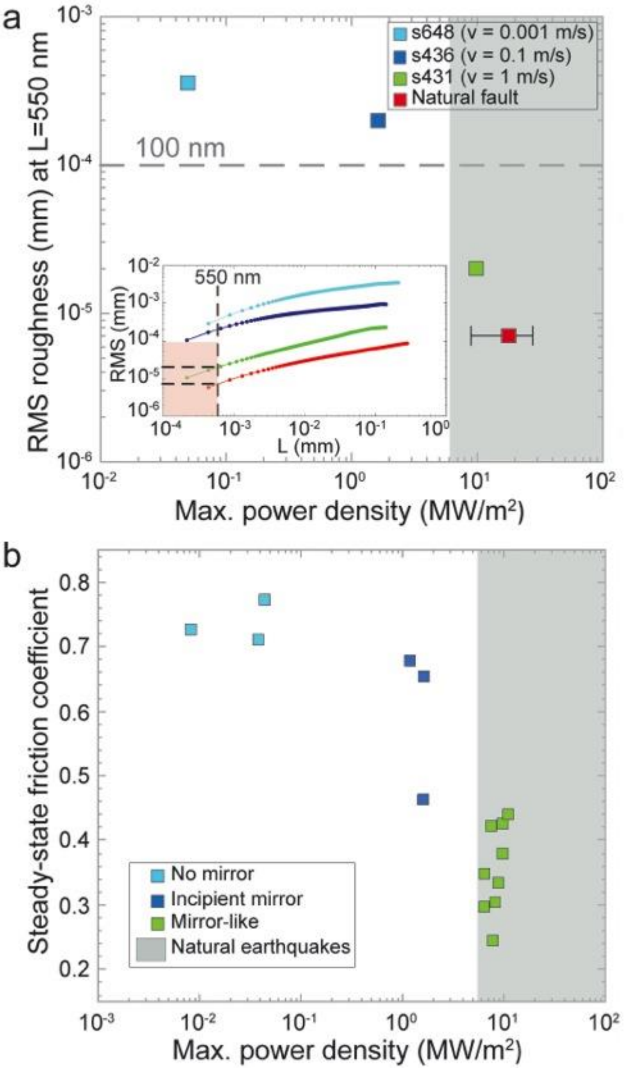

Fig.8 Slip surface roughness and power dissipation. (a) root mean square (RMS) roughness (at L = 550 nm) versus maximum power density (definition in text) for experimental samples at sub-seismic (s648), intermediate (s436), and seismic (s431) slip velocities, and comparison to natural slip surface. Natural and experimental mirror-like slip surfaces obey the Rayleigh criterion with RMS roughness <100 nm at L = 550 nm. For the natural slip surface power density values were estimated in the range 9–27 MW/m^2 (error bar in the plot; 18 MW/m^2 is the mean value) assuming a range of normal stress of 30–90 MPa (calculated as explained in section 3.1 by varying pore pressure from hydrostatic to zero), a representative seismic slip velocity of 1 m/s and a dynamic friction coefficient of 0.3 (obtained in our experiments). Shading (grey in color) shows range of power densities expected for natural earthquakes (Sibson, 1980). The inset plot shows the RMS roughness curves of the samples for length scales of 0.2–250 µm. Shading (red in color) indicates the conditions for which the Rayleigh criterion is met. (b) Steady-state friction coefficient (measured at maximum slip velocity) versus maximum power density. Mirror-like slip surfaces start to develop above a power density threshold of ~1 MW/m^2, but well-developed mirror-like slip surfaces are associated with power densities in the range 5–10 MW/m^2.

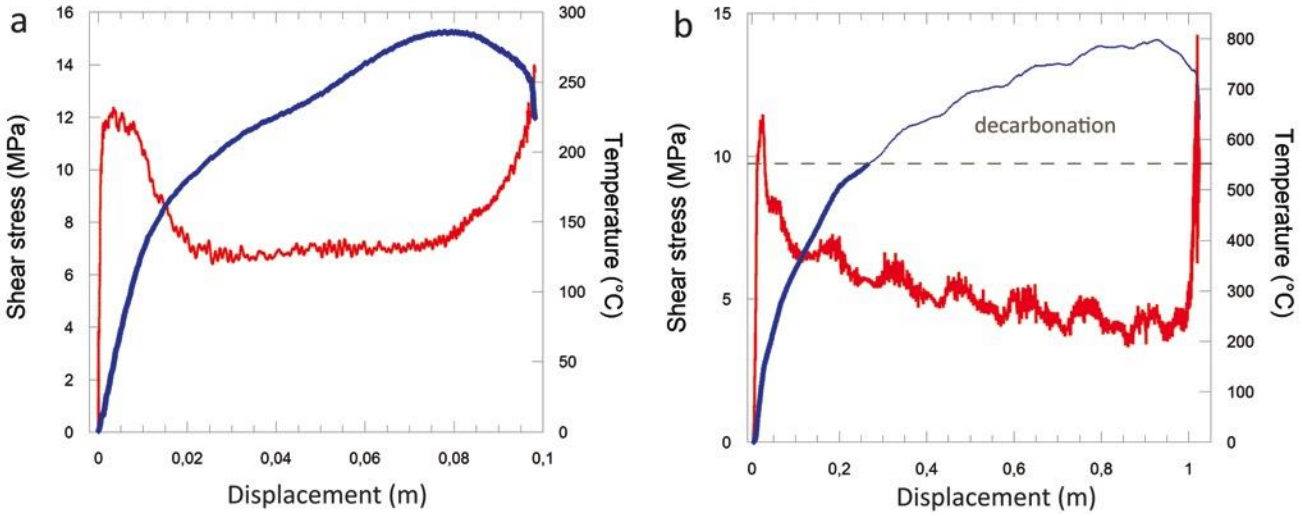

Fig.9 Temperatures calculated using the 1D heat diffusion equation of Carslaw and Jaeger (1959). These calculations do not consider any heat sinks as endothermic chemical reactions or heat radiation. (a) Shear stress (red curve) and calculated temperature evolution (blue curve) during experiment s432 (slip rate = 1.13 m/s, normal stress = 17.3 MPa, slip ~ 0.1 m, see Table 1). (b) Shear stress (red curve) and calculated temperature evolution (blue curve) during experiment s435 (slip rate = 1.13 m/s, normal stress = 17.3 MPa, slip ~ 1 m, see Table 1). It is likely that above 550 °C calculated temperatures along the slip surface are higher than the real ones due to the activation of dolomite decarbonation reactions which represent efficient heat sinks. To highlight this point temperature evolution above 550 °C is represented with a thinner blue curve.

5. Discussion and conclusions

Experimental results demonstrate that mirror-like slip surfaces started to develop in dolostone gouges when Φ exceeded a threshold value of ~1 MW/m^2 (i.e., slip rate ≥ 0.1 m/s for the applied normal stresses) (Fig.8b). However, the mirror-like surfaces along the FFZ have measured displacements as small as 0.04 m. At similar experimental displacements mirror-like slip surfaces were formed only when the target slip velocity was ~1 m/s and Φ approached values in the range of natural earthquakes (10–100 MW/m^2; Sibson, 1980) (Fig.8b).

Frictional power density dissipated in slip zones is a key parameter controlling the rate of change of temperature [$dT/dt \propto \Phi(t)$] and the onset of certain mechanically and thermally activated weakening processes (Di Toro et al., 2011; Sibson, 1980). Assuming that slip was entirely accommodated along the mirror-like slip surface once it formed, the maximum bulk temperature increase for two experimental samples (slip rate of ~1 m/s; mirror-like slip surfaces developed) was calculated (see section 3.6). In experiment s432 (normal stress = 17.3 MPa, slip = 0.1 m), the bulk temperature along the slip surface was ~200 °C after 0.02 m of slip, when a significant drop in shear stress occurred (Fig.9a). In experiment s435 (normal stress = 17.3 MPa, slip = 1 m), the temperature was ~600 °C after 0.3 m of slip, when a low value of shear stress was attained, increasing to ~750 °C after 1 m of slip (Fig.9b). Temperatures of 200–300 °C are consistent with the activation of crystal plasticity and sintering processes within the fine-grained gouges (grain sizes ≤ 1 µm) (Holyoke et al., 2013, and references therein), whereas temperatures above ~550 °C are associated with the formation of periclase and Mg-calcite from dolomite decomposition reactions (De Paola et al., 2011; Samtani et al., 2002). The similarity in microstructural characteristics and surface roughness suggests that extrapolation of the experimental results to the natural mirror-like slip surfaces of the Foiana Fault Zone is reliable, and that the natural mirror-like surfaces represent past seismic events.

The Foiana Fault Zone is exposed for c. 30 km along strike (see section 3 of Chapter 2), and individual mirror-like slip surfaces have estimated lengths of 30–300 m. Empirical length-magnitude scaling relationships (e.g. Wells and Coppersmith, 1994) indicate that the FFZ and the mirror-like surfaces may have hosted earthquake ruptures from M_w 2 to M_w 6.5 associated with average co-seismic slips ranging, respectively, from 0.01 to 0.5 m. Thus, even the mirror-like slip surfaces with the smallest measured displacements (0.04 m) may represent multiple slip events.

Mirror-like slip surfaces have been reported from other exhumed fault zones in both carbonate- and silicate- host rocks (e.g. Power and Tullis, 1989; Siman-Tov et al., 2013). Experimental results of this study indicate that small-displacement mirror-like slip surfaces in dolostone gouges represent a geological marker of seismic slip. Both the low frictional power density and relatively diffuse deformation occurring in dolostone gouges at sub-seismic slip rates suggest that mirror-like slip surfaces are unlikely to be formed at these slip rates even after larger displacements (i.e., tens to hundreds of meters). As a consequence, since active faults can also creep aseismically, the occurrence of mirror-like faults cutting dolostone gouges could be used to assess seismic hazard in areas with incomplete earthquake catalogues.

Chapter 4. Origin of in-situ shattered dolostones

Abstract

The occurrence of up to hundreds of meters thick belts of in-situ shattered dolostones is reported along the major transpressive Foiana Fault Zone exhumed from 1.5-2 km depth (FFZ, Italian Southern Alps). In situ-shattered dolostones are intensely damaged rocks reduced in fragments from few centimeters down to few millimeters in size passing to fine-grained layers in proximity to mirror-like faults. The main characteristic of the in-situ shattered dolostones is the absence of significant shear strain from the macro- to the microscale. To understand the origin of the in-situ shattered dolostones of the FFZ, dolostones of the Mendola Formation (i.e. host rock of the FFZ) were deformed in uniaxial compression both under low-strain rate (~ 10^{-3} s^{-1}) quasi-static loading and high-strain rate (> 50 s^{-1}) dynamic loading. Dolostones deformed up to failure under low-strain rate loading were affected by several discrete (i.e. not interconnected) extensional fractures sub-parallel to the loading direction. Dolostones deformed under high-strain rate loading start to be shattered over a strain rate threshold of ~ 200 s^{-1}, while they were split in few fragments or were macroscopically intact for lower strain rates. Experimentally shattered dolostones were reduced in to an non-cohesive material with rock fragments mostly of few millimeters in size elongated parallel to the loading direction. Diffuse microfracturing exploiting crystal boundaries and cleavage planes occurred along the main fractures. Qualitatively, the damage pattern of the experimentally shattered dolostones compares well with that of natural in-situ shattered dolostones of the FFZ. Moreover since shattered dolostones are produced only under high strain rate dynamic loading the in-situ shattered dolostones of the FFZ are interpreted to be possibly formed due to the cumulative effect of dynamic stress wave loading during the propagation of multiple earthquake ruptures. Finally since at similar seismic strain rates other lithologies, such as granites, were observed to be pulverized (i.e. shattered to smaller grain size, < 1 mm on average; e.g. Doan and Gary, 2009), the difference in the resulting damage pattern is discussed in terms of the higher mechanical and microstructural heterogeneity of the tested dolostones with respect to granites. However, further microstructural and mechanical work is needed to better understand the origin of in-situ shattering in dolostones.

This study was performed in collaboration with Mai-Linh Doan and Michele Secco. The material presented here was discussed with Mai-Linh Doan, Giulio Di Toro, Fabio Ferri and Steven Smith.

1. Introduction

Simplified models of the architecture of fault zones define a fault core, in which most of the fault displacement and shear strain is accommodated, bounded by a damage zone that passes laterally in to host rock affected by background deformation (Chester et al., 1993; Antonellini and Aydin, 1994; Caine et al., 1996; Childs et al., 2009). The fault core typically consists of tabular or lens-shaped volumes of fault rock (e.g. cataclasites, ultracataclasites, fault breccias, gouges; Sibson, 1977, 2003) delimited by variably localized slip zones. The damage zone is up to hundreds of meters thick and consists of secondary faults, fractures and veins delimiting relatively undeformed rock volumes (Cowie and Scholz, 1992; Billi et al., 2003; Mitchell and Faulkner, 2009).

Recent studies have reported the occurrence of up to hundreds of meters thick belts of pulverized rocks along large strike-slip faults as a peculiar example of fault-related damage (Brune, 2001; Dor, 2006a, 2006b, 2009; Rockwell et al., 2009; Mitchell et al., 2011). Pulverized rocks exhibit pervasive extensional microfracturing with rock fragments smaller than the original crystal/grain size of the intact rock (mostly smaller than 1 mm), while the primary structure of the host rock is preserved without significant shear strain. These characteristics indicate that pulverized rocks are shattered in-situ.

The origin of pulverized rocks is still debated, but most theories assume they are related to coseismic damage due to the off-fault stress perturbations produced in the wall rocks by the propagation of earthquake ruptures (Ben-Zion and Shi, 2005; Reches and Dewers, 2005). In addition experimental data suggest that rock pulverization is produced only at high strain rates (> 100 s^{-1}) which are attainable during the passage of high-frequency (i.e., 10-100 Hz) seismic waves (Doan and Gary, 2009; Doan and Billi, 2011; Yuan et al., 2011).

To date, pulverized rocks have been reported only within crystalline (i.e., igneous or metamorphic) host rocks (e.g., Brune et al, 2001; Wilson et al., 2005; Dor et al., 2006, 2009; Mitchell et al., 2011) with the exception of a sandstone outcrop along the San Andreas Fault (Dor et al., 2009). The only example of fault rocks termed as pulverized within carbonate host rocks was reported by Agosta et al. (2006) along the Venere Fault (Central Apennines, Italy). The so called pulverized rocks are a 1 m thick band of finely comminuted (maximum rock fragment size ~ 1 cm) limestones with preserved sedimentary bedding and parallel to the fault core. The pulverized limestones of the Venere Fault show larger average grain size with respect to the typical pulverized rocks found in silicate-built host rocks. Moreover the occurrence of low-strain fault-related breccias with rock fragments larger than 1 cm is relatively common within carbonate damage zones and their origin was generally related to the quasi-static growth of the fault zones (Billi et al., 2003; Salvini et al., 1999) rather than to the effect of past earthquake ruptures.

In this thesis (Chapter 2 section 3) I described the occurrence of large volumes (up to more than 300 m) of in-situ shattered dolostones within the Foiana Fault Zone (FFZ) (Italian Southern Alps). The FFZ consists almost entirely of fragmented dolostones reduced in rock fragments from few centimeters down to few millimeters in size. The fragmented dolostones are locally cut by very discrete faults with mirror-like slip surfaces lined by up to few centimeters thick fine-grained rock layers. Both the fragmented dolostones and the fine-grained rock layers exhibit pervasive extensional fracturing from the centimeter to the micrometer scale and absence of significant shear strain. Since it was demonstrated through a dedicated experimental study (see Chapter 3 of this thesis) that mirror-like slip surfaces similar to those found along the FFZ form only at seismic deformation conditions, the occurrence of in-situ shattered dolostones was interpreted as an evidence of coseismic damage.

To investigate the origin of in-situ shattered dolostones of the FFZ low- to high-strain rate uniaxial compressive tests were performed on dolostone rock cylinders of the Mendola Formation (host rock of the FFZ). After presenting the experimental and analytical methods of this study, I will describe both mechanical data of the tests and the resulting damage fabrics of the dolostone. Lastly I will compare the experimental results of my study (1) with those from previous experiments performed on different rocks (Carrara marble and Westerly and Tarn granite) and (2) with field observations of natural in-situ shattered dolostones of the FFZ.

2. Experimental and analytical methods

High-strain rate uniaxial compressive tests were performed with a Split Hopkinson Pressure Bar (SHPB) apparatus installed at the laboratory of the Institut des Sciences de la Terre, Grenoble, France. This device allowed to deform dolostone rock cylinders under dynamic stress wave loading (strain rates > 50 s^{-1}) with the aim of reproducing the extreme deformation conditions experienced in the wall rocks of a propagating seismic rupture.

Low-strain rate uniaxial compressive tests were run with a servo-controlled oil press at the Dipartimento di Geoscienze, Padova, Italy. This apparatus allowed to deform dolostone rock cylinders under quasi-static loading (strain rate ~ 10^{-3} s^{-1}).

Some of the rock cylinders were wrapped with a heat-shrinkable plastic jacket before the tests and were then recovered for microstructural characterization. Some of the recovered samples were analyzed by X-ray microtomography (micro CT) at the Dipartimento di Geoscienze in Padova (see section 2.4). The other samples were impregnated with epoxy and cut to produce polished thin sections both parallel and perpendicular to the loading direction. Observations of the thin sections were performed both by optical (OM) and scanning electron microscopy (SEM) at the Dipartimento di Geoscienze in Padova.

2.1 Sample collection and preparation

Intact blocks of dolostone of the Mendola Formation were collected at an outcrop located ~ 3 km to the east of the FFZ (Fig.1) and worked at the Dipartimento di Geoscienze in Padova. The outcropping dolostones were organized in sub-horizontal benches up to 0.5 m thick without evidence of macroscopic deformation (i.e. no faults, joints and veins). At the sub-centimeter scale the dolostones were quite heterogeneous since they were typically characterized by stromatolitic laminations, planar trails of fenestrae (up to several millimeters in size) and bioclastic layers. The dolostone blocks were cut with the saw in few centimeter-thick slices and the most crystalline and homogeneous (e.g., without visible cracks) were selected for coring to produce solid cylinders with diameters of ~ 20 mm, ~ 15 mm and ~ 10 mm. The bases of the rock cylinders were rectified using a lathe to obtain length (L) to diameter (D) ratio L/D ~ 1.

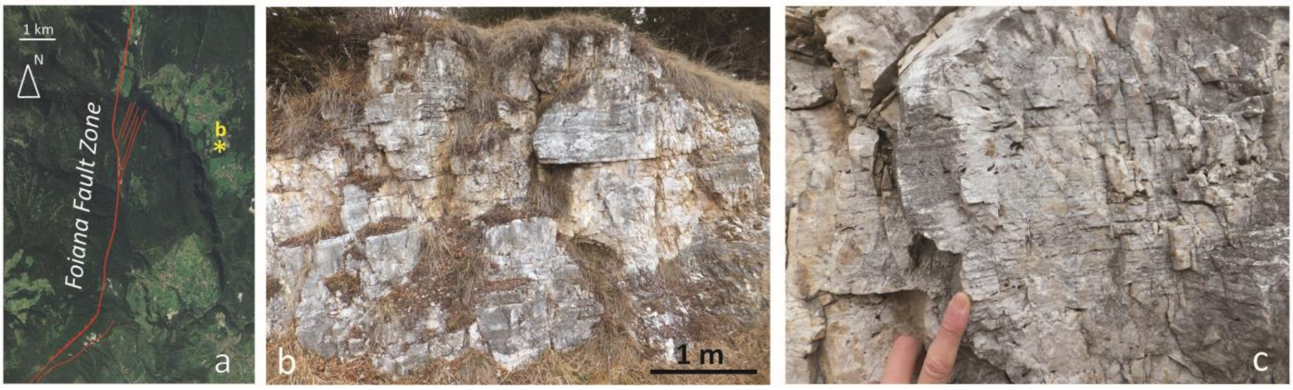

Fig.1 (a) Aerial view of the area around the Foiana Fault Zone (FFZ). Fault strands of the FFZ are represented with red lines. The yellow star indicates the location of the outcrop shown in (b) where dolostone blocks were collected. (b) Outcrop of dolostones of the Mendola Formation. (c) Detail of a typical facies of the dolostones of the Mendola Formation characterized by stromatolitic laminations and planar trails of fenestrae.

2.2 Experimental devices and procedures

Twenty-one high-strain rate uniaxial compressive tests were performed with the Split Hopkinson Pressure Bar apparatus shown in Fig.2 (list of tests in the results section, Table 1). The loading device consists of a spring gun and three aligned steel bars of 20 mm in diameter (the striker, the input bar and the output bar) which are free to move inside of virtually frictionless Teflon rings. The rock cylinder is placed between the input and output bars prior to the test. During the test the incident bar is impacted by the striker and the sample is loaded by the stress wave propagating along the bar. The incident stress wave splits into reflected and transmitted waves when it reaches the sample. The incident, reflected and transmitted waves are measured with strain gauges mounted on the input and output bars. In all the experiments reported here the striker was launched by a spring gun, whose spring was shortened up to 5.5 cm and then released to give a single, high energy loading pulse (average striker speed = 4.71 m/s). The SHPB is not servo-controlled, and the actual loading history depends on the sample. In particular given the approximately same momentum (product of the mass and impact velocity) of the striker, to investigate the role of the stress transmitted to the sample at the impact, we performed experiments on rock cylinders with diameters of ~ 20 mm, ~ 15 mm and ~ 10 mm, respectively. Moreover since the momentum, the loading duration and hence the strain experienced by the sample is controlled by the length of the striker, tests were conducted with strikers of 20 cm, 15 cm and 10 cm in length. In some experiments, a paper sheet was inserted at the entry extremity of the input bar (where the striker impacts with the input bar, Fig 2), which acted as a pulse shaper smoothing out the loading and hence reducing the strain rate.

The low-strain rate uniaxial compressive tests were run with a compressive testing machine (manufactured by Controls, model: 50-C6600) connected to a servo-hydraulic control system (Advantest 9) which can work up to a maximum oil pressure of 70 MPa. This device allows to press cylindrical or cubic samples between platens with diameter of 305 mm (Fig.3). Six tests were conducted on dolostone rock cylinders with diameter of 20 mm and loading rate of 0.2 MPa/s. Axial and radial strains were measured by two foil strain gauges , one parallel and one perpendicular to the loading axis, mounted on the rock cylinders (Fig. 3). Tests lasted up to the failure of the samples. A limit of the testing machine was the application of a pre-loading of 30 MPa to the sample but without recording of the strain data. Therefore the first phase of sample deformation was not documented.

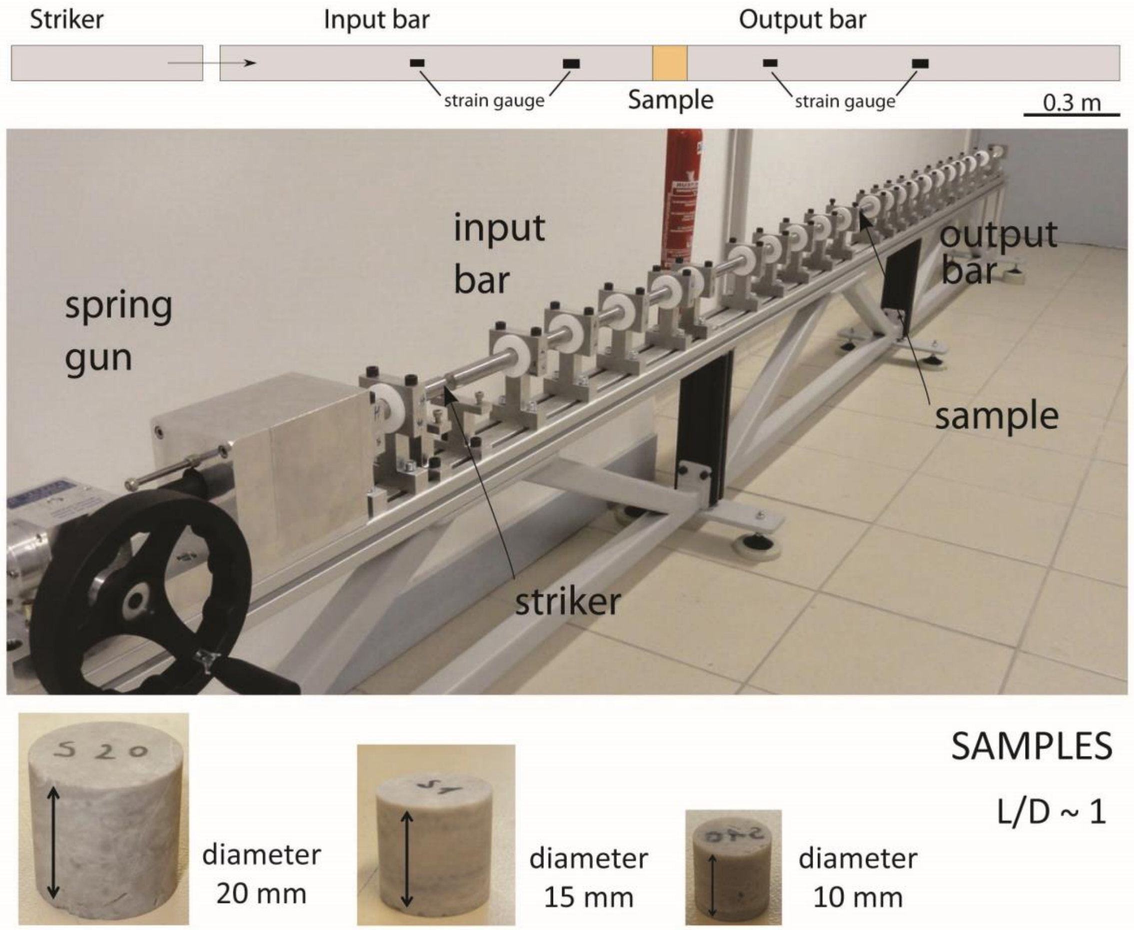

Fig.2 Image of the Split Hopinson Pressure Bar at IsTerre, Grenoble. The apparatus is ~ 4 m long and consists of a spring gun and three steel bars. The striker bar has variable length of 10 cm, 15 cm or 20 cm, while the input and output bars are 1.5 m long. The sample is inserted between the input and output bars. Rock cylinders with three diameters were tested: ~ 20 mm, ~ 15 mm and ~ 10 mm. In all samples, length vs. diameter ratio was ~ 1.

2.3 Data processing

In the SHPB tests strains associated with the passage of the incident, reflected and transmitted waves were measured at the strain gauges located along the input and output bars (Fig. 2). Classical processing of the SPHB data assumes 1D propagation of elastic waves. Strain and stress acting on the samples were recovered from the force and displacement at the edges of the bars. Calibration of the strain signals and calculation of the stress, strain and strain rate vs. time history of the sample was done basing on 1D elastic wave propagation equations and using a Matlab script suite realized by Mai-Lihn Doan.

In the low-strain rate uniaxial compressive tests axial and radial strains were measured at the strain gauges mounted on the sample while compressive stress directly resulted from the applied loading rate (usually 0.2 MPa/s). Calibration of the strain gauges recording channels was managed through the main control unit (Advantest 9).

2.4 X-ray microtomography

X-ray microtomography imaging of both intact and deformed samples was realized with a Skyscan1172 tomograph installed at the Dipartimento di Geoscienze in Padova. The microanalytical device is equipped with a X-ray source with voltage range of 20-100 kV, power range of 8-10 W and a CCD detector with 11×10^6 pixels. Only dolostone cylinders with diameter of ~ 10 mm were scanned, because larger samples (i.e., diameters of ~ 15 mm and ~ 20 mm) did not allow to reach spatial resolution < 10 µm. Therefore samples deformed in low-strain rate uniaxial compressive tests (diameter ~ 20 mm) were not scanned. The scans of the samples were performed with the following setup parameters: source voltage = 89 kV, sample to source distance = 94.69 mm, detector to source distance = 210.25 mm. This results in sample images with a pixel size (spatial resolution) of 8.04 µm. Reconstructions of the grey-level images of the sample slices (spacing of the slices along the vertical axis = 8 µm) were performed with the Skyscan software NRecon.

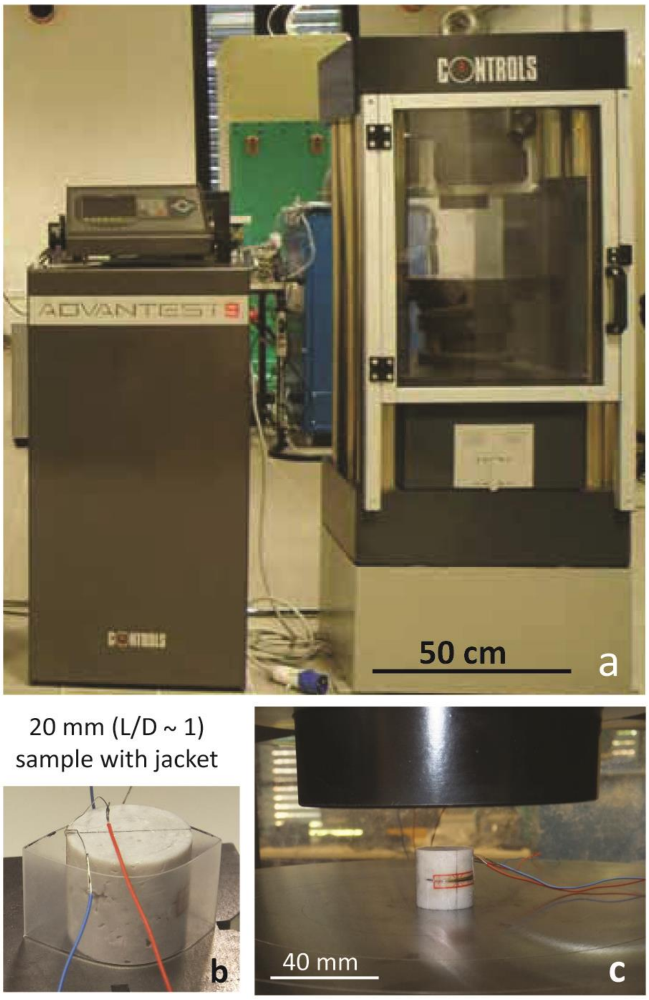

Fig.3 (a) Uniaxial compressive testing machine (manufactured by Controls, model: 50-C6600) to the rigth and a servo-hydraulic control system (Advantest 9) to the left (Dipartimento di Geoscienze, Padova). See the main text for details. (b) Rock cylinders with diameter ~ 20 mm and length diameter ratio ~ 1 with plastic jacket. The jacket is heated to shrink around the sample before the test. (c) Sample without jacket installed in the machine before application of the normal load. Strain gauges, one parallel and one perpendicular (the latter is not visible in the photo) to the loading direction (parallel to the axis of the cylinder) are attached to the sample.

3. Results

3.1 Mechanical data and damage patterns

3.1.1 High-strain rate uniaxial compressive tests

Samples recovered after the SHPB tests show three main states of damage: (i) apparently intact samples with no evidence of macroscopic fractures; (ii) samples axially split in few (less than five) fragments; (iii) samples shattered in multiple fragments mostly of few millimeters in size (Fig.4).

Samples with diameter of ~ 20 mm were all intact after the tests, samples with diameter of ~ 15 mm were intact and split, while samples with diameter of ~ 10 mm were both intact, split and shattered (Table 1). The loading phase of the samples shows variable trends likely related to the heterogeneity of the tested material (Fig.5). Average Young modulus calculated for samples with diameter of ~ 20 mm, which due to their larger size should be less influenced by heterogeneity effects, is ~ 40 GPa. Maximum stress is generally less than 100 MPa for intact samples and in the range 90-123 MPa for split samples. Maximum stress for pulverized samples is largely variable in the range 92-223 MPa (Fig.6a). All tests show a permanent strain, therefore also apparent intact samples were likely to be affected by microfracturing. Samples were split when strain exceeded 0.38%, whereas shattered samples accommodated strains beyond 1%. Fig. 6b shows the maximum strain rate versus maximum true strain of all the tests. Samples start to be effectively shattered over a strain rate threshold around 200 s^{-1}. Sample S7 (maximum strain rate = 184 s^{-1}) represents a transition from splitting to shattering (i.e. incipient shattering Fig.6b). Sample S11 (maximum strain rate = 270 s^{-1}) is macroscopically intact but starts to be shattered at one edge (Fig.6b). Sample S11 is stiffer with respect to other samples and highlights the strong mechanical heterogeneity of the tested dolostones.

Sample	Diameter (mm)	Jacket	Striker length (cm)	Pulse shaper	Max. stress (MPa)	Max. strain (%)	Max. strain rate (1/s)	State after the test
S1	15	yes	20	no	101	0.8	188	Intact
S2	15	no	20	no	103	0.4	111	Split
S3	15	yes	20	no	90	0.1	87	Split
S4	10	yes	20	no	158	1.8	238	Shattered
S5	10	no	20	no	111	1.7	201	Shattered
S7	10	yes	20	yes	165	1.1	184	Shattered (incipient)
S10	10	no	15	no	92	1.5	250	Shattered
S11	10	yes	15	no	223	0.8	270	Intact
S12	10	yes	10	no	77	0.6	176	Intact
S13	10	no	10	no	124	0.5	143	Split
S14	15	no	15	no	93	0.4	115	Split
S15	15	yes	15	no	104	0.4	125	Intact
S16	15	no	10	no	69	0.3	108	Intact
S18	15	yes	10	no	53	0.2	86	Intact
S19	20	no	10	no	38	0.2	72	Intact
S21	20	no	20	no	58	0.3	106	Intact
S22	20	yes	20	no	56	0.3	112	Intact
S24	20	yes	15	no	57	0.4	123	Intact
S25	20	no	15	no	58	0.2	101	Intact
S26	10	yes	20	no	184	1.4	268	Shattered
S28	10	yes	20	yes	213	0.5	104	Intact

Table 1 Summary of experimental data for high-strain rate uniaxial compression test with the Split Hopkinson Pressure Bar

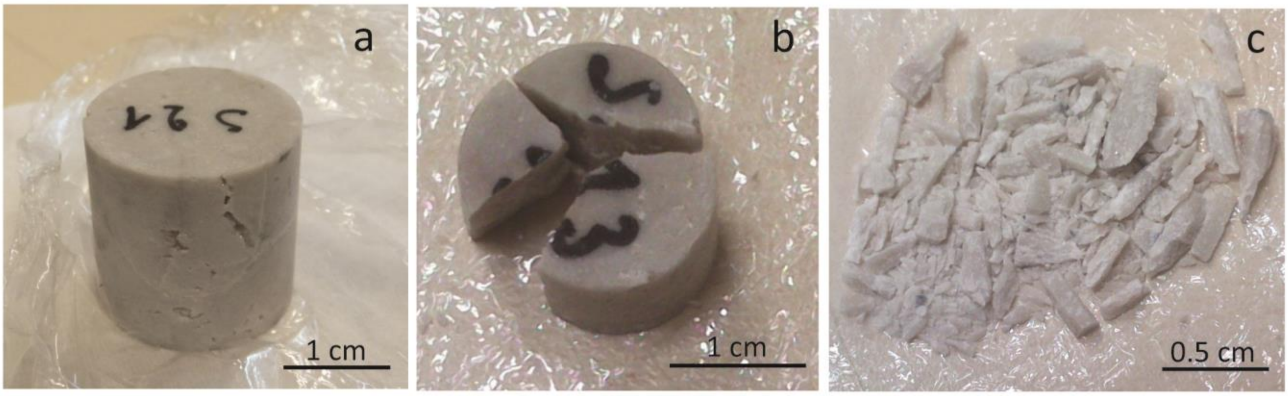

Fig.4 States of the samples deformed under high-strain rate dynamic loading with the Split Hopkinson Pressure Bar. (a) Macroscopically intact samples. (b) Split sample. (c) Shattered sample. See the main text for description.

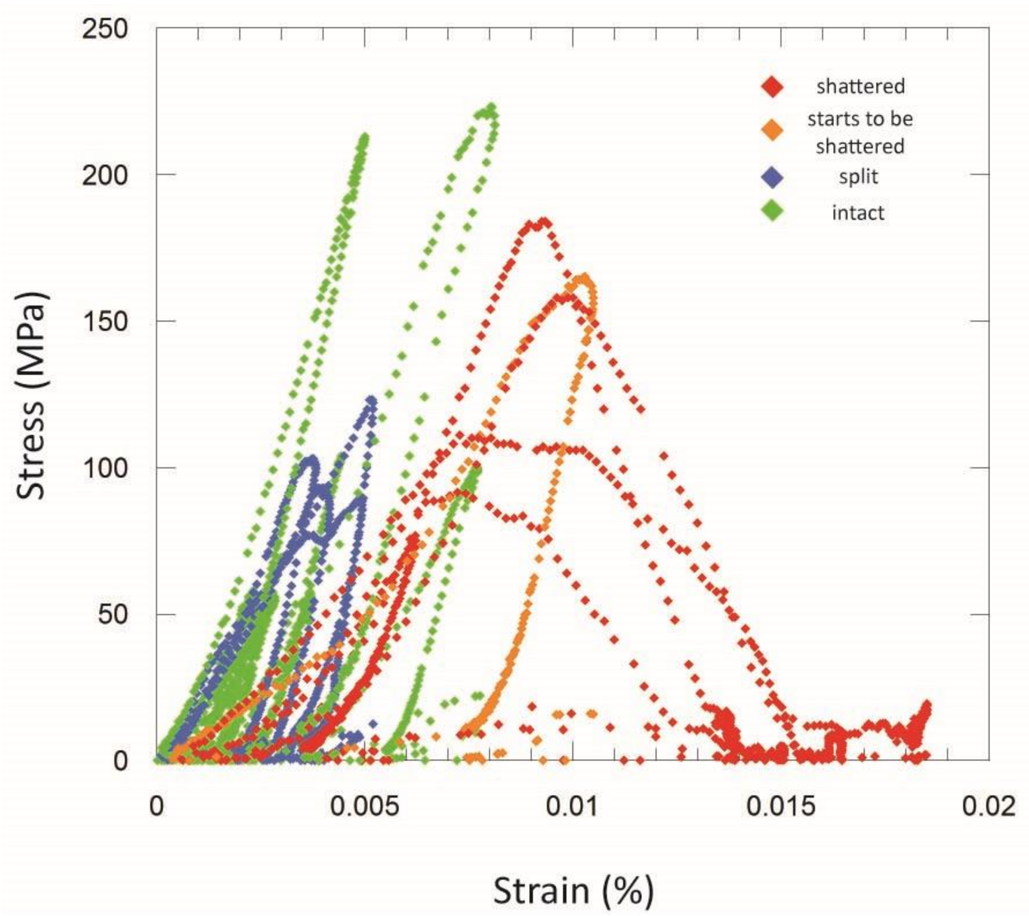

Fig.5 Stress vs. strain curves of the high-strain rate uniaxial compression tests with the Split Hopkinson Pressure Bar. Green curves refer to macroscopically intact samples. Blue curves refer to split samples. Red curves refer to shattered samples. The orange curve refers to sample S7 which shows incipient shattering.

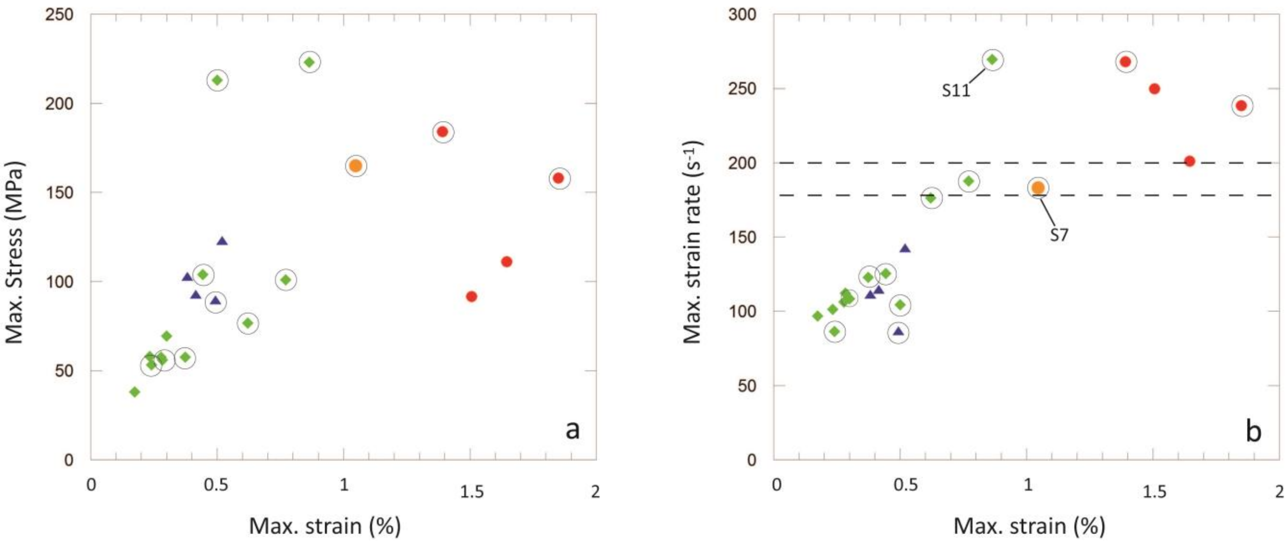

Fig.6 (a) Maximum true stress vs. maximum true strain for Split Hopkinson Pressure Bar tests. Colors are the same as in Fig.5. Black circles indicate jacketed samples. (b) Maximum true strain rate vs. maximum true strain for for Split Hopkinson Pressure Bar tests. Colors are the same of Fig.5. Black circles indicate jacketed samples. The presence of the jacket did not influence the mechanical data.

3.1.2 Low-strain rate uniaxial compressive tests

Samples recovered after the low-strain rate (~ 10^{-3} s^{-1}) uniaxial compressive tests are always split in several rock slices delimited by extensional fractures sub-parallel to the loading direction. Fractures are generally concentrated in the external part of the samples while the internal part is more intact.

Table 2 summarizes the mechanical data of the low-strain uniaxial compressive tests. Tested samples are ~ 20 mm in diameter with length to diameter ratio ~ 1. Uniaxial compressive strength varies in the range 203-274 MPa (Fig.7). Average Young modulus is ~ 78 GPa and average Poisson ratio is ~ 0.34.

One of the parameters which can significantly affect the uniaxial compressive strength of rock materials is the length to diameter ratio (L/D) of the test rock cylinders. It has been shown in literature that values of uniaxial compressive strength remain fairly constant with a L/D ratio > 2.5, show slight variations for L/D between 2 and 2.5 and reach higher values for L/D ratios < 2 (Tuncay et al., 2009). Therefore the sample geometry (L/D ~ 1) used in the tests here presented is not optimal, but it was chosen to be compared with high-strain rate tests performed on ~ 20 mm in diameter samples with the Split Hopkinson Pressure Bar. However, uniaxial compressive strengths typically larger than 200 MPa were measured for Dunham dolomite (L/D ratios in the range 1.5-4, Mogi et al., 1966, 2007) and for dolomite samples from the Southern Alps (L/D ratios ≥ 2, Ferri, unpublished data): such compressive strengths are similar to those determined here for the dolostones of the Mendola Formation. Moreover, the range of values of the Young modulus (60-100 GPa) is consistent both with that measured in other low-strain rate tests on dolostone samples (Ferri et al., in preparation) and with that retrieved from measurements of seismic wave velocity within dolostone rock samples in the laboratory (Faccenda et al., 2007).

Sample	Length (mm)	UCS (MPa)	E (GPa)	Poisson ratio
U1	20	245	62	
U2	20	203	62	0.26
U3	20	273	89	0.35
U4	20	207	71	0.37
U5	20		103	0.37
U8	20	207	80	

Table 2 Summary of experimental data for low-strain rate uniaxial compression tests. UCS is the uniaxial compressive strength. E is the Young modulus. Poisson ratio of tests U1 and U8 are not reported because are > 0.5, likely due to signal problems with the gauge recording the radial strain. UCS is not reported for test U5 because stopped before sample failure.

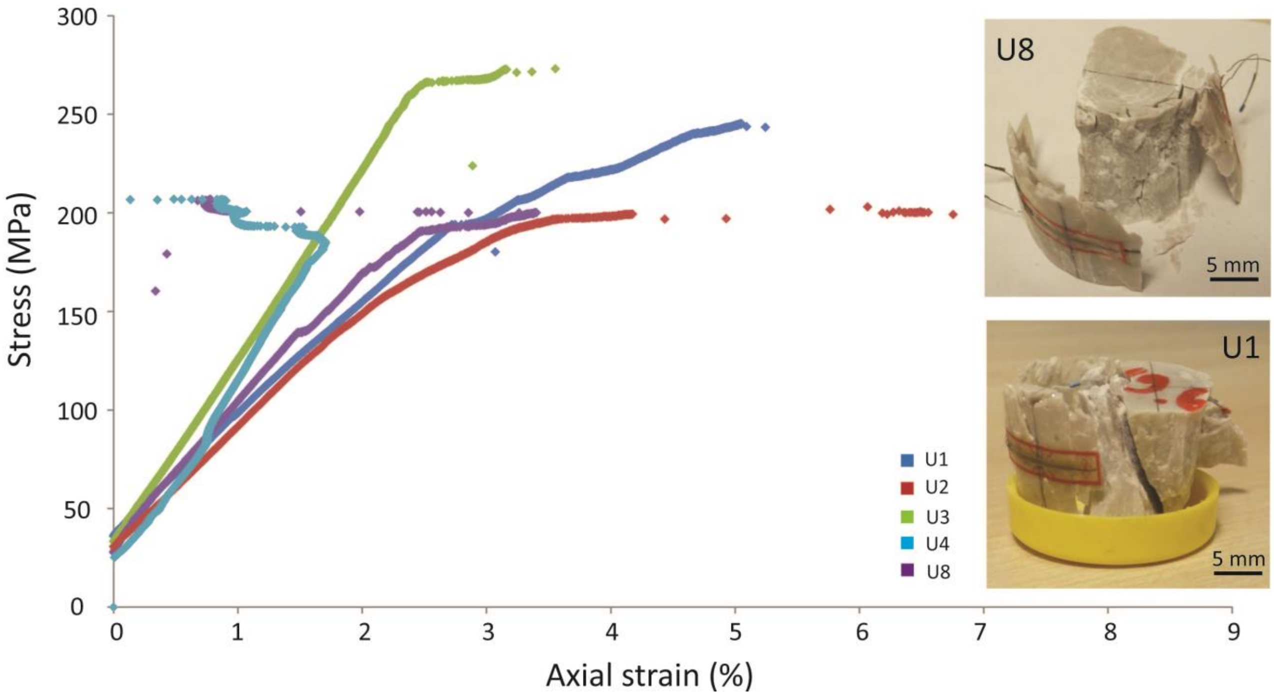

Fig.7 Stress vs. strain curves for low-strain rate uniaxial compression tests. Curves of tests U4 and U8 are good up to ~ 180 MPa, when data are spurious because of sample failure and breakege of the axial strain gauge. Values of uniaxial compressive strength are still correct. Photographs to the right show samples without jacket recovered after the tests. The samples are typically split in few rock fragments. Moreover the internal part of the samples is generally more intact with respect to the external one.

3.2 Microstructures of undeformed dolostones

Figure 8 shows the microstructure of the undeformed dolostone of the Mendola Formation. This sedimentary dolostone has an heterogeneous fabric with dolomite crystals ranging from hundreds to few micrometers in size. The largest dolomite crystals are rombohedral in shape and occur as cement infill within fenestrae or as mineral replacement of fossils (e.g. algae, gastropods). The smallest dolomite crystals occur within micrite plagues which often show a peloidal fabric (i.e. up to hundreds of micrometers rounded aggregates of micrite produced by microbial activity).

Scanning Electron Microscope images shows that individual dolomite crystals have a diffuse porosity with voids characterized by irregular contours and diameters up to tens of micrometers. Instead, dolomite crystals within fenestrae are free porous-free and in the BSE-SEM images are lighter in color with respect to the other dolomite crystals suggesting a slightly different elemental composition (Fig.8c).

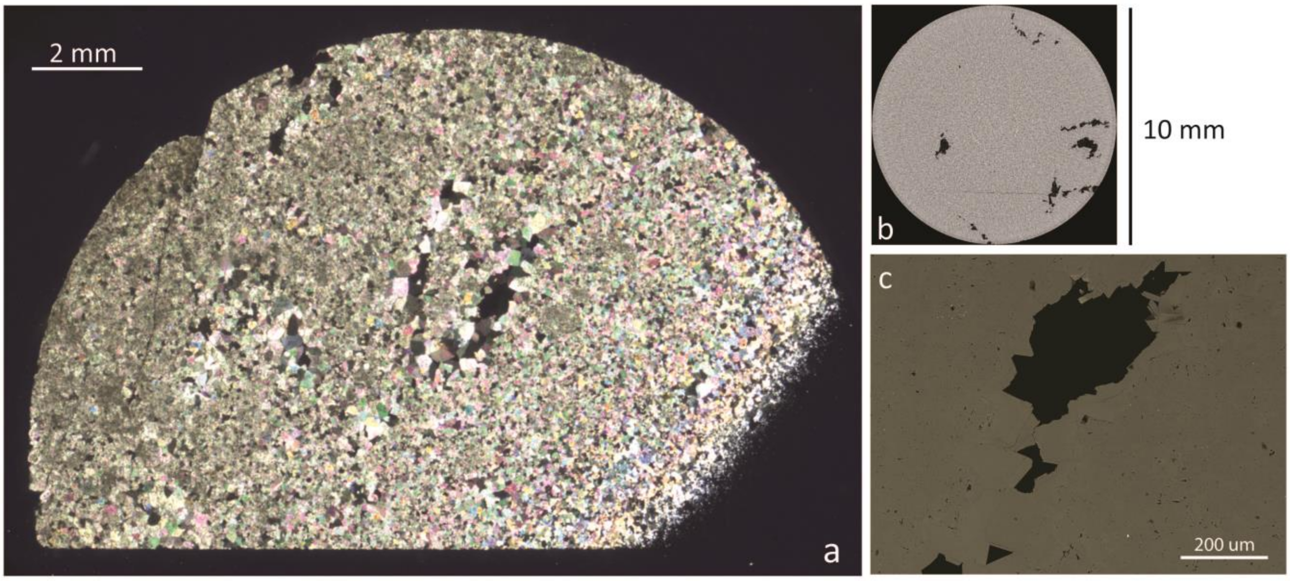

Fig.8 (a) High-resolution thin section scan (cross nicols) of an undeformed rock cylinder of dolostone of the Mendola Formation cut perpendicular to the axial length. Dolomite crystal size is highly variable from hundreds of micrometers to few micrometers. The largest dolomite crystals are within the fenestrae. (b) X-ray microtomography slice of an undeformed dolostone cylinder perpendicular to the length. The presence of up to few millimeters in size fenestrae is recognizable. (c) Detail of dolomite crystals within fenestrae (BSE-SEM image), which are free from porosity at the micrometer scale.

3.3 Microstructures of deformed dolostones

In this section I describe the microstructures of dolostones deformed in high- and low-strain rate uniaxial compressive tests. The samples were wrapped with shrinking plastic jackets before the tests. Investigation of the samples was performed by X-ray microtomography and both by optical and scanning electron microscopy on oriented thin sections.

3.3.1 High-strain rate uniaxial compressive tests

Fig.9a shows a thin section scan of a dolostone sample (Experiment S1, max stress = 101 MPa , max strain rate = 188 s^{-1}, max true strain = 0.8%) recovered after a high-strain rate compressive test. The rock consists of a microbial micrite with peloidal fabric cemented by dolomite crystals from tens to hundreds of micrometers in size. The sample is substantially undeformed with no evidence of microfracturing and the original rock fabric is preserved.

Split dolostone samples (e.g., Experiment S2, max stress = 103 MPa , max strain rate = 111 s^{-1}, max strain = 0.4%) are affected by few discrete extensional fractures cutting through?? the sample. No evidence of microfracturing in the dolostone around the leading fractures (e.g., the east wet trending one in Fig. 9b) is recognizable.

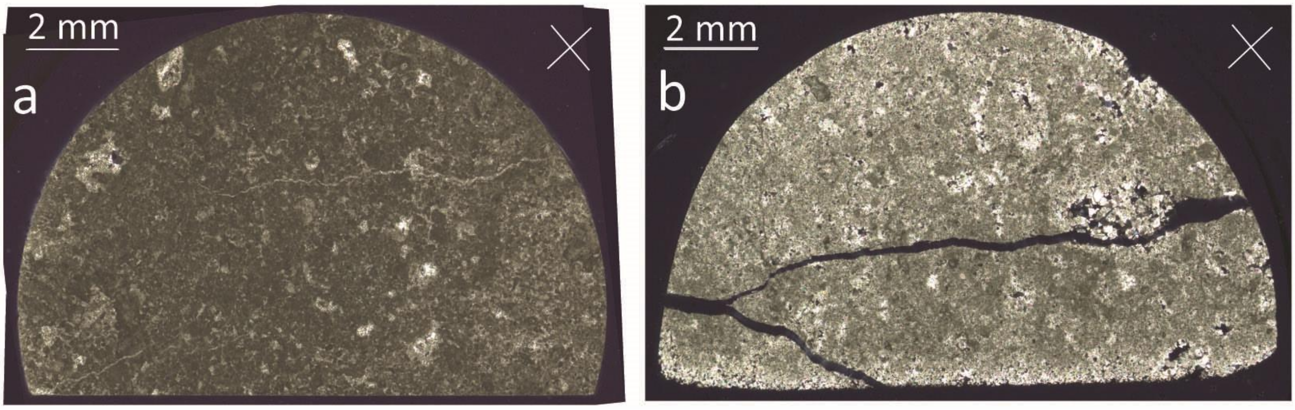

Fig.9 High-resolution thin section scans (cross nicols) of dolostone rock cylinders recovered after high-strain rate uniaxial compression tests cut perpendicular to the loading direction. (a) Intact sample, experiment SXXX. (b) Split sample, experiment Sxxx. See the main text for explanations.

Shattered dolostones samples consist of multiple rock fragments, mostly of few millimeters in size, delimited by extensional fractures. In sections perpendicular to the loading direction the fracture pattern is quite irregular and comprise radial fractures with straight traces and both concentric and interconnecting fractures with broken traces (Experiments S4 and S26; Figs.10a,b,c). In sections parallel to the loading direction the main fracture set is sub-vertical and parallel to the section while a secondary set of fractures is oriented almost perpendicular. The resulting rock fragments are elongated in the loading direction (Fig.11a). Up to 1 mm thick layers of fine-grained material with rock fragments ranging from 500 µm down to less than 1 µm in size are formed along the main set of fractures starting from the sample edge where the stress wave comes in (part of the fine-grained material was likely removed during thin section preparation) (Figs.11a,b). In the fine-grained layers both dolostone crystal boundaries and cleavage planes are disconnected (Figs.10d,e).

Pervasive extensional fracturing produce angular rock fragments down to the micrometer scale and no evidence of significant shear strain is recognizable. The presence of chains of elongated dolostone clasts parallel to the loading direction suggests the activation impingement processes in a material with a granular “gouge-like” behavior (Fig.11b) (Ben-Zion et al., 2011).

Regions of the samples in proximity to fenestrae are often fracture-free (Fig. 10b). This suggests that dolostone in proximity to the fenestrae is stiffer with respect to the dolostone around.

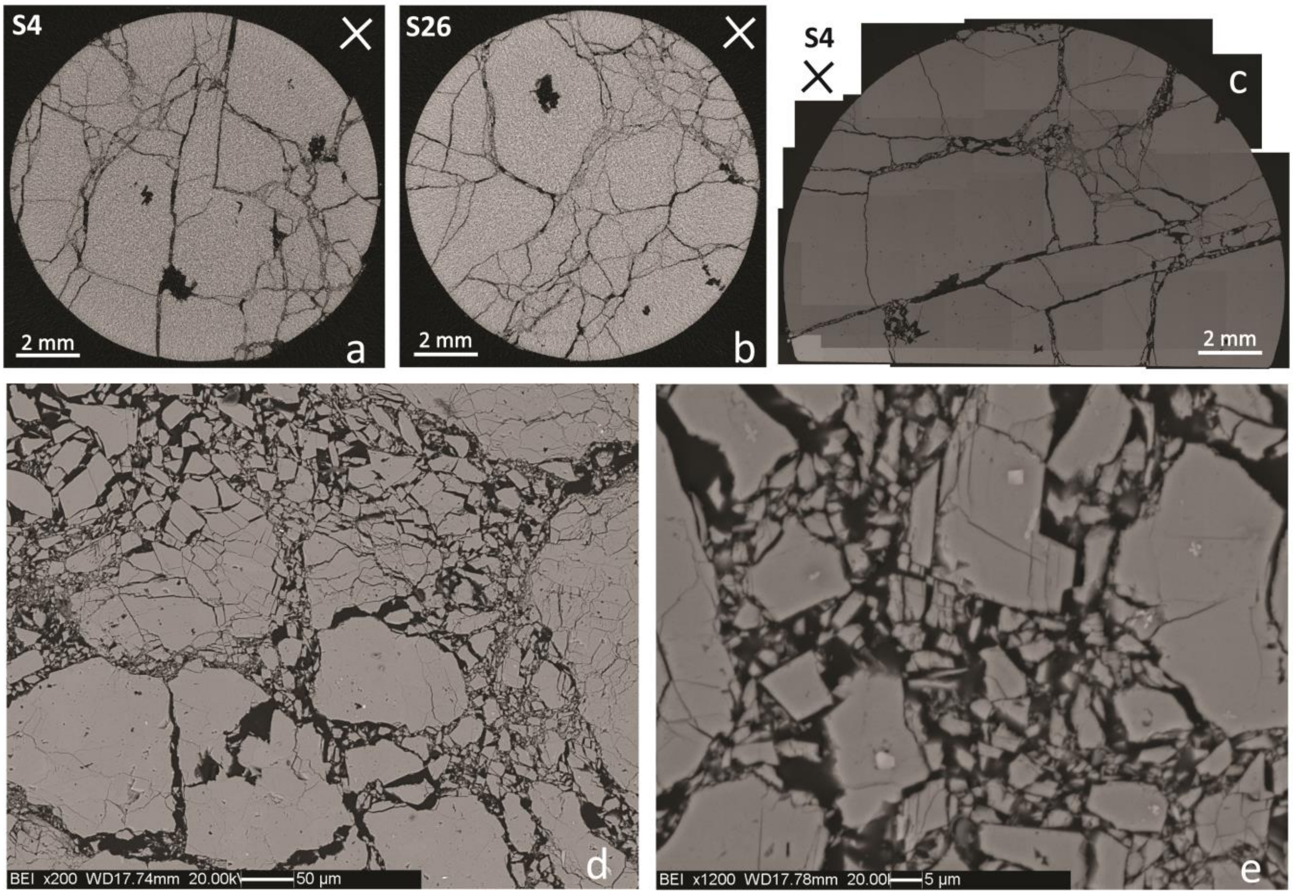

Fig.10 Shattered dolostones. (a, b) X-ray microtomography slices perpendicular to loading direction of dolostone rock cylinders recovered after high-strain rate uniaxial compression tests. S4: max. stress = 158 MPa, max. strain rate = 238 s^{-1}; max. strain = 1.8%. S26: max. stress = 184 MPa, max. strain rate = 268 s^{-1}; max. strain = 1.4%.The samples are reduced in multiple fragments mostly of few millimeters in size delimited by extensional fractures. Radial fractures, concentric fractures and interconnecting fractures with broken traces are present. Zone of diffuse microfracturing are recognizable. Zones around fenestrae are less fractured. The white cross indicates that the stress wave is entering the page. (c) Mosaic of BSE-SEM images of a shattered dolostone rock cylinder cut perpendicular to the loading direction, black cross indicates that the stress wave is entering the page. Few millimeters in size rock fragments delimited by fractures with straight traces are recognizable. (d,e) Details of zones of diffuse microfracturing (BSE-SEM images). Both dolomite crystal boundaries and cleavage planes are opened by extensional fractures.

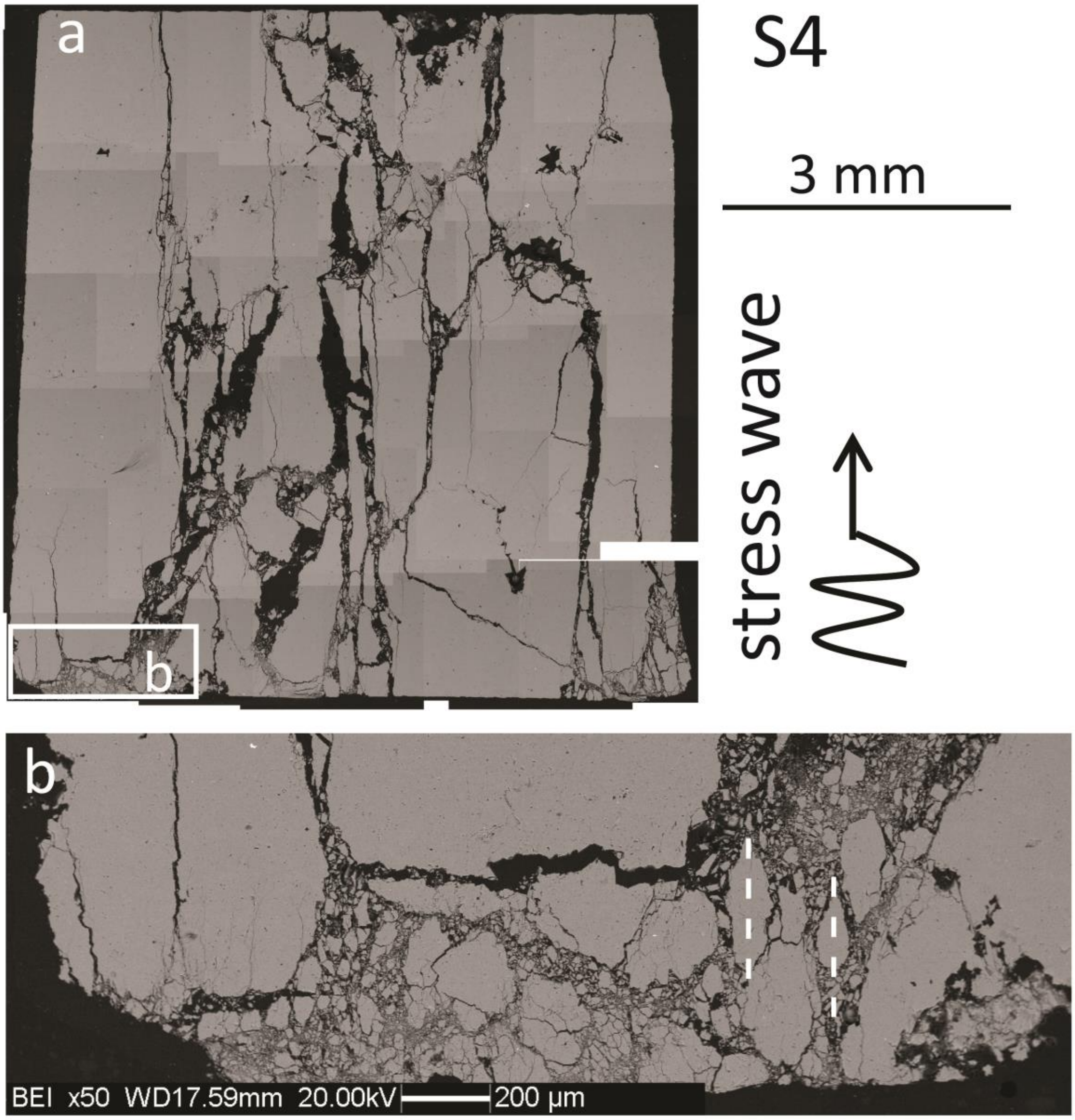

Fig.11 (a) Mosaic of BSE-SEM images of a shattered dolostone rock cylinder cut parallel to the loading direction. The shattered samples consists of few millimeters in size rock fragments elongated parallel to the loading direction and delimited by a main extensional fracture set. Zones of incipient microfracturing are present at the side where the stress wave enters the sample (impact bar) and along the main fracture set. (b) Detail of the zone of incipient microfracturing at the side of the sample where the stress wave comes in (BSE-SEM image). The dolostone is reduced in rock fragments ranging from hundreds to few micrometers in size. Chains of clasts parallel to the loading direction suggest impingement processes within the fine-grained material.

3.3.2 Low-strain rate uniaxial compressive tests

Figure 12 shows the damage of a dolostone sample deformed up to failure in a low-strain rate uniaxial compressive test. In sections perpendicular to the loading direction the sample is affected by extensional radial fractures nucleated from the sample edge (experiment U2)(Fig. 12a). Concentric fractures formed in the external part of the sample where confinement effect (Forrestal et al., 2004) is small. In general the internal part of the sample is less fractured with respect to the external part. In sections parallel to the loading direction the main fracture set is sub-vertical and parallel to the section (Fig. 12b). The fractures are extensional and are arranged in an en-echelon left-stepping pattern with short hybrid bridge fractures. The lateral overlapping of the tips of many fractures suggest a quasi-static fracture growth (Scholz, 2002; Paterson and Wong, 2005).

At the base of the sample, which is an area of stress concentration, and along major extensional fractures fine-grained material ranging from hundreds to tens of micrometer in size is produced. Fine-grained material down to less than 1 µm in size occurs along small fractures which seem to accommodate shear strain (Fig.12c).

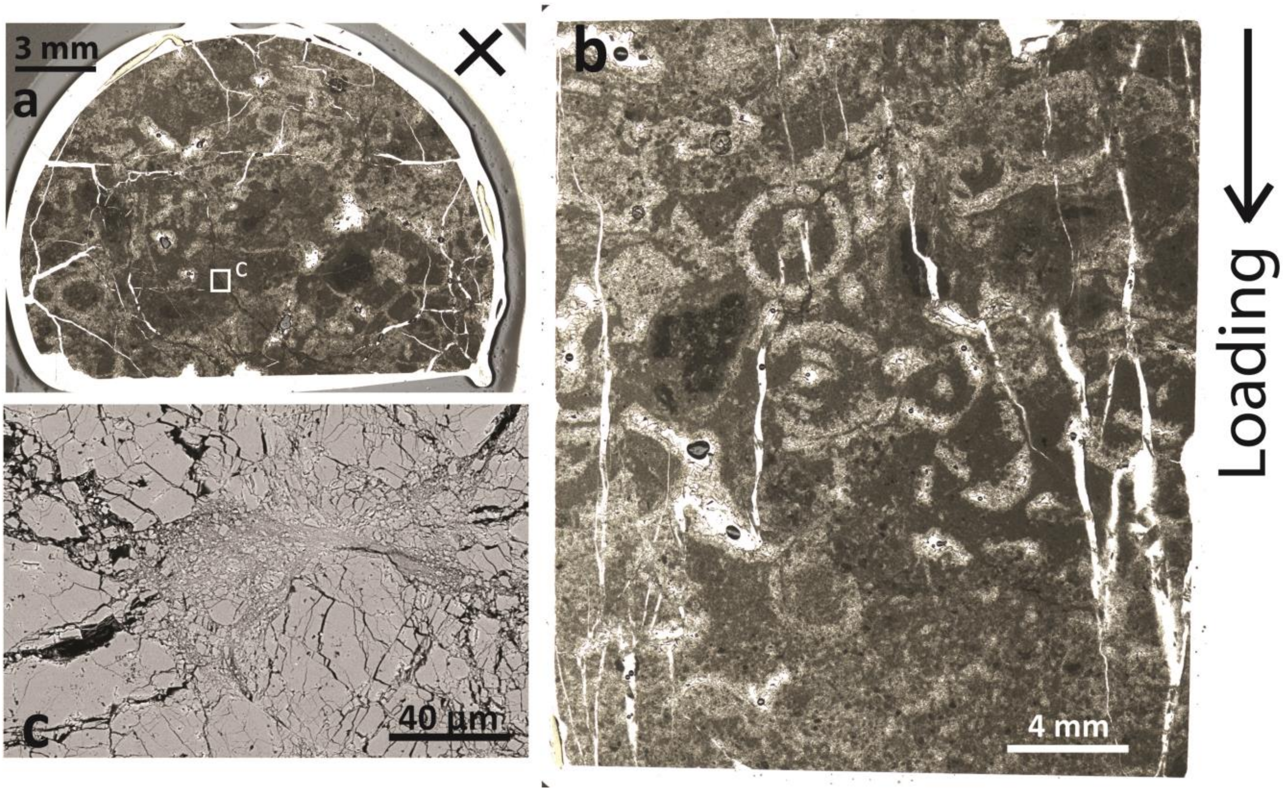

Fig.12 Sample U2 recovered after low-strain rate uniaxial compression test. (a) High-resolution thin section scan (parallel nicols) of a dolostone rock cylinder deformed up to failure cut perpendicular to the loading direction. Black cross indicate that the loading was directed in to the page. Radial extensional fractures nucleate from the edge of the sample. The internal part of the sample is more intact, but small fractures with fine-grained material are present (see Figure c). (b) High-resolution thin section scan (parallel nicols) of a dolostone rock cylinder deformed up to failure cut parallel to the loading direction. The sample is affected by discrete (not interconnected) extensional fractures arranged in a left-stepping en-echelon pattern. Few millimeters in size fossil fragmented replaced by hundreds of micrometer in size dolomite crystals are recognizable. (d) Detail of fine-grained material (down to the micrometer scale) along a small shear fracture (BSE-SEM image).

4. Discussion

4.1 Variability of mechanical data and rock heterogeneity

Both high- and low-strain rate uniaxial compressive tests highlight a large variability in the mechanical behavior of the dolostones of the Mendola Formation.

In the high-strain rate tests there is a significant overlapping in the maximum stress experienced (38-223 MPa) by shattered, split and intact samples (Fig.6a). In the low-strain rate tests the uniaxial compressive strength varies in the range of 203-274 MPa (Table 2). Moreover, the average Young modulus calculated for samples with the same diameter (~ 20 mm) from high-strain rate tests is smaller (~ 40 GPa) with respect to that calculated from low-strain rate tests (~ 78 GPa). This was unexpected, since the Young modulus should increase with increasing strain rate.

Since the tested rock cylinders were cored from the same block or from adjacent blocks collected from the same outcrop, the large variability in the mechanical behavior of the tested samples has to be ascribed to rock heterogeneities. Actually, the fabric of the dolostones of the Mendola Formation is characterized by strong variations down to the millimeter scale which are significant with respect to the dimension of the samples deformed in the experiments. The variations include (i) changes in crystal size, from few micrometers dolomite crystals (plagues of micrite) to hundreds of micrometers rombohedral dolomite crystals, (ii) presence of up to few millimeters in size fossil fragments (e.g. algae, gasteropods), and (iii) presence of up to few millimeters in size fenestrae with infill of secondary dolomite cement. These features are likely to act as mechanical heterogeneities resulting in different stiffness and strength within the samples. As an example, the absence of fractures around fenestrae in most deformed samples suggests that the strength of the dolostone is likely increased due to the precipitation of secondary dolomite as voids infill. Many of the samples deformed under low-strain rate uniaxial compression were characterized by the presence of up to few millimeters fossil fragments replaced by dolomite crystals and fenestrae. This might explain the relatively higher stiffness of these samples with respect to those deformed at higher strain rates with the SHPB. Given the large variability in the mechanical behavior of the tested dolostones, further investigations are needed to understand the relationships between mechanical properties and sedimentary facies (fabric latu sensu).

4.2 High-strain rate vs. low-strain rate damage in dolostones

Shattered dolostones were produced in high-strain rate uniaxial compressive tests over a strain rate threshold of ~ 200 s^{-1} and axial strain > 1% (Fig. 6). Shattered dolostones consisted of rock fragments, mostly of few millimeters in size, separated by extensional fractures and elongated parallel to the loading direction (Fig. 11). Fine-grained material ranging from hundreds to few micrometers in size formed along the main extensional fractures through the opening of crystal boundaries and cleavage planes (Figs. 10 and 11). No evidence of shear strain accommodation was recognizable. Shattered samples with no jackets were always reduced in to a non-cohesive granular material after the tests (see Fig.3c).

Samples deformed up to rupture in low-strain rate (~10^{-3} s^{-1}) uniaxial compressive tests accommodated axial strains > 3%. The samples were affected by a large number of discrete (not connected) extensional fractures with spacing of several millimeters, and did not have zones of diffuse microfracturing. Moreover deformed samples had the central part more intact with respect to the external one ("pillar-like structure, Fig.7).

These microstructural observations indicate that shattered dolostones, which were produced under high-strain rate dynamic loading, show a different damage pattern with respect to dolostones deformed under low-strain rate quasi-static loading.

4.3 Pulverized rocks vs. shattered dolostones

High-strain rate uniaxial compressive tests with the Split Hopkinson Pressure Bar were firstly performed by Doan and Gary (2009) to investigate the conditions for rock pulverization in granites. The authors demonstrated that granites collected from the damage zone of the San Andreas Fault (i.e. already affected by microfractures) were reduced into rock fragments mostly smaller than the average crystal size of the granite (i.e. few millimeters) over a strain rate threshold of 150 s^{-1}. The same type of experiments performed on intact granites gave similar products for strain rates over a threshold of ~ 250 s^{-1} (Doan and Gary, 2009; Yuan et al., 2011). Such experimentally-deformed rocks were comparable in terms of microstructures with natural pulverized crystalline rocks reported along major strike-slip faults (Brune, 2001; Dor, 2006a, 2006b, 2009; Rockwell et al., 2009; Mitchell et al., 2011). In particular both experimentally-deformed and natural pulverized rocks were characterized by diffuse extensional microfracturing and absence of significant shear strain. Basing on the experimental observations, rock pulverization was interpreted as a damage process activated only at high loading rates when strain localization is inhibited and many small fractures rather than few discrete fractures propagate simultaneously within the sample (Doan and Gary, 2009). Extreme strain rates (> 100 s-1) are expected to be reached in the wall rocks during seismic rupture propagation up to distances ranging from few centimeters to hundreds of meters from the slipping fault depending on the velocity of rupture propagation (Ben-Zion and Huang, 2002; Reches and Dewers, 2005; Di Toro et al., 2005; Templeton and Rice, 2008). As a consequence, pulverized rocks are widely interpreted as an evidence of coseismic fault zone damage (Dor et al., 2006a,b; Doan and Gary, 2009; Mitchell et al., 2011; Yuan et al., 2011).

Doan and Billi (2011) tested intact Carrara marble under high-strain rate loading with the SHPB and demonstrated that pulverized marbles were produced at strain rates > 100 s^{-1} and strains > 1.3%. Pulverized marbles were reduced in rock fragments mostly of few millimeters in size separated by zones of diffuse microfracturing down to the crystal size (i.e. few hundreds of micrometers on average). Therefore experimentally pulverized marbles showed larger grain sizes with respect to experimentally pulverized granites.

Shattered dolostones of the Mendola Formation described in this chapter were produced at strain rates > 200 s^{-1} and strain > 1%. Similarly to the pulverized marbles described by Doan and Billi (2011) many of the rock fragments were of few millimeters in size, thus significantly larger with respect to the average crystal size of the rock. Nevertheless zones of incipient microfracturing down to the micrometer scale were present. Considering that the damage pattern of the shattered dolostones showed some differences (e.g., shattered samples are not cohesive, fractures are interconnected, incipient microfracturing is diffused within the sample) with respect to that produced at low-strain rate quasi-static loading (see section 4.3), shattered dolostones can be interpreted as the product of high-strain rate damage associated to the propagation of earthquake ruptures. According to this interpretation in-situ shattered dolostones would be equivalent to pulverized rocks in crystalline protoliths.

The strain rate threshold over which the dolostones of the Mendola Formation started to be shattered (~ 200 s^{-1}) is much higher with respect to that of the intact marble (~ 100 s^{-1}; Doan and Billi, 2011) and a bit smaller with respect to that of the intact granite (~ 250 s^{-1}; Doan and Gary, 2009; Yuan et al., 2011).

The larger grain size of experimentally shattered dolostones (and partly of pulverized marble) with respect to experimentally pulverized granites is probably due to the strong fabric heterogeneity of the dolostones with respect to the granites. Indeed the heterogeneity of the rock fabric implies significant variations in the mechanical properties of the rock (e.g. see the high variability of the young modulus) at scales of few centimeters or less.

4.4 Implications for the origin of in-situ shattered dolostones of the FFZ

The Foiana Fault Zone (FFZ) is a major (~ 30 km long) sinistral transpressive fault zone cutting through sedimentary dolostones in the Italian Southern Alps (see Chapter 2, section 3 of this thesis). The exposed fault zone consists of fragmented dolostones with rock fragments from few centimeters to few millimeters in size, locally cut by networks of very discrete faults with highly-reflective "mirror-like" slip surfaces. Mirror-like faults are typically lined by up to few centimeters thick fine-grained rock layers with maximum clast size of few millimeters.

The fragmented dolostones form up to hundreds of meters thick belts along the FFZ and are affected by sets of extensional fractures spaced from few centimeters to few millimeters apart. One of the most remarkable characteristic of the fragmented dolostones within the FFZ is the absence of significant shear strain accommodation, which is documented by the preservation of the host rock primary sedimentary features without apparent distortion.

The fine-grained rock layers lining the mirror-like faults show peculiar microstructures such as (i) exploded clasts with radial fractures, (ii) pervasive extensional fracturing and splitting of clasts down to the micrometer scale, and (iii) chains of clasts at high angle to the fault surface which suggest impingement phenomena. All these microstructures indicate absence of significant shear strain accommodation within the fine-grained rock layers and the occurrence of in-situ shattering down to the micrometer scale.

Experimental shattered dolostones produced in high-strain rate uniaxial compressive tests with the Split Hopkinson Pressure Bar show similarities both with the fragmented dolostones and the fine-grained rock layers of the FFZ. Indeed experimental shattered dolostones consist of few millimeters in size rock fragments delimited by extensional fractures and elongated parallel to the loading direction. Moreover the sample edge where the stress wave comes in (impact bar, Fig. 11a,b) and the main extensional fractures (Fig. 11a) are decorated by fine-grained material with rock fragments ranging from hundreds to few micrometers in size. The fine-grained material is affected by pervasive extensional fracturing down to micrometer scale and does not show evidence of significant shear strain (Fig. 11b). The presence of clast chains parallel to the stress wave loading direction, which suggest impingement phenomena among the clasts, is recognized (Fig.11).

The above microstructural observations suggest that both fragmented dolostones and fine-grained rock layers within the FFZ might be the cumulative result of high-strain rate dynamic loading during the propagation of multiple earthquake ruptures along the FFZ. In particular the coseismic damage might be related both to the transient stress perturbations associated to the passage of the rupture tip, which are potentially able to pulverize the wall rock up to distances of few millimeters from the fault (Reches and Dewers, 2005), and to the passage of the fronts of high frequency compressive and shear loading waves up to distances of several meters from the faults (Yamashita, 2000; Ben-Zion and Huang, 2002; Kame et al., 2003; Andrews, 2005; Poliakov et al., 2002; Templeton and Rice, 2008). Moreover the interpretation of the fragmented dolostones and the fine-grained rock layers as the product of coseismic damage is also supported by the presence of mirror-like faults which are demonstrated to be formed by extreme shear strain localization during seismic slip (see Chapter 3 of this thesis for details).

5. Conclusions and open questions

The presence of wide zones (i.e. up to hundreds of meters thick) of fragmented rocks lacking evidence of significant shear deformation is relatively common within fault zones hosted in carbonate rocks (mainly limestones and dolostones) exhumed from shallow depth (i.e. < 3 km). These fault rocks are frequently termed low-strain fault breccias and are traditionally interpreted in relation to different deformation phases during the quasi-static growth of a fault zone (Billi et al., 2003; Salvini et al., 1999).

In this thesis (Chapter 2, section 3) I described the structure of a major fault zone cutting sedimentary dolostones in the Italian Southern Alps: the Foiana Fault Zone (FFZ). The FFZ consists of fragmented dolostones locally cut by very discrete faults with mirror-like slip surfaces lined by up to few centimeters thick fine-grained rock layers. Both the fragmented dolostones and the fine-grained rock layers appear to have been shattered in situ (i.e. pervasive extensional fracturing with absence of significant shear strain from the centimeters to the micrometer scale). Since it was demonstrated through a dedicated experimental study (see Chapter 3 of this thesis) that mirror-like slip surfaces similar to those found along the FFZ form only at seismic deformation conditions, the occurrence of in-situ shattered dolostones along the FFZ was interpreted as an evidence of coseismic damage.

To investigate this hypothesis low- to high-strain rate uniaxial compressive tests were performed on dolostone rock cylinders of the Mendola Formation (host rock of the FFZ). High-strain rate (> 50 s^{-1}) tests were performed with a Split Hopkinson Pressure Bar under dynamic stress wave loading, while low-strain rate (~ 10^{-3} s^{-1}) tests were performed with a servo-controlled oil press under quasi-static loading. Dynamic uniaxial compressive tests with the SHPB demonstrated that dolostones of the Mendola Formation start to be shattered in multiple rock fragments over a strain rate threshold of ~ 200 s^{-1}, while they were split in few rock fragments or were macroscopically intact for lower strain rates. Shattered dolostones consist of elongated rock fragments mostly of few millimeters in size separated by extensional fractures parallel to the loading direction. Fine-grained material ranging from hundreds to few micrometers in size is found along the main extensional fractures through the opening of crystal boundaries and cleavage planes. On the other hand dolostone rock cylinders deformed up to failure under quasi-static loading show a different damage pattern characterized by several discrete (i.e. not interconnected) fractures parallel to the loading direction. Moreover rock samples deformed under quasi-static loading were never reduced into a non-cohesive material.

The experimental and microstructural observations described here suggest that shattered dolostones form only at high strain rates and have a different damage pattern with respect to samples deformed under low-strain rate quasi-static loading. Moreover microstructural similarities are present between experimental shattered dolostones and both fragmented dolostones and fine-grained rock layers of the FFZ. Basing on these findings both fragmented dolostones and fine-grained rock layers bounding mirror-like fault surfaces within the FFZ might be the cumulative product of dynamic stress wave loading during multiple earthquake ruptures.

The conclusions reported here remain preliminary and partially speculative and need to be reinforced by further investigations. In particular in the near future three main topics are planned to be examined more in depth:

1) the quantitative microstructural characterization and comparison of experimental and natural in-situ shattered dolostones;
2) the detailed mechanical characterization of the different facies of the dolostones of the Mendola Formation;
3) the determination of the distance up to which off-fault in-situ rock shattering is expected during the propagation of an earthquake rupture in dolostones. Probably this has to be magnitude-dependent.

The first point will be addresses basing on further SEM observations of oriented thin sections of natural and experimental in-situ shattered dolostones and 3D quantification of the fracture network and particle size distribution starting from X-Ray microtomography data. The latter analyses might furnish an estimate of the fracture energy density of natural in-situ shattered dolostones. The second point will be addressed by relating the variability of mechanical parameters (e.g. uniaxial compressive strength, young modulus) measured from both low- and high-strain rate compressive tests with the different facies (i.e. rock fabric) of the dolostones through microstructural characterization of the samples. Eventually measurement of other elastic properties such as P- and S-wave velocity of the different facies of the dolostone will be performed. The third point will be investigated trying to extrapolate published solutions of dynamic stress, strain and strain-rate fields around the tips of seismic ruptures with different propagation velocities (e.g. Freund, 1990; Reches and Dewers, 2005) to the case of seismic ruptures propagating in a medium with the elastic properties of the dolostones of the Mendola Formation.

Reference list

Agosta, F. and Kirschner D. L., (2003). Fluid conduits in carbonate-hosted seismogenic normal faults of central Italy. Journal of Geophysical Research, 108, 2221, doi:10.1029/2002JB002013.

Agosta, F. and Aydin, A., (2006). Architecture and deformation mechanism of a basin-bounding normal fault in Mesozoic platform carbonates, central Italy. Journal of Structural Geology, 28(8), 1445-1467.

Agosta, F., Alessandroni, M., Tondi, E. and Aydin, A., (2009). Oblique normal faulting along the northern edge of the Majella Anticline, central Italy: Inferences on hydrocarbon migration and accumulation. Journal of Structural Geology, 31, 674-690.

Amato, A, Azzara, R., Chiarabba, C., Cimini, G.B., Cocco, M., Di Bona, M., Margheriti, L., Mazza S., Mele, F., Selvaggi, G., Basili, A., Boschi, E., Courboulex, F., Deschamps, A., Gaffet, S., Bittarelli, G., Chiaraluce, L., Piccinini, D., and Ripepe, M., (1998). The 1997 Umbria-Marche, Italy, earthquake sequence: a first look at the main shocks and aftershocks. Geophysical Research Letters, 25, 2861-2864.

Andrews, D. J., (2005). Rupture dynamics with energy loss outside the slip zone. Journal of Geophysical Research, 110, doi:10.1029/2004JB003191.

Anselmetti, F. S. and Eberli, G., (1993). Controls of sonic velocity in carbonates. Pure and Applied Geophysics, 141.

Anselmi, M., A. Govoni, P. De Gori, C. Chiarabba, (2011). Seismicity and velocity structures along the south-Alpine thrust front of the Venetian Alps (NE-Italy). Tectonophysics, 513, 37-48.

Antonellini, M. A. and Aydin, A., (1994). Effect of faulting on fluid flow in porous sandstones: petrophysical properties. American Association of Petroleum Geologists Bullettin, 78, 355-377.

Arai, Y., Sako, T. and Takebayashi, Y. (eds), (2002). Thermophysical Properties of Supercritical Fluids: Behavior of Supercritical Fluids. and Transport Properties of Supercritical Fluids. In Supercritical fluids : molecular interactions, physical properties, and new applications. Springer series in materials processing, Springer, Berlin.

Aretusini, S., (2013). Architecture and seismic markers of an exhumed fault zone in dolostones (Foiana Line, Italian Southern Alps). Master thesis, University of Padua, Geosciences Department; tutor: Di Toro, G.; cotutor: Fondriest, M..

Avanzini, M., Bargossi, G. M., Castiglioni, G. B., Dalmeri, G., Eccel, E., Mancabelli, A., Morelli, C., Neri, C., Picotti, V., Prosser, G., Sartori, G., and Zambotti, G., (2001). Carta Geologica della Provincia di Trento, tav. 26 III Fondo (a scala 1:25.000) con Note illustrative, 159 pp. Provincia Autonoma di Trento, Servizio Geologico.

Aydin, A., Antonellini, M., Tondi, E. and Agosta, F., (2010). Deformation along the leading edge of the Maiella thrust sheet in central Italy. Journal of Structural Geology, 32, 1291-1304.

Barka, A. and Reilinger, R., (1997). Active tectonics of the Eastern Mediterranean region: deduced from GPS, neotectonic and seismicity data. Annali di Geofisica, volume 40, 587-610.

Bastesen, E., Braathen, A., Nottveit, H., Gabrielsen, R.H., and Skar, T., (2009). Extensional fault cores in micritic carbonate - Case studies from the Gulf of Corinth, Greece. Journal of Structural Geology, 31, 403-420.

Beckmann, P. and Spizzichino, A., (1963). The scattering of electromagnetic waves from rough surfaces. International Series of Monographs on Electromagnetic Waves, (Oxford Pergamon Press), v. 4, p. 503.

Beeler, N.M., (2006). Inferring earthquake source properties from laboratory observations and the scope of lab contributions to source physics, *in* Abercrombie, R., et al., eds., Earthquakes: Radiated Energy and the Physics of Faulting: American Geophysical Union Geophysical Monograph 170, p. 99–119.

Ben-Zion, Y and Andrews, D. J., (1998). Properties and Implications of Dynamic Rupture along a Material Interface. Bulletin of the Seismological Society of America, 4, 1085-1094.

Ben-Zion, Y and Huang, Y., (2002). Dynamic rupture on an interface between a compliant fault zone layer and a stiffer surrounding solid. Journal of Geophysical Research, 107, 10.1029/2001JB000254.

Ben-Zion, Y and Shi, Z., (2005). Dynamic rupture on a material interface with spontaneous generation of plastic strain in the bulk. Earth and Planetary Science Letters, 236, 489-496.

Ben-Zion, Y, Dahmen, K. A and Uhl, T. J., (2011). A Unifying Phase Diagram for the Dynamics of Sheared Solids and Granular Materials. Pure and Applied Geophysics, 168, 2221-2237.

Bigi, G., Cosentino, D, Parotto, M., Sartori, R., and Scandone, P., (1990). Structural model of Italy. Sheet n.1 (Ed. by Bigi, G., A. Castellarin, M. Coli, G. V. Dal Piaz, R. Sartori, P. Scandone, and G. B. Vai). Sheet n.2 (Ed. by Bigi, G., A. Castellarin, M. Coli, G. V. Dal Piaz, and G. B. Vai). CNR Progetto Finalizzato Geodinamica.

Billi, A., and Di Toro, G., (2008). Fault-related carbonate rocks and earthquake indicators: recent advances and future trends. In “Structural Geology: new research”, Eds. Sean J. Landowe and Garth M. Hammler, Novascience.

Billi, A., Salvini, F. and Storti, F., (2003). The damage zone-fault core transition in carbonate rocks: implications for fault growth, structure and permeability. Journal of Structural Geology, 25(11): 1779-1794.

Billi, A., and Storti, F., (2004). Fractal distribution of particle size in carbonate cataclastic rocks from the core of a regional strike-slip fault zone. Tectonophysics, 384, 115-128, doi:10.1016/j.tecto.2004.03.015.

Billi, A., (2010). Microtectonics of low-P low-T carbonate fault rocks. Journal of Structural Geology 32, 1392-1402.

Boschi, E., Ferrari, G., Gasperini, P., Guidoboni, E., Smriglio, G. and Valensise G. (eds.), (1995). Catalogo dei forti terremoti in Italia dal 461 a.C. al 1980. ING-SGA, Bologna, 970 pp.

Bosellini, A., Neri, C., Bargossi, G. M., Prosser, G., Castiglioni, G. B., Avanzini, M., Borsato, A., Barazzuol, D., Bonani, A., Cucato, M., Montresor, L., Morelli, C., and Rigatti, G., (2007). Carta geologica foglio 26 Appiano, scala 1:25000, Provincia Autonoma di Bolzano.

Boullier, A., Koichiro, F., Tomoyuki, O., Roman-Ross, G., Lewin, E., Ito, H., Pezard, P. and Ildefonse, B., (2004). Textural evidence for recent co-seismic circulation of fluids in the Nojima fault zone, Awaji island, Japan. Tectonophysics, 378, 165-181.

Boullier, A., Yeh, E., Boutareaud, S., Song, S. and Tsai, C., (2009). Microscale anatomy of the 1999 Chi-Chi earthquake fault zone. Geochemistry Geophysics Geosystems, 10, doi:10.1029/2008GC002252.

Brantut, N., Schubnel, A., Rouzaud, J. N., Brunet, F. and Shimamoto, T., (2008). High-velocity frictional properties of a clay-bearing fault gouge and implications for earthquake mechanics. Journal of Geophysical Research, 113, B10401.

Bressan, G., Gentile, G. F., Perniola, B. and Urban, S., (2009). The 1998 and 2004 Bovec-Krn (Slovenia) seismic sequences: aftershock pattern, focal mechanisms and static stress changes. Geophys. J. Int., 179, 231-253, doi:10.1111/j.1365-246X.2009.04247.x.

Brodsky, E. E., Rowe, C. D., Meneghini, F. and Moore, D., (2009). A geological fingerprint of low-viscosity fault fluids mobilized during an earthquake. Journal of Geophysical Research, 114: B01303, doi:10.1029/2008JB005633.

Brodsky, E. E., Chester, F.M., Fulton, P. and Kodaira, S., (2013). Finding the fault: sampling the source of the M 9.0 Tohoku Earthquake. AAAS 2013 Annual Meeting, Boston, MA, 14–18 February 2013.

Brosch, F.J. and Kurz, W., (2008). Fault damage zones dominated by high-angle fractures within layer-parallel brittle shear zones: examples from the Eastern Alps. In: Geological Society of London Special Publication, vol. 299 75–95.

Brosse, E., Fabriol, H., Fleury, M., Grataloup, S. and Lombard, J. M., (2010). CO_2 Storage in the Struggle against Climate Change. Oil & Gas Science and Technology – Rev. IFP, Vol. 65 (2010), N. 3, 369-373

Brune, J., (2001). Fault normal dynamic loading and unloading: an explanation for non-gouge rock powder and lack of fault-parallel shear bands along the San Andreas fault. EOS Trans. Am. Geophys. Union, 82:47.

Bullock, R. J., De Paola, N., Holdsworth, R. H., Trabucho-Alexandre, J., (2013). Lithological controls on the deformation mechanisms operating within carbonate-hosted faults during the seismic cycle. Journal of Structural Geology, 58, 22-42.

Burrato, P., Poli, M. E., Vannoli, P., Zanferrari, A., Basili, R. and Galadini, F., (2008). Sources of Mw 5+ earthquakes in northeastern Italy and western Slovenia: An updated view based on geological and seismological evidence. Tectonophysics 453 (2008) 157–176

Burridge, R., Conn, G. & Freund, L. B., (1979). The stability of a rapid mode II shear crack with finite cohesive traction. J. Geophys. Res. 83, 2210–-2222.

Bussolotto, M., Micarelli, L., Benedicto,A., Invernizzi, C., Deiana, G., (2007). Deformation features within an active normal fault zone in carbonate rocks: the Gubbio fault (Central Apennines, Italy). Journal of Structural Geology 29 (12), 2017–2027.

Cadrobbi, M., (1965). Escursioni geologiche lungo la linea di Foiana (Valle di Non occidentale). Mem. Acc. Patavina, 77, 165-182.

Caine, J. S., Evans, J. P. and Forster, C. B., (1996). Fault zone architecture and permeabilità structure. Geology, 24, 1025-1028.

Candela, T., Renard, F., Bouchon, M., Brouste, A., Marsan, D., Schmittbuhl, J. and Voisin, C., (2009). Characterization of fault roughness at various scales: Implications of three-dimensional high resolution topography measurements. Pure and Applied Geophysics, v. 166, doi:10.1007/s00024-009-0521-2.

Castellarin, A., Cantelli, L., Fesce, A. M., Mercier, J. L., Picotti, V., Pini, G. A., Prosser, G. and Selli, L., (1992). Alpine cmpressional tectonics in the Southern Alps. Relationships with the N-Apenines. Annales Tectonicae, 6, 62-94.

Castellarin, A., Vai, G. B. and Cantelli, L., (2006). The Alpine evolution of the Southern Alps around the Giudicarie faults: A Late Cretaceous to Early Eocene transfer zone. Tectonophysics, 414, 203-223.

Castello, B., Moro, M., Chiarabba, C., Di Bona, M., Doumaz, F., Selvaggi, G. and Amato, A., (2004). Seismicity Map of Italy. Istituto Nazionale di Geofisica e Vulcanologia.World Wide Web Address: http://www.ingv.it/CSI/.

Celico, F., Petrella, E. and Celico, P., (2006). Hydrogeological behaviour of some fault zones in a carbonate aquifer of Southern Italy: an experimentally based model. Terra Nova 18, 308-313.

Chen, X., Madden, A. S., Bickmore, B. R. and Reches, Z., (2013). Dynamic weakening by nanoscale smoothing during high-velocity fault slip. Geology, 41, 739-742.

Chester, F.M., Evans, J.P., and Biegel, R.L., (1993). Internal Structure and Weakening Mechanisms of the San-Andreas Fault. Journal of Geophysical Research-Solid Earth, 98(B1), 771-786.

Chester, J. S., Chester, F. M. and Kronenberg, A. K., (2005). Fracture surface energy of the Punchbowl fault, San Andreas system. Nature, 437(7055), 133-136.

Chiarabba, C., Jovane, L. and Di Stefano, R., (2005). A new view of Italian seismicity using 20 years of instrumental recordings. Tectonophysics, 395, 251-268.

Chiarabba, C., Amato, A., Anselmi, M.,. Baccheschi, P., Bianchi, I.,. Cattaneo, M., Cecere, G., Chiaraluce, L., Ciaccio, M. G., De Gori, P., De Luca, G., Di Bona, M., Di Stefano, R., Faenza, L., Govoni, A., Improta, L., Lucente, F.P., Marchetti, A., Margheriti, L., Mele, F., Michelini, A., Monachesi, G., Moretti, M., Pastori, M., Piana Agostinetti, N., Piccinini, D., Roselli, P., Seccia, D. and Valoroso, L., (2009). The 2009 L'Aquila (central Italy) M_W 6.3 earthquake: Main shock and aftershocks. Geophysical Research Letters, 36: L18308, doi:10.1029/2009GL039627.

Chiarabba, C., Bagh, S., Bianchi, I., De Gori, P. and Barchi, M. R., (2010). Deep structural heterogeneities and the tectonic evolution of the Abruzzi region (Central Apennines, Italy) revealed by microseismicity, seismic tomography, and teleseismic receiver functions. Earth and Planetary Science Letters: doi:10.1016/j.epsl.2010.04.028.

Chiaraluce, L., M. Barchi, C. Collettini, F. Mirabella, and S. Pucci (2005), Connecting seismically active normal faults with Quaternary geological structures in a complex extensional environment: The Colfiorito 1997 case history (northern Apennines, Italy), Tectonics, 24, TC1002, doi:10.1029/2004TC001627.

Chiaraluce, L., Valoroso, L., Anselmi, M., Bagh, S. and Chiarabba, C., (2010). A decade of passive seismic monitoring experiments with local networks in four Italian regions. Tectonophysics, 476, 85-98.

Chiaraluce, L., Valoroso, L., Piccinini, D., Di Stefano, R. and De Gori, P., (2011). The Anatomy of the 2009 L'Aquila Normal Fault System (central Italy) Imaged by High Resolution Foreshock and Aftershock Locations. Journal of Geophysical Research, doi:10.1029/2011JB008352.

Chiaraluce, L., (2012). Unravelling the complexity of Apenninic extensional fault systems: A review of the 2009 L'Aquila earthquake (Central Apennines, Italy). Journal of Structural Geology, 10.1016/j.jsg.2012.06.007.

Chiaramonte, L., Zoback, M. D., Friedman, J. and Stamp, V., (2007). Seal integrity and feasibility of CO_2 sequestrationin the Teapot Dome EOR pilot: geomechanical site characterization. Environ. Geol., doi: 10.1007/s00254-007-0948-7.

Childs, C., Manzocchi, T., Walsh, J.J., Bonson, C.G., Nicol, A. and Schöpfer, M.P.J., (2009). A geometric model of fault zone and fault rock thickness variations. Journal of Structural Geology, 31, 117-127.

Cilona, A., Baud, P., Tondi, E., Agosta, F., Vinciguerra, S., Rustichelli, A. and Spiers, C. J., (2012). Deformation bands in porous carbonate grainstones: Field and laboratory observations. Journal of Structural Geology, 45, 1-21.

Cirella, A., Piatanesi, A., Cocco, M., Tinti, E., Scognamiglio, L., Michelini, A., Lomax, A. and Boschi, E., (2009). Rupture history of the 2009 L'Aquila (Italy) earthquake from non-linear joint inversion of strong motion and GPS data, Geophys. Res. Lett., 36, L19304, doi:10.1029/2009GL039795.

Collettini, C., Holdsworth, R. E. and S. A. F. Smith, (2009), Fault zone structure and deformation process along an exhumed low-angle normal fault. In: Fault-zone Properties and Earthquake Rupture Dynamics, edited by Fukuyama, E., International Geophysics Series, 94, 69-85, Elsevier.

Collettini, C., Viti, C., Tesei, T. and Mollo, S., (2013). Thermal decomposition along natural faults during earthquakes. Geology 41, 927e930. http://dx.doi.org/10.1130/G34421.1.

Cowan, D.S., (1999). Do faults preserve a record of seismic faulting? A field geologist's opinion: Journal of Structural Geology, v. 21, p. 995–1001, doi:10.1016/S0191-8141(99)00046-2.

Cowie, P.A. and Scholz, C.H. (1992). Physical explanation for the displacement-length relationship of faults usind a post-yield fracture mechanicsmodel. Journal of Structural Geology 14, 1133-1148.

Dal Piaz, G. B., (1942).Geologia della bassa Val d'Ultimo e del massiccio di Monte Croce con considerazioni sull'età e la giacitura delle masse intrusive periadriatiche e sulla tettonica del bacino dell'Adige. Mem. Mus. St. Nat. Ven. Trident., 5(2), 179-360.

Dal Piaz, G. V., and Martin, S., (1998). Evoluzione litosferica e magmatismo nel dominio austro-sudalpino dall'orogenesi varisica al rifting mesozoico. Mem. Soc. Geol., 53, 43-62.

De Paola, N., Collettini; C., Faulkner, D. R. and Trippetta, F., (2008). Fault zone architecture and deformation processes within evaporitic rocks in the upper crust. Tectonics, 27, TC4017, doi: 10.1029/2007TC002230.

De Paola, N., Hirose, T, Mitchell, T., Di Toro, G., Viti, C. and Shimamoto, T., (2011). Fault lubrication and earthquake propagation in thermally unstable rocks, Geology, 39; 1; 35-38; doi: 10.1130/G31398.1.

De Paola, N., Holdsworth, R.E., Faoro, I., Bullock, R., Viti, C. and Collettini, C., (2013). Frictional sliding vs. plastic flow during earthquake propagation in carbonate rocks. In abstract volume of the 40th workshop of the International School of Geophysics “Properties and processes of crustal fault zones”, Erice (Sicily, Italy) 18-24 May 2013.

De Paula, O. B., (2011). PhD thesis, Elastic Properties of Carbonates: Measurements and Modelling, Western Australian School of Mines Department of Exploration Geophysics.

De Pretto, O., (1920). Le due faglie di Schio. Studi di geologia dei Monti di Schio. Bollettino Società Geologica Italiana, 59, 254-312.

De Vecchi, G. P., (1966). I filoni basici ed ultrabasici dell’Altipiano di Tonezza (Alto Vicentino). Memorie degli Istituti di Geologia e Mineralogia dell’Università di Padova, 25, 1-58.

De Vecchi, G. P. and De Zanche, V., (1974). Fluidization and tuffization in the western Venetian Alps. Boll. Soc. Geol. It., 93, 317-330.

Dietzel, G. F. L., (1960). Geology and permian paleomagnetism of the Merano region (Province of Bolzano, N. Italy). Doct. thesis Utrecht, Geologica Ultraiectina, n. 4.

Di Luccio, F., Ventura, G., Di Giovambattista, R., Piscini, A. and Cinti, F. R., (2010). Normal faults and thrusts reactivated by deep fluids: The 6 April 2009 Mw 6.3 L’Aquila earthquake, central Italy. J. Geophys. Res., 115, B06315, doi:10.1029/2009JB007190.

Di Stefano, R., Chiarabba, C., Chiaraluce, L., Cocco, M., De Gori, P., Piccinini, D. and Valoroso, L., (2011). Fault properties heterogeneity affecting the rupture evolution of the 2009 (M_w 6.1) L’Aquila earthquake (Central Italy): insights from seismic tomography. Geophys. Res. Let., 38, doi:10.1029/2011GL047365.

Di Toro, G. and Pennacchioni, G., (2005). Fault plane processes and mesoscopic structure of a strong-type seismogenic fault in tonalites (Adamello batholith, Southern Alps). Tectonophysics, vol. 402/1-4, 54-79.

Di Toro, G., Nielsen, S. and Pennacchioni, G., (2005). Earthquake rupture dynamics frozen in exhumed ancient faults. Nature, 436, 1009-1012.

Di Toro, G., Pennacchioni, G. and Nielsen, S., (2009). Pseudotachylytes and Earthquake Source Mechanics. In: “Fault-zone Properties and Earthquake Rupture Dynamics”, Ed. Eiichi Fukuyama, published by the International Geophysics Series, Elsevier, 87-133.

Di Toro, G. and 12 others, (2010). From field geology to earthquake simulation: A new state of-the-art tool to investigate rock friction during the seismic cycle (SHIVA): Rendiconti Lincei-Scienze Fisiche e Naturali, v. 21, p. 95–114.

Di Toro, G., Mittempergher, S., Ferri F., Mitchell, T.M. and Pennacchioni, G., (2012). The contribution of structural geology, experimental rock deformation and numerical modeling in the understanding of the seismic cycle. Preface to the Special Volume "Physico-chemical processes in seismic faults". Journal of Structural Geology, 38, 3-10.

Doan, M.-L. and Gary, G., (2009). Rock pulverisation at high strain rate near the San Andreas Fault. Nat. Geosci. 2, 709-712.

Doan, M. and Billi, A., (2011). High strain rate damage of Carrara marble. Geophys. Res. Lett. 38 (38), L19302. doi:10.1029/2011GL049169.

Doglioni, C., (1990). The Venetian Alps Thrust Belt. In *Trust Tectonics*, 319-324, edited by McKlay, K., Chapmann & Hall.

Dor, O., Rockwell, T. K. and Ben-Zion, Y., (2006). Geological Observations of Damage Asymmetry in the Structure of the San Jacinto, San Andreas and Punchbowl Faults in Southern California: A Possible Indicator for Preferred Rupture Propagation Direction. Pure and Applied Geophysics, doi: 10.1007/s00024-005-0023-9.

Dor, O., Ben-Zion, Y., Rockwell, T.K. and Brune, J., (2006b). Pulverized rocks in the Mojave section of the San Andreas fault zone. Earth Planet. Sci. Lett. 245, 642e654.

Dor, O., Chester, J.S., Ben-Zion, Y., Brune, J.N. and Rockwell, T.K., (2009). Damage characterization in sandstones along the Mojave section of the San Andreas fault with a new method: implications for the depth and mechanism of rock pulverization. Pure Appl. Geophys. 166 (10e11), 1747e1773.

Dürr, H. H., Meybeck, M. and Dürr, S., (2005). Lithologic composition of the Earth's continental surfaces derived from a new digital map emphasizing riverine material transfer. Jouranl of Geophysical Research, vol. 19, doi:10.1029/2005GB002515.

Eberli, G.P., Masaferro, J.L. and Sarg, J.F. (Eds.), (2004). Seismic imaging of carbonate reservoirs and systems, AAPG Memoir 81.

Eberli, G.P., Baechle, G.T., Anselmetti, F.S. and Incze, M.L., (2003). Factors controlling elastic properties in carbonate sediments and rocks. The Leading Edge 22, 654-660.

Faccenda, M., Bressan, G. and Burlini, L., (2007). Seismic properties of the upper crust in the central Friuli area (northeastern Italy) based on petrophysical data. Tectonophysics, 445, 210-226.

Fagereng, A. and Sibson, R. H.. (2010). Melange rheology and seismic style. Geology, 38, 8, 751-754,doi: 10.1130/G30868.1.

Fang, Z. and Dunham, E., M., (2013). Additional shear resistance from fault roughness and stress levels on geometrically complex faults. Journal of Geophysical Research, doi:10.1002/jgrb.50262.

Faulkner, D. R., Lewis, A. C. and Rutter, E. H., (2003). On the internal structure and mechanics of large strike-slip fault zones: field observations of the Carboneras fault in southeastern Spain. Tectonophysics, 367, 235-251.

Ferri, F., Di Toro, G., Hirose, T. and Shimamoto, T., (2010). Evidence of thermal pressurization in high-velocity fiction experiments on smectite-rich gouges, Terra Nova, 22, 347–353, doi: 10.1111/j.1365-3121.2010.00955.x.

Ferri, F., Genevois, R., Iafelice, M. and Superchi, L., in preparation. Evaluation of strength and elastic properties of the Vajont STRATIGRAPHIC sequence (NE Italy) from uniaxial and triaxial compressive tests.

Fondriest, M., Smith, S. A. F., Di Toro, G., Zampieri, D. and Mittempergher, S., (2012). Fault zone structure and seismic slip localization in dolostones, an example from the Southern Alps, Italy. Journal of Structural Geology, 45, 52-67.

Fondriest, M., Smith, S. A. F., Candela, T., Mair, K., Nielsen, S. and Di Toro, G., (2013). Mirror-like faults and power dissipation during earthquakes. Geology, 41, 1175-1178.

Forrestal, M. J., Wright, T. W. and Chen, W., (2004). The effect of radial inertia on brittle samples during the split Hopkinson pressure bar test. Int. J. Impact Eng., 34, 405–411.

Fournier, F. and Borgomano, J., (2009). Critical porosity and elastic properties of microporous mixed carbonate-siliciclastic rocks. Geophysics 74 (2), E93e109.

Freund, L. B., (1990). Dynamic Fracture Mechanics, Cambridge Univ. Press, Cambridge, U. K., doi:10.1017/CBO9780511546761.

Galadini, F. and Galli, P., (1999). Palaeoseismology related to the displaced Roman archaeological remains at Egna (Adige Valley, northern Italy). Tectonophysics, 308, 171–191.

Galadini, F., Poli, M.E., Zanferrari, A., (2005). Seismogenic sources potentially responsible for earthquakeswith M≥6 in the eastern Southern Alps (Thiene–Udine sector, NE Italy). Geophys. J. Int. 161, 739–762.

Galli, P., Galadini, F. and Pantosti, D., (2008). Twenty years of paleoseismology in Italy. Earth-Science Reviews, 88(1-2): 89-117

Ghisetti, F. and Vezzani, L., (1999). Depth and modes of Pliocene – Pleistocene crustal extension of the Apennines (Italy). Terra Nova, 11(2-3): 67-72.

Graham, B., Antonellini, A., and Aydin, A., (2003). Formation and growth of normal faults in carbonates within a compressive environment. Geology, v. 31, no. 1, 11-14.

Gilbert, G. K., (1909). Earthquake forecast. Science, XXIX, 121-138.

Goldsby, D.L., and Tullis, T.E., (2011). Flash heating leads to low frictional strength of crustal rocks at earthquake slip rates. Science, v. 334, p. 216–218, doi:10.1126/science.1207902.

Gomberg, J., Reasenberg, P. A., Bodin, P. and Harris, R. A., (2005). Earthquake triggering by seismic waves following the Landers and Hector Mine earthquakes. Nature, vol. 411, p. 462-466.

Grady, D. E. and Kipp, M. E., (1987). Dynamic rock fragmentation. In “Fracture Mechanics of Rock”, Academic Press Inc. (London) Ltd., Chapter 10, p. 429-475.

Graham B., Antonellini, M. and Aydin, A., (2003). Formation and growth of normal faults in carbonates within a compressive environment. Geology, 31, 11-14.

Gratier, J.-P., Thouvenot, F., Jenatton, L., Tourette, A., Doan, M.-L. and Renard, F., (2013). Geological control of the partitioning between seismic and aseismic sliding behaviours in active faults: Evidence from the Western Alps, France. Tectonophysics, 600, 226-242.

Guéguen Y., Palciauskas, V., 1994. Introduction to the physics of rocks. Princeton University Press, 294 pp.

Han, R., Shimamoto, T., Hirose, T., Ree, J.H. and Ando, J., (2007a). Ultralow friction of carbonate faults caused by thermal decomposition. Science, 316(5826), 878-881.

Han, R.H., Shimamoto, T., Ando, J.I. and Ree, J.H., (2007b). Seismic slip record in carbonate-bearing fault zones: An insight from high-velocity friction experiments on siderite gouge. Geology, 35 (12): 1131-1134

Han., R., Hirose, T., and Shimamoto, T., (2010). Strong velocity weakening and powder lubrication of simulated carbonate faults at seismic slip rates. Journal of Geophysical Research, 115: B03412, doi: 10.1029/2008JB006136.

Han, R., Hirose, T., Shimamoto, T., Lee, Y. and Ando, J., (2011). Granular nanoparticles lubricate faults during seismic slip. Geology, 39, 599-602, doi: 10.1130/G31842.1.

Handy , M. R., Hirth, G. and Iovius, N, (2007). Tectonic Faults, Agent of change on a dynamic Earth. MIT Press, Cambridge, Mass., USA.

Hausegger, S., Kurz, W., Rabitsch, R., Kiechl, E. and Brosch, F, (2010). Analysis of the internal structure of a carbonate damage zone: Implications for the mechanisms of fault breccias formation and fluid flow. Journal of Structural Geology, 32, 1349-1362.

Hawkes, C., McLellan P. J. and Bachu S., (2005). Geomechanical factors affecting geological storage of CO2 in depleted oil and gas reservoirs. J. Can. Petrol. Technol., 44(10), 52-61.

Heidaryan, E., Hatami, T., Rahimi, M. and Moghadasi, J., (2011). Viscosity of pure carbon dioxide at supercritical region: Measurement and correlation approach. The Journal of Supercritical Fluids, 56, 144-151.

Heaton, T. H., (1990). Evidence for and implications of self-healing pulses of slip in earthquake rupture. Physics of the Earth and Planetary Interiors, 64, 1-20.

Holyoke, C.W., III, Kronenberg, A.K., and Newman, J., (2013). Dislocation creep of polycrystalline dolomite: Tectonophysics, v. 590, p. 72–82.

Hubbert, M. K. and Rubey, W. W., (1959). Role of fluid pressure in mechanics of overthrust faulting, Geological Society America, 70, 115-166.

Jackson, J., (1994). Active Tectonics of the Aegean Region. Annual Review of Earth and Planetary Sciences (22): 239-271.

Ide, S., Baltay, A. and Beroza, G. C., (2011). Shallow Dynamic Overshoot and Energetic Deep Rupture in the 2011 Mw 9.0 Tohoku-Oki Earthquake. Science, 2011. VOL 332, pp. 1426-1429.

Istituto Nazionale di Geofisica e Vulcanologia (INGV), 2012. Terremoto in Pianura Padana-Emiliana - 20 Maggio 2012 ML 5.9. (http://ingvterremoti.wordpress.com).

Ito, Y., T. Tsuji, Y. Osada, M. Kido, D. Inazu, Y. Hayashi, H. Tsushima, R. Hino and H. Fujimoto (2011). Frontal wedge deformation near the source region of the 2011 Tohoku-Oki earthquake. Geophys. Res. Lett., 38, L00G05, doi:10.1029/2011GL048355.

Kame, N., Rice, J. R., and Dmowska, R., (2003). Effects of prestress state and rupture velocity on dynamic fault branching. Journal of Geophysical Research-Solid Earth. vol. 108 (B5).

Kanamori, H. and Heaton, T.H., (2000). Microscopic and Macroscopic Physics of Earthquakes. In: J. Rundle, D.L. Turcotte and W. Klein (Editors), GeoComplexity and the Physics of Earthquakes, AGU, Washington, 147-163.

Kanamori, H. and Brodsky, E., (2004). The physics of earthquakes. Reports on Progress in Physics, v. 67, p. 1429–1496, doi:10.1088/0034-4885/67/8/R03.

Kaszuba, J. P., Williams, L. L., Janecky, D. R., Kirk Hollis, W. and Tsimpanogiannis, I. N., (2006). Immiscible CO_2-H_2O fluids in the shallow crust. Geochemistry Geophysics Geosystems, 7, 10.

Kim, Y-S and Sanderson, D. J., (2004). The relationship between displacement and length of faults: a review. Earth-Science Reviews, 68, 317-334.

Kyriakopoulos, C., Masterlark, T., Stramondo, S., Chini, M. and Bignami, C., (2013). Coseismic slip distribution for theMw 9 2011 Tohoku-Oki earthquake derived from 3-D FE modeling, J. Geophys. Res. Solid Earth, 118, doi:10.1002/ jgrb.50265.

Kurz, W., Imber, J., Wibberley, C. A. J., Holdsworth, R. E and Colletini, C., (2008). The internal structure of fault zones: fluid flow and mechanical properties. From: Wibberley, C. A. J., Kurz, W., Imber, J., Holdsworth, R. E. and Collettini, C. (eds.), The internal Structure of Fault Zones: Implications for Mechanical and Fluid-Flow Properties, 299, 1-3. Geological Society of London.

Lachenbruch, A.H., (1980). Frictional Heating, Fluid Pressure, and the Resistance to Fault Motion. Journal of Geophysical Research, 85(Nb11): 6097-6112.

Laubscher, H. P., (1971). The large scale kinematics of the Western Alps and the Western Apennines and its palinspastic implications. Am. J. Sci., 193-226.

Laubscher, H. P., (1988). The arcs of the Western Alps and the Northern Apennines: an updated view. Tectonophysics, 146, 67-78.

Laubscher, H., (1996). Shallow and deep rotations in the Miocene Alps. Tectonics 15: doi: 10.1029/96TC00432.

Lavecchia,G., de Nardis, R., Cirillo, D., Brozzetti, F. and Boncio, P., (2012). The May-June 2012 Ferrara Arc earthquakes (northern Italy): structural control of the spatial evolution of the seismic sequence and of the surface pattern of coseismic fractures. Annals of Geophysics, 55, 4, doi: 10.4401/ag-6173.

Li, H., Wang, H., Xu, Z., Si, J., Pei, J., Li, T., Huang, Y., Song, S.-R., Kuo, L.-W., Sun, Z., Chevalier, M.-L. and Liu, D., (2012). Characteristics of the fault-related rocks, fault zones and the principal slip zone in the Wenchuan Earthquake Fault Scientific Drilling Project Hole-1 (WFSD-1). Tectonophysics 584, 23–42.

Liebscher, A., (2010). Acqueous fluids at elevated pressure and temperature. Geofluids, 10, 3-19.

Lucente, F. P., De Gori, P., Margheriti, L., Piccinini, D., Di Bona, M., Chiarabba, C. and Agostinetti, N., (2010). Temporal variation of seismic velocity and anisotropy before the 2009 MW 6.3 L'Aquila earthquake, Italy. Geology, 38;1015-1018 doi: 10.1130/G31463.1.

Lucia, F.J., (1999). Carbonate Reservoir Characterization, vol. XII. Springer, p. 226.

Lucia, J. F., 2007, Carbonate reservoir characterization, an integrated approach: 2nd Edition.

Ma, S. and Andrews, D. J., (2010). Inelastic off-fault response and three-dimensional dynamics of earthquake rupture on a strike-slip fault. Journal Geophys. Res., 115, doi: 10.1029/2009JB006382.

Mancini, E.A., Blasingame, T.A., Archer, R., Panetta, B.J., Haynes, C.D. and Benson D.J., (2004). Improving hydrocarbon recovery from mature oil fields producing from carbonate facies through integrated geoscientific and engineering reservoir characterization and modeling studies, Upper Jurassic Smackover Formation, Womack Hill Field (Eastern Gulf Coast, USA). AAPG Bulletin 88, 1629-1651.

Malagnini, L., Herrmann, R. B., Munafò, I., Buttinelli, M., Anselmi, M., Akinci, A. and Boschi, E., (2012). The 2012 Ferrara Seismic Sequence: Regional Crustal Structure, Earthquake Sources, and Seismic Hazard. Geophysical Research Letters, 39, doi:10.1029/2012GL053214.

Marone, C. and Scholz, C., (1989). Particle-size distribution and microstructures within simulated gouge. Journal of Structural Geology, 11, 799-814.

Marone, C. (1998), Laboratory-derived friction laws and their application to seismic faulting, *Ann. Revs. Earth Plan. Sci., 26*, 643-696.

Massironi M., Zampieri, D. and Caporali, A., (2006). Miocene to Present major fault linkages through the Adriatic indenter and the Austroalpine-Penninic collisional wedge (Alps of NE Italy). In: Moratti, G. & Chalouan, A. (eds) Tectonics of the Western Mediterranean Region and North Africa. Geological Society, London, Special Publications, 262, 245-258.

Matonti, C., Lamarche, J., Guglielmi, Y and Marié, L., (2012). Structural and petrophysical characterization of mixed conduit/seal fault zones in carbonates: Example from the Castellas fault (SE France). Journal of Structural Geology, 39, 103-121.

Mazzullo, S.J., (2004). Overview of porosity evolution in carbonate reservoirs. Kansas Geological Society Bulletin, 79, 20-28.

McKenzie, D., (1978). Active tectonics of the Alpine-Himalayan belt: the Aegean Sea and surrounding regions. Geophys. J. R. astr. SOC, 55, 217-254.

Meneghini, F., Di Toro, G., Rowe, C. D., Moore, J. C., Tsutsumi, A. and Yamaguchi, A., (2010). Record of mega-earthquakes in subduction thrusts: the black fault rocks of Pasagshak Point (Kodiak Island, Alaska). Bulletin of the Geological Society of America, 122, 1280-1297.

Micarelli, L., Benedicto, A., and Wibberley, C.A.J., (2006). Structural evolution and permeability of normal fault zones in highly porous carbonate rocks. Journal of Structural Geology, 28(7), 1214-1227.

Miller, S. A., Collettini, C., Chiaraluce, L., Cocco, M., Barchi, M. and Kaus, B. J., (2004). Aftershocks driven by a high-pressure CO2 source at depth. Nature, 19, 724-727.

Mitchell, T. M. and Faulkner, D. R. (2009). The nature and origin of off fault damage surrounding strike-slip fault zones with a wide range of displacements: A field study from the Atacama fault zone, northern Chile. Journal of Structural Geology, 31(8), 802–816, doi:10.1016/j.jsg.2009.05.002.

Mogi, K., (1966).Some precise measurements of fracture strength of rocks under uniform compressive stress. Felsmechanik und Ingenieurgeologie, 4, 41–55.

Mogi, K., (2007). Experimental rock mechanics. Taylor & Francis, London, p 361.

Mollema, P. N. and Antonellini, M., (1999). Development of strike-slip faults in the dolomites of the Sella Group, Northern Italy. Journal of Structural Geology, 21, 273-292.

Molli, G., Cortecci, G., Vaselli, L., Ottria, G., Cortopassi, A., Dinelli, E., Mussi, M. and Barbieri, M., (2010). Fault zone structure and fluid-rock interaction of a high-angle normal fault in Carrara marble (NW Tuscany, Italy). Journal of Structural Geology, 32, 1334-1348, doi: 10.1016/j.jsg.2009.04.021.

Monzawa, N. and Otsuki, K., (2003). Comminution and fluidization of granular fault materials: implications for fault slip behavior. Tectonophysics, 367, 127-143.

Nemser, E.S. and Cowan, D.S., (2009). Downdip segmentation of strike-slip fault zones in the brittle crust. Geology, v. 37, p. 419-422.

Niemejier, A., Di Toro, G., Griffith, W. A., Bistacchi, A., Smith, S. and Nielsen, S. B., (2012). Inferring earthquake physics and chemistry using an integrated field andlaboratory approach. Journal of Structural Geology, 39, 1-35.

Noda, H., Dunham, E. M. and Rice, J. R., (2009). Earthquake ruptures with thermal weakening and the operation of major faults at low overall stress levels. Journal of Geophysical Research, 114, B07302.

Otsuki, K., Monzawa, N. and Nagase, T., (2003). Fluidization and melting of fault gouge during seismic slip: identification in the Nojima fault zone and implications for focal earthquake mechanisms. Journal of Geophysical Research, 108, doi:10.1029/2001JB001711 2192.

Patacca, E., Scandone, P., Di Luzio, E., Cavinato, G.P. and Parotto, M., (2008). Structural architecture of the central Apennines: Interpretation of the CROP 11 seismic profile from the Adriatic coast to the orographic divide. Tectonics, 27: TC3006, doi: 10.1029/2005TC001917.

Paterson, M. S. and Wong, T.-F., (2005). Experimental Rock Deformation – The Brittle Field, 2nd editin. 348 pp.. Berlin, Heidelberg, New York, Springer-Verlag.

Pittarello, L., Di Toro, G., Bizzarri, A., Pennacchioni, G., Hadizadeh, J. and Cocco, M., (2008). Energy partitioning during seismic slip in pseudotachylyte-bearing faults (Gole Larghe Fault, Adamello, Italy). Earth and Planetary Science Letters, vol. 269, 131-139.

Poliakov, A. N. B., Dmowska R. and Rice, J. R., (2002). Dynamic shear rupture interactions with fault bends and off-axis secondary faulting. Journal of Geophysical Research, 107, doi:10.1029/2001JB000572.

Pondrelli, S., Salimbeni, S., Morelli, A., Ekström, G. and Boschi, E., (2007). European–Mediterranean regional centroid moment tensor catalog: solutions for years 2003 and 2004. Phys. Earth Planet. Inter. 164, 90–112.

Power, W. and Tullis, T., (1989). The Relationship Between Slickenside Surfaces in Fine-Grained Quartz and the Seismic Cycle. Journal of Structural Geology, 11(7): 879-893.

Prosser, G., (1998). Strike-slip movements and thrusting along a transpressive fault zone: The North Giudicarie line (Insubric line, northern Italy). Tectonics, 17, 921-937.

Prosser, G., (2000). The development of the North Giudicarie fault zone (Insubric line, Northern Italy). Journal of Geodynamics, 30, 229-250.

Ratschbacher, L, Frisch, W., Linzer, H.-G. and Merle, O., (1991). Lateral extrusion in the eastern Alps, PArt 2: Structural analysis. Tectonics, 10, 257-271.

Reches, Z. and Dewers, T. A., (2005). Gouge formation by dynamic pulverization during earthquake rupture. Earth and Planetary Science Letters, 235, 361-374.

Reid, H. F., (1910). The Mechanics of the Earthquake, the California Earthquake of April 18, 1906. Report of the State Investigation Commission Vol. 2 Carnegie Institution of Washington, Washington, D. C..

Rice, J.R., (2006). Heating and weakening of faults during earthquake slip. Journal of Geophysical Research-Solid Earth, 111(B5), B05311, doi:10.1029/2005JB004006.

Rice, J. R. and Cocco, M., (2007). Seismic fault rheology and earthquake dynamics. In: Handy, M. R., Hirth, G. and Hovious, N. (eds.), The Dynamic of Fault Zones, 99-137. MIT Press, Cambridge, MA.

Rockwell, T., Sisk, M., Girty, G., Dor, O., Wechsler, N. and Ben-Zion, Y, (2009). Chemical and Physical Characteristics of Pulverized Tejon Lookout Granite Adjacent to the San Andreas and Garlock Faults: Implications for Earthquake Physics. Pure and Applied Geophysics, 166, 1725–1746.

Rossetti, F., Balsamo, F., Villa, I.M., Bouybaouenne, M., Faccenna, C. and Funiciello, R., (2007). Pliocene-Pleistocene high-T/low-P metamorphism during multiple granitic intrusions in the southern branch of the Larderello geothermal field (Southern Tuscany, Italy). Journal of the Geological Society, London 165, 247-262.

Rossetti, F., Tecce, F., Billi, A. and Brilli, M., (2007b). Patterns of fluid flow in the contact aureole of the late Miocene Monte Capanne pluton (Elba Island, Italy): the role of structures and rheology. Contributions to Mineralogy and Petrology 153, 743-760.

Rowe, C. D., Moore, J.C., Meneghini, F. and McKeirnan, A. W., (2005). Large-scale pseudothachylytes and fluidized cataclasites from an ancient subduction thrust fault. Geology, 33, 937-940.

Rowe; C. D., Fagereng, A, Miller, J. A. and Mapani, B., (2012b). Signature of coseismic decarbonation in dolomitic fault rocks of the Naukluft Thrust, Namibia. Earth and Planetary Science Letters, 333-334, 200-210.

Sagy, A., Brodsky, E. E. and Axen, G. J., (2007). Evolution of fault-surface roughness with slip. Geology, 35, 283-286.

Salvini, F., Billi, A. and Wise, D.U., (1999). Strike-slip fault-propagation cleavage in carbonate rocks: the Mattinata Fault zone. Journal of Structural Geology 21, 1731–1749.

Sammis, C., King, G. and Biegel, R., (1987). The kinematics of gouge deformation. Pure and Applied Geophysics, 125, 777-812.

Samtani, M., Dollimore, D., and Alexander, K.S., (2002). Comparison of dolomite decomposition kinetics with related carbonates and the effect of procedural variables on its kinetic parameters. Thermochimica Acta, v. 367–368, p. 285–295.

Santini, L. and Martin, S., (1988). Basamento Austroalpino e coperture sudalpine nella zona di Samoclevo (Val di Sole, Trentino Occientale). Mem. Sci. Geol. Padova, 40, 275-284.

Scholz, C. H., (2002). The Mechanics of Earthquakes and Faulting. Cambridge University Press, Cambridge.

Schönborn, G., (1999). Balancing cross sections with kinematic constraints: The Dolomites (northern Italy). Tectonics, 18, 527-545.

Sedea, R. and Di Lallo, E., (1984). Carta Geologica dell’area di Valli del Pasubio-Posina-Laghi, alla scala 1:20000. Centro di Studio per i problemi dell’orogeno delle Alpi Orientali del Consiglio Nazionale delle Ricerche presso l’Università di Padova, Memorie di Scienze Geologiche, S.E.L.C.A., via R. Giuliani 153, Firenze.

Semenza, E., 1974. La fase giudicariense, nel quadro di una nuova ipotesi sull’orogenesi alpina nell’area italo-dinarica. Mem. Soc. Geol. It. 13, 187-226.

Sibson, R., (1973). Interaction between temperature and pore-fluid pressure during earthquake faulting–A mechanism for partial or total stress relief. Nature, 243: 66-68.

Sibson, R.H., (1974). Frictional constraints on thrust, wrench and normal faults. Nature, v. 249, p. 542–544, doi:10.1038/249542a0.

Sibson, R.H., (1975). Generation of pseudotachylyte by ancient seismic faulting. Geophysical Journal of the Royal Astronomical Society, v. 43, p. 775–794, doi:10.1111/j.1365-246X.1975.tb06195.x.

Sibson, R., (1977). Fault rocks and fault mechanisms. Journal of the Geological Society, London 133, 191-213.

Sibson, R. H., (1989). Earthquake faulting as a structural process. Journal of Structural Geology, 11(1), 1-14.

Sibson, R.H., (1980). Power dissipation and stress levels on faults in the upper crust. Journal of Geophysical Research, v. 85, p. 6239–6247, doi:10.1029/JB085iB11p06239.

Sibson, R., (1990a). Conditions for fault-valve behavior. In: Knipe R. J. and Rutter, E. H. (Editors), Deformation Mechanisms, Rheology and Tectonics. Geol. Soc. London, Spec. Publ.,54.

Sibson, R.H., (2003). Thickness of the seismic slip zone. Bulletin of the Seismological Society of America, 93(3), 1169-1178.

Sibson, R. H., (2003). Thickness of the seismic slip zone. Bulletin of the Seismological Society of America, 93(3), 1169-1178.

Sibson, R.H. and Toy, V., (2006). The habitat of fault-generated pseudotachylyte: Presence vs. absence of friction-melt, in Abercrombie, R., et al., eds., Earthquakes: Radiated Energy and the Physics of Faulting: American Geophysical Union Geophysical Monograph 170, p. 153–166.

Siman-Tov, S., Aharonov, E., Sagy, A. and Emmanuel, S., (2013). Nanograins form carbonate fault mirrors. Geology, v. 41, p. 703–706, doi:10.1130/G34087.1.

Sleijko, D., Carulli, G. B. et al., (1989). Seismotectonics of the eastern Southern Alps. Bollettino di Geofisica Teorica ed Applicata, 31, 109–136.

Smith, S. A. F., Billi, A., Di Toro, G. and Spiess, R., (2011). Microstructures of Principal Slip Zones in Limestones, and Implications for the Seismic Cycle (Tre Monti fault, central Appennines, Italy). Pure and Applied Geophysics, doi:10.1007/s00024-011-0301-7.

Smith, S. A. F., Collettini, C. and Holdsworth, R. E., (2008). Recognizing the seismic cycle along ancient faults: CO_2-induced fluidization of breccias in the footwall of a sealing low-angle normal fault. Journal of Structural Geology, 30, 1034-1046.

Smith, S.A.F., Di Toro, G., Kim, S., Ree, J.-H., Nielsen, S., Billi, A., and Spiess, R., (2013). Coseismic recrystallization during shallow earthquake slip: Geology, v. 41, p. 63–66, doi:10.1130/G33588.1.

Spitz, A, (1919). Eine Querstörung bei Meran. Verh. Geol. Staatsanst., p. 62-66, Wien.

Stein, R. S., (1999). The role of stress transfer in earthquake occurrence. Nature, 402, pp. 605-609.

Stiros, S., (1995). Unexpected shock rocks an aseismic area, EOS, 5,1.

Storti, F., Billi, A. and Salvini, F., (2003). Grain size distributions in natural carbonate fault rocks: insights for non-self-similar cataclasis. Earth and Planetary Science Letters, 206, 173–186.

Sulem, J. and Famin, V., (2009). Thermal decomposition of carbonates in fault zones: Slip weakening and temperature limiting effects *J. Geophys. Res.,* 114, B03309.

Sutherland, R., Toy, V.G., Townend, J., Cox, S.C., Eccles, J.D., Faulkner, D.R., Prior, D.J., Norris, R.J., Mariani, E., Boulton, C., Carpenter, B.M., Menzies, C.D., Little, T.A., Hasting, M., De Pascale, G.P., Langridge, R.M., Scott, H.R., Lindroos, Z.R., Fleming, B. and Kopf, A.J., (2012). Drilling reveals fluid control on architecture and rupture of the Alpine fault, New Zealand. Geology 40, 1143–1146.

Schwinner, R., (1915). Zur Tektonik des nördlichen Etschbuchtgebirges. Verh. K. k. geol. Reichsanst., 7, p. 135-138, Wien.

Templeton, E. L. and Rice, J., (2008). Off-fault plasticity and earthquake rupture dynamics: 1. Dry materials or neglect of fluid pressure changes. Journal of Geophysical Research, 113, doi:10.1029/2007JB005529.

Tesei, T., Collettini, C., Viti, C. and Barchi, M. R., (2013). Fault architecture and deformation mechanisms in exhumed analogues of seismogenic carbonate-bearing thrusts. Journal of Structural Geology, 55, 167-181.

Thurber, C. H., (2013). Fault zone properties from seismic tomography and joint inversions. In abstract volume of the 40th workshop of the International School of Geophysics “Properties and processes of crustal fault zones”, Erice (Sicily, Italy) 18-24 May 2013.

Tiab, D. and Donaldson, E.C., (1996). Petrophysics: Theory and Practice of Measuring Reservoir Rock and Fluid Transport Properties, vol. XIV. Gulf Professional Publishing, p. 706.

Tisato, N., Di Toro, G., De Rossi, N., Quaresimin, M., Candela, T., (2012).Experimental investigation of flash weakening in limestone. Journal of Structural Geology, 38, 183-199.

Tondi, E., Antonellini, M., Aydin, A., Marchegiani, L. and Cello, G., (2006). The role of deformation bands, stylolites and sheared stylolites in fault development in carbonate grainstones of Majella Mountain, Italy. Journal of Structural Geology, 28, 376-391.

Transalp Working Group, (2002). First deep seismic images of the Eastern Alps reveal giant crustal wedges. Geophysical Research Letters, 29, 10 1029-10 1032.

Tuncay, E. and Hasancebi, N, (2009). The effect of length to diameter ratio of test specimens on the uniaxial compressive strength of rock. Bull Eng Geol Environ, 68, 491–497, doi: 10.1007/s10064-009-0227-9.

Turcotte, D. L., (1986). Fractals and fragmentation. J. Geophys. Res., 91, 1921-1926.

Ujie, K., Yamaguchi, A., Kimura, G. and Toh, S., (2007). Fluidization of granular material in a subduction thrust at seismigenic depths. Earth and Planetary Science Letters, 259, 307-318.

Ujiie, K., Tsutsumi, A. and Kameda, J., (2011). Reproduction of thermal pressurization and fluidization of clay-rich fault gouges by high-velocity friction experiments and implications for seismic slip in natural faults. Geological Society, London, Special Publications, 359, 267-285.

Valoroso, L., Chiaraluce, L., Piccinini, D., Di Stefano, R., Schaff, D., Waldhauser, F., (2013). Radiography of a normal fault system by 64,000 high-precision earthquake locations: the 2009

L'Aquila (central Italy) case study. Journal of Geophysical Research—Solid Earth. http://dx.doi.org/10.1002/jgrb.50130.

Van Hilten, D., (1960). *Geology and Permian paleomagnetism of the Val di Non area. Geologica Ultraiectina*, 5, 1-95.

Ventura, G. and Di Giovanbattista, R., (2013). Fluid pressure, stress field and propagation style of coalescing thrusts from the analysis of the 20 May 2012 ML 5.9 Emilia earthquake (Northern Apennines, Italy). doi: 10.1111/ter.12007.

Viganò, A., Bressan, G., Ranalli, G. and Martin, S., (2008). Focal mechanism inversion in the Giudicarie-Lessini seismotectonic region (Southern Alps, Italy): Insights on tectonic stress and strain. Tectonophysics, 460, 106-115.

Viganò, A., Tumiati, S., Recchia, S., Martin, S., Marelli, S. and Rigon, R., (2011). Carbonate pseudotachylytes: evidence for seismic faulting along carbonate faults. Terra Nova, doi: 10.1111/j.1365-3121.2011.00997.

Wells, D. L. and Coppersmith, K. J., (1994). New Empirical Relationships among Magnitude, Rupture Length, Rupture Width, Rupture Area, and Surface Displacement. Bulletin of the Seismological Society of America, 84, 974-1002.

Verberne, B. A., De Bresser, J. H. P., Niemeijer, A. R. Spiers, C. J., De Winter, D. A. M. and Plümper, O., (2013a). Nanocrystalline slip zones in calcite fault gouge show intense crystallographic preferred orientation: Crystal plasticity at subseismic slip rates at 18–150°C. Geology 41, 863–866.

Verberne, B. A., Spiers, C., J., Niemeijer, A. R., De Bresser, J. H., P., De Winter, D. A. M. and Plümper, O., (2013b). Frictional Properties and Microstructure of Calcite-Rich Fault Gouges Sheared at Sub-Seismic Sliding Velocities. doi: 10.1007/s00024-013-0760-0.

Werling, E., (1992). Tonale-, Pejo- und Judicarien-linie: Kinematik, Mikrostrukturen und Metamorphose von Tektoniten aus räumlichen interferierenden aber verschiedenaltrigen Verwerfungszonen. Diss. ETH, 9923, 1-276.

Westaway, R. and Jackson, J., (1984). Surface faulting in the southern Italian Campania-Basilicata earthquake of 23 November 1980. Nature, 312: 436-438.

Wibberley, C.A.J., Yielding, G. and Di Toro, G., (2008). Recent advances in the understanding of fault zone internal structure: a review. In: Wibberley, C.A.J., Kurz, W., Imber, J., Holdsworth, R.E., Collettini, C. (Eds.), The Internal Structure of Fault Zones: Implications for Mechanical and Fluid Flow Properties. The Geological Society of London, London, p. 5–33.

Williams, J. C., (1976). The segregation of particulate materials. A review. Powder Technology, 15, 245–251.

Wilson, B., Dewers, T., Reches, Z and Brune, J. N., (2005). Particle size and energetics of gouge from earthquake rupture zones, Nature 434, 749–752.

Yamashita, T., (2000). Generation of microcracks by dynamic shear rupture and its effects on rupture growth and elastic wave radiation. Geophys. J. Int., 143, 395– 406.

Yeo, S. D. and Kiran, E., (2005). Formation of polymer particles with supercritical fluids: A review. Journal of Supercrital Fluids, 34, 287–308.

Yuan, F., V. Prakash, and T. Tullis, (2011). Origin of pulverized rocks during earthquake fault rupture. Journal of Geophysical Research, 116, B06309, doi:10.1029/2010JB007721.

Zampieri, D., (1995). Tertiary extension in the southern Trento Platform Southern Alps, Italy. Tectonics, 14, 3, 645-657.

Zampieri, D., Massironi, M., Sedea, R. and Sparacino, V., (2003). Strike-slip contractional stepovers in the Southern Alps (northeastern Italy). Eclogae Geologicae Helvetiae, 96, 115-123.

Zampieri, D. and Massironi, M., (2007). Evolution of a poly-deformed relay zone between fault segments in the eastern Southern Alps, Italy. Geological Society, London, Special Pubblications, 290, 351-366, doi:10.1144/SP290.13.

Zattin, M., Viola, G., Martin, S., Bigazzi, G and Balestrieri, M. L., (1997). Neogene kinematics of the Giudicarie Line (Central Eastern Alps, Italy): New apatite fission track data. Terra Nova 9, Abstr. Suppl. 1, 492.

Zoback, M.D., Hickman, S., Ellsworth, W.L. and SAFOD Science Team, (2011). Scientific drilling into the San Andreas Fault Zone—an overview of SAFOD's first five years. Scientific Drilling 11, 14–28.